Understanding, Constructing, and Probing Highly-Entangled Phases of Quantum Matter

by

Andrew C. Potter

Sc.B., Brown University (2008)

Submitted to the Department of Physics
in partial fulfillment of the requirements for the degree of

Doctor of Philosophy in Physics

at the

MASSACHUSETTS INSTITUTE OF TECHNOLOGY

August 2013
[SEPTEMBER 2013]

Author .....
Department of Physics
July 22, 2013

Certified by .....
Patrick A. Lee
William and Emma Rogers Professor of Physics
Thesis Supervisor

Accepted by .....
John Belcher
Professor and Associate Department Head for Education

Understanding, Constructing, and Probing Highly-Entangled Phases of Quantum Matter

by

Andrew C. Potter

Submitted to the Department of Physics
on July 22, 2013, in partial fulfillment of the
requirements for the degree of
Doctor of Philosophy in Physics

Abstract

In this thesis, I explore three classes of quantum phases of matter that cannot be understood purely on the basis of symmetry, and can be regarded (to varying degrees) as having highly-entangled ground-states. The first Part describes topological superconductors with non-Abelian defects, and develops realistic routes to constructing these exotic superconductors from more elementary materials. Particular attention is payed to practical issues such as disorder. The second Part examines the role of interactions in electron topological insulators (TIs). Non-perturbative definitions of the familiar topological band-insulator are given, and new strongly-correlated TIs with no band-structure analogs are identified. The last Part turns exotic gapless phases without quasi-particle excitations, focusing on topics related to recently discovered quantum spin-liquid (QSL) materials. The possibility of a gapless QSL in the vicinity of the metal-insulator transition in doped semiconductors is explored, and optical conductivity is developed as an experimental tool to examine the nature of the QSL candidate Herbertsmithite. The material of this thesis is closely parallels that of Refs [1, 2, 3, 4, 5, 7, 8, 9, 10, 11].

Thesis Supervisor: Patrick A. Lee
Title: William and Emma Rogers Professor of Physics

Acknowledgments

I am deeply indebted to my supervisor, Professor Patrick Lee, and also to Professor T. Senthil for their invaluable guidance and mentorship. Our many discussions and collaborations over the years taught a great deal about how to think intuitively about physics problems, and how to identify and tackle interesting research questions.

Thanks also to Professor Jagadeesh Moodera and Dr. Peng Wei for taking an interest in our metallic thin-films proposal and for many illuminating discussions on related experimental aspects.

Thanks also to my fellow CMT graduate students and post-docs, especially David F. Mross and Rahul Nandkishore, whose interactions were one of the most valuable parts of my doctoral education. Their support and encouragment were especially valuable in seeing me through unproductive periods. Additionally, our frequent discussions over the last five years were incredibly educational and helped me sort out a great number of confusions. Special thanks to Chong Wang, who was an essential driver for the work reported in Part II of this thesis, and who patiently taught me much of what I currently know about topological field theory.

Additionally, I would like to thank of Professors Pablo Jarillo-Herrero, Tomas Palacios, and Leonid Levitov, for their patience and encouragement during the meandering journey that led me to my current research.

The work in this thesis was facilitated by the support of the Interdisciplinary Quantum Information Science and Engineering NSF IGERT fellowship at MIT, which enabled many of my collaborations. I thank Professor Leonid Levitov for sponsoring my participation in this program.

Lastly, I am incredibly grateful to my fiancee, Clancey, for her continued love, support, patience, and encouragement over the last five years.

Contents

List of Figures

List of Tables

Chapter 1

Introduction - Highly Entangled Phases of Matter

Quantum condensed matter physics concerns itself with the study of phenomena arising from the collective behavior of many coupled atoms and electrons. An important task is to understand the equilibrium physics of a quantum system at low-temperature; for this purpose, it is sufficient to understand the nature of the quantum ground-state and low-energy excited states, as these control the response of the system to low-energy external probes. Most of 20th century physics concerned itself with understanding systems whose dynamics were symmetric under some symmetry operation, like spin-rotation or time-reversal symmetry, that was spontaneously broken at low-temperatures.

The understanding of the equilibrium properties of symmetry-breaking states, such as magnets and superfluids, is by now quite mature: symmetry-breaking phases can be characterized by a local order parameter (e.g. magnetization density in a magnet, or the local superfluid phase in a superconductor). With few exceptions[1], the low-energy physics of symmetry-broken phase, and of phase transitions between symmetry-broken phases are completely governed by long-wavelength dynamical fluctuations of this order parameter.

However, since the discovery of quantum Hall phases, it has been apparent that symmetry considerations are not sufficient to distinguish all distinct phases of matter. Namely, phases of matter may have precisely the same set of symmetries but nevertheless have sharply distinct physical properties. Such phases cannot be distinguished by a local-order parameter, but only by more subtle means. While all aspects of such phases are not always well-understood in detail, the best available modern understanding of what distinguishes these non-symmetry-breaking phases from ordinary symmetry-breaking ones is that their ground-states have a high-degree of quantum entanglement between spatially separated degrees of freedom. Therefore, for lack of better terminology, I will refer to such phases as "highly-entangled". Highly-entangled states with a gap to excitations, are typically distinguished from

[1]There can also be gapless electron excitations. These are dynamically decoupled from the order parameter in the symmetry-broken phase, but can dramatically modify the dynamics of critical fluctuations at phase-transitions.

weakly-entangled phases by robust gapless, or otherwise unconventional, boundaries, that lead to sharply quantized response to external probes. Such sharply quantized features often receive the adjective: "topological", as they are robust to smooth-deformations of the system's Hamiltonian that do not close the system's excitation gap.

1.1 Defining Highly-Entangled

The very simplest many-particle solid-state system imaginable is a collection of decoupled atoms with a filled shell of electrons. In this decoupled atomic limit, each atom is completely isolated and un-entangled with its surrounding atoms. One can move slightly away from this extreme limit by allowing a small amount of tunneling between electrons on adjacent atoms. The interatomic tunneling generates quantum entanglement between different atoms, but the resulting state is clearly in the same phase as the trivial decoupled atom system and should clearly not be regarded as highly-entangled. It is useful to refine our notion of highly entangled to distinguish between phases that are essentially trivially decoupled atoms, and those which are not.

For this purpose, I adopt the perspective first explained by X.G. Wen. Let us begin by considering only systems that have a unique ground-state with a finite energy gap to excited states. For this restricted class, one can define an equivalence class of quantum ground-states as follows: two ground-states $|\Psi_{0,1}\rangle$ of local quantum Hamiltonians $H_{0,1}$ (describing thermodynamically large systems) are considered to be smoothly connected to each other, if H_0 can be smoothly deformed into H_1 by a continuous sequence of local unitary operations:

$$H_\lambda = U(\lambda) H_0 U(\lambda)^\dagger \qquad U(\lambda) \equiv \mathcal{P}_\lambda \left[e^{-i \int_0^\lambda d\tilde{\lambda} \int d^d x \hat{\mathcal{O}}_{\tilde{\lambda}}(x)} \right] \tag{1.1}$$

where H_λ is a sequence of gapped Hamiltonians labeled by the adiabatic parameter $\lambda \in [0,1]$ (such that $H_{0,1} = \lim_{\lambda \to 0,1} H_\lambda$), and $\hat{\mathcal{O}}_\lambda(x)$ is a sequence of local operators that each has finite support near spatial point x.

If a state is smoothly deformable to the trivial decoupled atomic limit, in the above sense, I will call that state weakly-entangled. States that cannot be smoothly deformed to an unentangled state of decoupled atoms, will be regarded as highly-entangled. For example, ordinary electronic band-insulators are adiabatically connected to the decoupled atomic system, since the latter can be obtained by the former by continuously dialing the inter-atom electron tunneling to zero. In this sense, ordinary band-insulators weakly-entangled phases of matter.

1.2 Some Examples

1.2.1 Chiral Band-Insulators

In the previous section we saw that ordinary band-insulators are smoothly connected to the trivial atomic limit. However, not all band-insulators are weakly-entangled. The simplest examples of highly-entangled band-insulators are chiral insulators with protected gapless edge states that propagate in only one direction. These arise for filled Landau levels of electrons in a magnetic field, or their lattice analogs: Chern-insulators. Chiral band-insulators have a bulk gap, but protected gapless chiral edge states. Since these chiral edge states cannot be removed from the edge without destroying the bulk gap, Chern insulators are clearly highly-entangled by the above definition.

The distinction between ordinary insulators and those with chiral edge states is 'topological' in the sense that the number of chiral edge-states of a band-insulator is an integer invariant that is insensitive to small perturbations that do not affect the bulk gap.

Such topological distinctions are captured by integer invariants. This is most easily formulated for non-interacting lattice-insulators with discrete translation symmetry. Consider such a non-interacting two-dimensional band-insulator on a lattice. The ground-state is characterized by a filled set of single-electron eigen-states, $|\psi_n(\mathbf{k})\rangle$, with energy $\varepsilon_{n,\mathbf{k}}$. Here $\mathbf{k}$ labels wave-vectors in the Brillouin zone (BZ), and the index n describes degrees of freedom within the unit cell. Defining the Berry connection:

$$\mathcal{A}(\mathbf{k}) = i \sum_n \theta\left(\varepsilon_{n,\mathbf{k}}\right) \langle \psi_n(\mathbf{k}) | \partial_{\mathbf{k}} | \psi_n(\mathbf{k}) \rangle \tag{1.2}$$

which encodes how the phase of the wave-function winds from one point in the BZ to another, the following quantity is a quantized topological invariant known as the Chern number:

$$\mathcal{C} = \frac{1}{2\pi} \int_{BZ} \varepsilon^{ij} \partial_{k_i} \mathcal{A}_j \tag{1.3}$$

which measures the number of chiral edge states. Such topological distinctions among different phases of matter typically has dramatic consquences for the properties of non-trivial phases. For example, Chern insulators have quantized electrical and thermal Hall-conductivity:

$$\sigma_{xy} = \frac{e^2}{h}\mathcal{C} \qquad \kappa_{xy} = \frac{\mathrm{L}e^2}{h}\mathcal{C} \tag{1.4}$$

where L is the Lorenz number.

Electron band-type insulators with non-zero Chern number are routinely produced in the laboratory by confining electrons to a 2D layer (e.g. in a semi-conductor heterostructure or in a purely 2D material like graphene), and applying a strong perpendicular magnetic field. Lattice versions with no external magnetic field are

much more rare, but an example was recently produced[12].

1.2.2 Fractionalization and Topological Order

The chiral band-insulators described in the previous section are stable without inter-electron interactions, and can be understood purely within the framework of non-interacting band-structure. Strong interactions can stabilize even more exotic states with no free-particle analogs. The most famous examples are fractional quantum Hall (FQH) liquids, which have quasi-particle excitations that carry a fraction of the charge of an electron, despite being fundamentally made up of the collective motion of discrete, indivisible electrons. These fractionally charged quasi-particles also have fractional exchange statistics interpolating between bosonic and fermionic.

FQH phases are an example of a more general class of phases with what is called topological order (TO). Phases with TO are gapped and have quasi-particle excitations with fractional self- or mutual-statistics. The existence of excitations with fractional statistics directly implies that a TO'd phase is sensitive to the topology of the manifold upon which it is placed. In particular, when placed on a closed manifold of genus g, a phase with TO has a d^g-fold degenerate ground-state, where d is a characeristic of the phase known as the quantum dimension.

1.2.3 Symmetry-Protected Topological Phases (SPT)

The distinction between weakly- and highly-entangled states is enriched if we add the further restriction that the sequence of Hamiltonians, H_λ, connecting H_0 and H_1 respect a set of symmetries, such as spin-rotation or time-reversal invariance. Whereas the ground states of H_0 and H_1 may be smoothly connectable in the absence of symmetry, it may no longer be possible to connect them by a sequence of Hamiltonians that all preserve the symmetries. This immediately implies that such phases cannot have intrinsic topological order, which is robust even in the absence of symmetry. Phases that are distinct from the ordinary band-insulator only when symmetry constraints are enforced are called "symmetry-protected topological phases" or SPTs. In this sense SPTs are marginal-cases, that should be regarded as weakly entangled in the absence of symmetry, and highly-entangled in the presence of symmetry constraints.

Especially interesting cases are SPT phases protected by a internal symmetries, like time-reversal or charge-conservation symmetry. Unlike spatial symmetries, like rotation or translational symmetry, which can be disrupted by defects and impurities, such internal symmetries are present even in disordered systems. Consequently, such SPT phases can be robust even in realistic, imperfect materials.

1.2.4 Gapless Phases without Quasi-Particles

So far, we have only considered gapped states, where the above-defined notion of adiabatic equivalence is cleanly defined. Gapless phases, on the other hand, necessarily have singular thermodynamic behavior, and are generically more difficult to

understand. Certain types of gapless phases can be easily incorporated into a broader classification. For example, phases with spontaneously broken continuous symmetries have gapless Goldstone modes, that are long-wave-length fluctuations of the local order parameter. However, these Goldstone fluctuations can be removed by applying a weak external field that explicitly breaks the symmetry in question and pins the order parameter, or by the formal device of gauging the corresponding global symmetry.

Metals (or more generally Fermi-liquids) provide a more complicated example, in which there is a finite density of gapless fermion excitations. However, due to visionary work by Lev Landau in the 1950's, these phases have long been understood. Landau argued that the presence of a Fermi-surface greatly restricts interaction effects at infinitesimally low energies. He showed that excitations near the Fermi-surface of a metal are in one-to-one correspondence to those of a free fermion gas, and that there is a well-defined sense in which the interacting Fermi-liquid is adiabatically connected to the free-Fermi gas, despite the presence of gapless excitations.

While relatively rare, there are known examples of gapless phases of matter that have no well-defined quasi-particles, and are clearly not connected to a free-particle gas. Such gapless phases without quasi-particles constitute the most highly-entangled and poorly understood class of matter. The earliest discovered example of such a system is the strange-metal phase of hole-doped high-temperature cuprate superconductors[13][2]. Here, the the scattering rate of electron excitations appears to scale linearly with their energy above the Fermi-surface, invalidating the central assumption of Landau's argument for having well-defined quasi-particles.

However, understanding the high-Tc cuprate superconductors has so far proved an insurmountable problem, and it has been highly desirable to find simpler alternative examples that might serve as a "warm-up" for the harder high-Tc problem. In the past decade, three new materials have emerged as promising candidates[14, 15, 16]. These are Mott insulating phases of electrons, in which some combination of geometric frustration and/or large quantum fluctuations due to proximity to a Mott transition prevent symmetry-breaking antiferromagnetic order. Instead, the electron spins form a quantum-disordered liquid phase, known as a quantum spin-liquid. Additionally, in all three cases, there appear to be large numbers of gapless excitations that can transport spin but not charge, providing the first clear examples of spin-charge separation in 2D systems. These quantum spin-liquid materials offer an important chance to refine the theoretical understanding of gapless non-Fermi liquids.

1.3 Plan of the Thesis

In the last decade or so, the list of distinct highly-entangled phases has been growing at an accelerated rate. Along the way it has become quite clear that such phases are not just pathological counter-examples, but rather constitute important classes

[2]It is not settled whether this strange-metal behavior could alternatively arise from being within the high-temperature quantum critical fan of some putative zero-temperature critical point that is covered by the superconducting dome. In that case, the strange metal would not be regarded as a stable quantum phase of matter.

of phases that must be incorporated into our broader understanding. Therefore, the most pressing outstanding tasks for theoretical (equilibrium) quantum condensed matter physics are to:

1. Develop a theoretical framework for understanding highly-entangled phases matter. Here it is important, not only to construct a taxonomy of phases, but also to elucidate their physical properties.

2. Identify experimentally realistic routes to construct new phases in the laboratory

3. Propose realistic experimental probes to test, verify, and refine theoretical understanding.

Items 2) and 3) are important both in order both to test speculative aspects of theory against experimental reality, and also to exploit potential technologically useful properties, such as unusual electromagnetic responses or enhanced capacity for quantum information storage and processing. In this thesis, I will develop these three themes of understanding, constructing, and probing for three classes of highly-entangled phases of matter: topological superconductors with non-Abelian excitations, interacting electron SPTs, and gapless quantum spin-liquids.

The first example considered will be superconducting analogs of IQH states: 2D chiral superconductors and related 1D topological superconducting wires. Here, all three elements are well developed. These systems have quasi-particle excitations with non-Abelian statistics, that can be used to store and process quantum information non-locally in a manner that is fundamentally immune from noise and decoherence. Despite these rather exotic properties, the experimental prospects for constructing such topological superconductors are quite hopeful. Understanding the main properties of these phases is largely straightforward, because they are well-described by treating superconductivity at the mean-field level, thereby reducing the problem to one of free-particle band-structures. Based on this understanding, realistic routes for building a topological superconductor from only conventional, well-understood materials have recently been identified[17, 18, 19]. Feasible experimental signatures of these non-Abelian particles have also been proposed[20, 21]. This progress has been sufficiently promising to prompt serious experimental effort[22, 23, 24, 25, 26]. In light its imminent experimental relevance, particular emphasis will be placed on discussing practical barriers for experimental implementation and strategies to overcome these barriers.

Next, I will turn to marginally-entangled SPT phases of electrons in 3D, focusing on the most realistic set of symmetries for electron systems: time-reversal (TR) and charge-conservation ($U(1)_C$). Non-interacting electrons with these symmetries can be understood from examining SPT aspects of free electron band-structures. Within the free-particle band-structure classification, there is a single non-trivial band-insulator, dubbed the topological band-insulator (TBI), that is not smoothly connected to the trivial atomic limit so long as TR and $U(1)_C$ symmetries are preserved. The 3D TBI has an insulating bulk, but non-trivial surface-states. The most familiar examples

of which are a gapless surface state with an odd-number of Dirac cones, or gapped magnetic or superconducting states that break either or both of TR and $U(1)_C$. The aim of this section is to incorporate interactions between electrons. The chief modification is that strong interactions enable 6 new types of strongly-correlated topological insulators (TIs) that cannot be understood from a free-electron band structure picture. In addition, interactions enable a third, previously undiscussed, surface state for the ordinary TBI, that is both gapped and symmetry preserving. Compared to the topological superconductors described above, the understanding of strongly-correlated TIs is much more a work in progress; only a classifiation and rudimentary understanding of the possible phases is currently available. The task of identifying realistic experimental routes to realizing these phases, and of developing experimental probes to explore them remains an entirely open question for future work.

The last chapter of this thesis will be devoted to the most highly-entangled and poorly understood phases of matter: strongly-correlated gapless phases without well-defined quasi-particles. After describing the best known candidate materials for gapless quantum spin-liquids, I will describe a proposal for constructing a new type of gapless spin-liquid in doped semiconductors. As we will see, the theoretical framework for describing gapless phases without quasi-particles is rather subtle, and it is hard to decide whether, and under what conditions theoretically possible phases will be realized in real materials. Therefore, it will be particularly important to identify experimental tests for theoretical proposals. To this end, I will also describe how optical conductivity can be used to refine our understanding of the nature of gapless quantum spin-liquids.

Part I

Topological Superconductors and Majorana Fermions

The first part of the thesis explores realistic routes to producing topological superconductors and superconducting wires exhibiting non-Abelian defects with Majorana zero-modes. The first chapter describes topological aspects of idealized topological superconductors made of spinless (or fully spin-polarized) electrons. Fermi-statistics dictates that spinless electrons can only pair in odd-angular momentum channels. The minimal such channel is p-wave pairing. We will see that fully gapped superconductors with p-wave pairing symmetry have topologically protected chiral neutral edge modes, analogous to Chern insulators. This property also implies the existence of fermionic zero-modes bound to superconducting vortices. These zero-modes endow the vortices with non-local properties that enable them to store and process quantum information in a topologically robust manner.

The study of these idealized superconductors serves as a warmup for more realistically achievable models described in subsequent chapters. In the second chapter, more experimentally realistic proposals are explored, and attention is paid to the role of practical issues such as multi-band effects and disorder.

In the final chapter of this part, tunneling-signatures of Majorana fermions in superconducting nano-wires are described. Here again, it will turn out that disorder can have important effects, producing "red-herring" tunneling signatures that mimic those of true Majorana fermions, but which do not have a topological origin.

The work in this Part of the thesis is adapted directly from a synthesis of Refs. [1, 2, 3, 4, 5, 6], with some added exposition.

Chapter 2

Topological Superconductors of Spinless Electrons

2.1 Chiral Superconductors and Majorana Fermions

Chiral band-insulators also have superconducting analogs, that are 2D fully gapped bulk-superconductors with topologically robust gapless chiral edge-states. In contrast to the band-insulator case, in a chiral superconductor the presence of a superfluid of Cooper pairs mixes electron and hole excitations. For zero-energy gapless states, this mixing is perfect, and such states become exactly equal superpositions of particle and hole, known as Majorana fermions. Therefore, chiral superconductors have *neutral* chiral Majorana edge-modes. Therefore a chiral superconductor with n chiral Majorana edge-modes has vanishing electrical Hall conductance, but quantized thermal Hall conductance:

$$\kappa_{xy} = \frac{\text{Ł}e^2}{h}\frac{n}{2} \tag{2.1}$$

Notice that the fundamental thermal conductance of a chiral Majorana edge-mode is *half* that of a charged fermion edge-mode in a Chern band. In chiral one-dimensional systems, the thermal conductance divided by $\frac{\text{Ł}e^2}{h}$ is known as the chiral central charge, c_c, which can be interpreted as counting the number of degrees of freedom of the underlying particle excitations in the system. In this sense, neutral Majorana fermions are effectively half an ordinary electron. An alternative way of stating that Majorana fermions have half-as many degrees of freedom is the following: denote the annihilation operator for a chiral Majorana edge-state with momentum k along the edge by γ_k. These states have energy $\varepsilon_k = vk$ where v is the edge-velocity. There is a corresponding operator with opposite momentum $-k$, γ_{-k}. Whereas for fermions these two would be distinct operators, for Majorana states they are related by

$$\gamma_k = \gamma_{-k}^\dagger \tag{2.2}$$

The situation is even more dramatic if there is a superconducting vortex piercing

the system. Ordinarily, for a chiral superconductor with edge circumference L_C, momenta of edge-excitations are quantized to values of $\frac{\pi(n+1/2)}{L_C}$ where n is an integer[1]. The presence of an $\frac{hc}{2e}$ vortex in the bulk 'twists' the edge modes so that the wave-vectors become $\frac{\pi n}{L_C}$, and there is a single boundary mode, γ_0, with precisely zero momentum. For this zero-mode Eq. 2.2 becomes:

$$\gamma_0 = \gamma_0^\dagger \tag{2.3}$$

If we had two such zero modes, γ_a and γ_b, they could be combined to create a single ordinary fermion level:

$$\psi = \frac{\gamma_a + i\gamma_b}{2} \qquad \psi^\dagger = \frac{\gamma_a - i\gamma_b}{2} \tag{2.4}$$

satisfying the usual anti-commutation relation: $\{\psi, \psi^\dagger\} = 1$. The operators ψ and $\psi^\dagger$ span a 2-state quantum system: $|0\rangle$ and $|1\rangle = \psi^\dagger|0\rangle$ defined by $\psi|0\rangle = 0$. This is two-state system is the smallest non-trivial Hilbert space possible, and it is not spanned by either γ_a or γ_b alone, but rather is 'shared' by both operators. In this sense, we can assign $\gamma_{a,b}$ quantum-dimension $d = \sqrt{2}$, since together the operators span a two-dimensional Hilbert space.

2.1.1 Single Chiral Edge Mode and Majorana Bound States

In the case of a superconductor with a single chiral Majorana edge mode ($c_c = \frac{1}{2}$), threaded by a vortex, the presence of a Majorana zero-mode γ_0 at the boundary implies that the boundary has a fractional number of electron degrees of freedom. Since the chiral superconductor is fundamentally made of electrons, and must have integer dimensional Hilbert space, there must be another un-paired Majorana zero-mode, γ_{v1}. Unsurprisingly, since the bulk superconducting vortex was responsible for the existence of γ_0 at the boundary, γ_v is localized to the vortex excitation.

2.1.2 Multiple Vortices and Non-Abelian Statistics

We have so far considered a single vortex. If we next consider adding a second vortex to the bulk of the superconductor, then the boundary wave-vectors will be further shifted back to $\frac{\pi(n+1/2)}{L_C}$, and there is no true zero-energy mode at the boundary. Since the vortices can be arbitrarily well separated from each other and from the boundary, γ_{v1} cannot be removed from the first vortex by the insertion of the second vortex. Therefore, the second vortex must also contain a Majorana zero-state, γ_{v2}, bound to its core, so that the total system has an integer number of degrees of freedom. From these considerations, we see that each vortex of a $c_c = \frac{1}{2}$, chiral superconductor carries a Majorana bound-state.

[1]For the usual particle on a ring the momenta are quantized to $\frac{\pi n}{L_C}$. The offset of $\frac{\pi}{2L_C}$ comes from the π Berry phase accumulated by an electron circumnavigating the sample boundary, due to the twisted phase of the superconducting pairing

Each pair of vortices then shares a two-level quantum system, indicating that N_v vortices share a $2^{N_v/2}$ dimensional Hilbert space. If the underlying vortices are well separated, then the quantum state, $|\Psi_{N_v}\rangle$, of this $2^{N_v/2}$ state system cannot be measured by local operations that only have access to a single vortex at a time. Since most sources of noise originate from such localized processes, a collection of such vortices can in principle store quantum information without decoherence. Even more surprisingly, exchanging two such vortices, v_i and v_j, implements a non-trivial unitary operation[28]: $|\Psi_{N_v}\rangle \rightarrow U_{ij}|\Psi_{N_v}\rangle$. Importantly, U_{ij} depends only on topological properties of the exchange process such as: which vortices are inter-changed, and whether the interchange happened in the clockwise or counterclockwise sense. Local excitations, such as vortices carrying zero-energy Majorana fermion bound states, with these properties are said to have non-Abelian exchange statistics.

This raises the intriguing possibility of not only storing quantum information in a collection of non-Abelian vortices, but also in performing robust error-free computational operations simply by exchanging vortices. Unfortunately, until recently there were very few experimental candidates for systems with non-Abelian excitations. The best studied candidate is the $\nu = 5/2$ fractional quantum Hall state, which is thought to be a chiral superconductor of composite fermions: collective electron excitations that can be thought of as electrons each attached to two magnetic flux quanta. However, the $\nu = 5/2$ is difficult to produce, and despite decades of extensive experimental and theoretical scrutiny, the state is rather poorly understood. A more fundamental problem, is that vortex-like objects are difficult to control and manipulate.

2.2 Topological Superconducting Wires

However it was recently realized that Majorana bound-states also occur in 1D superconducting wires. Namely, imagine rolling a chiral superconductor with $c_c = \frac{1}{2}$ into a long tightly-wrapped cylinder of radius R and length $L \gg R$. This cylinder has two circular edges of length $2\pi R$. It turns out that the act of rolling up the 2D planar system into a cylinder shifts the momentum quantization of the edge modes to $k_n = \frac{\pi n}{2\pi R}$, with energies: $\varepsilon_n = \frac{vn}{2\pi R}$. If the radius, R, is sufficiently small, then only the $n = 0$ zero mode remains, and the wire formed from rolling up the chiral superconductor has two Majorana zero-modes, one bound to each end of the wire.

While this device of rolling up a 2D chiral superconductor to produce a wire is conceptually useful, it is not a practical experimental recipe. Fortunately, a more realistic route was recently identified theoretically: using a spin-orbit coupled wire, in close proximity to an ordinary superconductor, it turns out that one can artificially engineer superconducting wires with Majorana end-states[17, 18, 19]. While it is not directly obvious that any residue of the non-Abelian statistics of vortices in the 2D chiral superconductor survive in the 1D realization, it turns out that Majorana bound-states can be moved around networks of topological superconducting wires, and that exchanging Majorana bound-states in such networks implements precisely the same operations U_{ij} as in the fully 2D system[47]. Moreover, the process of moving Majorana bound-states around wire-networks can be accomplished simply by

constructing a series of gates that can locally deplete sections of the wire to drive them into conventional superconducting phases. For these reasons, artificially engineered 1D topological superconducting wires offer a much more promising route to realizing and manipulating non-Abelian Majorana excitations than naturally existing intrinsic 2D chiral superconductors, which are fragile and hard-to-control.

2.2.1 Kitaev's Wire

The occurance of Majorana end-states in p-wave superconducting wires can be easily understood with from a simple model of spinless, superconducting electrons in a 1D wire:

$$H_{\text{Kitaev}} = \sum_i \left[-t c_i^\dagger c_{i+1} + \Delta c_i c_{i+1} + \text{h.c.} \right] - \sum_i \mu c_i^\dagger c_i \tag{2.5}$$

by using the following trick due to Kitaev[20]. The electron operator c can be decomposed into two Majorana operators[2] $\gamma_{a,b}$ as follows:

$$c_j = \frac{\gamma_{a,j} + i\gamma_{b,j}}{2} \qquad c_j^\dagger = \frac{\gamma_{a,j} - i\gamma_{b,j}}{2} \tag{2.6}$$

Here $\gamma_{a,b}^2 = 1$, and γ's on different sites anti-commute.

This can be depicted graphically (see Fig. 2-1), but drawing each complex electron operator on a site, c_j, as a large oval, encompassing the corresponding Majorana operators, shown as smaller circles. There are two special points at which the system decomposes into a set of paired Majoranas:

1. Trivial Point ($t = \Delta = 0$, and $\mu \neq 0$): Here, the system breaks into decoupoled sites, and the Majorana operators $\gamma_{a,i}$ and $\gamma_{b,i}$ are coupled to each other, but not to other Majorana operators on different sites (See top panel of Fig. 2-1)

2. Topological Point: ($t = \Delta$, $\mu = 0$): Here, the system again breaks into pairs of Majoranas, however the pairs are no longer on the same site. Rather $\gamma_{a,i}$ is coupled to $\gamma_{b,i+1}$ but not to $\gamma_{a,i}$. These couplings are indicated in Fig. 2-1 as lines. For an infinite wire, the couplings shown in the top and bottom panels of Fig. 2-1 would be identical up to a shift of the coupling lines. However, for a finite N-site system at the topological point, there are two unpaired Majorana operators: $\gamma_{a,0}$ and $\gamma_{b,N}$ dangling at the ends of the wires. (See bottom panel of Fig. 2-1)

Since the system is fully gapped at both of these two special points, perturbing the system slightly will not change the topological property of whether or not unpaired Majorana modes occur at the ends. In fact, so long as the chemical potential resides in the hopping bands of the electrons ($2|t| < |\mu|$), and the superconducting pairing does not vanish ($\Delta \neq 0$), the system will exhibit Majorana end-states. However,

[2]This re-writing of a complex fermion system as a system of twice the number of real Majorana fermion fields is always possible, but is especially useful in what follows.

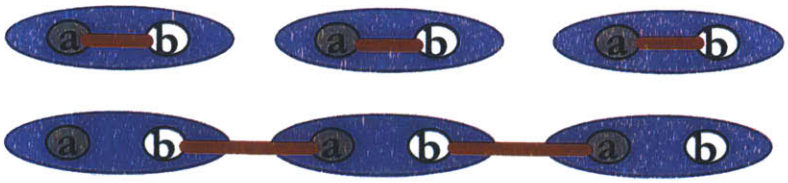

Figure 2-1: Schematic illustration of the two simple limiting cases for Kitaev's Majorana wire. Blue ovals indicate physical sites in the 1D chain. Electron operators on each site are decomposed into Majorana operators $\gamma_{a,b}$ indicated by the circles labeled a and b. Non-zero bilinear couplings in the Hamltonian are indicated by red-lines. The top panel shows the trivial limit point, where Majorana states are paired on the same site. The bottom panel shows the topological limit-point where Majorana's are paired between adjacent sites, leaving an unpaired Majorana at each end.

away from the special point, $t = \Delta$, these Majorana end-states will no longer be confined to precisely one site, but rather will be exponentially localized to the wire ends, with characteristic confinement length: $\xi_0 \approx t/\Delta$. The wave-function of the Majorana state also oscillates rapidly on the scale of the Fermi-wavelength, which for the physically relevant regime: $|t| \gg |\Delta|$, is much shorter than ξ_0.

2.3 Multiband Wires and the 2D to 1D Crossover

In the previous section, we saw that a strictly 1D wire with nearest neighbor (p-wave) pairing, had a topological regime with Majorana end-states. As topologically robust pheneomena, one expects that these end-states should survive away from the strict 1D limit, but what precisely happens to these end-states as we fatten the 1D wire? Also, how are these Majorana end-states of the 1D wire related to the chiral edge states of the 2D superconductor? These questions are of practical importance, since it is quite difficult to fabricate a purely 1D wire. Fortunately it turns out that robust Majorana end-states can occur for a substantial range of widths.

These questions can be answered either by starting with a 2D chiral superconductor and continuously shrinking one of its dimensions down to produce a 1D wire, or by making increasingly fat wires by stacking more and more 1D topological superconducting wires next to each other. These approaches provide useful complimentary perspectives, and will both be considered in turn.

2.3.1 2D to 1D Crossover

First consider starting with rectangular $p_x + ip_y$ superconductor of length $L \gg \xi_0$, and width W, and then decreasing the width W to produce an increasingly 1D system. For sufficiently large W, the system is fully two-dimensional and the low lying ($\varepsilon < \Delta$) states are chiral edge modes with a gap set by the finite circumference of the sample. This gap is required by the fact that a single zero-energy Majorana state cannot exist

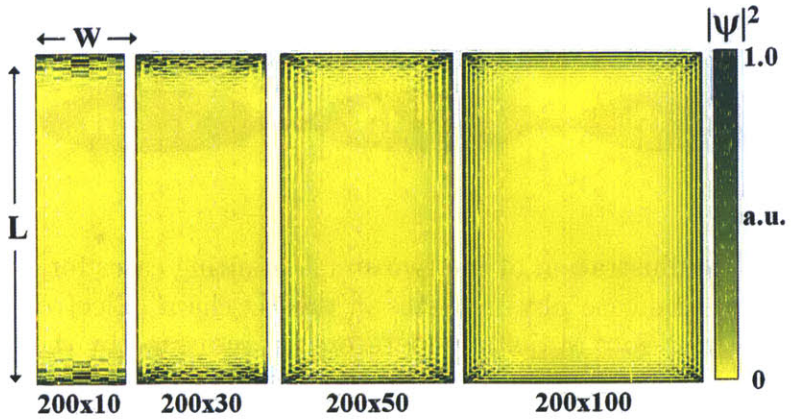

Figure 2-2: (Color online) $|\Psi|^2$ for zero-mode wave-functions at fixed coherence length: $\xi_0 \sim t/\Delta = 10$, chemical potential $\mu = -2t$, fixed sample length: $L = 200$, and various sample widths: $W = 10$, 30, 50 and 100 (from left to right). These widths span the range from $W < \xi_0$, $W \sim \xi_0$, to $W \gg \xi_0$, and depict the crossover from the 1D regime with Majorana zero-modes localized at each end, to the 2D limit with chiral edge mode.

in isolation, but can only occur in pairs. The question is: how are these chiral edge states connected with the zero energy Majorana end states as the width decreases?

To probe this crossover from 2D to 1D, we consider a square-lattice tight-binding model, $H = H_t + H_{\text{p-BCS}}$, of a single species of electrons with $p_x + ip_y$ BCS pairing:

$$\begin{aligned} H_t &= \sum_{\langle ij \rangle} -t \left(c_i^\dagger c_j + \text{h.c.} \right) - \sum_j \mu c_j^\dagger c_j \\ H_{\text{p-BCS}} &= \sum_j \Delta \left(-i c_{j+\hat{x}}^\dagger c_j^\dagger + c_{j+\hat{y}}^\dagger c_j^\dagger \right) + \text{h.c} \end{aligned} \tag{2.7}$$

where $c_j^\dagger$ creates an electron on site j, t is the hopping amplitude, μ is the chemical potential, Δ is the p-wave pairing amplitude, and we work in units where the lattice spacing is unity.

Fig. 2-2 shows the lowest energy state wave-function, obtained by numerically diagonalizing Eq.(2.7), for a sequence of samples with increasing widths. For $W < \xi_0$, there are two well isolated Majorana end states localized at opposite ends. As W is increased to $\gtrsim \xi_0$, these Majorana end states begin to spread along the edges of the sample with extent $\sim e^{W/\xi_0}$. For fixed L, these wave-functions eventually circumnavigate the sample to match up with the 2D edge mode picture for $W \gg \xi_0$. The results of these simulations can be understood as follows: in the 2D limit, the edge modes are localized near the sample boundary and decay into the bulk with characteristic length ξ_0. As W is decreased and approaches ξ_0, the tails of the edge mode wave-functions on opposite edges overlap and mix. The mixing of these two counter-propagating edge modes forms a gap of order e^{-W/ξ_0} along the mid-section of the sample, and squeezes the lowest energy state towards opposite ends of the

sample. For sufficiently long samples ($L \gg e^{W/\xi_0}$) one finds spatially isolated zero-energy Majorana end states residing in opposite ends.

As in shown Fig. 2-3d, the Majorana end modes are protected from low-energy excitations by a spectral gap that scales as $\sim \Delta e^{-W/\xi_0}$. Therefore, while a sample of any W can in principle support Majorana end-states for sufficiently large $L \gg e^{W/\xi_0}$, in practice we have the restriction $W \lesssim \xi_0$ to avoid an exponentially small excitation gap. For $W < \xi_0$ and $L \gg \xi_0$, this gap is a sizeable fraction of the bulk superconducting gap, Δ, and is largely insensitive to both L and W.

Actually, this is not the whole story: in addition to decaying away from the edge, the wave-functions of the conter-propagating edge modes of the 2D chiral superconductor also oscillate rapidly with characteristic lengthscale $1/k_F$. As the wire is shrunk to $W < \xi_0$ the counter-propagating modes on opposite edges begin to overlap, but, due ot the oscillatory structure the splitting resulting from this overlap is modulated by a factor like $\sin k_F W$. There are numerous values of W for which this modulating factor vanishes, decoupling the chiral end-states and leading to a gapless wire. It turns out that the Majorana end-states disappear upon one gap-closing and re-appear on the next in an alternating fashion, and are apparently only associated with a fixed sign of the overlap between the counter-propagating chiral modes. To see exactly what is going on here, it is much simpler to start from the opposite limit, and build up a quasi-1D wire by stacking purely 1D wires next to each other.

2.3.2 1D to 2D

Let us now consider the opposite procedure: building towards a 2D by fattening a purely 1D system. As a warm-up, consider stacking two copies of a purely 1D p-wave superconductor described by Eq. 2.5, and introducing tunneling $t_\perp$ of electrons between them. We can decompose the two-wire system into orthogonal sub-bands (in this case, even and odd superpositions of electrons on one and the other wire). The system then decomposes into two decoupled Kitaev wire: one for each sub-band, each of which will exhibit a Majorana end-state if occupied. However, when both sub-bands exchibit Majorana end-states, there are two low-energy Majorana states sharing the same spatial region. In general, these Majorana modes can be coupled and gapped out and this situation is not stable to perturbations. In particular, if we turn on an ip_y component, Δ_y to the superconducting pairing (i.e. intra-wire pairing with relative phase i to the inter-wire pairing), then the two Majorana zero-modes will be coupled and split from zero-energy.

Next consider stacking three 1D wires. Now there will be three sub-bands. If only one is occupied, there will be Maojorana end-states. If any two are occupied, then the Majorana end-states are not stable and will generically be removed. However, if all three are occupied, then there will again be a single unpaired Majorana state at each end which is now a hybridization of the Majorana end-states from all three channels.

More generally, in a system with multiple sub-bands, each sub-band contributes a Majorana mode at each end of the sample. An even number of Majorana fermions localized at a given end will mix and pair into full electron states at non-zero energy.

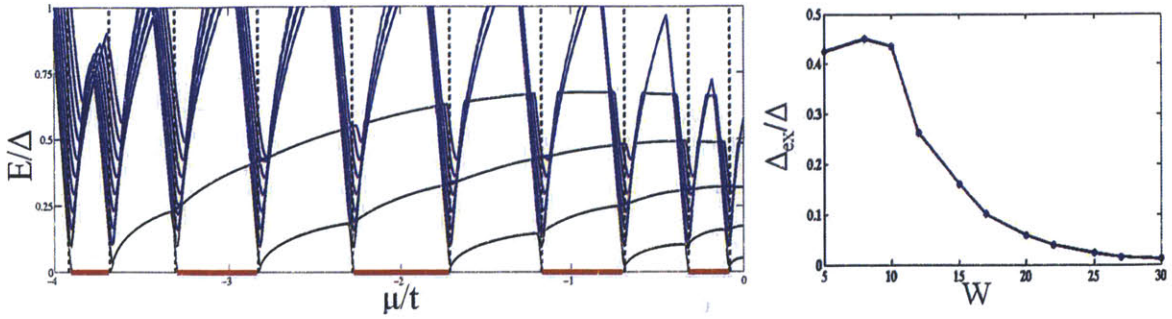

Figure 2-3: The left panel shows the excitation spectrum as a function of chemical potential, μ, for 100×10 site lattice strip of $p_x + ip_y$ superconductor with $t/\Delta = 10 \sim \xi_0$. Blue lines are bulk excitations. Dashed lines denote the transverse confinement band-bottoms, which coincide with topological phase transitions between phases with Majorana zero-modes (shown in red), to topologically trivial gapped phases. The right panel shows the exponential sensitivity of the excitation gap Δ_{ex} to W for clean samples with $L = 1000$, $t/\Delta = 5 \sim \xi_0$ and μ near $-2t$ (fine tuned to support a zero-mode).

For an odd number, however, there is always one remaining unpaired Majorana mode per end. Thus, as a function of chemical potential μ the system undergoes a series of topological phase transitions between topological states with spatially isolated Majorana zero-modes to topologically trivial gapped states with no Majorana modes.

To confirm this picture, we conducted simulations of quasi-1D multi-band wires with $p_x + ip_y$ pairing, and adjusted the number of occupied sub-bands by changing chemical potential μ. The top panel of Fig.2-3 shows the low lying excitation energies as a function of μ for an $L = 100$, $W = 10$ lattice with $t/\Delta = 10 \sim \xi_0$. The higher energy states shown in blue reside in the bulk and form two branches: excitations across the pairing gap and excitations to the next higher sub-band which respectively increase/decrease in energy with μ. Due to the p-wave pairing symmetry, the pairing gap vanishes when μ coincides with a sub-band bottom (dashed lines). Similar results were also found in Ref. [110].

We now focus on low energy states lying within the bulk gap. Starting from the lowest transverse sub-band and increasing μ, one finds an alternating sequence of transitions between states with a non-degenerate zero-mode (shown in red) and doubly degenerate gapped states as described above. The transition points coincide with μ passing through the bottom of a transverse sub-band, and are accompanied by a closing of the bulk gap (as is required for any topological phase transition).

We have verified the Majorana-nature of the end-states in this picture by checking that the non-degenerate (red) states have energy that is exponentially small in L, and that their wavefunctions can be written as $\psi = a + ib$, where a and b are real fermions localized in opposite ends. On the other hand, the gapped states are doubly degenerate due to spatial parity symmetry $(x, y) \to -(x, y)$ and are complex fermions localized in the sample ends.

Chapter 3

Engineering a Topological Superconductor

In the previous chapter, we saw that gapped superconductors with p-wave pairing symmetry have defects (vortices in 2D or wire-ends in 1D) that carry Majorana bound-states, which endow these defects with interesting non-Abelian properties. Unfortunately, such superconductors are hard to come by in nature. In fact, only a few naturally occuring two-dimensional candidates exist: 1) ^{3}He A is known to be a $p+ip$ superfluid, 2) Sr_2RuO_4 is thought to have p-wave pairing, and 3) the Moore-Read FQH state, thought to underly the oberved $\nu = 5/2$ plateau, is effectively a $p+ip$ superconductor of composite-fermions. However, all of these naturally occuring candidates are hard to produce and very difficult to work with. In particular, it would be extremely challenging to probe non-Abelian statistics in these materials by precisely manipulating vortices.

Fortunately, while nature has not provided a convenient naturally occuring topological superconductor, it has been kind enough to provide the materials to build an one. In this chapter, we review recently proposed routes for constructing chiral 2D topological superconductors and 1D topological superconducting wires by combining simple and well-understood materials. The key idea is to produce effectively spin-less electrons by locking spin to momentum via an appropriate combination of spin-orbit coupling and magnetic fields. Once this is accomplished, superconductivity can be induced by proximity to a conventional s-wave superconductor. Since the electrons are now effectively spin-less the induced s-wave pairing takes on an effective p-wave character, producing the desired topological characteristics.

3.1 Engineering a Topological Superconductor

3.1.1 Step 1: Stripping Electrons of their Spin

The first step in constructing a topological superconductor is to remove the electron spin as a dynamical degree of freedom. The conceptually simplest way to accomplish this would be to impose a large magnetic field to fully polarize the electron spins.

However, such a large magnetic field would be detrimental to ordinary s-wave superconductivity, and such a scheme would require an intrinsic tendency towards p-wave pairing; this is exactly what we are trying to avoid!

Luckily, there are alternative ways to producing effectively spin-less electrons without strongly suppressing suppressing superconducting pairing. In particular, spin-orbit coupling (SOC) tends to lock the electron spin perpendicular to its propagation direction. Spin-orbit coupling arises from relativistic effects in which a static electric field in the laboratory frame develops a magnetic component in the co-moving frame of a rapidly moving electron:

$$\mathbf{B}_{\text{moving}} = \frac{\mathbf{v}}{c} \times \mathbf{E}_{\text{lab}} \tag{3.1}$$

This magnetic component couples to the electron-spin, $\mathbf{S}$, through the usual Zeeman effect:

$$H_{\text{so}} = -\frac{\mu_0}{mc}\mathbf{S} \cdot (\mathbf{p} \times \mathbf{E}_{\text{lab}}) \tag{3.2}$$

where $\mu_0 = \frac{g}{2}\mu_B$. Uniform SOC requires a static uniform component of the electric field $\mathbf{E}$, which breaks inversion symmetry. Consequently, any system with uniform inversion symmetry breaking will have some component of uniform SOC. The magnitude of SOC from inversion symmetry breaking is strongest in materials with large nuclei, which create strong atomic scale electric fields.

Consider a 2D planar material, that lacks inversion about the perpendicular direction $\hat{z}$. This inversion symmetry breaking produces a uniform component of SOC of the form:

$$H_{\text{Rashba}} = \alpha_R \hat{z} \cdot (\mathbf{S} \times \mathbf{p}) \tag{3.3}$$

SOC of this type is known as Rashba SOC (RSOC). The formerly doubly degenerate quadratic band is split by the RSOC into two shifted quadratic bands, in which spin and momentum are locked perpendicular to each-other.

We can also view the Rashba band-structure as a large outer Fermi-surface in which spin is locked perpendicular to momenta in the right-hand sense, and a smaller inner Fermi-surface in with the opposite helicity. The presence of both helicities indicates that, even though spin is mixed with momentum, there is still a degenerate dynamical degree of freedom which survives. This is because RSOC preserves time-reversal symmetry, each state is still doubly degenerate with a time-reversed partner of opposite spin.

To avoid this situation, we can introduce a magnetic field:

$$H_B = -\mu_0 \mathbf{B} \cdot \mathbf{S} \tag{3.4}$$

to break time-reversal symmetry[1] This Zeeman field opens a gap in the vicinity of

[1]For simplicity we ignore orbital effects of this field. Later we will focus on 1D wires which are more convenient for producing, detecting and manipulating Majorana states. For 1D wires, it will

where the inner Fermi-surface collapses to a point.

The not-yet superconducting system with RSOC and B-field can be modeled by the Hamiltonian:

$$H_0 = \sum_{\mathbf{r}} c^\dagger_{\mathbf{r},\alpha} \left(\frac{-\nabla^2}{2m} - \mu - i\alpha_R \hat{z} \cdot (\boldsymbol{\sigma} \times \nabla) - \mu_0 \mathbf{B} \cdot \boldsymbol{\sigma} \right)_{\alpha\beta} c_{\mathbf{r},\beta}$$

Here α_R is the Rashba velocity, related to the spin orbit coupling energy scale by $E_{\text{so}} = \frac{1}{2} m \alpha_R^2$, $\mu_= \frac{g\mu_B}{2}$ is the Zeeman coupling to the magnetic field $\mathbf{B}$ taken throughout to point along the wire (in the $\hat{x}$ direction), and Δ_0 is the proximity–induced pairing amplitude. The Rashba coupling α_R creates two helical bands with energies $\varepsilon^{(R)}_\pm = \xi_k \pm \alpha_R |k|$ with corresponding eigen-operators: $c_\pm$. The Zeeman term, $\mu_0 B$, cants the helical bands by angle $\theta_M(k)$ out of the xy-plane modifying the surface eigenstates and corresponding dispersions:

$$\begin{aligned} \varepsilon^{(\text{R/B})}_\pm &= \xi_k \pm \sqrt{\mu_0 B^2 + E^2_{\text{so}} \tfrac{k^2}{2m}} \\ c^{(\text{R/B})}_\pm &= e^{-i\phi_k \sigma_z/2} e^{-i\theta_M \sigma_x/2} \left(\frac{c_{k,\uparrow} \pm c_{k,\downarrow}}{\sqrt{2}} \right) \\ \theta_M(k) &= \tan^{-1}\left(\mu_0 B / \sqrt{(\mu_0 B)^2 + E^2_{\text{so}} \tfrac{k^2}{2m}} \right) \end{aligned} \tag{3.5}$$

If the chemical potential is then tuned into this gap, then only excitations of the outer Fermi-surface remain at low-energies. We see that a combination of Rashba and Zeeman fields have enabled us to isolate a branch of electrons with fixed helicity, for which there is no residual degenerate spin- or spin-like degree of freedom.

3.1.2 Step 2: Inducing Superconductivity by Proximity

To describe superconducting pairing, it is useful to enlarge our basis of electron operators by introducing the Nambu spinors:

$$\Psi_k = \begin{pmatrix} \psi_k \\ \mathcal{T}\psi_k \end{pmatrix} = \begin{pmatrix} \psi_k \\ -i\sigma_y \mathcal{K} \psi_k \end{pmatrix} = \begin{pmatrix} \begin{pmatrix} c_{k,\uparrow} \\ c_{k,\downarrow} \end{pmatrix} \\ \begin{pmatrix} c^\dagger_{-k,\downarrow} \\ -c^\dagger_{-k,\uparrow} \end{pmatrix} \end{pmatrix} \tag{3.6}$$

which is convenient for discussing superconductivity. Here we take the usual representation $\mathcal{T} = -i\sigma_y \mathcal{K}$ of the time-reversal operator, where $\{\sigma_{x,y,z}\}$ are Pauli matrices in the spin basis, and $\mathcal{K}$ denotes complex conjugation.

Next, consider placing the Rashba coupled system in close proximity to a conventional s-wave superconductor, so that electrons can tunnel between the two materials.

turn out to be advantageous to apply the magnetic field along the wire, and so long as the flux through the cross-section of the wire is negligible, orbital effects can be safely ignored.

Virtual tunneling of electrons from the RSOC surface into the gapped superconductor induces a pairing term in the wire of the form:

$$H_\Delta = \Delta \sum_k c^\dagger_{k,\uparrow} c^\dagger_{-k,\downarrow} + h.c. = \sum_k \Delta \psi^\dagger_k (\mathcal{T}\psi_k)^\dagger + h.c. = \sum_k \Psi^\dagger_k \Delta \tau_1 \Psi_k \tag{3.7}$$

Here $\{\tau_{1,2,3}\}$ are Pauli matrices in the particle-hole basis. [2]

Re-expressing H_Δ in the eigenbasis of both Rashba and Zeeman couplings, one finds that, in addition to $p \pm ip$ pairing $\Delta_{\rm p}(k)\hat{\mathbf{k}}^\pm \sim \langle c_{k,\pm} c_{-k,\pm}\rangle$ between fermions both in band $\varepsilon_\pm$, the canting θ_M introduces an s-wave pairing component $\Delta_{\rm s}(k) \sim \langle c_{k,+} c_{-k,-}\rangle$ between fermions c_+ and c_- in bands ε_+ and ε_- respectively where:

$$\begin{pmatrix} \Delta_{\rm s}(\mathbf{k}) \\ \Delta_{\rm p}(k) \end{pmatrix} = \frac{1}{2\sqrt{\mu_0 B^2 + E^2_{\rm so}\frac{k^2}{2m}}} \begin{pmatrix} \mu_0 B \\ -\sqrt{E^2_{\rm so}\frac{k^2}{2m}} \end{pmatrix} \Delta \tag{3.8}$$

and $\hat{\mathbf{k}}^\pm = (k_y \pm i k_x)/k$. When the Zeeman-gap $\mu_0 B$ strongly exceeds the superconducting pairing amplitude Δ, we expect to have an effective p-wave superconductor with pairing essentially only between electrons on the outer Fermi-surface with the same helicity. Indeed, it turns out [45] that one has a topological superconductor with potential Majorana bound states so long as $\mu_0 B > \Delta$, and so long as μ lies within the Zeeman gap ($|\mu| < \mu_0 B$). It is most advantageous to set $\mu = 0$, placing the chemical potential in the middle of the Zeeman gap (which can be done either by electrostatic gating or chemical doping), and we will take $\mu = 0$ throughout the remainder of this paper.

In this system, there are two excitation gap energy-scales: the first is the pairing gap at the Fermi surface ($k = k_F$) given by:

$$\Delta_{FS} = 2\Delta_p = \sqrt{\frac{E_{\rm so}}{\Delta_{BG}}}\Delta \tag{3.9}$$

$$\Delta_{BG} = \frac{\varepsilon^{(\rm R/FM)}_+ - \varepsilon^{(\rm R/FM)}_-}{2} = \sqrt{\mu_0 B^2 + E_{\rm so}\frac{k_F^2}{2m}} \tag{3.10}$$

The second is the Zeeman gap at $k = 0$, given (for $\mu = 0$) by $|\mu_0 B - \Delta|$. The smaller of these two energy scales sets the bulk gap to single-particle excitations which would destroy the non-local information stored among Majorana bound-states. We note that the relative strength of the Rashba spin-orbit coupling $E_{\rm so}$ and the Zeeman splitting $\mu_0 B$ determines the size of the pairing gap at k_F. For $\mu_0 B \gg E_{\rm so}$, the pairing gap

[2] Here we have chosen a gauge in which the pairing order parameter Δ is purely real (this is justified, as we are not presently concerned with situations where the superconducting phase is inhomogenous or fluctuating).

Virtual tunneling between the RSOC layer and the SC also renormalizes the RSOC and Zeeman terms of the surface layer by a factor of $Z_{\rm T}$ which measures the fractional weight of the electron wave-function in the RSOC layer. Below, we will present a more detailed model of the proximity effect, but for now we will implicitly assume that such renormalizations are built into the parameters α_R and B.

is only a small fraction of originally induced Δ. If the Zeeman gap closes (i.e. if $\mu_0 B \leq \Delta$), then both helicities are present and the system is topologically trivial.

3.1.3 Proximity Induced Superconductivity

In previous sections, we have assumed that proximity to a nearby superconductor simply introduces a pairing term into the RSOC material. In addition, the couplng to the superconductor renormalizes the effective Hamltonian of the wire. In this section, we examine the effects of proximity closer using a simple model for the tunneling coupling to the bulk superconductor.

We examine the the interface between a bulk s-wave superconductor a 2D electron gas with RSOC with induced magnetization $\mu_0 B$. For short, we will call the RSOC 2D electron layer the "surface", in anticipation of the fact that it will be realized near the surface of a semiconductor heterostructurc, or at the surface of a metallic film. As a simple model of this interface, we consider a bulk superconductor described by the BCS Hamiltonian:

$$H_B = \sum_{k,\sigma} \left[\varepsilon_{B,k} b^\dagger_{k,\sigma} b_{k,\sigma} + \left(\Delta_0 b^\dagger_{k,\uparrow} b^\dagger_{-k,\downarrow} + h.c. \right) \right] \tag{3.11}$$

coupled to the surface through a clean planar interface described by the bulk–surface tunneling term:

$$H_{\text{B-S}} = \sum_{\mathbf{k}_\parallel, k_\perp, \sigma} \Gamma b^\dagger_{(\mathbf{k}_\parallel, k_\perp), \sigma} c_{\mathbf{k}_\parallel, \sigma} + h.c. \tag{3.12}$$

which conserves momentum $\mathbf{k}_\parallel$ parallel to the interface, and is independent of the transverse momentum $k_\perp$ perpendicular to the interface. Here $b^\dagger_{k,\sigma}$ and $c^\dagger_{k,\sigma}$ are the electron creation operators (with momentum k and spin σ) for the bulk superconductor and surface respectively, ε_B is the non-superconducting bulk dispersion which we will linearize about the chemical potential μ, and Δ_0 is the bulk s-wave pairing amplitude.

Since surface–bulk tunneling conserves in-plane momentum, the bulk tunneling dcnsity of statcs (in thc absence of superconductivity) is given by thc one-dimensional expression $N_B(\varepsilon_B(k)) = (\partial \varepsilon_B(k)/\partial k_z)^{-1}$. Assuming that N_B varies slowly with energy, $H_{\text{B-S}}$ induces the following self-energy correction to the surface Green's function:

$$\Sigma_\Gamma(i\omega) = \frac{\pi\gamma}{\sqrt{\Delta_0^2 + \omega^2}} (-i\omega + \Delta_0 \tau_1) \tag{3.13}$$

where $\gamma = N_B(0)|\Gamma|^2$ is convenient measure of the strength of surface-bulk coupling corresponding to the width of the surface resonance that would result from $H_{\text{B-S}}$ without bulk-superconductivity ($\Delta_0 = 0$).

Incorporating Σ_Γ into the surface Green's function gives:

$$\mathcal{G}_S(i\omega) = \frac{Z_\Gamma}{i\omega - Z_\Gamma \mathcal{H}_{\text{RS}} - (1 - Z_\Gamma)\Delta_0 \tau_1} \tag{3.14}$$

where $\mathcal{H}_{\mathrm{RS}}$ is the Hamltonian density of the Rashba-coupled surface, and Z_Γ is the reduced in quasi-particle weight due to the bulk–surface hybridization:

$$Z_\Gamma(i\omega) = \left(1 + \frac{\pi\gamma}{\sqrt{\Delta_0^2 + \omega^2}}\right)^{-1} \tag{3.15}$$

The quasi-particle weight can be interpreted as the fraction of time that a propagating electron resides in the surface, as opposed to the bulk. The surface-bulk tunneling induces a pairing term $\tilde{\Delta}\tau_1$ in the surface where:

$$\tilde{\Delta} = (1 - Z_\Gamma)\Delta_0 \tag{3.16}$$

For strong surface-bulk coupling ($\gamma \gg \Delta_0$ or equivalently $Z_\Gamma \ll 1$) a sizeable fraction of the bulk pairing is induced on the surface.

However, this is not the only effect of the interface. From Eq. 3.14 we see that the surface-bulk coupling renormalizes the surface Hamiltonian, effectively rescaling the coefficients by a factor of Z_Γ:

$$\mathcal{H}_{\mathrm{RS}} \to \tilde{\mathcal{H}}_{\mathrm{RS}} = Z_\Gamma \mathcal{H}_{\mathrm{RS}} \tag{3.17}$$

3.1.4 Surface Resonances

So far, we have been implicitly considering an artificial interface between a 2D material (either a TI surface or Rashba 2DEG) and a different superconducting material. A potentially simpler alternative for realizing $p + ip$ superconductivity, is to use the naturally occuring interface between a bulk-superconductor and its surface. This approach would eliminate the need to find compatible materials to engineer an appropriately transparent interface.

The formalism developed above applies equally well in this case. Namely, if electronic states on the surface of a bulk metal occur at the same energy and momentum as bulk states, then the surface states decay into the bulk leaving behind broadened resonances. If the bulk becomes a superconductor, the surface-bulk coupling induces superconductivity on the surface. Denoting the width of the surface-resonance (in the absence of bulk-superconductivity) by γ, the induced superconductivity is again described by Eqs. 3.14 and 3.15. It is also possible that surface states coexist at the same energy as bulk bands, but reside in regions of the Brillouin zone for which there are no bulk-states. In this case there is no direct tunneling from the surface into the bulk, and the surface state would remain sharp state rather than broadening into a resonance. Consequently to obtain superconductivity on the surface, one would need to rely on some scattering process (e.g. phonon, electron-electron, or disorder scattering) to transfer electrons between surface and bulk states.

For natural superconducting metals with strong spin-orbit coupling (such as Pb), the electrostatic potential created by the material's surface interupts the bulk inversion symmetry, giving rise to a surface Rashba coupling. If the surface Hamiltonian has appropriate combinations of Rashba spin-orbit coupling and magnetization (as

described above), then the induced surface superconductivity will again have effective $p + ip$ pairing symmetry.

A related approach is possible for topological insulator materials, where it has been demonstrated[41] that doping can produce superconductivity with transition temperatures $T_C \sim 0.15 - 5.5K$. Furthermore, it is common[42] that samples of materials such as Bi_2Se_3 that are expected to be bulk-insulators, are actually metallic. In these "topological metals", the topologically protected surface states that would appear for a bulk insulator appear instead as resonances[42]. In fact a large amount of experimental effort is currently focused on finding materials with genuinely insulating bulks in order to investigate surface electron transport. However, for the purpose of engineering a $p + ip$ superconductor, this surface-bulk coexistence is actually advantageous, and the combination of bulk superconductivity and surface-bulk coupling will result in an effective $p + ip$ superconductor at the surface of a superconducting topological metal.

To examine whether $p + ip$ superconductors built from surface resonances also exhibit Majorana bound states, for example in vortex cores or at the ends of one-dimensional magnetic domains, one can write down the T–matrix for scattering from a vortex or domain wall and look for poles at zero-energy. For a static vortex or domain wall configuration, the T–matrix at zero-energy is constructed from various products of surface Green's functions (see Eq.3.14) also at zero-energy. Since $\Sigma_\Gamma(\omega = 0) = Z(\omega = 0)\Delta_0\tau_1$, the surface Green's function is identical to that of an ideal $p+ip$ superconductor with gap $\Delta = Z\Delta_0$. *Therefore surface-resonance $p+ip$ superconductors will exhibit zero-energy Majorana bound-states under exactly the same conditions as the effective $p+ip$ superconductor discussed previously.* These Majorana states are localized to the surface layer and are protected against decaying into bulk states because of the bulk superconducting gap.

3.2 Multi-band Spin-Orbit Coupled Superconducting Wires

So far, we have described how to produce a 2D chiral superconductor from a RSOC layer, proximity coupled to a conventional s-wave SC. In the previous chapter, we argued that one-dimensional wires or wire-networks provided a much more convenient platform for producing, detecting, and manipulating Majorana fermions. Clearly, starting from the above-described 2D construction, one could straightforwardly produce 1D wires by introducing spatial confinement.

Since the proposals based on RSOC have many relevant energy scales (E_{so}, B, Δ, etc...), there are options for how to the topological superconductivity to 1D. Some examples include:

1. Spatial confinement: the electrons can be confined within a lithographically defined- or self-assembled- wire.

2. Electrostatic confinement: creating a 2D topological superconductor requires fine-tuning the chemical potential to within the Zeeman gap of the inner Ferm-

surface. By electrostatic gating, one can create an inhomogeneous chemical potential profile such that only a narrow 1D segment satisfies this condition.

3. Ferromagnetic Strip: so far we have assumed that the Zeeman splitting comes from an externally applied field. Alternatively, one can deposit a ferromagnetic insulator, such as EuS, that induces Zeeman explitting by proximity. A narrow strip of such an insulator could create a 1D domain of topological superconductivity.

Each of these schemes has its own practical advantages that need to be weighed against the complexity of implementation. For example, using ferromagnetic strips can produce strong Zeeman splitting in the surface without harming the bulk superconductivity. However, this introduces extra materials challenges associated with engineering the interface between RSOC layer and ferromagnetic insulator.

A minor but practically important detail is that for a strictly 1D system, the magnetic field **B** need not be perpendicular to the plane of the wire. Rather, **B** must simply be perpendicular to the spin-orbit direction: $\hat{z} \times \hat{k}$, where $\hat{k}$ is the direction of propagation of the electrons. This allows for the field to point either out of the plane of the substrate, or in the plane of the substrate along the wire. For strictly 1D wires, these two choices are equivalent. However, in practice one inevitably deals with multi-band wires, and placing the field along the wire offers important advantages.

Out-of-plane Field

The dispersion without superconductivity in the presence of a perpendicular field is:

$$\varepsilon_{\mathbf{k},\lambda} = \frac{k^2}{2m} - \mu + \lambda\sqrt{\alpha_R^2 k^2 + (\mu_0 B)^2} \tag{3.18}$$

where $\lambda = \pm 1$. The resulting phase diagram for a superconducting wire obtained from numerical simulation is shown in Fig. 3-1a. Topological phase transitions occur when the chemical potential coincides with the bottom of a transverse sub-band, so long as the transverse sub-band spacing is larger than Δ_S. For $\mu > 0$, the sub-band splitting due to the applied field can be estimated by setting $k_x = 0$ and $k_y \approx \pm k_F$ in Eq. 3.18.

Consider the energy ε_n of the n^{th} sub-band for $B = 0$. For $k_x = 0$ there are four different states with $\varepsilon_{\lambda,(k_x=0,k_y)} = \varepsilon_n$, labeled by different k_y. In the wire, linear superpositions of these four states are formed to satisfy the hard-wall boundary-conditions (which can only be satisfied for a discrete set of energy values). In the absence of a magnetic field, the four k_y states at energy ε_n form two degenerate combinations related by time-reversal symmetry. Due to the Rashba SOC, the spin of each of the k_y states lies in the plane, and a perpendicular field does not directly mix the two states. Consequently, the sub-band splitting from the field occurs through virtual admixture of higher energy states, and scales like $\Delta E_{\text{sb}} \approx \frac{B^2}{\Delta_{\text{so}}}$ where $\Delta_{\text{so}} = \alpha_R k_F$. Inside the bulk Zeeman gap, ($|\mu| < \mu_0 B$), it is always possible to occupy an odd number of sub-bands. As chemical potential is increased outside of the bulk Zeeman-

gap, $\Delta_{\rm so}$ increases until $\Delta E_{\rm sb} < \Delta_S$, at which point the topologically nontrivial regions stop occuring.

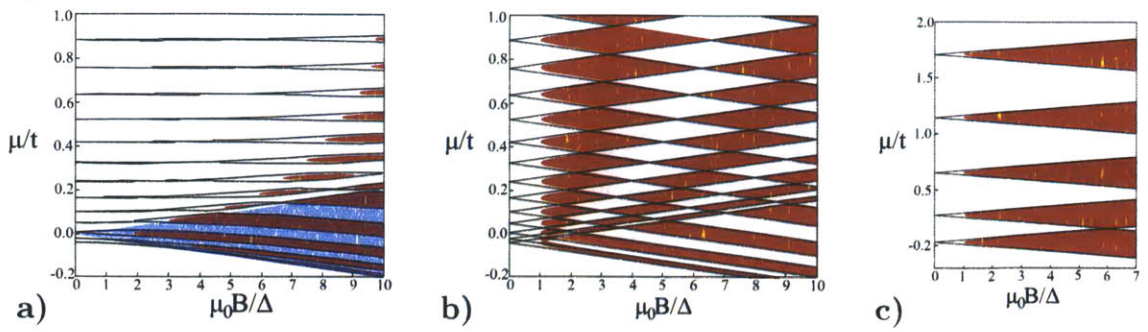

Figure 3-1: (a) Numerical phase diagram for 40-site wide wire in perpendicular field ($\mathbf{B} \sim \hat{z}$), as a function of chemical potential μ and magnetic field $\mu_0 B$. Black lines indicate sub-band bottoms in the normal state (without superconductivity), red filled regions indicate the presence of Majorana end-states, which occur when the sub-band degeneracy is removed and the sub-band splitting is sufficiently larger than the pairing gap Δ. The sub-bands are initially degenerate for $B = 0$, and split quadratically as B is increased. Blue shaded region indicates the Zeeman gap for a full two-dimensional sample. In the wire, the topological region extends slightly outside the Zeeman gap for sufficiently large B (for $\mu_0 B^2/\Delta_{SO} \gtrsim \Delta$). Simulation parameters: $t = 50$, $\alpha_R^2/t = 10$, $\Delta_S = 1$. (b) Same setup described in a) but with the magnetic field applied along the wire ($\mathbf{B} \sim \hat{x}$). Unlike the perpendicular field case, the wire always remains in the topological region so long as $\mu_0 B > \Delta_S$ and an odd number of sub-bands is occupied. Unlike the parallel field case, the black lines that indicate sub-band bottoms split linearly in the applied field, giving rise to a criss-crossing diamond pattern of topological and non-topological phases. (c) Parallel field phase diagram for 10-site wide wire, topological regions occupy smaller fraction of the phase-diagram.

Field along the Wire

The dispersion without superconductivity in the presence of a parallel field is:

$$\varepsilon_{\mathbf{k},\lambda} = \xi_k + \lambda \alpha_R \sqrt{k_x^2 + \left(k_y + \frac{\mu_0 B}{\alpha_R}\right)^2} \tag{3.19}$$

For $\mu > 0$,[3] the sub-band bottoms occur for $k_x = 0$. Unlike the perpendicular field case described above, the initially degenerate sub-band bottoms are split linearly by parallel B, $\Delta E_{\rm sb} \approx \mu_0 B$, independent of the spin-orbit coupling strength. The linear sub-band Zeeman–splitting leads to the criss-crossing pattern of diamonds shown in Fig.3-1b. So long as $\mu_0 B > \Delta_S$, we expect to be able to occupy an odd number of sub-bands and achieve a topologically non-trivial state with Majorana end-states.

[3]For $\mu < 0$, the sub-band bottoms occur for $k_x \neq 0$ due to the "mexican-hat" shape of the Rashba band. Despite this, the topological phase transitions are still signaled by the gap closing at $k_x = 0$.

The topological phase diagram obtained from numerical simulations and shown in Fig. 3-1b,c bears out this expectation, exhibiting topologically non-trivial phases for arbitrarily large chemical potential. These results were also obtained in [51], and are qualitatively similar to the orbital effects of a magnetic field applied along the axis of a TI nanowire[52].

Two illustrative cases are shown in Fig. 3-1b,c. In Fig. 3-1b the sub-band spacing is comparable to the SC gap, $\Delta E_{\text{sb}} \approx \Delta_S$, corresponding to the metallic strip having width comparable to the SC coherence length, $W \approx \xi_0$. In this case, the topological and non-topological phases occupy roughly equal portions of the phase diagram, allowing one to more easily tune into the topological region by changing B or gate voltage. In Fig. 3-1c the sub-band spacing is larger than the SC gap, $\Delta E_{\text{sb}} > \Delta_S$, corresponding to $W < \xi_0$. Here, for small fields, the non-topological regions occupy a larger fraction of the phase diagram.

Having $\Delta E_{\text{sb}} \approx \Delta_S$ is especially important for the gateless setup shown in Fig.3-10a, where tuning sub-band number is accomplished purely by changing $\mu_0 B$. If $\Delta E_{\text{sb}} \gg \Delta_S$, then, without controlling μ, the wire is most likely to be deep in the topologically trivial region. This would likely require applying large $\mu_0 B \gg \Delta_S$ in order to tune into the topological phase. In contrast, for $\Delta E_{\text{sb}} \approx \Delta_S$, the maximum require $\mu_0 B$ is $\approx \Delta_S$ regardless of the initial μ, allowing one to readily tune to the topological phase without controlling μ.

3.3 Smoothly Meandering Wires

In the long rectangular strip geometries considered above, the system is neatly separable in the x and y directions. So far, the existence of discrete transverse sub-bands (in the y-direction) has played a central role in understanding the topological phase transitions in these structures. Naturally, one might therefore wonder whether the existence of transverse sub-bands is essential to the formation of Majorana end-states. Specifically, the presence of spatially varying and non-parallel edges mixes different transverse sub-bands, destroying the notion of the "number of occupied channels". Since, for rectangular samples, Majorana end-states exist only for an odd-number of transverse channels, it is possible that the mixing of even and odd number of channels may destroy the Majorana end-states in non-rectangular samples.

Suppose one has a wire whose width, $W(x)$, varies along the length of the wire, defined to be in the x direction. For fixed x, one can define a local "number of sub-bands", $N(x)$, equal to the number of sub-bands in an infinitely long wire of width $W(x)$. We can then imagine decomposing the wire into linear segments with definite $N(x)$. Denote the typical length of such segments by $L_{\delta N}$. If we ignore the coupling between segments, then segments with odd N have Majorana end-states of characteristic size ξ_0. Denote these Majorana states by γ_i, and their locations by x_i.

When we account for coupling between the segments, the would-be Majorana states located at x_i and x_j couple with strength $E_{L_{\delta N}} \approx \Delta_0 e^{-|x_i - x_j|/\xi_0} \approx \Delta_0 e^{-L_{\delta N}/\xi_0}$. For a smoothly varying wire, this coupling is weak, and all other states besides γ_i will have energy $\gg E_{L_{\delta N}}$, and can be integrated out perturbatively. This results in

a description purely in terms of γ_i and the (renormalized) couplings between them, which is valid at low-energy scales.

Since there must be an even number of γ_i's overall, by symmetry, this low-energy description can only take the form of an inhomogeneous Kitaev wire with short-ranged (though not purely nearest neighbor) couplings. When the randomness in the couplings between γ's is not too strong ($L_{\delta N}$ not too much larger than ξ_0), this renormalized Kitaev wire again has two phases: 1) a gapped, topologically trivial phase where the Majorana states at the end of the wire are paired with other nearby γ's, and 2) a gapped topological phase where there are unpaired Majorana states localized to both ends. Changing the chemical potential of the wire adjusts the residual coupling between the γ_i's and can tune between these two phases.

In general, there will be rare γ_i's that are only weakly coupled to other γ's, and remain as low-energy excitations. For stronger randomness ($L_{\delta N} \gg \xi_0$), we expect, in analogy to the work of Motrunich et al.[190], these rare "Griffiths"-type effects will eventually dominate, leading to a gapless strong-disorder phase with a power-law type density of states in the bulk of the wire. In this Griffiths phase, the former Majorana end-states are no longer exponentially localized to the wire ends, but rather have power-law extent into the bulk.

From the above considerations, we see that if $L_{\delta N} \lesssim \xi_0$, then the coupling between γ_i is comparable to proximity induced gap, Δ_0, and the wire has a robust gap. If the variations of W occur on too short of a length-scale, $L_{\delta N} \approx 1/k_F$, they induce large-angle scattering similar to that of point-like impurities. As we will see in the subsequent chapter, such large-angle scattering is pair-breaking and suppresses the proximity induced SC gap.

Therefore, to maintain a robust gap along the length of the wire, we see that one can tolerate smooth variations with typical lengthscale:

$$\frac{1}{k_F} \ll L_{\delta N} \lesssim \xi_0 \tag{3.20}$$

This requirement is quite manageable in metallic systems, where $\xi_0 \sim 1\mu$m, and $\frac{1}{k_F} \sim 10\mathring{A}$. The requirement is slightly more stringent in semiconducting systems, however, semiconducting wires can be made rather pristine, e.g. by using self-assembly growth techniques.

Simulations

To quantitatively address the issue of variable wire width, we simulate samples confined to a narrow region by electrostatic confinement potential $V_{\text{conf}}(x, y)$ with smooth, random meandering boundaries. Here it is important that the edge variation is relatively smooth, as jagged edge variations produce a scattering mean-free path $\ell \simeq W$. Due to the condition $W \lesssim \xi_0$, scattering from sharp edge variations tends to destroy the p-wave pairing gap[1].

To produce random edges with width variance σ_W and correlation length ξ_D, we start by choosing the y-location of the top and bottom edges $y_{t,b}(x)$ independently for

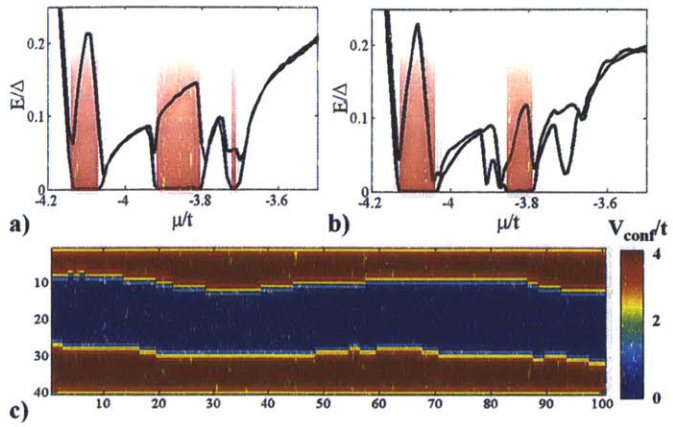

Figure 3-2: Panels (a) and (b) show the two lowest energy in-gap excitations for an electrostatically confined strip with $L_x = 100$, $\overline{L}_y = 20$, $t = 10$, $\Delta = 1$, $V_z = 2$, $\alpha_R = 2$. Red shading indicates the presence of isolated Majorana end-modes at zero-energy. The results in (a) are for straight edges ($\sigma_W = 0$), and those in (b) are for a random sample with $\sigma_W = 4$ and $\xi_D = 15$; (c) shows a colormap of the random edge geometry used to generate (b). Importantly the Majorana edge states survive, retaining a substantial excitation gap even for large edge variation (in this case $\sim 40\%$ of the average width $\overline{L}_y$) and demonstrating that these states do not rely on the existence of transverse sub-bands.

each x, identically distributed normally with variance $\sqrt{2\sigma_W^2\xi_D}$ and mean $\overline{L}_y/2$ (where the over-bar indicates averaging with respect to edge configuration). We then apply an exponential smoothing filter $y_{t,b}(x) \to \sum_{x'} \frac{1}{\xi_D} e^{-|x-x'|/\xi_D} y_{t,b}(x')$, which correlates $y_{t,b}(x)$ and $y_{t,b}(x')$ on lengthscales, $|x - x'| \lesssim \xi_D$, on the order of the edge-correlation length ξ_D.

Since the sample width at any x must be an integer number of lattice spacings, $\{y_{t,b}(x)\}$ are rounded to the nearest integer, resulting in discrete steps rather than smooth edges. These steps introduce sharp, short range scattering potentials, and in order to separate out the effects of this discretization, from those of the smoothly wandering edges, we smooth the V_{conf} along the lateral (y–) direction with a Gaussian filter of width 2 lattice spacings.

Fig. 3-2a. and b. show the results of simulations with a smoothly random electrostatic confinement potential for samples with average width $\overline{L}_y = 20$, length $L_x = 100$, edge correlation length $\xi_D = 15$, and with edge variance $\sigma_W = 0$ and 4 respectively. We find that the Majorana end modes, and corresponding sequence of alternating phase transitions survives even for substantial edge variations, that is, even when there are no well-defined transverse sub-bands. Despite the lack of transverse sub-bands, as one sweeps μ, discrete bulk levels inside the superconducting gap are still pulled down one-by-one across zero-energy, resulting again in an alternating sequence of topological phase transitions. However, the locations of these transitions occur at different values of μ compared to the rectangular case. In contrast to the rectangular sample case, these discrete levels cannot be simply identified with transverse band-bottoms, but rather are bulk states with some more complicated structure.

The excitation gap protecting Majorana end-states in these random edge geometries is reduced from the rectangular case. However, as seen by comparing Fig. 3-2a. and b., this excitation gap remains a substantial fraction of the straight edge rectangular case even for large variations in the edge geometry (in the case of Fig. 3-2 b. the fractional variation in width, $(\overline{\delta y_t^2} + \overline{\delta y_b^2})/\overline{L}_y = 2\sigma_W/\overline{L}_y$, is 40%).

These simulations demonstrate that the existence Majorana end-states is highly insensitive to the details of sample geometry, and in particular *does not require the existence of transverse sub-bands.* This robustness to edge-variations highlights the truly topological nature of these states. Also from a practical perspective, the ability to tolerate substantial (smooth) edge variance eases the requirements for sample fabrication, making an experimental realization more feasible.

3.4 Disorder

A crucial practical issue facing proposals to produce Majorana fermions is understanding and managing the detrimental effects of disorder. In this chapter, we consider the effects of impurities. The focus will be on impurities residing within the spin-orbit coupled nanowire (for 1D or quasi-1D systems) or surface-layer (for 2D effective $p + ip$ superconductors). However, other types of scattering will be considered towards the end of this section. We will see that disorder is very harmful for Rashba systems with weak spin-orbit coupling ($\alpha_R k_F \ll \Delta_0$), and strongly suppresses the proximity-induced pairing gap. In contrast, systems with strong spin-orbit coupling ($\alpha_R k_F \gg \Delta_0$) can tolerate much larger amounts of disorder. This observation will be important in choosing an appropriate class of materials, as is discussed in greater detail below. In the next chapter, we will also demonstrate that impurities can produce tunneling signatures that masquerade as true Majoranas but have no topological origin.

To model disorder, we consider a random on-site potential

$$H_{\text{disorder}} = \sum_{\mathbf{r},\sigma} V_{\text{imp}}(\mathbf{r}) c^\dagger_{\mathbf{r},\sigma} c_{\mathbf{r},\sigma} \tag{3.21}$$

that has only short-range correlations:

$$\overline{V_{\text{imp}}(\mathbf{r}) V_{\text{imp}}(\mathbf{r}')} = W^2 \delta(\mathbf{r} - \mathbf{r}') \tag{3.22}$$

where W is the disorder strength and $\overline{(\cdots)}$ indicates an average over disorder configurations. It is useful to parameterize disorder either by the scattering time $\tau \equiv 1/N(0)W^2$ or the mean free path $\ell = v_F \tau$ where v_F is the Fermi velocity of the surface layer and $N(0)$ is the surface–density of states. Furthermore, we consider moderate disorder that is too weak to induce localization, specifically that $k_F \ell \gg 1$, but make no other assumptions on disorder strength. Since non-planar disorder scattering diagrams are sub-leading in $(k_F \ell)^{-1}$, the regime $k_F \ell \gg 1$ allows for a controlled expansion for the disorder self-energy.

The assumption of short-range impurity correlations is completely appropriate for

metalic systems, or highly doped semiconductor systems, where charged-impurities are screened on a short length-scale. For dilute semiconductor systems, the assumption of short-range correlations becomes less accurate. However, even for these systems the short-range correlated model is expected to produce the right qualitative trends, and we continue to rely on this assumption for theoretical simplicity. Correlated disorder has also been considered in other works[71], where it was shown that nearly resonant impurity scattering can produce very low-energy sub-gap states.

3.4.1 Time-Reversal Symmetry and Anderson's Theorem for Proximity Induced Superconductivity

In the subsequent discussion of disorder, the presence or absence of time-reversal (TR) symmetry plays a key role. We will presently show that when (TR) symmetry is present, proximity-induced superconductivity is immune to the presence of disorder. The proof of this principle is most conveniently conducted in the basis of time reversed pairs[43] (see Eq. 3.6), in which the Hamiltonian for the disordered system with time-reversal symmetric s-wave pairing induced by proximity effect can be written as the following block-matrix:

$$H = \begin{pmatrix} H_0 + V_{\text{imp}} & \Delta\mathbb{I} \\ \Delta\mathbb{I} & -(H_0 + V_{\text{imp}}) \end{pmatrix} \tag{3.23}$$

Here H_0 is the Hamiltonian of the (clean) surface, V is random on-site disorder, Δ is the induced pairing amplitude, $\mathbb{I}$ is the $N \times N$ identity matrix where N is the number of degrees of freedom in the system. Since $\Delta\mathbb{I}$ commutes with H_0 and V_{imp}, the eigenvalue problem $\det(H - \varepsilon) = 0$ can be simplified:

$$0 = \det(H - \varepsilon) = \det\left(\varepsilon^2\mathbb{I} - (H_0 + V_{\text{imp}})^2 - \Delta^2\right) \tag{3.24}$$

Denoting the eigenvalues of $H_0 + V_{\text{imp}}$ by $\{\tilde{\varepsilon}_n\}$, the eigenvalues of H are $\pm\tilde{E}_n$ where:

$$\tilde{E}_n = \sqrt{\tilde{\varepsilon}_n^2 + \Delta^2} \tag{3.25}$$

which is bounded below by Δ, independent of the particular disorder configuration.

These manipulations show that, so long as the 2D surface Hamiltonian is TR invariant, disorder cannot reduce the superconducting gap. As an aside, it is useful to note that the above considerations do not depend on V_{imp} being spin-independent so long as it preserves TRI. In particular strong spin-orbit impurity scattering will also not reduce the superconducting gap.

It turns out that it is not possible to produce a topological superconductor with Majorana bound-states in strictly 1D or 2D systems that preserve time-reversal symmetry. Therefore, lower-dimensional realizations will necessarily have some degree of vulnerability to disorder. In contrast, it turns out to be possible to realize a superconductor with non-Abelian defects at the surface of a 3D topological insulator (TI), while preserving TR symmetry (see the subsequent Part of the thesis on electron

topological insulators). Consequently, superconductors at the surface of 3D TIs may provide a promising platform for realizing Majorana fermions without suffering from adverse disorder effects.

3.4.2 Perturbative Calculation for 2D Rashba System

The disorder averaged self-energy and Green's function are related by the following set of coupled equations:

$$\begin{aligned} \overline{\mathcal{G}}(i\omega, k) &= \left[\mathcal{G}_0(i\omega, k)^{-1} - \Sigma(i\omega)\right]^{-1} \\ \Sigma(i\omega) &= W^2 \tau_3 \sum_k \overline{\mathcal{G}}(i\omega, k)\tau_3 \end{aligned} \tag{3.26}$$

where the bare (non-disordered Green's function) $\mathcal{G}_0$ is given by Eq. 3.14, and incorporates the proximity induced superconductivity.

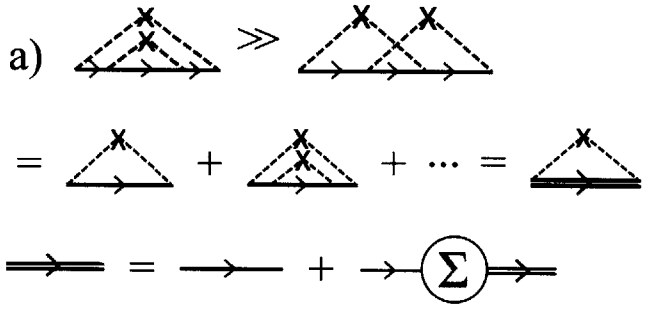

Figure 3-3: Panel A shows a diagrammatic representation of Eq. 3.26 for the disorder averaged Green's function and self-energy respectively. Disorder scattering is represented by dashed line originating from an $\times$. For delta-function-correlated impurities only multiple scatterings from the same impurity contribute. Panel B shows an example of a crossed diagram (right) that is sub-leading in $(k_F\ell)^{-1}$ compared to the non-crossed diagram with the same number of disorder scatterings (left).

In contrast to the TI case, creating a topological superconductor from a Rashba 2DEG requires explicitly breaking TR symmetry by inducing surface magnetization $\mu_0 B$. Without TR symmetry, the general arguments outlined above do not apply, and the induced pairing is vulnerable to disorder scattering. The analysis below demonstrates that the pair-breaking effects of disorder scattering are dramatically enhanced by the singular density of states at the superconducting gap edge, and furthermore that these effects are especially pronounced in systems with weak Rashba coupling. Since the pairing amplitude on the surface is induced by the bulk, it never vanishes. However, we shall see that the resulting pairing gap can be greatly reduced by even a small amount of disorder unless $E_{so} \gg \mu_0 B$. In fact, when $E_{so} \ll \mu_0 B$, the suppression due to disorder is more severe than for conventional superconductors with magnetic impurities for which the superconducting gap typically closes for $\xi_0/\ell \sim 1$. We will see, for $E_{so} \ll \mu_0 B$, that disorder strongly suppresses the induced superconductivity even for very weak disorder.

The wave-functions of electrons in the surface leak into the bulk superconductor. The fraction of the surface–resonance wave–function which lies on the surface is Z_Γ whereas the fraction residing in the bulk superconductor is $(1 - Z_\Gamma)$. To account for this leakage, it turns out to be sufficient to replace the bare disorder scattering time for the surface layer, $\tau^{-1} = \pi N(0) W^2$ (where $N(0)$ is the surface density of states), by an effective disorder scattering time

$$\left(\tau^{-1}\right)_{\text{eff}} = Z_\Gamma^2 \tau^{-1} \tag{3.27}$$

We see that effects of surface disorder are suppressed in the limit of strong surface–bulk tunneling. More generally, all of the bare non-superconducting terms in the Hamiltonian will be renormalized by surface-bulk tunneling:

$$\begin{aligned} \alpha_R &\to \tilde{\alpha}_R = Z_\Gamma \alpha_R \\ \mu_0 &\to \tilde{\mu}_0 B = \left(Z_\Gamma g_S + (1 - Z_\Gamma) g_B\right) \frac{\mu_B}{2} \end{aligned} \tag{3.28}$$

where g_S is the g-factor of the SOC-surface, and g_B is that of the bulk-SC (typically $g_B \approx 2$, but g_S can greatly exceed 2). Here we have assumed that there is negligible spin-orbit coupling inside the bulk superconductor.

Using these effective parameters, we now turn to the problem of solving the self-consistency relations given in Eq. 3.26 using the surface Green's function in Eq. 3.14 which includes the effects of proximity to the bulk superconductor. For ordinary disordered superconductors, the strength of disorder is conveniently parametrized by the ratio of the coherence length $\xi_0 = \pi v_F / \Delta$ to the mean free path $\ell = v_F \tau$. For the proximity induced superconductivity these parameters are renormalized by surface–bulk coupling. We will see that the effects of disorder depends on disorder strength only through the ratio $\tilde{\xi}_0 / \ell_{\text{eff}}$, where $\tilde{\xi}_0 = \pi \tilde{v}_F / \tilde{\Delta}$ is the surface coherence length and $\ell_{\text{eff}} = \tilde{v}_F \tau_{\text{eff}}$ is the effective mean-free path for disorder electrons. This effective ratio can be written in terms of the intrinsic ratio of the intrinsic mean-free path, ℓ (unrenormalized by proximity induced superconductivity) and coherence length of the bulk superconductor, ξ_0, as follows:

$$\frac{\tilde{\xi}_0}{\ell_{\text{eff}}} = \frac{Z_\Gamma^2}{1 - Z_\Gamma} \frac{\xi_0}{\ell} \tag{3.29}$$

Analytic Expressions for Weak Disorder

For weak disorder ($\tilde{\xi}_0 / \ell_{\text{eff}} \ll 1$), it is sufficient to evaluate the self-energy to lowest order in disorder scattering strength, corresponding to the first diagram for the self-energy shown in the top line of Fig. 3-3:

$$\Sigma^{(1)}(i\omega) = W^2 \tau_3 \sum_k \tilde{\mathcal{G}}_0(i\omega, k) \tau_3 \tag{3.30}$$

Here he value of W^2 should be appropriately renormalized according to Eq. 3.27. For $\tilde{\Delta}_{FS} \ll \tilde{\mu}_0 B$, the dominant contributions to the k-integral come from near the

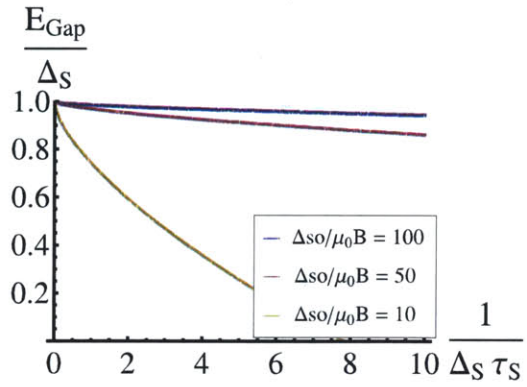

Figure 3-4: For very strong spin orbit coupling, the disorder renormalization of the excitation gap E_{gap} is perturbatively small. This plot shows the excitation gap as a function of disorder strength, computed from the analytic perturbative expressions. For weak to moderate spin-orbit coupling, non-perturbative effects become important and a numerica treatment is required, see Fig. 3-5.

Fermi-surface. Linearizing the Bogoliubov dispersion about the Fermi-surface, and performing the integration yields:

$$\begin{aligned}
\Im m\Sigma^{(1)}(i\omega) &\approx -x\omega\left[\frac{1}{2}+2\frac{\tilde{\mu}_0 B}{\tilde{\Delta}_{BG}^2}\sigma_z\left(\tilde{\Delta}\tau_1-\tilde{E}_{\text{so}}\tau_3\right)\right] \\
\Re e\Sigma^{(1)}(i\omega) &\approx \frac{x}{\tilde{\Delta}_{BG}^2}\left[\left(\omega^2-\tilde{\Delta}^2\right)\tilde{E}_{\text{so}}\tau_3+\tilde{\mu}_0 B\left(\tilde{\Delta}^2+\omega^2\right)\sigma_z+2\tilde{E}_{\text{so}}^2\tilde{\Delta}\tau_1\right] \\
x &\equiv \frac{\pi N(0)W^2}{\sqrt{\tilde{\Delta}_{FS}^2+\omega^2}} \equiv \frac{\tau_{\text{eff}}^{-1}}{\sqrt{\tilde{\Delta}_{FS}^2+\omega^2}}
\end{aligned} \tag{3.31}$$

where τ_{eff}^{-1} is a measure of the disorder strength, given by Eq. 3.27.

This self-energy alters the spectrum of the disorder averaged BdG Hamiltonian. For weak disorder, we expect the gap at the Fermi surface to change only slightly. To find the correction to Δ_{FS} due to disorder, one needs to analytically continue the self-energy to real frequency, and then look for a pole in the disorder averaged Green's function at $\omega = \Delta_{FS} - \delta\omega$, i.e. to solve:

$$0 = \det\left[\tilde{\Delta}_{FS}-\tilde{\delta}\omega-\mathcal{H}(k_F)-\Sigma^{(1)}\left(\omega=\tilde{\Delta}_{FS}-\delta\omega\right)\right] \tag{3.32}$$

to leading order in $\delta\omega$ one finds:

$$\delta\omega = \Psi_0^\dagger\Sigma^{(1)}\left(\omega=\tilde{\Delta}_{FS}-\delta\omega\right)\Psi_0 \tag{3.33}$$

where $\Psi_0 = \begin{pmatrix} u_\uparrow & u_\downarrow & v_\downarrow & -v_\uparrow \end{pmatrix}^T$ is the eigenvector of $\mathcal{H}(k_F)$ with energy $\tilde{\Delta}_{FS}$.

In the limiting case where $\tilde{\mu}_0 B \gg \tilde{E}_{\text{so}}$, $\Psi_0 \simeq \frac{1}{\sqrt{2}}\begin{pmatrix}0 & 1 & 0 & 1\end{pmatrix}^T$, and one finds

$$\delta\omega \simeq \frac{\tilde{\Delta}^2}{4\mu_0 B} x \simeq \frac{\tilde{\Delta}^2 \tau_{\text{eff}}^{-1}}{4\tilde{\mu}_0 B\sqrt{2\tilde{\Delta}_{FS}\delta\omega}} \tag{3.34}$$

Using $\Delta_{FS} \simeq \Delta\sqrt{\frac{\tilde{E}_{\text{so}}}{\tilde{\mu}_0 B}}$, and solving for $\delta\omega$ gives the following expression for the disorder renormalized pairing gap at the Fermi-surface:

$$\tilde{\Delta}_{FS}(\tau_{\text{eff}}^{-1}) \simeq \tilde{\Delta}\sqrt{\frac{\tilde{E}_{\text{so}}}{\tilde{\mu}_0 B}}\left[1 - \left(\frac{\tilde{\mu}_0 B}{4\sqrt{2}\tilde{E}_{\text{so}}}\frac{\tilde{\xi}_0}{\ell_{\text{eff}}}\right)^{2/3}\right] \quad (\tilde{\mu}_0 B \gg \tilde{E}_{\text{so}}) \tag{3.35}$$

The unusual non-analytic dependence on disorder strength stems from the singular behavior of x as $\omega \to \tilde{\Delta}_{FS}$, which in turn reflects the Van-Hove singularity in the superconducting density of states at the gap edge. This Van-Hove singularity enhances the effective disorder strength x, and in particular leads to an infinite slope of $\tilde{\Delta}_{FS}(\tau_{\text{eff}}^{-1})$ as $\tau_{\text{eff}}^{-1} \to 0$.

In the opposite limit, where $\tilde{E}_{\text{so}} \gg \tilde{\mu}_0 B$, $\Psi_0 \simeq \frac{1}{2}\begin{pmatrix}1 & -1 & 1 & -1\end{pmatrix}^T$ and consequently the weak disorder correction to the gap energy vanishes to leading order. Including sub-leading contributions in $\tilde{E}_{\text{so}}/\tilde{\mu}_0 B$ results in:

$$\tilde{\Delta}_{FS}(\tau_{\text{eff}}^{-1}) \simeq \tilde{\Delta}\left[1 - \left(\frac{18}{\sqrt{2}}\frac{\tilde{\mu}_0 B^2}{\tilde{E}_{\text{so}}^2}\frac{\tilde{\xi}_0}{\ell_{\text{eff}}}\right)^{2/3}\right] \quad (\tilde{E}_{\text{so}} \gg \tilde{V}z) \tag{3.36}$$

Numerical Solution for Moderate Disorder

For stronger disorder, Eq. 3.26 must be solved self-consistently, which can be done numerically. In order to regulate the numerical integrals in the UV we replace the continuum dispersion with a periodic one of the form $\xi_k = -2t\cos(k)$ which naturally introduces a finite band-width. The top and bottom panels of Figure 3-5 show the dependence of the induced superconducting gap on disorder strength for $\tilde{E}_{\text{so}} \gtrsim \tilde{\mu}_0 B$ and $\tilde{\mu}_0 B \gg \tilde{E}_{\text{so}}$ respectively.

For very weak disorder, $\tilde{\xi}_0 \ll \ell_{\text{eff}}$, the excitation gap exhibits non-analytic infinite initial slope predicted by Equations 3.35 and 3.36. Stronger disorder never fully closes the superconducting gap, however for $\tilde{\mu}_0 B \gg \tilde{E}_{\text{so}}$, the gap is largely suppressed even when $\tilde{\xi}_0$ is only a few percent of ℓ_{eff}. In most cases, E_{gap} is suppressed smoothly with increasing disorder strength, however, the $E_{\text{gap}}/\tilde{\Delta}$ curves for $\tilde{E}_{\text{so}} \simeq \tilde{\mu}_0 B$ have a knee-shaped kink at $\tilde{\xi}_0/\ell_{\text{eff}} \simeq 0.07$ after which E_{gap} drops abruptly. This knee occurs when disorder reduces of the magnetization gap at $k = 0$ below the pairing gap $\tilde{\Delta}_{FS}$ at the Fermi-surface.

Here we see a second drawback of using materials with low Rashba coupling: in addition to limiting the size of the induced pairing gap in the absence of disorder, small Rashba coupling renders the topological superconductor susceptible even to

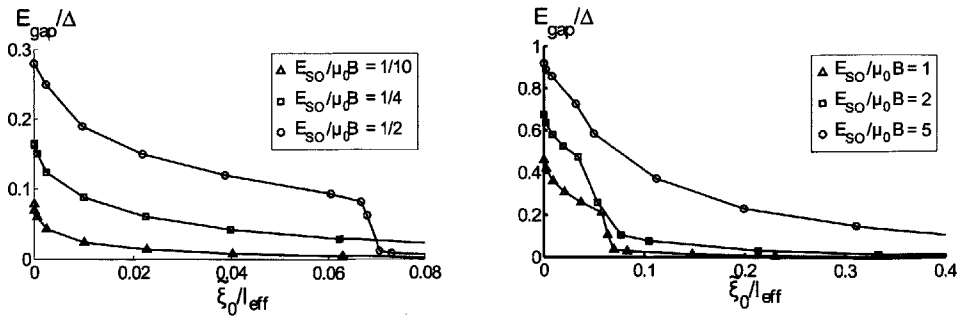

Figure 3-5: The excitation gap E_{gap} as a function of coherence length $\tilde{\xi}_0 = \pi v_F/\tilde{\Delta}$ to the effective mean free path $\ell_{\text{eff}} = \tilde{v}_F \tau_{\text{eff}}^{-1}$. E_{gap} is obtained from numerically solving Eq. 3.26 for a Rashba 2DEG with induced magnetization $\tilde{\mu}_0 B$ and superconductivity $\tilde{\Delta}$. Here $\widetilde{(\cdots)}$ indicates renormalization due to the proximity effect. The parameters used in this simulation were $t = 1$, $\tilde{\mu}_0 B = 0.1$, $\tilde{\Delta} = 0.01$, and various values of $\tilde{E}_{\text{so}}$. The top panel shows curves for $\tilde{\mu}_0 B \gg \tilde{E}_{\text{so}}$, the regime appropriate for semiconductor materials, whereas the bottom panel shows curves in the $\tilde{E}_{\text{so}} \gtrsim \tilde{\mu}_0 B$ regime which could be achieved by using metallic thin films with stronger spin-orbit coupling. The magnetization $\tilde{\mu}_0 B$ breaks time reversal symmetry rendering the induced pairing susceptible to disorder. For $\tilde{\mu}_0 B \gg \tilde{E}_{\text{so}}$ the gap is already strongly supressed when $\tilde{\xi}_0$ is only a few percent of ℓ_{eff}.

small amounts of disorder ($\tilde{\xi}_0/\ell_{\text{eff}} \ll 1$). While bulk semiconductors are typically cleaner than metallic thin films, their extreme sensitivity to disorder will likely be problematic. In particular, great care would need to be taken to limit interfacial roughness between the semiconductor and adjacent bulk superconductor and magnetic insulating film.

Before concluding, we remark on two possible extensions of this analysis. Firstly, the effects of disorder were treated for fully two-dimensional structures, whereas Majorana fermions emerge in one-dimensional (or quasi-one-dimensional) geometries. The effects of disorder in quasi-one-dimensional Rashba coupled structures were analyzed numerically in Ref. [1, 2], and give similar results to those given above for two-dimensions. Finally, while this analysis has been carried out for the case of Rashba-type spin-orbit coupling, we expect similar results for systems in which both Rashba and Dresselhaus-type spin-orbit couplings are present. The relevant factor in either case is the presence of magnetization $\mu_0 B$ which breaks time-reversal symmetry and renders the induced superconductivity susceptible to disorder regardless of spin-orbit type.

3.4.3 Disordered Superconductor Bulk

For superconductivity induced by proximity effect, the surface state wave-functions are localized to the surface, but extend into the superconductor with characteristic lengthscale ξ_L. Therefore electrons residing in the Rashba material are scattered

not only by impurities in the Rashba material and interface roughness, but also by impurities in the superconductor. Whereas semiconductor systems with Rashba spin-orbit coupling can be made quite clean, proximity induced superconductivity requires a nearby metal which will be comparitively much more dirty. For good metals the mean-free path is roughly: $\ell_{\text{metal}} \sim 10^2 - 10^3/k_F^{(\text{metal})}$. But since $k_F^{(\text{metal})} \approx 10^2 - 10^3 k_F^{(\text{semi-conductor})}$, this implies $\ell_{\text{metal}} k_F^{(\text{semi-conductor})} \approx 1$. Therefore, if scattering from impurities in the nearby bulk-SC were pair-breaking, this would pose a serious obstacle for realizing Majorana fermions. Fortunately, it turns out that while the scattering rate in the bulk-SC is quite high, bulk-scattering events have negligible pair-breaking effects for the proximity induced SC in the Rashba coupled layer.

The pair-breaking effects of bulk-impurities come from processes like that in Fig. 3-6. In this process, an electron tunnels from the surface into the bulk, where it is scattered by a bulk-impurity before returning to the surface. Importantly, the surface-layer is two-dimensional (or one-dimensional in the case of wires) whereas the bulk superconductor is three-dimensional. Here we show this mixed dimensionality strongly constrains the available phase-space for these scattering processes, and that the pair-breaking effects of bulk-impurities is negligible. While we only consider the case of a 2D electron gas with SOC, the following argument can also be applied to a 1D (or quasi-1D) wire in contact with a 3D bulk superconductor.

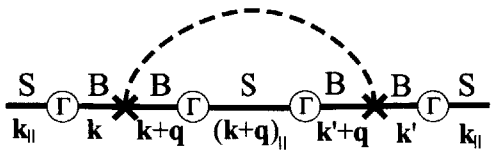

Figure 3-6: Diagrammatic depiction of the pair-breaking process due to bulk impurities. The geometrical constraints on scattering due to the different dimensionality of the surface and bulk (see Fig. 3-7) suppress these processes by a factor of $\gamma/\varepsilon_F \ll 1$. Circles with Γ show surface–bulk tunneling (S and B label surface or bulk Green's functions), bulk impurities are denoted by $\times$, and the dashed line indicates that both $\times$ refer to the same impurity.

For a clean interface, the components of momentum parallel to the surface–bulk interface (x and y components) are conserved whereas the perpendicular (z) component is not. An electron initially in the surface-layer with momentum $\mathbf{k}_\parallel$ can tunnel into any bulk states with momentum $\mathbf{k} = (\mathbf{k}_\parallel, k_z)$, but pays a large energy cost unless k_z is within $\sim \gamma/v_F$ of the bulk Ferm-surface (FS). Here v_F is the bulk Fermi-velocity and $\gamma = \pi N_B |\Gamma|^2$ where N_B is the bulk tunneling density of states and Γ is the surface–bulk tunneling amplitude. Once in the bulk the electron can scatter to any momentum $\mathbf{k} + \mathbf{q}$ within $\sim 1/\tau v_F$ of the bulk FS, where τ^{-1} is the bulk disorder scattering rate. However, in order to subsequently return to the surface-layer, the in-plane component of $\mathbf{k} + \mathbf{q}$ must again be within γ/v_F of the surface FS. Therefore, the available phase-space for such scattering is $\approx (2\pi k_F)(\frac{1}{\tau v_F})(\frac{\gamma}{v_F})$. In contrast, the phase space available for arbitrary bulk impurity scattering is $\approx 4\pi k_F^2(\frac{1}{\tau v_F})$. The

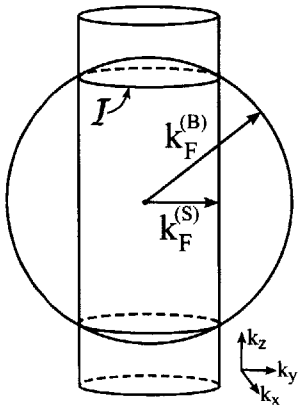

Figure 3-7: Momentum space geometry for surface–bulk tunneling. The 2D surface Fermi-surface (FS) is extended into a cylinder since tunneling does not conserve the momentum perpendicular to the interface (in the z-direction). Surface–bulk tunneling events involve only states near the intersection, $\mathcal{I}$, of the surface and bulk FS's.

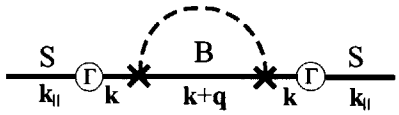

Figure 3-8: Diagrammatic depiction of a non-pair breaking scattering process for surface-electrons due to bulk impurities. Unlike the pair-breaking process shown in Fig. 3-6, this process has an unconstrained phase space.

pair-breaking scattering rate τ_{pb}^{-1} is smaller than the bulk impurity scattering rate τ^{-1} by the ratio of these two phase-space volumes: $\tau_{\text{pb}}^{-1}/\tau^{-1} \approx \frac{\gamma}{2v_F k_F} \sim \frac{\gamma}{\varepsilon_F} \ll 1$ where ε_F is the bulk-Fermi energy. In a typical superconducting metal, ε_F will greatly exceed γ, hence the pair breaking due to bulk disorder can be safely neglected.

Before concluding, we would like to emphasize the distinction between the scattering rate, $\tau_{\text{S-B}}^{-1}$, for surface-electrons from bulk-impurities and the pair-breaking rate τ_{pb}^{-1}. The scattering rate, $\tau_{\text{S-B}}^{-1}$ includes all possible bulk-disorder processes, and is dominated by processes like the one shown in Fig. 3-8, where an electron tunnels from surface to bulk, scatters from a bulk impurity and then continues to propagate in the bulk. This type of scattering is not pair breaking since, after scattering, the electron propagates only in the bulk where time-reversal symmetry is intact and pairing is not disrupted. Such processes do not suffer the same phase-space restrictions described above, and consequently $\tau_{\text{S-B}}^{-1}$ can be quite large even though the pair-breaking rate τ_{pb}^{-1} is small. Therefore, it is not that the surface-electrons are largely unaffected by bulk impurities, but rather that scattering from these impurities is predominantly not pair-breaking.

3.4.4 Interface Disorder

So far we have discussed impurities within the spin-orbit coupled layer (which were pair-breaking), and those within the bulk superconductor (which are only very-weakly pair-breaking). In addition, there can also be pair breaking effects due to interfacial roughness or impurities between the Rashba layer and the bulk superconductor. This can be the dominant source of scattering in self-assembled semiconducting nanowires, which tend to have large mean-free path in the absence of the nearby superconductor. Despite this, interface roughness could still contribute strong pair-breaking scattering in these systems.

Momentum non-conserving tunneling processes between the surface and bulk states are depicted in Fig. 3-9.

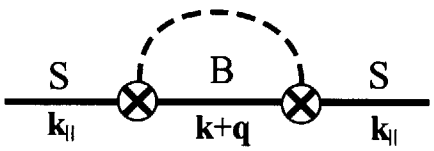

Figure 3-9: Diagrammatic depiction of the pair-breaking process due to interface roughness or interfacial-impurities. Circled $\times$'s denote momentum non-conserving tunneling/scattering between surface/wire and bulk-superconductor states.

Denoting the momentum non-conserving tunneling rate between Rashba and bulk-SC layers by $\Gamma_{\text{roughness}}$, then the effective pair-breaking rate from the interface-roughness is:

$$\tau_{\text{pb}}^{(\text{interface})} \approx \pi |\Gamma_{\text{roughness}}|^2 N_B(0) \tag{3.37}$$

We see that the interface scattering plays a similar role to the pair-breaking scattering within the surface or wire itself.

3.5 Candidate Materials

3.5.1 Semiconductor Wires

The original proposals for producing topological superconducting wires in RSOC systems all focused on semiconducting nanowires with heavy elements (e.g. InSb). Such materials tend to have small band-gaps, and strong atomic spin-orbit coupling, which lead to greatly enhanced g-factors as high as 50. This enables one to couple an external magnetic field selectively to the wire, without substantially harming the adjacent superconductor. Moreover, growth techniques for making semiconducting nanowires by self-assembly are well-developed, and it is possible to make rather clean samples.

For these practical and historical reasons, the majority of theoretical and experimental work has so far focused on semiconducting materials. However, there is a major drawback to these systems: semiconductor wires tend to have tiny Rashba spin-orbit coupling: $E_{\text{so}} \approx 1 - 2\text{K}$. Despite being made from heavy-element systems,

the inversion symmetry in these wires comes only from sitting on top of a substrate. Since electrons in these wires are spread out over the $\approx$ 100nm diameter of the wire, they feel the inversion breaking of the substrate only very weakly, and the resulting Rashba component of spin-orbit is very small.

Even in clean systems, small RSOC limits the scale of the proximity induced gap in the topological regime. Moreover, we have seen in the previous section that wires with small RSOC are extremely sensitive to the pair-breaking effects of impurities. This small RSOC and corresponding sensitivity to disorder may require working at prohibitively low-temperatures, and is a serious disadvantage for semiconductor materials.

In the next section, we propose an alternative class of materials, metallic thin-films, which have orders of magnitude larger RSOC. These thin-film realizations may be more promising platforms for producing robust Majorana states, if the disorder sensitivity of semiconductor materials proves to be insurmountable.

3.5.2 Metallic Surface States

In the previous section, we saw that semicondutor materials had rather weak spin-orbit coupling, making them very sensitive to the detrimental effects of disorder. The problems associated with small spin–orbit coupling led to proposals for building a topological superconductor from metallic surface–states[1, 2, 3]. Surface states of heavy-metals are typically tightly bound to the surface, with very small spatial extent. Consequently, the surface–state electrons are strongly effected by the inversion asymmetry of the surface–interface, generating large Rashba spin-orbit couplings. For example, the Au(111) surface hosts a well studied surface–state with Rashba splitting of $\Delta_{so} \approx$ 50meV[53], orders of magnitude stronger than the best Δ_{so} available in semiconductor nanowires. Even larger Rashba splittings, $\Delta_{so} \approx 0.5$eV, are available in the surface states of the Ag(111) surface alloyed with Bi and Pb[54].

The proposed setup is shown in Fig. 3-10a. A thin metallic film is deposited on top of a conventional superconductor. By the proximity effect, the bulk states of the metal film will inherit some of the superconducting gap Δ_0 from the nearby superconductor. If the metal film thickness is smaller than or comparable to the superconducting coherence length, ξ_0, then the induced bulk gap, Δ_B, will be large ($\Delta_B \approx \Delta_0$). However, the surface state on the top surface of the metal is nominally isolated from the bulk states and does not couple directly to the superconductor (see the Fig. 3-10d). Instead, we must rely on disorder and interactions to provide some mixing between the surface–state and bulk bands in order to transmit the bulk SC to the surface–state. Because SC develops in the surface–state only through indirect scattering processes, the surface–pairing gap, Δ_S will generically be smaller than the bulk pairing gap, $\Delta_B \approx \Delta_0$. In this case, the surface–state SC can be revealed by tunneling measurements, which will show a coherence peaks at the edge of the bulk gap, and a smaller sub-gap corresponding to Δ_S (see Fig. 3-10c).

Once SC is established, one can pattern the metallic film into a quasi-one dimensional wire. By applying a magnetic field, one can remove the sub-band degeneracy, and tune the chemical potential so that an odd-number of sub-bands is occupied.

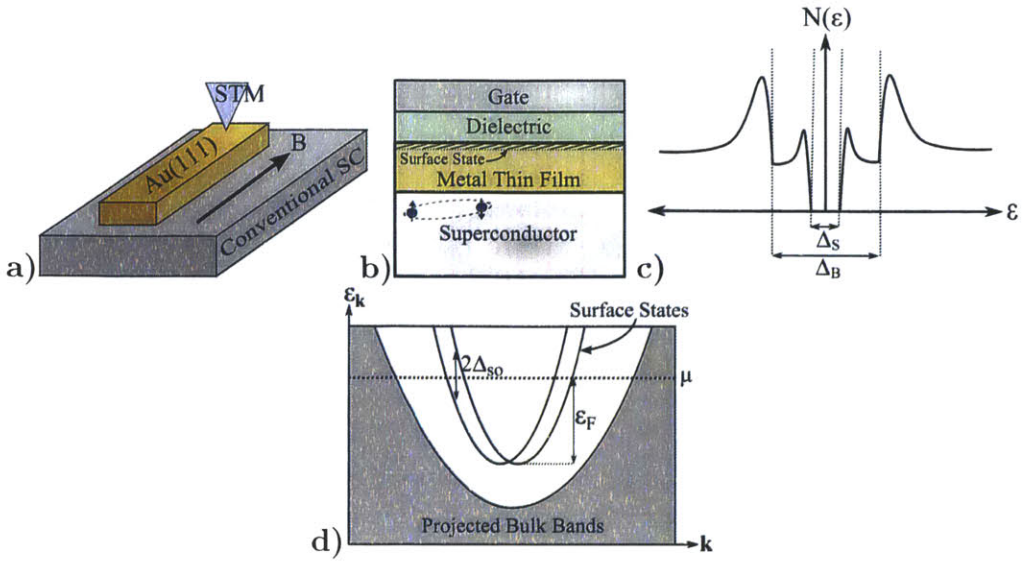

Figure 3-10: (a) Simplest possible version of the proposed setup: a strip of Au(111) thin-film (or any other metal with Rashba-split surface state) is deposited on top a conventional superconductor. An external field is applied parallel to the wire, in order to drive the system into a topological SC state. Majorana end-states can be detected by tunneling, e.g. with an STM tip. (b) So long as the surface–state survives the deposition of a gate–dielectric, the surface state chemical potential can be controlled by a top–gate. (c) Tunneling density of states, $N(\varepsilon)$, as a function of energy, ε; the full superconducting gap Δ_B is induced on the bulk states, by proximity effect. The surface gap develops a smaller gap Δ_S due to indirect scattering from disorder and interactions. (d) Sketch of band-structure of metal with a Rashba spin-orbit split surface band. Bulk states are projected onto the plane of the surface, and non-zero bulk projected density of states is indicated by gray shading. The surface-state band forms within a region momentum space where there is no bulk states. The figure shows a one-dimensional cut through the surface Brillouin zone. The chemical potential, μ, is represented by a dashed line. The surface Fermi-energy, ε_F, and spin-orbit splitting at the Fermi–surface, Δ_{so}, are indicated for the surface bands.

If the width of the wire is comparable or smaller than ξ_0, then, occupying an odd number of sub-bands will result in Majorana end-states protected by the surface-state pairing gap Δ_S[1, 2, 58, 55].

In the simplest version of the proposed setup, shown in Fig. 3-12a, tuning to an odd number of sub-bands is accomplished simply by applying an external magnetic field, without gating. The simplicity of this setup, consisting just of a metallic strip on a bulk superconductor, makes it promising for the initial detection of Majoranas. To perform more complicated experiments, in which Majoranas are braided, it is necessary to control the local topological phase of different segments of the wire. For this purpose, one could also add a top gate, as shown in 3-10b. In order for the top-gate geometry to work, one needs to check that the surface–state is not destroyed by the presence of the gate dielectric.

Consider a thin film of a spin-orbit coupled metal with a surface state, deposited on top of a conventional s-wave superconductor. If the metal is in good contact with the superconductor and the film thickness does not greatly exceed the superconducting coherence length, ξ_0, then nearly the full superconducting gap $\Delta_B \approx \Delta_0$ will be induced in the bulk-bands of the metal film.

However, in a pristine sample and in the absence of interactions, the metal surface-state has no overlap with the bulk metal bands (see Fig.3-10d). Consequently we must rely on indirect scattering between the bulk and surface bands to transmit the bulk superconductvity to the surface states. This indirect scattering can occur either by elastic scattering off of static impurities, or by inelastic scattering due to Coulomb interactions or phonons. Below we discuss both types of scattering, starting with the simpler case of elastic impurity scattering.

Surface-Bulk Mixing from Elastic Impurity Scattering

As a simple model of screened impurities, we consider a random potential $V_{\rm imp}(\mathbf{r})$ with zero average $\overline{V_{\rm imp}(\mathbf{r})} = 0$ and short range correlations, $\overline{V_{\rm imp}(\mathbf{r})V_{\rm imp}(\mathbf{r}')} = W^2\delta(\mathbf{r}-\mathbf{r}')$. Here $\overline{(\dots)}$ indicates averaging over impurity configurations. The impurity scattering from the surface state to the bulk bands gives rise to the following self-energy, evaluated within the self-consistent Born approximation:

$$\begin{aligned}\Sigma_{\rm imp}(i\omega) &= \overline{V_{\rm imp}(\mathbf{r}_\parallel, z=0)G_B(\mathbf{r},0;\mathbf{r}'_\parallel,0)V_{\rm imp}(\mathbf{r}_\parallel,z=0)} \\ &= -W^2\tau_3\sum_k \frac{i\omega-\Delta_0\tau_1}{\omega^2+\xi_k^2+\Delta_B^2}\tau_3 \\ &= -\frac{1}{2\tau_B}\frac{i\omega-\Delta_0\tau_1}{\sqrt{\omega^2+\Delta_B^2}} \end{aligned} \tag{3.38}$$

Here ω is the Matsubara frequency corresponding to Fourier transforming in imaginary time, $\tau_B = 2\pi\nu_B(0)W^2$ is the elastic scattering time for bulk electrons, $\nu_B(0)$ is the density of states at the bulk Fermi-surface, and $G_B = 1/\left(i\omega - \xi_k\tau_3 - \Delta_B\tau_1\right)$ is the Green's function for bulk fermions with dispersion ξ_k and bulk pairing gap Δ_B. This expression is valid so long as localization corrections can be ignored in the bulk, i.e. so long as $\varepsilon_{F,B}\tau_B \gg 1$, where $\varepsilon_{F,B}$ is the bulk Fermi-energy. We emphasize that the impurity induced surface–bulk mixing is sensitive only to impurities near the surface.

Incorporating $\Sigma_{\rm imp}$ into the surface state Green's function yields:

$$\begin{aligned} G_S(i\omega,\mathbf{k}) &= \left[\left(G_S^{(0)}\right)^{-1} - \Sigma_{\rm imp}\right]^{-1} \\ &= \frac{Z(i\omega)}{i\omega - Z(i\omega)H_0 - (1-Z(i\omega))\Delta_B\tau_1} \end{aligned} \tag{3.39}$$

where $G_S^{(0)}(i\omega) = \left[i\omega - H_0\right]^{-1}$ is the bare surface Green's function, $H_0 = (\frac{k^2}{2m} - \mu -$

$\alpha_R \hat{z} \cdot (\boldsymbol{\sigma} \times \mathbf{k}))\tau_3 - \mu_0 B \sigma_z$ is the surface Hamiltonian, and

$$Z(i\omega) = \left[1 + \frac{1/2\tau_B}{\sqrt{\Delta_B^2 + \omega^2}}\right]^{-1} \tag{3.40}$$

is the surface quasi-particle residue.

The effective pairing gap from impurity induced surface–bulk mixing is given by smallest pole of G_S which occurs at frequency ω_p defined by: $\left(\frac{\Delta_B}{\omega_p} - 1\right)^2 = 4\tau_B^2\left(\Delta_0^2 - \omega_p^2\right)$. For the limiting cases of strong and weak disorder the induced gap reads:

$$\Delta_{\text{imp}} = \omega_p = \begin{cases} (1 - 4\Delta_B^2\tau_B^2)\Delta_B; & \Delta_B\tau_B \ll 1 \\ 1/2\tau_B; & \Delta_B\tau_B \gg 1 \end{cases} \tag{3.41}$$

For strong disorder, $\Delta_B\tau_B \ll 1$, the induced gap is nearly equal to the full bulk gap, whereas for weak disorder, $\Delta_B\tau_B \gg 1$ only a small fraction of the bulk gap is transmitted to the surface state.

Eq. 3.41 suggests that if the surface states are too well isolated from the bulk bands, then it may actually be advantageous to introduce surface disorder to ensure sufficient mixing of the surface and bulk bands. However, in order to drive the system into a topological superconducting state one must apply an external magnetic field, in which case time-reversal symmetry is broken and disorder is pair-breaking[3, 59, 60]. One might therefore worry that increasing disorder may tend to suppress rather than enhance superconductivity. However, the size of the pair-breaking component of disorder scattering was shown to be strongly dependent on the ratio of the spin-orbit coupling Δ_{so} to the Zeeman splitting $\mu_0 B$[3] In particular, for very strong spin-orbit coupling, the pair–breaking effects of impurities is small.

For heavy metal materials with surface states Δ_{so} is commonly quite large, on the order of $\approx$ 100meV[53, 54, 39]. In contrast, the typical Zeeman splitting needed is of the order $\mu_0 B \approx 2\Delta_0 \approx$ 1meV. In this regime, the reduction of the surface pairing gap, $\delta\Delta_S$, due to disorder will be quite small[3]:

$$\left(\frac{\delta\Delta_S}{\Delta_S}\right)_{\text{disorder}} \approx -\left(\frac{(\mu_0 B)^2}{\Delta_{\text{so}}^2}\frac{1}{\Delta_S\tau_S}\right)^{2/3} \approx -10^{-3}\left(\frac{1}{\Delta_S\tau_S}\right)^{2/3} \tag{3.42}$$

where τ_S is the elastic lifetime for surface-states due to disorder. The reduction of the SC gap due to surface disorder is shown in Fig. 3-4, where for $\Delta_{\text{so}}/\mu_0 B \approx 100$ we see almost no effect at all from disorder. Therefore, so long as spin-orbit coupling is large, it is possible to enhance the surface–state pairing by adding disorder without suppressing the pairing gap by pair-breaking scattering.

Surface-Bulk Mixing from Inelastic Scattering

The surface-state and bulk bands are also mixed by inelastic electron-electron scattering and electron-phonon scattering. The middle and bottom rows of Fig. 3-11

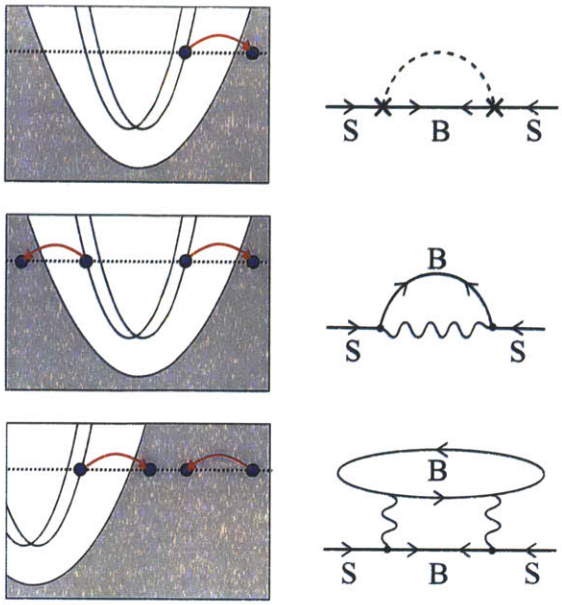

Figure 3-11: Depiction of virtual scattering processes which mix bulk and surface bands and generate surface superconductivity (left column) along with representative Feynman–diagrams (right column). In the diagrams, lines labeled by 'S' and 'B' indicate surface–state and bulk–state propagators respectively; propagators with left (right) arrows are conventional particle (hole) propagators, whereas propagators with both left and right arrows are anomalous propagators due to the Cooper-pair condensate. Each process shown in the left column represents half of the corresponding diagram (to complete the diagram, the process is repeated in reverse). The top row depicts elastic scattering from impurities, represented diagrammatically by $\times$'s connected by a dashed line (indicating scattering off of the same impurity). The middle and bottom rows show inelastic processes that generate surface pairing; wavy-lines represent either screened Coulomb interactions or phonons. The middle row shows inelastic pair-scattering from surface–to–bulk, and the bottom row shows interaction induced surface–bulk tunneling which is accompanied by the creation of a bulk particle–hole pair.

illustrate two processes that induce pairing in the surface state. In the process shown in the middle row, a pair of surface–electrons are virtually scattered into bulk states, where they develop pair correlations before returning to the surface. The process shown in the bottom row shows interaction driven (virtual) tunneling between surface and bulk states accompanied by a virtual particle-hole excitation.

In contrast to the surface–bulk mixing, which depends only on the easily measurable quantities τ_B and Δ_B, the inelastic surface–bulk mixing is difficult to accurately estimate. Doing so would require detailed knowledge of screening properties, phonon dispersion, and electron-phonon coupling matrix elements. These quantities are highly non-universal, and difficult to measure. Therefore, rather than attempting a detailed calculation, we simply illustrate that interaction driven processes can also contribute to surface–state superconductivity.

Gating Metallic Surface States

One often stated worry about proposals to realize Majoranas in nanowires with induced superconductivity, is that, since the wire is necessarily in good contact with a superconductor, the chemical potential of the wire may be pinned to the Fermi-energy of the superconductor making it impossible to gate the nanowire. This worry would also apply to the setup discussed here, using metallic surface states.

Here we address this worry, and demonstrate that the pinning of the surface chemical potential due to the bulk Fermi-surface is not strong enough to prevent gating. Rather, under experimentally realistic assumptions it should be straightforward to tune the surface chemical potential across 100's of sub-bands.

Consider applying a voltage, V_g, to a gate separated from the surface of the grounded metal sample by a dielectric of dielectric constant ϵ and thickness d (see Fig. 3-12). The applied voltage induces a bulk screening charge density $\rho_B(z)$ confined within a screening length, $\lambda_{TF} = \sqrt{\frac{\epsilon_0}{e^2 N_B}}$, of the surface, and also induces a surface-state charge density ρ_s. For simplicity, we assume that the extension of the surface-state into the bulk is much smaller than the screening length $\lambda_{TF} = \sqrt{\frac{\epsilon_0}{e^2 N_B}}$, and approximate the surface state as infinitesimally thin. Incorporating a finite surface-state width is straightforward, but does not substantially alter the results.

Within the Thomas-Fermi approximation the bulk screening charge is: $\rho_B(z) = -e^2 N_B \phi(z)$ where N_B is the bulk density of states, and the induced surface charge is $\rho_s(z) = -e^2 N_s \phi(0)\delta(z)$, where N_s is the surface density of states, and $\phi(0)$ is the chemical potential at the metal surface ($z = 0$). Solving Poisson's equation we find for the surface potential

$$\phi(0) = \epsilon_R \frac{\lambda_{TF}}{1 + N_S/\lambda_{TF} N_B} \frac{V_g}{d} \tag{3.43}$$

where ϵ_R is the relative permittivity of the gate dielectric.

We see that the consequence of applying the gate voltage is to shift the chemical potential of the surface by $\delta\mu_S = -e\phi(0)$ compared to the bulk chemical potential. For typical metals, $v_F \approx 1 \times 10^6 \mathrm{m/s}$, and the bulk and surface band masses are comparable to the bare electron mass, giving $\frac{N_S}{\lambda_{TF} N_B} \approx 4$. Break-down fields for typical gate dielectrics (e.g. SiO_2) are of on the order of $E_{\max} \approx 1\mathrm{V/nm}$, and typical screening metallic lengths are $\lambda_{\mathrm{TF}} \approx 1\mathring{A}$. For SiO_2, with $\epsilon_R = 4.9$, this gives $\delta\mu_s^{(\max)} \approx \pm 100\mathrm{meV}$. In comparison, for a metallic wire with width of the order of the superconducting coherence length, the typical sub-band spacing is $\approx \Delta_0 \approx 1\mathrm{meV}$, indicating that one could tune across hundreds of sub-bands. Furthermore, using a higher-K dielectric such as HfO_2 would allow one to tune the surface-potential over an even larger range.

From simple electrostatic modeling, we have shown that the close proximity to a metal does not substantially impede the ability to tune the surface-state chemical potential by a gate voltage. This analysis also implies that one could use a top gate to control the chemical potential of semiconducting nanowires placed on top of a superconductor. However, in order to get strong proximity induced SC, it is

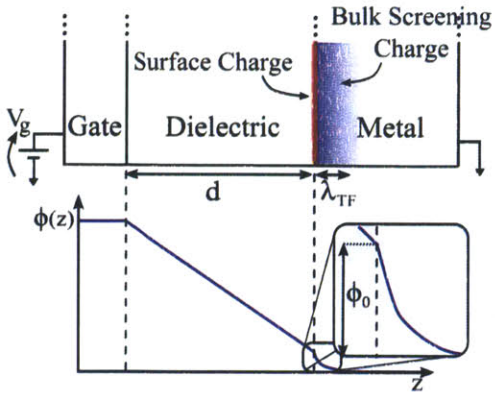

Figure 3-12: Electrostatic potential profile from applied gate voltage(bottom) aligned with the proposed materials stack (top, shown here rotated 90° relative to Fig. 3-10b). The surface chemical potential is shifted by $\delta\mu_s = -e\phi(0)$ relative to the bulk chemical potential. Estimates using typical material parameters demonstrate that one can readily tune the chemical potential by $\pm$100meV, despite the presence of a large density of states from the metallic bulk.

typically necessary to deposit nanowires on an insulating substrate and coat them with a superconductor. In this setup, one would need to employ a back-gate, which offers poor electrostatic control (since the wire would be coated on three sides by superconductor). Therefore, more complicated geometries are required; for example, one could partially coat the wire with superconductor and partially with a gate[40]. In contrast, the metallic-surface state chemical potential can be tuned using just a simple top-gate geometry, substantially simplifying the fabrication requirements.

3.5.3 3D TI Surface

We previously remarked that the superconducting surface of a 3D TI could be used to realize Majorana fermions in a TR symmetric manner. Since the 3D TI surface cannot be spatially confined, however, this works only for the 2D surface where Majorana fermions arise in vortex cores.

The simplest route to confining the superconducting state of a 3D TI into a 1D wire is to break TR symmetry outside of a 1D strip by depositing a ferromagnetic (FM) insulator. This can produce aend-states in an island of topological insulator (TI) with induced superconductivity (SC), surrounded by ferromagnetic (FM) insulator (see Fig. 3-13). One can take advantage of the sensitivity of the existence of Majorana end states to the chemical potential by adopting the geometry shown in Figure 3-13. In this geometry, the Majorana modes could be moved around by selectively applying gate voltages to locally tune the number of occupied sub-bands, thus obviating the need to create and manipulate vortices.

The introduction of a FM insulator, necessary to confine the topological superconductivity to a 1D strip, breaks TR symmetry and concedes the protection against

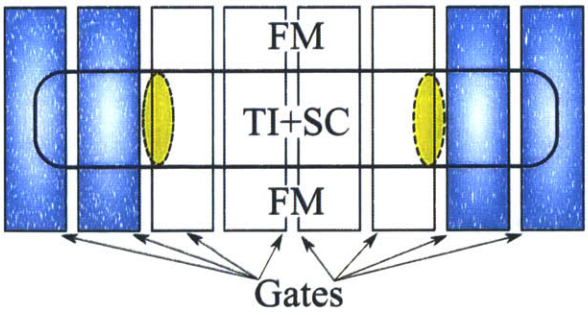

Figure 3-13: Proposed setup for electrically manipulating Majorana end-states in topological insulator (TI) materials. The proposed device would be fabricated on the surface of a 3D topological insulator. A strip of superconductor (labeled TI+SC) induces superconductivity in the underlying TI. This superconducting strip is embedded in a ferromagnetic insulator (labeled FM). Top gates (shown as overlayed rectangles) are used to locally control the number of occupied sub-bands. Blue shaded gates indicate an even number of sub-bands, demarking a non-topological region, whereas un-shaded gates indicate an odd number of sub-bands, demarking a topological region. Majorana bound states (shown as yellow blobs) emerge at the boundary between topological and non-topological regions.

impurity effects enjoyed by the symmetric TI surface. However, if the induced FM gap is very large, then the FM correlation length, ξ_{FM} can be very short compared to the superconducting correlation length ξ_0. In this case, TR symmetry can be only very weakly broken inside the superconducting strip, and the TI surface may still enjoy a greater tolerance for impurities than the strictly 1D or 2D RSOC counterparts.

Chapter 4

Tunneling Signatures of Majorana End-States

Tunneling provides one of the simplest experimental probes to detect putative Majorana end-states for quasi-1D topological superconducting wires. Tunneling from a normal wire into a topological superconducting wire with a Majorana end-state yields a quantized $G(0) = \frac{2e^2}{h}$ conductance peak at zero-bias[57, 21, 56]. This quantized zero-bias peak (ZBP) constitutes one of the simplest and most direct experimental probes for a Majorana fermion, and is likely to be the first test conducted on any putative topological superconducting wire. The observation of quantized zero-bias conductance with $G(0) = \frac{2e^2}{h}$ ZBP requires temperature, T to be sufficiently smaller than the intrinsic width, γ, of the Majorana peak, due to hybridization with the normal lead. For T comparable to or somewhat larger than γ a ZBP may still occur, but is no longer quantized and can take any value less than $\frac{2e^2}{h}$[57, 21, 56].

A recent set of experiments on InSb nanowires coated with a superconducting NbTiN layer report the observation of non-quantized ZBP's when a magnetic field of sufficient strength is applied along the wire[22]. Similar results have since been reported by other groups[24, 23]. These experimental observations are qualitatively consistent with the existence of Majorana end-states, and constitute an important first step towards the realization of Majorana fermions in solid-state systems. Given the potential significance of these findings, it is important to build a more quantitative understanding of the experimental system. In particular, we would like to establish whether observed non-quantized ZBP's definitely correspond to thermally broadened peaks from Majorana end-states, or whether they could be produced by some other mechanism.

To this end, we have conducted numerical simulations of tunneling conductance for spin-orbit coupled wires with proximity-induced superconductivity. Our simulations use realistic energy scales appropriate for InSb wires, and consider the various experimentally relevant non-idealities including: multiple occupied sub-bands[46, 1, 2, 58], modest amounts of disorder[1, 3, 60, 59], and non-zero temperature. Our study reveals important features absent in previous studies of clean- or very weakly disordered wires[61, 62, 63, 64].

We find that, at non-zero temperature and in the presence of multiple sub-bands

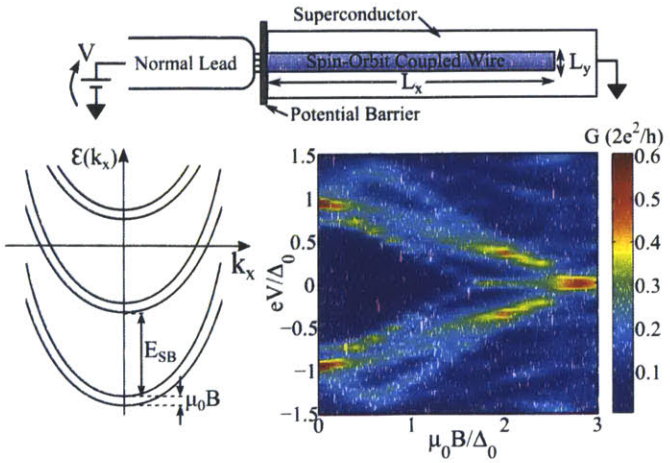

Figure 4-1: (Top) Schematic of tunneling geometry. (Lower Left) Dispersion of sub-bands in multi-band wire. Each sub-band is split by $\mu_0 B$ due to the magnetic field. Majorana fermions appear only when an odd number of sub-bands is occupied. (Lower Right) Color plot of tunneling conductance, G, at finite temperature as a function of applied field $\mu_0 B$ and lead-wire voltage, V, for a multi-band wire with realistic amounts of disorder (see Fig. 4-3 for detailed parameters). A stable zero-bias peak appears despite the fact that there is no Majorana end-state. At lower temperature, the peak is revealed to come from a cluster of low-energy states (see Fig. 4-3).

and weak disorder, zero-bias peaks generically occur even when the wire is in the topologically trivial regime and does not have Majorana end-states. Furthermore, we find that the ZBP's persist even when disorder is sufficiently strong to destroy the topological phase and fuse the Majorana fermions on each side of the wire[1, 3, 60, 59]. Such ZBP's are also found outside the range in chemical potential where Majorana end states are expected in the clean limit, and are produced by ordinary fermion states localized to the wire ends and clustered near the Fermi-energy. These states are in some sense, remnants of Majoranas, and appear and disappear with magnetic field in the same way as true Majorana end-states. Therefore, we argue, that the only way to definitely rule out a non-topological origin to the ZBP is to lower temperature below the thermally broadened regime and observe a truly quantized zero-bias conductance peak, well isolated from other background states.

4.1 Model

We consider a three-dimensional rectangular wire of length L_x along the $\hat{x}$ direction and cross sectional area $L_y \times L_z$ in the yz-plane. The continuum Hamiltonian for the spin-orbit coupled wire without proximity induced superconductivity is:

$$H = \sum_{\mathbf{r}} c^\dagger_{\mathbf{r},\alpha} \left(\frac{-\nabla^2}{2m} - \mu - i\alpha_R \hat{z} \cdot (\boldsymbol{\sigma} \times \nabla) - \mu_0 \mathbf{B} \cdot \boldsymbol{\sigma} \right)_{\alpha\beta} c_{\mathbf{r},\beta} \tag{4.1}$$

Parameter	Symbol	TB Equivalent	InSb Value
Wire Diameter	$L_{y,z}$	$N_{y,z}a$	100nm
Wire Length	L_x	$N_x a$	$\approx$ 2-3μm
Band Mass	m	$(2ta^2)^{-1}$	$0.015m_e$
Spin-Orbit	$E_{\rm so} = \frac{1}{2}m\alpha_R^2$	$U_R = \sqrt{E_{\rm so}t}$	50μeV
Induced SC Gap	Δ_0	Δ_0	250μeV[65]
Mean Free Path	ℓ	(see text)	$\approx 3\mu$m[66]
Min. Temperature	T		$0.03\Delta_0$

Table 4.1: Tight-binding (TB) model parameters, and estimated values for InSb/NbTiN experiment[22]. a denotes lattice spacing in the TB model.

Here α_R is the Rashba velocity, related to the spin orbit coupling by $E_{\rm so} = \frac{1}{2}m\alpha_R^2$, $\mu_= \frac{g\mu_B}{2}$ is the Zeeman coupling to the magnetic field $\mathbf{B}$ taken throughout to point along the wire (in the $\hat{x}$ direction), and Δ_0 is the proximity–induced pairing amplitude.

To model this system, we approximate the continuum Hamiltonian by the following discrete tight binding Hamiltonian, defined on a $N_x \times N_y \times N_z$ site prism:

$$\begin{aligned} H_{\rm tb} = &\sum_{\mathbf{r},\mathbf{d}} c^\dagger_{\mathbf{r}+\mathbf{d},\alpha}\left[-t\delta_{\alpha\beta} - iU_R\hat{z}\cdot\left(\boldsymbol{\sigma}_{\alpha\beta}\times\hat{d}\right)\right]c_{\mathbf{r},\beta} - \\ &- \sum_{\mathbf{r}} c^\dagger_{\mathbf{r},\alpha}\left[\mu\delta_{\alpha\beta} + \mu_0\mathbf{B}\cdot\boldsymbol{\sigma}_{\alpha\beta}\right]c_{\mathbf{r},\beta} + \\ &+ V_{\rm imp}(\mathbf{r})\sum_{\mathbf{r}} c^\dagger_{\mathbf{r},\alpha}c_{\mathbf{r},\alpha} \end{aligned} \tag{4.2}$$

Here, we have included a random impurity potential $V_{\rm imp}(\mathbf{r})$, which is chosen independently for each site, identically distributed according to a Gaussian with variance $\overline{V(\mathbf{r})V(\mathbf{r}')} = W^2\delta_{\mathbf{r},\mathbf{r}'}$, where $\overline{(\cdots)}$ indicates averaging with respect to disorder configuration.

Table 4.1 relates the tight-binding parameters to the continuum model and gives estimated values for InSb nanowires. There is considerable uncertainty in the estimated spin-orbit strength, which was measured without the superconducting layer[65]. Since $E_{\rm so}$ derives solely from the inversion symmetry breaking potential of the substrate-wire and superconductor-wire interfaces, the actual value could be rather different than 50μeV, and one should consider the possibility that $E_{\rm so}$ is much smaller (or larger). The mean-free path from disorder is $\ell = v_F\tau$ where $\tau^{-1} \approx 2\pi\frac{W^2a}{L_yL_z}N(\mu)$ is the elastic scattering rate due to impurities. Here $N(\mu)$ is the 1D density of states at the chemical potential: $N(\mu) = \sum_n \frac{1}{2\pi a\sqrt{t(\mu-\varepsilon_n)}}$, where the sum is over occupied sub-bands labeled by n and having band-bottoms located at energy ε_n. Transport experiments estimate $\ell \approx$ 300nm (again without a superconducting layer)[66]. Since these measurements were done at large source-drain bias, this value reflects a sort of average over the lowest 3-4 sub-bands, and should be taken as a rough guide.

Since only the outer-boundary of the wire is in contact with the superconductor,

there will in general be different proximity induced gaps for different sub-bands. These multi-band effects can be important for reproducing the observed data for InSb wires. There, coherence peaks are observed at energy, $\Delta_0 \approx 250\mu$eV, but non-zero conductance occurs within the proximity induced "gap". We note that the experiment [22] shows large sub-gap tunneling conductance at $B = 0$. While the coherence peaks of various sub-bands are Lorentz-broadened by coupling to the leads, our sub-gap conductance is generally much smaller than the data.[1] Below we focus on the magnetic field induced structures.

4.2 Tunneling Conductance

We use the iterative transfer matrix method to construct the Green's function for the end of the wire, and compute the scattering matrix from the Green's function[68, 56]. Experimentally, the wires are terminated by a large gap superconductor and only Andreev reflection contributes to tunneling current:

$$I(V) = \frac{2e^2}{h} \int d\varepsilon \left(f(\varepsilon - eV) - f(\varepsilon)\right) \mathrm{tr}|\hat{r}_{eh}(\varepsilon)|^2 \tag{4.3}$$

where $\hat{r}_{eh}(\varepsilon)_{ij}$ is the electron-hole part of the reflection matrix from channel i to channel j in the lead, and f is the Fermi distribution. Throughout, we take the lead to have position and energy independent density of states $N_0 = 1/(\pi v_F)$, and model the tunneling barrier by a weak hopping link with hopping strength t_{LW}.[2] The lead-wire coupling is characterized by $\gamma_{\mathrm{LW}} = N_0|t_{\mathrm{LW}}|^2$.

Proximity induced superconductivity is modeled by coupling the boundary of each cross-section in the yz-plane to an infinite superconductor, producing the self-energy[36, 3]:

$$\Sigma_{\mathrm{SC}}(\omega_+, y, z) = \hat{\mathcal{P}}_{\mathrm{edge}} \frac{\gamma_{\mathrm{SC}} \left(\omega_+ - \Delta_B \tau_3\right)}{\sqrt{\Delta_B^2 - \omega_+^2}} \tag{4.4}$$

The projection $\hat{\mathcal{P}}_{\mathrm{edge}}(y, z) = 1$ if (y, z) is on the outer edge of the wire ($y \in \{0, N_y\}$ or $z \in \{0, N_z\}$) and is zero otherwise. Here, $\omega_+ = \omega + i\eta$ where η positive and infinitesimal, τ_3 is the z-Pauli matrix in the Nambu/Gorkov particle-hole basis: $\Psi(\mathbf{k}) = \left(c_{\mathbf{k},\uparrow} \quad c_{\mathbf{k},\downarrow} \quad -c^\dagger_{-\mathbf{k},\downarrow} \quad c^\dagger_{\mathbf{k},\uparrow}\right)^T$, where $c_{k,s}$ destroys an electron with momentum $\mathbf{k}$ and spin $s \in \{\uparrow, \downarrow\}$. Δ_B is the pairing gap of the adjacent bulk superconductor $\gamma_{\mathrm{SC}} = \pi N_B(0)|\Gamma|^2$ is the strength of coupling between the wire and superconductor, $N_B(0)$

[1] Important effects, not accounted for in our treatment, could in principle, arise due to localization effects in the bulk superconductor, which have been observed[67] to give rise to sub-gap density of states in the strongly disordered NbTiN films used in Ref. [22]. However, such effects are expected to be relatively weak for low energy scales on the order of the induced gap, Δ_0 which is $\ll$ than Δ_B, the bulk superconductor gap.

[2] This weak link provides an energy-independent transmission, and is conceptually simpler[64] than the smooth barrier used in Ref. [22]. However, we caution that quantiative details, such as the magnitude of the tunneling current for states above the superconducting gap, depend sensitively on the nature of the tunneling barrier and may not match in every detail.

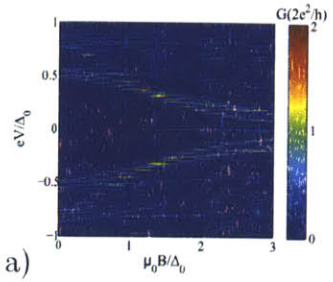

Figure 4-2: (Left) Zero-bias peak for a true Majorana state in a long, clean wire, ($N_y \times N_z \times N_x = 6 \times 5 \times 360$, or about twice as long as the wires in [22], and $W = 0$). Tight-binding parameters: $t = 36.5$, $U_R = 2.7$, $\gamma_{SC} = 2$, $\gamma_{LW} = 0.3$, and $\mu = -175.2$ corresponding to 5 occupied sub-bands. Δ_0 is superconducting gap for the highest occupied sub-band, and is identified by the magnetic field for which the Majorana appears.

is the density of states of the bulk superconductor near the Fermi-surface, and Γ is the wire-superconductor tunneling amplitude.

4.2.1 Conditions for Majorana End-states

In a multiband wire, when $\mu_0 B > \Delta_0$, one can think of each sub-band as contributing a Majorana end-state which then mix. For an even number of occupied sub-bands, the Majoranas fuse into ordinary fermions and are pushed away from zero-energy. By contrast, for an odd number of occupied sub-bands a single Majorana state always remains at zero-energy[1]. More quantitatively, to observe a Majorana, μ must fall within specific intervals of size $\approx \pm|\mu_0 B - \Delta_0|$. In [22] ZBP's are observed for $\mu_0 B \gtrsim \Delta_0 \approx 250\mu$eV. Indicating that Majorana end-states can exist only in narrow regions of μ of size $\approx 250\mu$eV, or $\approx \frac{1}{10}$ of the typical sub-band spacing $E_{sb} \approx 2.5$meV.

Problems can arise for short wires[20, 61]. If the wire is not sufficiently long, then the Majorana states on each end of the wire can overlap, splitting into ordinary fermion states. For example, the InSb wires in [22], had aspect ratios of $L_x \approx 20 - 30L_y$. Tight-binding simulations of such a wire, with the parameters as in Table 4.1, show that Majorana end-states hybridize with splitting of a few percent of Δ_0 even for clean wires. This issue is exacerbated by disorder, which is strongly pair-breaking[3, 59, 60] and reduces the gap protecting Majorana end-states, allowing them to spread out and hybridize more strongly. Indeed, realistic amounts of disorder corresponding to the estimated ℓ readily destroy the quantized conductance peak from Majorana end-states.

Despite these issues, ZBP's are still observed in InSb wires. This suggests that ZBP might occur rather generally and may not necessarily tied to the presence of zero-energy Majorana end-states. Below, we will show that this is indeed the case, and that stable ZBP's frequently appear without Majorana states.

4.2.2 Ideal Tunneling Signatures

To start, we first consider an idealized case, showing quantized Majorana peaks. Fig. 4-2 shows conductance data for a long, perfectly clean wire of length $N_x = 360$ in the center of the 3rd topological region (i.e. with 5 occupied sub-bands including spin). This case has been previously discussed[57, 21, 56]. We note that, even for a clean wire, the observation of this quantized peak requires wires 2-3 times longer than those used in [22], and an order of magnitude larger than in [23].

4.2.3 Disorder Induced Tunneling Peaks

Under realistic experimental conditions for semiconducting wires, disorder is expected to play an important role[3, 59, 60]. Disorder can produce zero-bias peaks by two different mechanisms. The most important effect for our purposes, is that disorder reduces the mini-gap to end-states from other occupied sub-bands. In the absence of disorder, these end-states are pushed up above induced gap where they get absorbed by a continuum of extended states. In a field, disorder reduces the mini-gap splitting, causing these end-states to cluster near zero-energy. Our simulations show that, that clusters emerging from mini-gap states frequently remain localized near the end of the wire, and at temperature larger than the mini-gap splitting merge into a single ZBP.

In addition, the pair-breaking effects of disorder can create localized sub-gap states bound to impurities[70, 71]. ZBPs due to impurity bound-states are distinct fromt those arising from a small mini-gap: 1) impurity bound-states are not localized to the wire-ends and can occur throughout the wire; 2) these bound-states require special resonant disorder configurations to produce near zero-energy states which happens comparitively infrequently, and 3) impurity bound-states tend to produce only a single low-energy state, whereas the generic ZBPs observed in our simulations consist of a cluster of multiple states.

Fig. 4-3d. shows a color plot of zero-bias conductance for tunneling not just into the end of the wire, but also into various positions along the wire. The modest amount of disorder included here ($W = 22$) corresponds to a long, experimentally realistic mean-free path ($\ell \approx 300$nm), but is nevertheless sufficient to destroy Majorana end-states. Despite this, zero-bias peaks frequently appear. These peaks are predominately localized at the wire ends, and are typically stable over intervals of $\Delta\mu \approx \Delta_0$ although they are no-longer tied to the topological region $|\mu - \mu_3| < \sqrt{(\mu_0 B)^2 - \Delta_0^2}$. Fig. 4-3a. and b. show a typical example of this non-topological ZBP developing as a function of applied field. At $T = 0$ (a), one can resolve the ZBP into multiple peaks near zero-energy, however at $T = 0.03\Delta_0$ (b) the peaks are smeared into a single ZBP.

These peaks appear and disappear under very similar magnetic field conditions as true Majorana states would: 1) they appear only when $\mu_0 B \gtrsim \Delta_0$ when pair-breaking effects or disorder become important, 2) they disappear when the field is rotated to point perpendicular to the wire (see Fig. 4-3)c. However, unlike ZBP's tied to Majorana states, these non-topological ZBP's appear commonly throughout the range of chemical potentials between adjacent sets of sub-bands, meaning that

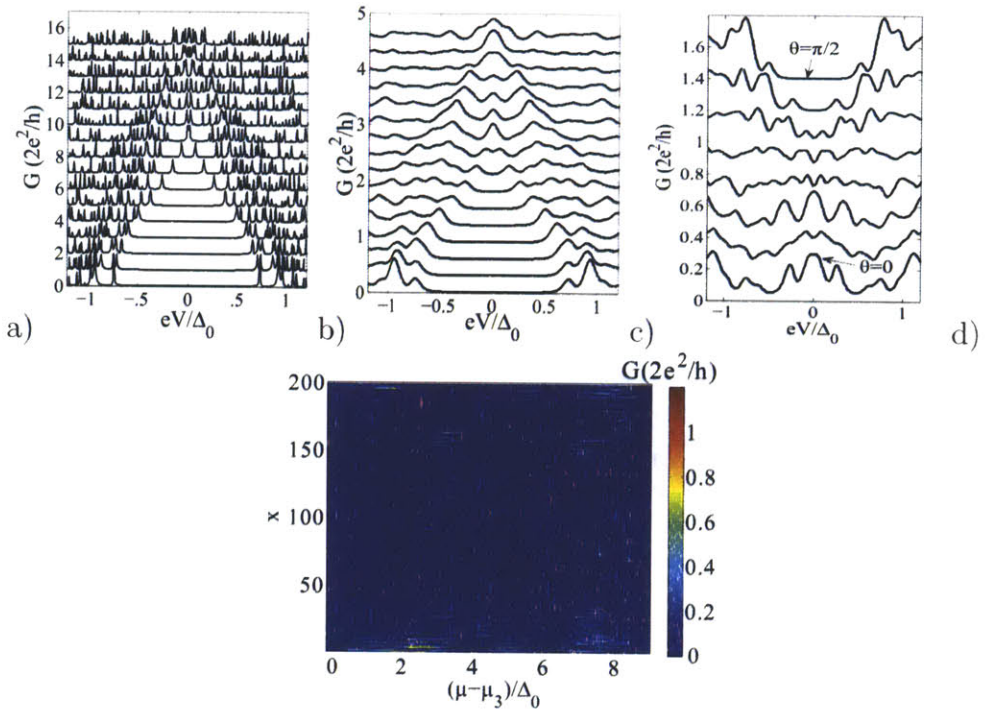

Figure 4-3: (a) and (b) Conductance traces for a disordered multi-band wire as a function of $\mu_0 B$ for $T = 0$ (a) and $T = 0.03\Delta_0$ (b). From bottom to top $\mu_0 B$ ranges from 0 to $3\Delta_0$ in steps of $0.2\Delta_0$ (curves are offset for clarity). $\mu = -172$ corresponding to 6 occupied sub-bands (including spin). ZBPs appear for $\mu_0 B \approx \Delta_0$ just as for a Majorana end-state, despite having an even number of occupied sub-bands. Wire dimensions are $N_y \times N_z \times N_x = 6 \times 5 \times 180$. Tight-binding parameters: $W = 12$, $t = 36.5$, $U_R = 2.7$, $\gamma_{SC} = 2.5$, and $\gamma_{LW} = 0.3$. (c) Angle dependence of non-topological ZBP is similar to that of a true Majorana derived ZBP (curves are offset for clarity). θ measures angle of $\mathbf{B}$ and the x-axis in the x-y plane. (d) ZBPs occur predominately at the ends of the wire, as demonstrated in this plot showing the spatial profile of zero-bias conductance for tunneling into different positions along the x-direction of a wire with $\mu_0 B = 2\Delta_0$, $T = 0.03\Delta_0$ and μ varied between 5-6 sub-bands ($\mu_3 = -175.2$ is the center of the third topological region). All other parameters are the same as (a) and (b) except $W = 22$, and $N_x = 200$.

they would be more readily observed without strongly tuning μ (see Fig. 4-3d).

4.2.4 Reduction of the Mini-Gap by Disorder

There are two salient features of the disorder induced ZBPs reported here: 1) they predominately occur only at the end of the wire, as seen in Fig. 4-4 which shows the spatial profile of tunneling conductance from tunneling into different points along the wire. 2) The disorder induced ZBPs tend to appear as clusters of multiple low-energy states rather than a single low-energy state (as would be expected, for instance for an impurity bound-state that happened to be accidentally close to zero energy).

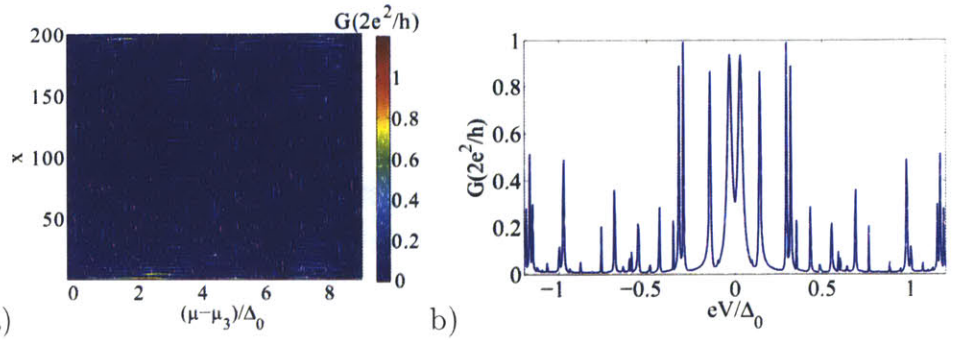

Figure 4-4: (c) a spatial map of conductance as a function of position along the wire and chemical potential. The other tight-binding parameters are: $w = 22$, $t = 36.5$, $U_R = 2.7$, $\mu_0 B = 2\Delta_0$. (b) Conductance as a function of voltage showing disorder induced zero-bias peaks for $\mu - \mu_3 = 2.2\Delta_0$.

For these two reasons, we attribute the observed disorder induced ZBPs to a strong suppression of the mini-gap to localized end-states. The structure of end-states in a multi-band wire can be most easily understood by initially ignoring the spin-orbit coupling along the y-direction: $\alpha_R k_y \sigma_x \rightarrow 0$[74]. In this limit, the different sub-bands remain uncoupled even in a finite length wire, and each occupied sub-band contributes a Majorana zero-mode at each end of the wire. Re-introducing the spin-orbit coupling in the y-direction mixes the different end-states, and splits them away from zero-energy in pairs. For an even number of sub-bands, no states are left at zero-energy after the inter-band mixing is included, whereas for an odd number of sub-bands a single unpaired Majorana zero-mode remains.

The size of the energy splitting of the end-states, known as the mini-gap spacing δ, depends on the details of the particular model under consideration. For a clean spin-orbit coupled wire, sub-bands come in time-reversed pairs that are split by the magnetic field. When both sub-bands of a time-reversed pair are occupied, the spatial profile of their end-state wave-functions is very similar, and their end-states strongly hybridize with splitting leading to a large mini-gap spacing, $\delta \approx \Delta_{so} > \Delta_B$[74]. For a clean spin-orbit coupled wire, the mini-gap spacing actually exceeds the proximity induced superconducting gap to bulk extended states, meaning that no sub-gap states are left at the end (aside from a single zero-energy Majorana mode when the number of sub-bands is odd).

However, in the presence of disorder and a magnetic field, the spatial profile of the end-state wave-functions for different sub-bands can be very different even for sub-bands related by time-reversal. In this case, disorder will suppress the mini-gap scale δ. In this appendix, we give a simple estimate of the size of this reduction.

Consider the case where $2N$ sub-bands are occupied. Since the spin-orbit coupling is proportional to k_F, the deeply occupied sub-bands will be strongly paired and will not contribute sub-gap end-states. Therefore, we focus our attention on bands $2N$ and $2N-1$, whose spin-wave-functions are related by time-reversal. In the absence of transverse spin-orbit coupling, $H_{\rm so,y} = \alpha_R k_y \sigma_x$, sub-bands $2N$ and $2N-1$ contribute end-states $|\phi_\sigma\rangle$ and $|\phi_{\bar\sigma}\rangle$ respectively, where $\phi_\sigma(x) \sim \frac{1}{\sqrt{\xi_0}} e^{-x/\xi_0}$, and ξ_0 is the coherence length for the $2N^{\rm th}$ sub-band. In the absence of disorder, turning on $H_{\rm so,y}$, mixes these states giving rise to mini-gap spacing $\delta \approx E_{\rm so}$. The presence of a random impurity potential $V(x)$ alters the spatial profile of these wavefunctions by virtually admixing the end-state with extended states, $|a,\sigma\rangle$. Incorporating this correction to order V^2 gives:

$$|\phi_\sigma\rangle \to |\tilde\phi_\sigma\rangle \approx |\phi_\sigma\rangle \left(1 - \frac{1}{2}\sum_a \frac{|V_{a,\sigma}|^2}{E_{a,\sigma}^2}\right) + \sum_a \frac{V_{a,\sigma}}{E_{a,\sigma}} |a,\sigma\rangle \tag{4.5}$$

Here, $V_{a,\sigma} = \langle a,\sigma|\phi_\sigma\rangle$, and the quantity in parantheses in the first term maintains the normalization of the wave-functions.

The mini-gap splitting, averaged with respect to disorder, assuming delta-function correlated disorder: $\overline{V(x)V(x')} = W^2\delta(x-x')$, becomes:

$$\begin{aligned}\bar\delta = \langle\tilde\phi_{\bar\sigma}|H_{\rm so,y}|\tilde\phi_\sigma\rangle &\approx \langle\phi_{\bar\sigma}|H_{\rm so,y}|\phi_\sigma\rangle \left[1 - \sum_{a,\sigma}\frac{\overline{|V_{a,\sigma}|^2}}{2E_{a,\sigma}^2}\right] + \sum_{a,b}\frac{\overline{V_{a,\bar\sigma}^* V_{b,\sigma}}}{E_{a,\bar\sigma}E_{b,\sigma}}\langle a,\bar\sigma|H_{\rm so,y}|b,\sigma\rangle \\ &\equiv \delta_0 + \delta_V \end{aligned} \tag{4.6}$$

where $\delta_0 = \langle\phi_{\bar\sigma}|H_{\rm so,y}|\phi_\sigma\rangle$ is the mini-gap in the absence of disorder. Here we have ignored coherence factors associated with the particle-hole structure of BCS theory, as these will not play an important role.

We approximate the extended states $|a,\sigma\rangle \to |k,\sigma\rangle$ as simple plane-waves with energy $E_{k,\sigma} \approx \sqrt{\left(\frac{k^2}{2m} - \mu_\sigma\right)^2 + \Delta_B^2}$, with $\mu_\sigma = \mu + \sigma\frac{\mu_0 B}{2}$ ($\sigma = \pm$) and linearize the dispersions near the Fermi-level. With these approximations, it is straightforward to compute that the fractional correction to the typical mini-gap:

$$\frac{\delta_V}{\delta_0} \approx -\left(\frac{\mu_0 B}{\Delta_B}\right)^2 \frac{1}{\Delta_B \tau} \tag{4.7}$$

The proportionality to magnetic field can be understood by noting that in the absence of field, the disorder effects both sub-bands identically and does not impact the overlap of their end-sates. The negative sign indicates that δ is always reduced by disorder, which agrees with the expectation that having randomly different spatial structure will reduce the end-state mixing.

From this estimate, we see that the disorder strength required to substantially reduce the mini-gap is comparable to that required to suppress the bulk gap: $\Delta_B \tau \approx 1$. However, since the prefactor $\left(\frac{\mu_0 B}{\Delta_B}\right)^2$ is necessarily larger than unity, the collapse of the mini-gap due to disorder may precede the collapse of the bulk superconducting gap.

The reduction of the mini-gap due to disorder explains a few important features of the observed ZBPs: 1) The mini-gap states are really just weakly paired Majoranas, which are necessarily tied to the end of the wires. 2) A small cluster of mini-gap states always produces at least two low-energy states, which agrees with the simulations that show ZBPs as coming from clusters of low-energy states.

4.2.5 Additional Structure Accompanying Disorder Induced Peaks

We find that, like a true Majorana, the formation of a zero-bias peak is accompanied by a feature that appears as a gap closing. As was pointed out in [73], the collapse of the superconducting gap is more visible in the tunneling conductance than for a true Majorana.

In addition, the detailed sub-structure of the conductance plot in Fig. 1 of the main text is more complicated than that for the true Majorana state. In Fig. 1, there appear to actually be two gaps collapsing, one near $\mu_0 B \approx 1.5\Delta_0$ and the other at $\mu_0 B \approx 2.5\Delta_0$. Furthermore, the experimental data of Mourik et al. appears to show a stable superconducting coherence peak whose energy varies only very slowly as a function of field, which is absent in Fig. 1. In principle, one might expect that the details of such additional substructure may be used to distinguish the disorder induced zero-bias peaks from true Majorana peaks.

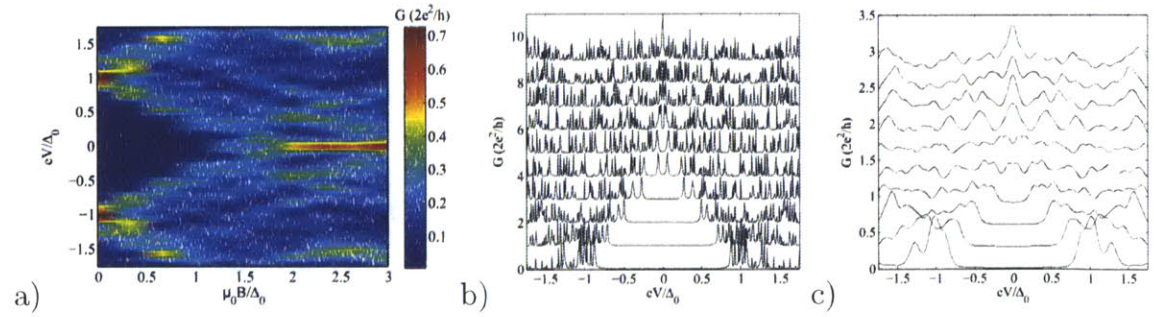

Figure 4-5: a) $T = 0.03\Delta_0$ conductance as a function of $\mu_0 B$; b) corresponding zero-temperature conductance curves for values of $\mu_0 B$ ranging from 0 to $3\Delta_0$ in steps of $\Delta_0/3$ and c) $T = 0.03\Delta_0$ curves (curves offset for clarity). Simulation parameters: $N_x \times N_y \times N_z = 6 \times 5 \times 180$, $t = 36.5\Delta_0$, $\mu = -133.7\Delta_0$ (12 occupied sub-bands), $\gamma_{SC} = 2\Delta_0$, $W = 24\Delta_0$.

However, we caution against drawing strong conclusions based on such fine details. Firstly, the large background conductance seen in the Mourik et al. experiments would likely mask the sort of gap collapsing features shown in Fig. 1. Secondly, the smooth

tunneling barrier used in these experiments can have a strongly bias-dependent transmission, which can suppress the visibility of sub-gap tunneling conductance features. Finally the structure of these gap collapsings depends very sensitively on many details of the system.

For example, Fig. 4-5 shows another disorder induced zero-bias peak for a 12-band wire. In this figure, there is only a single gap collapsing feature, which is substantially less visible than the zero-bias peak. Furthemore, there are stable conductance peaks around $eV \approx \pm 1.5\Delta_0$ that be mistaken for the stable coherence peaks seen in experiments.

4.3 Implications for Experimental Detection of Majorana States

We have shown that, under experimentally realistic conditions for semiconducting wires with rather modest amounts of disorder, Majorana end-states are destroyed and do not give rise to quantized ZBPs. Nevertheless, at finite temperature, ZBPs of a non-topological origin often appear due to the effects of disorder, which lead to clusters of low-energy states localized near the wire end. These non-topological ZBPs are typically stable with respect to variations of chemical potential and magnetic field, and appear and disappear under nearly identical conditions to those of true Majorana peaks.

These results strike a note of caution for interpreting recent experimental evidence of Majorana states in tunneling data[22, 24, 23]. In order to truly identify Majorana end-states and rule out a non-topological origin of observed ZBPs, it is crucial to push to lower temperatures, and observe a quantized conductance peak. At sufficiently low temperature non-topological ZBPs will reveal themselves as clusters of states, and can be distinguished. Spurious disorder induced peaks can also be ruled out by more complicated measurements, such as the 4π Josephson effect[20], which does not survive once Majoranas are destroyed by disorder[69].

Our simulations indicate that to realize Majorana states in semiconductors, one likely needs to produce substantially longer and cleaner wires. These difficulties suggest that it may be beneficial to seek materials with larger spin-orbit coupling[5].

Part II

Electron Topological Insulators

The previous Part of this thesis focused on routes to engineering topological superconductors with non-Abelian defects carrying Majorana zero-mode bound-states. There, topological superconductivity was obtained by coupling a helical 1D or 2D metal to an ordinary s-wave superconductor. In these lower-dimensional materials we had to work quite hard to arrange a special combination of couplings to produce a metal with definite helicity. In particular, it was essential to break time-reversal symmetry to remove electrons with the opposite helicity from the low-energy spectrum.

In contrast, 2D helical metals emerge quite naturally at the surface of time-reversal symmetric bulk-3D topological band-insulators (TBIs). This property makes 3D-TBIs a natural platform for the pursuit of Majorana states. This is but one of many interesting properties of 3D-TBIs. This Part of the thesis delves further into the 3D electron topological insulators.

We start by fitting TBIs into the general conceptual framework of symmetry-protected topological phases of matter (SPTs). SPTs are insulating phases of matter without bulk topological order (TO) that cannot be smoothly connected to a trivial insulator in the presence of a certain set of symmetries. The barrier to smoothly deforming an SPT into a trivial band-insulator is some variety of non-trivial surface state. For example, when symmetry is preserved, the free-electron TBI surface is a helical metal. Given this property, suppose we could deform the bulk of the TBI to a trivial band-insulator while preserving symmetry. This would result in a strictly 2D helical metal that used to be the surface of the bulk TI. However, we know that such a helical metal cannot be produced in strictly 2D system with TR symmetry, providing a contradiction.

On the other hand, when symmetry is broken at the surface, for example by introducing a strong Zeeman field or superconducting pairing, the surface can be gapped. However, when only one of either TR symmetry or $U(1)_C$ charge-conservation is broken at the surface, the surface state still inherits non-trivial properties from the unconventional bulk. For example, the superconducting TI surface has non-Abelian vortices with Majorana-fermion core modes, which cannot be accomplished in a 2D system while preserving TR symmetry.

In addition to having either a gapless symmetric surface-state or a gapped symmetry broken state, there is a third possibility: a 3D SPT may have a fully gapped and fully symmetric surface state with 2D intrinsic topological order[84, 85, 7, 75, 76, 77]. Since the bulk SPT is not deformable to a trivial insulator in the presence of symmetry, a symmetric surface-topologically order (STO) termination of the bulk TI must have non-trivial properties that cannot be produced in a purely 2D system. Generally, the STO has the same topological order as a purely 2D system, but with symmetry implemented in a way that is not allowed in strict 2D. In the first Chapter of this Part, we construct an STO for the electron TBI.

For the ordinary electron TBI the heavy-machinary of STO may seem excessively complicated, since there is a much simpler band-structure understanding. However, a symmetric STO phase serves as a complete non-perturbative definition of the bulk phase that does not rely on the assumption of weak interactions. This provides a powerful perspective that will enable us to classify all possible interacting phases of 3D electron TIs with TR symmetry. In particular, we show that in addition to the

familiar TBI, there are 6 additional electron TIs arising from strong inter-electron interactions that cannot be understood from a simpler band-structure picture.

Finally, we close this Part of the thesis by describing some experimental probes to detect the presence of Majorana states in the unconventional TBI surface state.

Chapters 5, 6, and 6 are adapted directly from Refs. [7, 8, 9] respectively, with only slight modifications and added introductory material.

Chapter 5

Symmetry-Preserving Surface Topological Order

The Fu-Kane-Mele electronic TI (eTI)[82] is the first known 3D example of an SPT phase. Its non-trivial surface states are protected by bulk time-reversal symmetry (TRS) and charge conservation ($U(1)_C$) symmetry. If either of these symmetries is broken in the bulk, the eTI can be smoothly deformed into a trivial insulator. It is, by now, well known that the surface can either be 1) a gapless, symmetry-preserving state, or 2) a gapped state that breaks one (or both) of TRS and $U(1)_C$. For some time, it was implicitly assumed that these options exhausted the possible surface phases. Indeed these are the only possibilities accessible in a weakly interacting description of the surface. However in the presence of strong correlations other options for the surface may become available. In particular, we will show that it is possible for the eTI surface to be both fully gapped and preserve all symmetries. The price to pay for having a gapped and symmetric surface is that the surface develops intrinsic topological order (even though the bulk does not). We describe this surface topologically ordered state of the eTI and show that it has non-Abelian quasiparticles. The physical symmetries are realized in this surface topological ordered state in a manner forbidden in a strictly two dimensional insulator with the same topological order.

The prime impetus for our study comes from recent progress in describing bosonic SPT phases in three dimensions. For bosons, interactions are essential to obtain an insulator. Consequently the study of boson SPTs is necessarily non-perturbative in the interaction strength. For such bosonic SPT phases, it was shown that the surface can be both gapped and symmetry preserving[84] if it possesses intrinsic two-dimensional surface topological order (STO). This STO however realizes symmetry in a manner prohibited in strictly two dimensional systems. The STO provides a particularly simple non-perturbative insight into the bulk SPT phase. Indeed targeting such an STO is a useful conceptual tool for constructing SPT phases[85, 86], and can provide very general constraints on lower-dimensional phases[84, 85]. In light of the simplicity and power of the STO as a surface termination of strongly interacting bosons SPTs it is natural to construct the STO appropriate for the fermionic topological insulator. We note that for fermionic topological superconductors in 3D protected by TRS very recently possible STO phases were constructed[87].

Our strategy is to start from the TR-symmetric non-Abelian surface superconductor [34], and to restore $U(1)_C$ without destroying the superconducting gap by proliferating vortices in the superconducting phase. The minimal $\frac{hc}{2e}$ superconducting vortices cannot be directly condensed due to their non-Abelian statistics arising from unpaired core Majorana modes. It turns out that, despite being Abelian, the doubled $\frac{hc}{e}$ vortex is a semion and can also not be condensed while preserving TRS. Identifying an appropriate vortex field that can be condensed to disorder the superconductor without breaking TRS requires some care. We find that there are 4-fold ($\frac{2hc}{e}$) vortex fields that can be condensed without breaking any symmetries as a minimal route to producing the STO starting from the surface superconductor.

The resulting phase has identical topological order and charge assignments as the 2D Moore-Read quantum Hall state[32] accompanied by an extra neutral semion. However, in strictly two-dimensions this topological phase cannot be realized in a TR symmetric manner. We will show that the fact that the eTI can realize this TO while preserving TRS provides a complete, non-perturbative definition of the bulk eTI.

5.1 Vortices in the eTI Surface Superconductor

Starting from the superconducting surface of the eTI, we know that there should be some obstruction to proliferating superconducting vortices to form an ordinary band-insulator, and indeed the $\frac{hc}{2e}$-vortices in the superconducting TI surface-state are non-Abelian objects that cannot be directly condensed[34]. Since $\frac{hc}{e}$ vortices do not have an unpaired Majorana core state, they are Abelian, and one is tempted to follow the above construction to obtain a $\mathbb{Z}_2$ topologically ordered state by proliferating $\frac{hc}{e}$ vortices.

However, this naive approach fails to produce a symmetric STO state. It turns out that in the eTI surface SC, $\frac{hc}{e}$ vortices have semionic self-statistics[1], and cannot be condensed without breaking TRS. The $\frac{3hc}{2e}$ vortices again have unpaired Majorana cores, and are non-Abelian. We show however that there are $\frac{2hc}{e}$ vortices that are bosonic. Therefore, the minimal route to restoring $U(1)_C$ is to condense such bosonic $\frac{2hc}{e}$ vortices.

We now establish the Abelian statistics of $\frac{hc}{e}$ and $\frac{2hc}{e}$ vortices in the surface-superconductor, by arguing based on the Θ-term electromagnetic response of the bulk.

5.1.1 Bulk Argument for Semionic Statistics of $\frac{hc}{e}$ Vortices

A useful conceptual device for what follows is to modify the problem by coupling the electrons to a weakly fluctuating dynamical compact $U(1)$ gauge field. It is well known that the topological insulating bulk leads to a Θ-term, with $\Theta = \pi$, in the effective action (apart from the usual Maxwell term) for this gauge field obtained by

[1] To precisely define vortex statistics, it is necessary to consider a gauged $U(1)_C$ symmetry (as is the case for real electrons coupled to the physical electromagnetic field, which has very weak fluctuations)

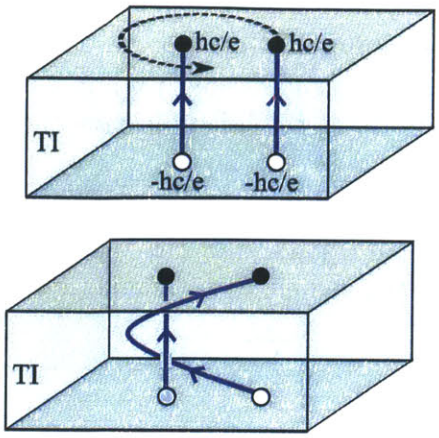

Figure 5-1: Exchanging two $\frac{hc}{e}$ vortices at the superconducting surface of a TI slab (top panel) leads to a linking of their magnetic field lines, which gives a phase of -1, demonstrating that $\frac{hc}{e}$ vortices are semionic.

integrating out the electrons. Also well-known is the effect of this Θ term: a unit strength magnetic monopole of this $U(1)$ gauge field acquires electric charge $\frac{1}{2}$ (the Witten effect[90]). Now imagine tunneling such a monopole from the vacuum into the bulk of the (gauged) topological insulator. Such a tunneling process will leave behind at the surface a $\frac{hc}{e}$ vortex. This implies that the $\frac{hc}{e}$ vortex field in the vortex Landau-Ginzburg theory formally also has electric charge $\frac{1}{2}$. As a composite made of charge-1/2 and 2π flux it is natural to expect that this vortex will have semionic statistics.

To demonstrate the semionic statistics of $\frac{hc}{e}$ vortices, consider a slab of bulk eTI with a top and bottom interface with a trivially insulating vacuum. Then create a pair of $\frac{hc}{e}$ vortices on the top surface and a pair of $-\frac{hc}{e}$ vortices on the bottom surface. Since the gauge field A^μ is free, except at the superconducting surface, closed magnetic flux lines carrying $\frac{hc}{e}$ flux are condensed in the bulk and in the vacuum. Since the surface is superconducting, a magnetic flux tube can only penetrate the surface at a vortex. For the vortex configuration of Fig. 5-1, there are only two magnetic flux lines that leave the TI bulk. Let us consider just one representative flux line configuration, as shown in Fig. 5-1. Next consider dragging one of the $\frac{hc}{e}$ vortices on the top surface all the way around the other, as shown in Fig. 5-1 without moving the $-\frac{hc}{e}$ vortices on bottom surface. The new magnetic flux configuration differs from the initial one by a single linking of the magnetic flux lines that thread the vortices.

Due to the bulk topological Θ-term for A:

$$\mathcal{L}_\Theta = i\frac{\varepsilon^{\mu\nu\lambda\rho}}{8\pi}\partial_\mu A_\nu \partial_\lambda A_\rho \tag{5.1}$$

this linking produces a phase of -1 relative to unlinked configurations. This phase can be computed directly from $\mathcal{L}_\Theta$ by considering any convenient choice of A with a linked vortex line. Alternatively, one can imagine creating a linked field line configuration

in the bulk by starting with an infinite flux line, creating a monopole anti-monopole pair and dragging the monopole around the flux line before annihilating it with the anti-monopole. Since monopoles in the TI bulk have charge $\frac{e}{2}$, dragging one around a 2π-flux line contributes phase $e^{2\pi i \cdot \frac{1}{2}} = -1$.

We have illustrated this -1 phase for a particular magnetic field line configuration. More generally, the ground-state, $|\Psi_{\rm EM}\rangle$, of the bulk gauge field, A^μ, is a quantum-superposition of various configurations, $\mathcal{C}$, of magnetic flux lines:

$$|\Psi_{\rm EM}\rangle = \sum_{\mathcal{C}} (-1)^{L_\mathcal{C}} \Psi_0(\mathcal{C}) |\mathcal{C}\rangle \tag{5.2}$$

weighted by phase $(-1)^{L_\mathcal{C}}$, where $L_\mathcal{C}$ is the number of linked loops in the configuration $\mathcal{C}$, and by amplitude, $\Psi_0(\mathcal{C})$, that is determined by the non-topological dynamical terms for the gauge-field.

This follows directly from computing the wave-function for a given configuration, $\mathcal{A}(\mathbf{r})$, from the (imaginary time) path integral:

$$\begin{aligned} \Psi[\mathcal{A}] &= \langle \mathcal{A}|\Psi\rangle \\ &= \int D[A]\big|_{A_\mu(\mathbf{r},t=0)=\mathcal{A}(\mathbf{r})} e^{-\int_{-\infty}^{0} d\tau \int d^3r \mathcal{L}_\Theta[A]} \\ &\sim e^{i\int d^3r \frac{\varepsilon^{\mu\nu\lambda}}{8\pi} \mathcal{A}_\mu \partial_\nu \mathcal{A}_\lambda} = (-1)^{L_{\mathcal{C}[\mathcal{A}]}} \end{aligned} \tag{5.3}$$

we see that the resulting wave-function contains a Chern-Simons (CS) term which just counts the linking number of flux lines of $\mathcal{A}$.

For any configuration of closed bulk field-lines, $\mathcal{C}$, the two-fold exchange of $\frac{hc}{e}$ introduces a single extra linking number. Therefore the two-fold exchange of $\frac{hc}{e}$ vortices produces phase (-1), indicating that a single exchange produces phase $\pm i$; the $\frac{hc}{e}$ vortices are semionic. Let us denote the quantum field that creates a $\frac{nhc}{e}$ vortex with electric charge q by $\Phi_{n,q}$. With this notation $\Phi_{1,\frac{1}{2}}$ is a semionic $\frac{hc}{e}$ vortex with charge $\frac{1}{2}$. The field $f\Phi_{1,\frac{1}{2}}$ produces a neutral fermion bound to this vortex and hence creates an antisemionic $\frac{hc}{e}$ vortex with charge $\frac{1}{2}$. These two $\frac{hc}{e}$ vortices will play an important role below.

Let us now consider strength-4 ($\frac{2hc}{e}$) vortices. A similar argument as above shows that $\frac{2hc}{e}$ vortices are either bosonic or fermionic (fermionic and bosonic $\frac{2hc}{e}$ vortices can be interchanged by binding a neutral f quasi-particle). Note that if we combine two charge-1/2 semionic $\frac{hc}{e}$ vortices, we end up with a charge-1 bosonic $\frac{2hc}{e}$ vortex. *i.e* $(\Phi_{1,\frac{1}{2}})^2 = \Phi_{2,1}$. An electrically *neutral* $\frac{2hc}{e}$ vortex may be obtained by considering the combination $c\Phi_{2,1}$, *i.e* by removing an electron from the charge-1 $\frac{2hc}{e}$ vortex. Clearly this is a fermion.

These strength-4 vortices at the surface correspond in the bulk to strength-2 monopoles. At $\Theta = \pi$, such monopoles always carry integer electric charge. We will denote bulk dyons with magnetic charge n and electric charge q by (n, q). These correspond to surface vortices created by $\Phi_{n,q}$. It is readily seen that the bulk $(2, 1)$ dyon (at $\Theta = \pi$) is a boson while the electrically neutral strength 2 monopole (the

$(2,0)$ particle) is clearly a fermion. This is in complete accord with our discussion of surface vortices above. Arguments using bulk monopole properties to constrain surface physics were also recently used for boson topological insulators in Ref. [91].

To disorder the surface superconductor we need to identify bosonic vortices which we can then condense. Though the $\frac{2hc}{e}$ vortex with electric charge-1 seems like a candidate it is problematic. To preserve time reversal we should clearly also condense (with equal amplitude) the $-\frac{2hc}{e}$ vortex with electric charge 1. But then the resulting state also has a condensate of ordinary Cooper pairs so that it is still a superconductor (albeit an exotic one). The neutral $\frac{2hc}{e}$ vortex described above is a fermion and hence cannot condense. Fortunately we also have a different neutral fermion in our theory - the spinon (the f particle). By binding f to the fermionic $\frac{2hc}{e}$ vortex we obtain an electrically neutral bosonic $\frac{2hc}{e}$ vortex. Equivalently this bosonic neutral $\frac{2hc}{e}$ vortex may be viewed as being obtained from the charge-1 bosonic $\frac{2hc}{e}$ vortex by binding to b (*i.e* by removing a chargon). This neutralizes the charge but keeps the statistics as bosonic. We are then free to condense this vortex to destroy the superconducting order.

We emphasize that the bosonic neutral $\frac{2hc}{e}$ vortex is not simply a 4π vortex of the chargon b but requires also binding to the spinon f. An 8π ($\frac{4hc}{e}$) vortex of b, $\Phi_{4,0}$,is an electrically neutral boson. The corresponding bulk monopole is a $(4,0)$ particle which is also a boson. Condensation of the bosonic vortex $f\Phi_{2,0}$ automatically implies condensation of $\Phi_{4,0}$ as the spinon f is paired.

5.2 Surface Topological Order

We are now in a good position to construct a symmetry preserving STO phase from the SC phase. In the parton construction $c_\sigma = bf_\sigma$, we can describe the SC topological insulating surface state by condensing b, $\langle b \rangle \neq 0$, and placing f in the eTI band-structure with a superconducting surface. From the previous section, we saw that the minimal route to restoring the $U(1)_C$ symmetry is to proliferate the electrically neutral bosonic $\frac{2hc}{e}$ vortices.

What topologically distinct classes of particles remain after their proliferation? Since b and f have trivial mutual statistics with the $\frac{2hc}{e}$ vortices, they will clearly survive as gapped quasi-particles with unaltered charge and statistics. Quite generally the condensation of such $\frac{2hc}{e}$ vortices will produce an insulator with gapped bosonic excitations with fractional charge $1/2$. We will call this particle β. Clearly two β particles make a chargon: $b = \beta^2$.

Vortices in the superconductor become dressed by the $\frac{2hc}{e}$ condensate. We will see later that they survive as topological quasiparticles but with sharp non-zero electric charge (unlike in the example reviewed above of 2D $\mathbb{Z}_2$ topologically ordered states produced by disordering a proximate superconductor, where the visons are charge neutral). For now, we put aside the charge assignment for these topological particles and focus just on identifying the different particle types.

Going from the superconductor to the STO phase, the non-Abelian $\frac{hc}{2e}$ vortex, v, becomes a new object, τ_v, which is a quantum superposition of odd-strength vortices

in the superconductor whose vorticity differs by a multiple of $\frac{2hc}{e}$. Similarly, the $-\frac{hc}{2e}$ anti-vortex, $\bar{v}$, becomes a different object, $\tau_{\bar{v}}$, which is made up of a quantum superposition of $\frac{(4n-1)hc}{2e}$ vortices of the superconductor (with $n \in \mathbb{Z}$).

In the SC, an $\frac{hc}{2e}$ vortex, v, carries a Majorana zero mode in its core[34], and a pair of v's shares a single complex fermion level that can be either occupied or unoccupied. Consequently, there are two possible outcomes from fusing two v's, $v_{\pm}^2$, both of which have net vorticity $\frac{hc}{e}$ and which differ from each other by adding a neutral Bogoliubov fermion, f. Upon moving into the STO phase by condensing 4-fold vortices, $v_{\pm}^2$ will turn into distinct objects, $\tau_{\pm}^2$, which differ by a fermion: $\tau_+^2 = \tau_-^2 \times f$.

Similarly, in the superconductor, a pair of $\bar{v}$'s can fuse to two different $-\frac{hc}{e}$ vortex objects that differ by a fermion, f. Upon condensing $\frac{2hc}{e}$ vortices however, the $\pm\frac{hc}{e}$ vortices become mixed, and fusing two $\tau_{\bar{v}}$ particles should have the same outcome as fusing two τ_v particles: $\tau_{\bar{v}} \times \tau_{\bar{v}} = \tau_v \times \tau_v = \tau_+^2 + \tau_-^2$.

Lastly, in the superconductor, the vortex and anti-vortex pair also share a non-local fermion level due to their Majorana cores. Fusing a v and $\bar{v}$, then produces either the superconducting ground state, $\mathbb{I}$, or the ground-state plus an extra Bogoliubov particle: $v \times \bar{v} = \mathbb{I} + f$. Consequently, in the STO phase, we must have two possible fusion outcomes for $\tau_v \times \tau_{\bar{v}}$, which differ by an f. Naively, one might be tempted to have τ_v and $\tau_{\bar{v}}$ fuse $1 + f$ as in the superconductor. However, more generally we may also have: $\tau_v \times \tau_{\bar{v}} = X \times (1 + f)$ where X is some to-be determined particle that is condensed in the SC. This is consistent with the fusion rules of the surface SC if X is condensed in the SC phase. This requires X to be a boson. Below we will show that X is just the fractional chargon: β.

Finally, we note that $\tau_+^2 \times \tau_+^2 = \beta^2$, and that $\tau_+^2 \times \tau_-^2 = \beta^2 \times f = c$, the physical electron.

A summary of the particle content and fusion rules produced by this line of reasoning is summarized in Tables 5.1 and 5.2 respectively.

Topological Superselection Sector ("Particle Type"):	$\mathbb{I}$	β	f	τ_v	$\tau_{\bar{v}}$	τ_+^2	τ_-^2	τ_v^3	$\tau_{\bar{v}}^3$
Conjugate Sector (anti-particle):	$\mathbb{I}$	$\beta^3 \equiv \beta^{-1}$	f	$\beta^{-1}\tau_{\bar{v}}$	$\beta^{-1}\tau_v$	$\beta^{-2}\tau_+^2$	$\beta^{-2}\tau_-^2$	$\beta^{-2}\tau_v$	$\beta^{-2}\tau_{\bar{v}}$
Quantum Dimension (d):	1	1	1	$\sqrt{2}$	$\sqrt{2}$	1	1	$\sqrt{2}$	$\sqrt{2}$
Topological Spin (θ):	1	1	-1	$e^{i\pi/4}$	$e^{-i\pi/4}$	$e^{i\pi/2}$	$e^{-i\pi/2}$	$-e^{i\pi/4}$	$-e^{-i\pi/4}$
Charge (q_e):	$2ne$ ($n \in \mathbb{Z}$)	$\frac{e}{2}$	0	$\frac{e}{4}$	$\frac{e}{4}$	$\frac{e}{2}$	$\frac{e}{2}$	$\frac{3e}{2}$	$\frac{3e}{2}$
Time-Reverse Partner:	$\mathbb{I}$	β	f	$\tau_{\bar{v}}$	τ_v	τ_-^2	τ_+^2	$\tau_{\bar{v}}^3$	τ_v^3
$\mathcal{T}^2$ value (if meaningful):	1	1	-1						

Table 5.1: Summary of the topological content of the surface-topological order phase and the implementation of charge-conservation and TR symmetries. Topological superselection sectors are topological equivalence classes of particle types. The anti-particle of a particle in sector a resides a's conjugate sector. A particle has the same quantum-dimension and $\mathcal{T}^2$ value as its anti-particle, but opposite electrical charge and conjugate topological spin. Other distinct topological particles such as β^2, $\beta\tau_v$, etc... can be obtained by combining the above listed objects. The properties of these composites and anti-particles follows straightforwardly from the information listed above. Superselection sectors have the same quantum dimension, opposite charge, and same topological spin compared to their conjugate sectors (anti-particles). Empty entries in the $\mathcal{T}^2$ row indicate that there is no gauge invariant meaning to the value of $\mathcal{T}^2$ for that type of particle. In addition, there is the physical electron, c, which has $d = 1$, $\theta_c = -1$, $\mathcal{T}_c^2 = -1$. This could be regarded as part of the vacuum sector $\mathbb{I}$ since it has trivial mutual statistics with all other particles. However, since fusing c to another particle changes that particle's topological spin factor of -1 it is convenient to distinguish c from $\mathbb{I}$.

$\beta \times \beta = \beta^2$ $\beta^2 \times \beta = \beta^3 = \beta^{-1}$ $\beta^3 \times \beta = \mathbb{I}$ $\beta^n \times a = \beta^n a$ (for any sector $a \neq \beta$ and $n = 1, 2, 3$)
$f \times f = 1$ $f \times \tau_v = \tau_v$ $f \times \tau_{\bar{v}} = \tau_{\bar{v}}$
$\tau_v \times \tau_v = \tau_+^2 + \tau_-^2$ $\tau_{\bar{v}} \times \tau_{\bar{v}} = \tau_+^2 + \tau_-^2$ $\tau_v \times \tau_{\bar{v}} = \beta + \beta f$
$\tau_\pm^2 \times f = \tau_\mp^2$ $\tau_\pm^2 \times \tau_\pm^2 = \beta^2$ $\tau_+^2 \times \tau_-^2 = \beta^2 \times f = c$
$\tau_v^3 = \tau_v \times \tau_\pm^2$ $\tau_{\bar{v}}^3 = \tau_{\bar{v}} \times \tau_\pm^2$

Table 5.2: Fusion rules for the surface-topological order phase.

5.3 Charge Assignments

Having specified the topologically distinct particle classes and fusion rules for the STO phase, we now turn to their symmetry properties under $U(1)_C$. The resulting charge assignments explained below are summarized in Table 5.1.

Since b and f are unaffected by the vortex condensation, b still carries charge e and that f is charge-neutral. What about the excitations that descend from superconducting vortices? $\tau_\pm^2$ particles descend from $\Phi_{1,1/2}$ vortex fields of the superconductor, and hence can be created by dragging a magnetic monopole from the vacuum through the STO surface into the bulk. Since the monopole carries fractional electric charge: $\pm\frac{e}{2}$, its corresponding surface excitations must also have charge $\mp\frac{e}{2}$. Moreover, since τ_+^2 and τ_-^2 differ by a neutral fermion, f they must have the same charge. For concreteness, and without loss of generality, we choose $\tau_\pm^2$ to have charge $+\frac{e}{2}$ and their anti-particles, $\tau_\pm^{-2}$, to have charge $-\frac{e}{2}$. It then immediately follows from the fusion rule: $\tau_v \times \tau_v = \tau_+^2 + \tau_-^2$ that τ_v has charge $\frac{e}{4}$.

It is instructive to understand how these charge assignments come about directly from the surface without recourse to bulk monopoles. To obtain the STO from the SC, we are condensing 4π vortices of the chargon b that are bound to the neutral fermion f. The neutral fermion acquires a π phase when it encircles the $\frac{hc}{2e}$ vortex in the superconductor. Consequently, the $\frac{hc}{2e}$ vortex is a mutual semion with the condensed bosonic $\frac{2hc}{e}$ vortex. As a result, the $\frac{hc}{2e}$ vortex can survive in the STO phase only by binding with some other particle to produce trivial mutual statistics with the condensed bosonic $\frac{2hc}{e}$ vortex. The only possibility is for the $\frac{hc}{2e}$ vortex to bind a fractional charge, $\frac{e}{4}$, which also obtains π-phase upon encircling an $\frac{2hc}{e}$ vortex.

Thus we conclude that the particles $\tau_v, \tau_{\bar{v}}$ in the STO phase are the remnants of the $\frac{hc}{2e}$ vortices of the SC phase which have been dressed by charge $e/4$.

Since τ_v and $\tau_{\bar{v}}$ descend from $\pm\frac{hc}{2e}$ vortices in the superconductor, they are related by time-reversal and must have the same charge. Above, we saw that the $v \times \bar{v} = 1 + f$ fusion rule for the surface-SC generalized to: $\tau_v \times \tau_{\bar{v}} = X \times (1 + f)$ in the STO phase, with X to-be-determined particle. The above arguments show that X must have charge $\frac{e}{2}$. Since X is a $\frac{1}{2}$-charge boson that must be condensed in the SC phase, the only possibility is: $X = \beta$.

5.4 Topological Spins

The topological spin, θ_a, of a particle in sector a is defined as the phase factor accumulated when an a-particle is adiabatically rotated by 2π in the counter-clockwise (CCW) sense. For Abelian particles, the topological spin coincides with the phase obtained through CCW exchange of a pair of a-particles.

Clearly $\theta_b = 1$ and $\theta_f = -1$. The charge assignments from the previous section readily allow us to deduce the exchange statistics of the descendants of vortices: since τ_v is a charge $\frac{e}{4}$ object descending from a $\frac{hc}{2e}$ vortex in the superconductor it has topological spin $\theta_{\tau_v} = e^{i\pi/4}$. Similarly, $\theta_{\tau_{\bar{v}}} = e^{-i\pi/4}$.

We have already established that $\tau_\pm^2$ are semionic with topological spin either $e^{i\pi/2}$ or $e^{-i\pi/2}$. Since $\tau_\pm^2$ descend from $\frac{hc}{e}$ vortices, they have trivial mutual statistics with f. Moreover, since τ_+^2 differs from τ_-^2 by a fermion $\theta_{\tau_v} = -\theta_{\tau_{\bar{v}}}$. Therefore, we are free to choose $\theta_{\tau_\pm^2} = e^{\pm i\pi/2}$ (the opposite choice of $e^{\mp i\pi/2}$ is not distinct as it differs only by relabeling $\tau_+^2 \leftrightarrow \tau_-^2$).

5.5 Exchange Statistics

In a system with non-Abelian particles that have multiple possible fusion outcomes, the phase obtained by the CCW exchange of two particles, a and b, will depend on the fusion channel. When a and b fuse to c, the phase factor obtained by adiabatic CCW exchange of a and b is denoted by R_c^{ab} (for a pedagogical review see Ref. [92]). The R matrices are related to the topological spin of the underlying particles[92] by $(R_c^{ab})^2 = \theta_c/\theta_a\theta_b$. This identity just encodes the fact that dragging b around a is nearly the same as rotating the entire a-b composite system CCW by 2π, or equivalently to fusing to c and rotating CCW by 2π giving: θ_c. However, rotating the entire system also rotates a and b individually, which is not part of the exchange process. The factor of $\theta_a\theta_b$ in the denominator compensates for this unwanted rotation of a and b. The proper branch of the square-root can be identified by writing $\theta_{a,b,c} \equiv e^{i\phi_{a,b,c}}$, and choosing an exchange protocol such that the phase is accumulated monotonically over the course of time T: $R_c^{ab} = \lim_{t \to T^-} e^{i(\phi_c - \phi_a - \phi_b)t/2T}$.

For Abelian particles a and b, there is a unique fusion channel, and the lower-index on R is redundant. Therefore, it is common to just specify the mutual statistics of a and b by: $\theta_{a,b} = (R_{a\times b}^{ab})^2$, which is the phase factor obtained by adiabatically

dragging b CCW around a. Consequently, the braiding statistics for all particles follows straightforwardly from the previously obtained fusion rules and topological spins tabulated in Tables. 5.1 and 5.2 respectively.

For example, consider the mutual statistics of τ_v and $\tau_\pm^2$. The composite $\tau_v \times \tau_\pm^2 = \tau_v^3$ has topological spin: $\theta_{\tau_v^3} = -e^{i\pi/4}$, indicating:

$$\theta_{\tau_v,\tau_\pm^2} = \frac{\theta_{\tau_v \times \tau_\pm^2}}{\theta_{\tau_v}\theta_{\tau_\pm^2}} = \frac{-e^{i\pi/4}}{e^{i\pi/4}e^{\pm i\pi/2}} = -e^{\mp i\pi/2} \tag{5.4}$$

5.6 Time-Reversal Properties

We have already identified appropriate charge assignments, which encode the transformation properties of various particles under the $U(1)_C$ symmetry. In this section, we address how TR is implemented in the proposed STO phase. The results of this section are summarized in Table. 5.1.

The first task for implementing TRS is to specify how topological equivalence classes of particles are exchanged under TR. This is relatively straightforward since we have constructed the STO state from the well-understood TR-symmetric superconductor phase. The τ_v descends from an $\frac{hc}{e}$ vortex in the superconductor, which becomes a $-\frac{hc}{e}$ vortex under TR; in turn the $-\frac{hc}{e}$ vortex becomes $\tau_{\bar{v}}$ in the STO phase. Therefore under TR:

$$\tau_v \overset{\mathcal{T}}{\longleftrightarrow} \tau_{\bar{v}} \tag{5.5}$$

Similarly, by going to the superconductor it is clear that f, and $\beta^2 \cong b$ are preserved under TR. It is also clear that the β sector is preserved under TR.

Under TR, counter-clock-wise and clock-wise exchange are interchanged, and hence topological classes of particles that are related by TR must have conjugate topological spin. We see that this is true for all of the above TR transformation rules.

Since $\tau_\pm^2$ descend from both $\pm\frac{hc}{e}$ vortices, we cannot determine their TR properties directly from the superconductor. However, since τ_+^2 and τ_-^2 have conjugate topological spins, they must be exchanged by $\mathcal{T}$:

$$\tau_+^2 \overset{\mathcal{T}}{\longleftrightarrow} \tau_-^2 \tag{5.6}$$

In addition to the action of $\mathcal{T}$ on topological superselection sectors, for sectors that are not interchanged by $\mathcal{T}$, it is meaningful to ask about their eigenvalues under the unitary operation of double-time-reversal, $\mathcal{T}^2$. For particles that reside in TR-invariant superselection sectors, $\mathcal{T}^2 = -1$ has definite physical interpretation as a TRS-protected Kramers degeneracy. Our STO state arises naturally from the superconductor where b has $\mathcal{T}^2 = 1$ and f has $\mathcal{T}^2 = -1$ respectively; hence β^2 and f also have $\mathcal{T}^2 = 1$ and $\mathcal{T}^2 = -1$ in the STO phase. Similarly, β^2 has $\mathcal{T}^2 = 1$ since it is a fraction of b, and since β can be condensed to obtain the SC from the STO phase.

However, for particles, like $\tau_\pm^2$, whose superselection sectors are changed by $\mathcal{T}$, the $\mathcal{T}^2$ eigenvalue does not imply a further degeneracy within that particle sector. Furthermore, for such particles, it turns out that it is not even possible to assign a local gauge-invariant representation of $\mathcal{T}^2$. In the next two sections we further describe the issue of symmetry localization on gauge non-invariant particles.

5.6.1 Gauge (non)-invariance TR Properties for Fractionalized Particles

Fractionalized particles (i.e. particles with non-trivial self- or mutual-statistics) cannot be individually created from the ground-state. Rather, one can only create groups of excitations that fuse to $\mathbb{I}$. For example, to isolate a fractionalized particle X, one can create a particle anti-particle pair, X and X^{-1}, from the ground-state, and pull them far apart from one another. The operator that implements this sequence consists of a string of electron operators connecting the final locations, R_1 and R_2, of X and X^{-1} respectively. This string of operators can be divided into two local operators $\Psi_X^\dagger(R_1)$ and $\Psi_X(R_2)$, that create X and X^{-1} respectively, and a non-local gauge-string, $W_{1,2} = \prod_\Gamma e^{iq_X a_{ij}}$, where i and j label sites on the lattice where Ψ_X is defined, Γ is directed path of links $\langle ij \rangle$ connecting sites R_1 to R_2, q_X is the internal gauge-charge of the particle X, and a_{ij} is a discrete-valued emergent gauge field. This division into particles and strings is inherently arbitrary, which is reflected by the local gauge invariance under the transformations $\Psi_{X,i} \to e^{2\pi i n_i q_x} \Psi_{X,i}$, and $a_{ij} \to a_{ij} - (n_i - n_j)$ (with $n_{i,j} \in \mathbb{Z}$).

Due to the non-local gauge structure there is not always a well-defined gauge invariant way to assign symmetry-transformation properties locally to the particle creation operators $\Psi_X^\dagger$. Rather, one must generically keep track of the transformation property of both the particles, and their gauge-strings, W. However, in special cases it is possible to associate a well-defined action of a symmetry locally on $\Psi_X^\dagger$ even for gauge non-invariant objects. For simplicity, in what follows, we will not distinguish between the label X for a topological class of particles and the corresponding (gauge-non-invariant) annihilation operator Ψ_X.

Since $f \times f = \mathbb{I}$, the phase of f has a sign ambivalence, indicating that f's have $\frac{1}{2}$-gauge charge (i.e. change sign under $e^{2\pi i q_f} = -1$) and are connected pairwise by (unobservable) unoriented $\mathbb{Z}_2$ gauge strings. Similarly $\beta^2 \times f$ is a physical electron c, and so β^2 also has a $\mathbb{Z}_2$ gauge charge. It then follows from $\tau_\pm^2 \times \tau_\pm^2 = \beta^2$, that $\tau_\pm^2$ has internal $\frac{1}{4}$-gauge charge, and that oriented $\mathbb{Z}_4$ gauge strings emanate from $\tau_\pm^2$ particles. We know that $\tau_\pm^2$ have opposite internal gauge charge, since $\tau_+^2 \times \tau_-^2 = c$, and c is a physical (gauge-invariant) local electron. Therefore, we can choose the orientation convention that $\mathbb{Z}_4$ lines emanate from τ_+^2 and terminate on τ_-^2 particles.

5.6.2 $\mathcal{T}^2$ Properties For Sectors that are Exchanged by $\mathcal{T}$

With this gauge-string picture in mind, we now turn to the task of determining to what extent $\mathcal{T}^2$ is defined on particles whose topological classes are interchanged by $\mathcal{T}$. To see why it is important to consider the effects of $\mathcal{T}$ on the gauge string, consider

a τ_+^2-τ_-^2 pair. Suppose that we represent $\mathcal{T}$ locally on the particle operators as: $\mathcal{T}^{-1}\tau_+^2\mathcal{T} = e^{i\alpha}\tau_-^2$ and $\mathcal{T}^{-1}\tau_-^2\mathcal{T} = e^{i\beta}\tau_+^2$ where α and β are unknown phases. Then one has: $\mathcal{T}^{-2}\tau_\pm^2\mathcal{T}^2 = e^{\pm i(\beta-\alpha)}$, and naively it appears that $\mathcal{T}^{-2}\tau_+^2\tau_-^2\mathcal{T}^2 = |e^{i(\beta-\alpha)}|^2\tau_+^2\tau_-^2$. However, this cannot be the whole story, since $\tau_\pm^2$ fuse to the physical electron, c, which is a Kramers doublet with $\mathcal{T}^2 = -1$.

This puzzle is resolved by noting that $\tau_+^2 \overset{\mathcal{T}}{\leftrightarrow} \tau_-^2$, implies that $\mathcal{T}$ reverses the direction of the gauge string connecting a given τ_+^2-τ_-^2 pair. Then acting twice with $\mathcal{T}^2$ doubly flips the orientation of the connecting gauge-string. A two-fold re-orientation of the gauge-string can also be accomplished by dragging τ_+^2 around τ_-^2. Due to their semionic mutual statistics, this observation dictates that the gauge string contributes an additional factor of -1 to the overall $\mathcal{T}^2$. Therefore, the action of $\mathcal{T}^2$ cannot be consistently implemented in a purely local fashion for the gauge-non-invariant particles $\tau_\pm^2$, which interchange under $\mathcal{T}$.

Note that a nearly identical argument can be applied to monopoles in the bulk of the electron TI to formally establish the intimate connection between the $\theta = \pi$ electromagnetic response of the TI and the Kramers degeneracy of the electron[8] (see also Ref. [75]). This is indeed appropriate, since the $\tau_\pm^2$ particles are the surface-avatars of these bulk dyons.

The issue of non-locality is even more pronounced for the non-Abelian excitations τ_v and $\tau_{\bar{v}}$, since a collection of these particles share a degenerate Hilbert space of non-local fermion modes, and the action of $\mathcal{T}^2$ depends on the total fermion parity of this non-local Hilbert space, which is a global property of the system.

5.7 2D TR Breaking Analog

For bosonic SPT bulk phases, the topological properties of the STO phase can always be realized by a strictly 2D system that does not preserve the underlying symmetries of the 3D SPT. In this section, we provide an analogous construction for the electron TI. Specifically, we show that the STO phase has the same topological order as the Moore-Read QH phase[32] supplemented by an extra neutral semion. We begin by reviewing the Moore-Read and related 2D phases in the language of the parton construction $c_\sigma = bf_\sigma$ used above.

5.7.1 $p + ip$ Superconductor and Kitaev Spin-Liquid

We begin with the $p+ip$ superconductor, and its topologically ordered analog, which are in some sense the simplest "roots" of the non-Abelian Ising topological order for the STO phase. A TR-breaking superconductor with $p+ip$ pairing symmetry, and the TR-broken B-phase of Kitaev's Honeycomb Model (henceforth denoted Kitaev Spin-Liquid, or KSL) are closely related states with non-Abelian Ising anyon excitations. The latter is obtained from the former by condensing $\frac{hc}{e}$-vortices. In the language of the parton construction, this is equivalent to placing b in a Mott insulator, and f into a $p + ip$ superconductor. The resulting phase contains topological particle classes: $\mathbb{I}$

(vacuum), b, f, and a non-Abelian vison, σ that descends from the $\pm\pi$-vortices of the $p+ip$ superconductor.

In the resulting KSL phase, b has charge e, and all other particles are neutral. The edge of this phase contains a single chiral Majorana fermion that contributes $\sigma_H = 0$ and $\kappa_H = \frac{1}{2}$. The fusion rules are:

$$\begin{aligned} b \times f &= c \\ b \times b &= c^2 \cong \mathbb{I} \\ f \times f &= \mathbb{I} \\ \sigma \times f &= \sigma \\ \sigma \times b &= \sigma \\ \sigma \times \sigma &= 1 + f \end{aligned} \tag{5.7}$$

and the topological spins are:

$$\begin{aligned} \theta_b &= 1 \\ \theta_f &= -1 \\ \theta_\sigma &= e^{i\pi/8} \end{aligned} \tag{5.8}$$

5.7.2 Moore-Read Quantum Hall State

The Moore-Read state[32] can be obtained from the KSL phase by placing b in a $\nu = 1/2$ bosonic-Laughlin quantum Hall phase rather instead of a Bose-Mott insulator. This phase is characterized by the idealized wave-function:

$$\Psi_{\mathrm{MR}} \sim \prod_{i<j} (z_i - z_j)^2 \mathrm{Pf}\left(\frac{1}{z_i - z_j}\right) \tag{5.9}$$

where $z_j = x_j + iy_j$ is the complexified coordinate of the j^{th} electron. The factors of $(z_i - z_j)^2$ stem from the b sector, and the Pf denotes the Pfaffian of the anti-symmetric matrix with entries $\frac{1}{z_i - z_j}$, which describes the BCS wave-function with $p+ip$-pairing[27].

In this phase, the vison, σ of the f-sector is bound to a π-flux of the Bosonic QH fluid which we denote v (similarly, denote a $-\pi$ flux of the Bosonic QH fluid by $\bar{v}$). A π-flux in a $\sigma_H = \frac{1}{2}$ system has charge $\frac{e}{4}$ and hence v has topological spin $e^{i\pi/8}$. Denoting the non-Abelian vison/charge-$\frac{e}{4}$ vortex composite as σ_v, we have: $\theta_{\sigma_v} = e^{i\pi/4}$. Since $\bar{v}$ is a $-\pi$-vortex bound to charge $-\frac{e}{4}$ it also contributes an extra $e^{i\pi/8}$ to the vison topological spin, indicating that the composite, $\sigma \times \bar{v} \equiv \sigma_v^{-1}$, has $\theta_{\sigma_v^{-1}} = \theta_{\sigma_v} = e^{i\pi/4}$.

5.7.3 2D TR-Breaking Analog

The MR state looks somewhat similar to the STO phase constructed above: there Ising non-Abelions attached to charged Abelian vortices. However, unlike in the TI

STO phase, $\sigma_v \times \sigma_v^{-1} = 1 + f$ is charge-neutral. More generally, since σ_v and $\sigma_{\bar{v}}$ have opposite charge, and the same topological spin, it is hard to see how TR-invariance could be implemented in the MR phase, even at the surface of the STO.

We can cure this problem by introducing an extra counter-propagating anti-semion particle, s, with topological spin $\theta_s = e^{-i\pi/2}$ to the boson sector (in the parton language this corresponds to further fractionalizing $b \to b_1 b_2$, with b_1 carrying charge e in a bosonic $\nu = 1/2$ QH phase, and b_2 a charge-neutral in a $\nu = -1/2$ bosonic QH phase). Making the following identifications:

$$\begin{aligned} \beta^{-1} \times \tau_+^2 &= s \\ \tau_v &= \sigma_v \\ \tau_{\bar{v}} &= \sigma_v \times s \\ \tau_v^{-1} &= \sigma_v^{-1} \\ \tau_{\bar{v}}^{-1} &= \sigma_v^{-1} \times s \end{aligned} \tag{5.10}$$

we see that this 2D TR-breaking phase has the same topological order and charge assignments as the STO phase described above. For brevity we denote the 2D TR-breaking phase: MR×AS.

5.8 Connection Between STO and Familiar Non-Fractionalized Surface Phases

In the previous section, we have constructed an STO phase by quantum disordering the TRS surface superconductor state. The fact that a TI can realize this topological order with both $U(1)_C$ and TR symmetries intact actually serves as a non-perturbative definition of the $U(1)_C \ltimes \mathbb{Z}_2^T$ fermion topological insulator. To see this, we need to show that we can obtain all of the usual symmetry broken non-topologically ordered surface phases of the familiar fermion TI through a sequence of surface-phase transitions that do not affect the TI bulk.

5.8.1 STO to TR-Symmetric Non-Abelian Surface SC

Since we have constructed the STO phase from the TR-invariant surface SC, it is straightforward to recover the familiar surface SC. We have already argued that the superconducting surface can be obtained from the STO phase by condensing β. Here we provide some further details.

Since $\beta^2 = b = \sqrt{\rho_b} e^{i\phi_b}$ we may write $\beta = (\rho_b)^{1/4} e^{i\phi_\beta}$. Then 2π vortices of ϕ_β are 4π vortices of ϕ_b, which are condensed in the STO phase. In other words, the STO phase can be viewed as a Mott insulator of β. Then, to recover the TRS surface superconductor from the STO phase, one can simply condense β. Since β has non-trivial mutual statistics with all other particles besides f, the particles $\tau_v, \tau_{\bar{v}}, \tau_\pm^2$ etc... will all be confined in the $\langle \beta \rangle \neq 0$ phase. However, these confined objects do not completely dissapear from the theory, rather they are bound to vortices of ϕ_β

(which are now-gapped) to form composites that have trivial mutual statistics with the β-condensate.

Since, β has the same mutual statistics with τ_v as with a $\pi/2$-vortex of ϕ_β they are bound-together in the superconductor. Since β is charged a $+\pi/2$-vortex of ϕ_β has physical circulating charge current. and the τ_v object becomes the superconducting $\frac{hc}{2e}$ vortex (or, more generally, a $\frac{(4n+1)hc}{2e}$ vortex with $n \in \mathbb{Z}$). Similarly, $\tau_{\bar{v}}$ becomes a $\frac{(4n-1)hc}{2e}$ vortex, and $\tau_\pm^2$ become a $\frac{nhc}{e}$ vortices (with n odd).

5.8.2 STO to 1/2-integer quantum Hall

Next, we connect the STO to the $U(1)_C$ preserving but TR-breaking $\frac{1}{2}$-integer surface quantum Hall insulator (SQHI). In the previous section, we showed that the topological order and charge assignments of the STO can be realized in strict 2D at the expense of breaking TRS. The analogous TR breaking phase was equivalent to the Moore-Read QH phase with an extra neutral semion, denoted MR×AS. Importantly, the MR×AS has $\sigma_H = \kappa_H = \frac{1}{2}$. There is a closely related phase, which we denote $\overline{\text{MR} \times \text{AS}}$, obtained from MR×AS by switching all of the particles of MR×AS with their anti-particles, which has $\sigma_H = \kappa_H = -\frac{1}{2}$.

Starting with the STO phase of the TI, let us "deposit" a layer of $\overline{\text{MR} \times \text{AS}}$ on the TI surface (or alternatively, imagine adjusting the interactions and other parameters of a layer of the bulk near the surface to drive that layer into the $\overline{\text{MR} \times \text{S}}$ phase). Then, suppose we allow the f particle of the $\overline{\text{MR} \times \text{AS}}$ to hybridize with (i.e. tunnel into) the f particle of the STO phase. This confines each non-Abelian τ_v of the STO is bound to a similar non-Abelian τ_v^{-1} of the deposited layer, thereby neutralizing the non-Abelian statistics of the composite object. The resulting composites are all Abelian and have trivial self-statistics, and hence can be straightforwardly condensed (since TR symmetry is already broken). In particular, if we condense the particles containing a τ_v of the STO layer and a τ_v^{-1} of the deposited layer, all other particles are trivially confined, and no excitations with fractional statistics remain.

We have thereby eliminated the surface-topological order, at the expense of breaking TR-symmetry on the surface. What is the quantum Hall response of this non-fractionalized insulating state?

To answer this question we note that we could have equally well followed a time-reversed version of the above procedure, by depositing a different surface layer related to $\overline{\text{MR} \times \text{AS}}$ by TR, which we denote $\overline{\text{MR}^* \times \text{AS}^*}$ and has $\sigma_H = \kappa_H = \frac{1}{2}$. Consider a spherical TI, depicted in Fig. 5-2, and imagine depositing a layer of $\overline{\text{MR} \times \text{AS}}$ on the bottom hemisphere of the TI surface and a layer of $\overline{\text{MR}^* \times \text{AS}^*}$ on the top hemisphere. The edges of the deposited 2D layers meet at the equator, and each contributes a chiral Majorana fermion, a co-propagating charged boson mode and a counter-propagating neutral boson mode. The chiral Majorana fermions from the top and bottom hemisphere propagate in the same direction, and when coupled, combine into a complex (neutral) chiral fermion. The combined edge has overall chirality with a single chiral charged mode, and hence has $\sigma_H = \kappa_H = 1$. This σ_H and κ_H is not effected by condensing τ_v composites in order to remove the topological order.

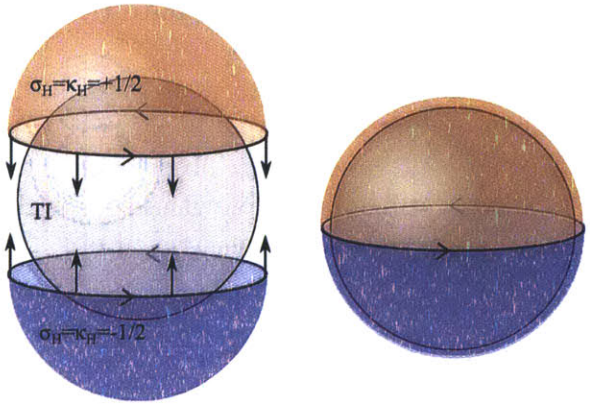

Figure 5-2: The non-fractionalized TR-breaking quantum Hall insulator (QHI) with coating the TI surface with a 2D TR-breaking topologically ordered state with $\sigma_H = \kappa_H = \pm\frac{1}{2}$ (depicted in orange and purple respectively), as explained in the text. The half-integer quantum Hall conductance can be seen by considering a domain between these two coatings as shown in the above figure for a spherical TI,

This line of reasoning shows that, even after destroying the surface-topological order, the interface at the equator possesses a single 1D chiral charge fermion. The non-fractionalized phases that we have produced on the top and bottom hemisphere therefore differ by an electron $\nu = 1$ quantum Hall layer. Since these two phases are related by TR-symmetry, we must democratically assign them $\sigma_H = \kappa_H = \pm\frac{1}{2}$ respectively. We have therefore succeeded in recovering the familiar non-fractionalized surface QH insulating phases from the STO phase.

5.8.3 STO to Gapless Dirac Fermion Surface

In the previous section, we showed how to obtain the surface QH insulator from the STO phase by breaking TR. The resulting phase can have either $\sigma_H = \kappa_H = \pm\frac{1}{2}$. From here, it is straightforward to produce the symmetry preserving gapless Dirac cone phase by proliferating domain walls between the $\sigma_H = \pm\frac{1}{2}$ surface phases. Such domain walls carry a single chiral (complex) fermion, and it is well known (for example from network models[84]) that their proliferation results in a single gapless Dirac cone.

5.8.4 $\mathbb{Z}_2$ Nature of Surface Order

It is well known that two copies of the ordinary electron topological insulator can be smoothly deformed into the trivial insulator without a bulk phase transition. Therefore, as a final consistency check for the proposed STO, we demonstrate that two coupled STO phases can be deformed to a trivial insulator by surface phase-transitions that leave the bulk gap untouched.

Consider starting with two layers of the STO phase, labeled 1 and 2 respectively, coupled such that electrons can tunnel between them: $\langle c_1^\dagger c_2 \rangle$, $\langle c_2^\dagger c_1 \rangle \neq 0$. It is straight-

forward to check that the following set of composite particles are charge-neutral self-bosons with trivial mutual-statistics, which can be simultaneously condensed without breaking either $U(1)_C$ or TRS:

$$\{\beta_1^\dagger \beta_2, \quad \tau_{v1}\tau_{v2}\beta^\dagger, \quad \tau_{\bar{v}1}\tau_{\bar{v}2}\beta^\dagger, \quad \text{and h.c.'s}\} \tag{5.11}$$

with h.c.'s indicating that all operators related by Hermitian conjugation to those listed are also condensed. In order to preserve TRS, we must condense TR conjugate particles with equal amplitude: $\langle \tau_{v1}\tau_{v2}\beta^\dagger \rangle = \langle \tau_{\bar{v}1}\tau_{\bar{v}2}\beta^\dagger \rangle \neq 0$.

It is also straightforward to verify that after condensing these objects, all non-trivial particles in the theory are either confined or condensed, and there are no fractionalized excitations. In particular, f and β^2 both have mutual (-1) statistics with the condensed $\tau_{v1}\tau_{v2}\beta^\dagger$ particles, and are confined together to form the physical electron: $c = \beta^2 f$. The resulting phase has only gapped, physical electron excitations, c, and hence is a trivial band-insulator. Therefore, we have verified that the bulk phase described by our proposed STO indeed has a $\mathbb{Z}_2$ group structure (i.e. that combining two copies of our phase produces a trivial phase) as required for the electron TI.

This set of particles in Eq. 5.11 has a natural physical interpretation: starting with two coupled layers of the TRS surface-SC phase, we know that we can obtain a trivial bulk insulator by condensing the (now Abelian) $\pm\frac{hc}{2e}$ vortices, which now occur in the same location in both layers due to the interlayer tunneling. The set of particles condensed here to trivialize the double-layer STO phase are simply the descendants of these vortices.

5.9 Discussion

We have shown that, in addition to the familiar gapless Dirac surface state, and gapped symmetry-broken states, the electronic topological insulator (TI) can support a gapped and fully symmetric phase with surface topological order (STO). This STO phase provides a complete, non-perturbative definition of the electron TI. Like STO phases of analogous bosonic TIs, the electron TI STO phase has the same topological-order as a 2D phase, but with symmetry implemented in a way that is not allowed in strict 2D.

For boson TIs, the lens of STO provides a useful perspective into 3+1D strongly correlated boson TIs as well as 2+1D gauge theories[85]. The hope is then that understanding of the electron TI STO will enable similar progress for strongly-correlated electronic phases. An essential component for boson TIs was a systematic understanding of symmetry implementation for strictly-2D Abelian bosonic systems[93, 94]. One potentially complicating factor in adapting this approach to fermions is that the electron TI STO is inherently non-Abelian. Consequently an important outstanding task for making progress along these lines is to develop a systematic understanding of symmetry implementation in 2D non-Abelian theories. These theories are not amenable to the simple K-matrix methods that have so successfully utilized for boson systems[93, 94]. However, methods of similar spirit based on using the bulk-boundary

correspondence to reduce the problem to symmetry implementation in 1+1D conformal field theories of the edge may still prove fruitful. Such a pursuit would go far beyond the scope of the present paper and is left as a challenge for future work.

Chapter 6

Interacting Electron Topological Insulators

In the previous Chapter, we constructed a symmetric gapped surface phase for the ordinary electron TBI, providing the last missing piece of the puzzle to completely fit the electron TBI into the framework of symmetry-protected topological phases. This excercise serves as a warm-up for tackling the more general conceptual question of whether interactions can play an important role in electron TIs.

In this chapter, we seek to answer the following questions: Can interaction dominated phases be in a topological insulating state? Are there new kinds of topological insulators that might exist in interacting electron systems that have no non-interacting counterpart? How do we think generally about a topological insulator without the crutch of a free fermion model?

For systems of interacting bosons (or the closely related quantum magnets) there has been dramatic progress in answering such questions. A classic example is the Haldane spin-1 chain. This has a bulk gap and no fractionalization but nevertheless has non-trivial end states that are protected by symmetry. A classification of all such phases in $d = 1$ exists[97]. In higher-d substantial progress toward classification in diverse dimensions[79] has been reported. The physical properties of various such bosonic SPT phases in both two[98, 99, 100, 101] and in three dimensions[84, 102, 85, 86, 75, 103] have also been described in some detail.

The identification of bosonic SPTs arising from strong-correlations clearly suggests that there will also be strongly-correlated fermion TIs with no band-structure analog. Afterall, strong-correlations can easily produce a system where the low-energy excitations are all bosonic. For example, strong attraction could bind all electrons into bosonic Cooper pairs. Alternatively, strong repulsion can produce a Mott insulator where charge is frozen and only Bosonic spin-degrees of freedom remain. In both cases, the resulting boson excitations can in principle be driven into bosonic SPT phase.

We will consider both possibilities in turn. An important point is that two SPT phases are distinct if and only if their surface states cannot be connected by depositing a strictly 2D system. Otherwise we must regard the two as the same bulk phase with different surface terminations. Once we add electrons into the mix, there are many

more allowed 2D electronic systems than exist with bosons alone. Consequently, not all SPT phases of purely bosonic systems will remain distinct in the presence of local fermionic electrons.

6.1 Boson SPTs from Fermion Systems

Before addressing the problem of effectively bosonic SPTs arising from strongly-correlated electron systems, we take a brief diversion to review some salient features of SPTs in intrinsically boson systems.

6.1.1 3D Bosonic SPTs

Consider a 3D, time-reversal symmetric system of bosons having unit-charge under a global $U(1)$ charge-conservation symmetry. To obtain an insulating bulk, we can always imagine starting from a bulk superfluid, and condensing the 2π vortex lines in the phase of the boson operator $b \sim e^{i\phi}$. Starting from an ordinary superfluid, and condensing ordinary vortices, we would obtain a trivial Bose-Mott insulator.

However, we can consider decorating the vortex lines, such that the end of a vortex line has non-trivial structure such that it cannot condensed without breaking symmetry. Then, the we are still free to proliferate closed vortex loops in the 3D bulk to produce a bulk insulator. However producing a trivial insulator at the boundary is not allowed, as this would require proliferating open vortex lines that terminate on the surface, which by assumption will break symmetry. The three possibilities that do not lead to bulk topological order are:

1. The end of a vortex line is fractionally charged - in which case its condensation will leave $U(1)$ broken on the surface.[1]

2. The vortex line ends in a Kramer's doublet (like a half-integer spin) which cannot be condensed without breaking TR symmetry.

3. The vortex line ends in a fermion, which cannot be condensed even in the absence of $U(1)$ charge-conservation.[2]

In all three cases, the doubled vortex is trivial, and can be condensed without breaking symmetry. The resulting surface phase has intrinsic topological order, like that discussed for the electron TBI in the previous chapter. In contrast, for the bosonic systems, the topological order has a much simpler Abelian structure. In this case, one that is identical to 2D $\mathbb{Z}_2$ gauge theory. The particle content of the surface STO is comprised of three particles e, m, and ε any pair of which are mutual semions. From the above-described double-vortex condensation it is natural to interpret the particles as follows:

[1]Note that the vortex can only have half-integer charge, otherwise bulk loops will have fractional Berry-phase contributions for linking corresponding to bulk topological order.

[2]Note that we cannot make the end of a vortex line anyonic, without producing bulk topological order, so these possibilities are exhaustive.

1. m: a vison particle descending from the $\pm\pi$-vortices of the surface superfluid
2. e: the fractional part of the boson field b that is dual to the condensed double-vortex field. By construction, e has mutual π statistics with m.
3. ε: a fermionic bound-state of e and m

However, one should not strictly insist on this interpretation as one can freely relabel the particles as is convenient.

With the $\mathbb{Z}_2$ STO in hand, we can now systematically classify 3D SPT phases whose STO cannot be trivially confined by condensing one of the e, m, or ε particles, without breaking symmetry. As described previously, we can prevent particles from condensing in a symmetry-preserving fashion by making the 1/2-integer charged (denoted C), Kramers doublets under time-reversal (denoted T), or fermions (denoted $_f$), or combinations thereof. For example, e and m could be Kramers-singlet bosons with half-integer charge (denoted $eCmC$); then ε is a fermion, and none of the three particles can be condensed in a symmetric fashion. Another possibility is that e and m are both Kramers-doublet bosons with integer charge (denoted $eTmT$). A third possibility is that e, m, and f are all fermions (denoted e_fm_f).

Various combinations of these states are also possible. These are all generated by the three root states: $eCmC$, $eTmT$, and e_fm_f described above. The total number of surface-inequivalent states depends on whether the symmetry group is $U(1) \ltimes \mathbb{Z}_2^T$ or $U(1) \times \mathbb{Z}_2^T$. For a more complete discussion the reader is referred to [85]. Having discussed the general structure of boson SPTs, let us turn to the question of how they can arise in electronic systems.

6.1.2 Topological Cooper Pair Insulators ($U(1) \ltimes \mathbb{Z}_2^T$)

Consider adding strong attractive interactions to an electron system, such electrons are bound into integer-spin Cooper pairs. There is now a gap for unpaired electrons, and for the purposes of understanding topological properties of the phase, we may take this gap to be arbitrarily large so that we can essentially forget about unpaired electrons. The Cooper pairs can be regarded as charge-2 bosons, which can now be effectively thought of as the 'fundamental' particles of the system.

Denoting the Cooper pair field by $b \sim e^{i\phi}$, we have $\mathcal{T}^{-1}b\mathcal{T} = b$ under TR, indicating that $\phi \xrightarrow{\mathcal{T}} -\phi$.[3] In this case, $\mathcal{T}$ does not quite commute with $U(1)$ charge-rotations due to $\mathcal{T}$'s anti-unitary nature, and the symmetry operations do not quite have a pure direct product structure, indicated by: $U(1) \ltimes \mathbb{Z}_2^T$.

6.1.3 Topological Spin Paramagnets ($\mathbb{Z}_2^T$ or $U(1) \times \mathbb{Z}_2^T$)

An alternative to the last section is to consider making a bosonic system from strong repulsive interactions such that the electrons are bound to holes leaving only spin-degrees of freedom. Here the 'fundamental' bosonic degrees of freedom are charge-0 bosons.

[3] These representations are schematic as b will generically have multiple components.

In general, we may have a situation where no component of spin is conserved. In this case, there is only $\mathbb{Z}_2^T$ symmetry, and there is no notion of the $eCmC$ phase which relies on sharply defined fractional charge.

Alternatively, the system may have a residual conserved component of spin (e.g. along a particular axis). Since the direction of spins is odd under $\mathcal{T}$, denoting the the spin-lowering operator (for a chosen quantization axis) by $S^- \sim e^{i\phi}$ we have $\mathcal{T}^{-1}S^-\mathcal{T} = \mathcal{T}^{-1}b\mathcal{T} = S^+ = e^{-i(\phi+\text{const})}$.[4] In this case, $\mathcal{T}$ commutes with charge-rotations and the symmetry operations have a direct product structure: $U(1) \times \mathbb{Z}_2^T$.

6.1.4 Modification By Microscopic Electrons

With these basic notions under our belt, let us examine whether these root states remain distinct in the presence of microscopic electrons.

For example, consider a Cooper pair insulator. Recall that the smallest unit of bosonic charge is twice the charge of an electron, so a 1/2-charge Cooper pair has odd-integer electron charge. This charge can be removed by binding an electron to e and m. Since the electron is local with respect to the fractional particles of the STO, this simply changes the self-statistics of e and m to be fermionic. Moreover, since the microscopic electron is a Kramers doublet, so now too are e and m. From this, we see that $eCmC$ is equivalent to e_fTm_fT. Morover, e_fTm_fT can be produced by combining e_fm_f and $eTmT$ by allowing the ε particles of both theories to tunnel between theories (this confines e of e_fm_f to e of $eTmT$ due to the mutual semionic statistics, and similarly for the m particles).

Therefore, in the presence of microscopic electrons there are only two of the original three root states $eCmC$, $eTmT$, and e_fm_f are distinct. The same conclusion can be reached starting from a spin-SPT. For an electron system with only charge-conservation and time-reversal symmetry, we should exclude an additional $U(1)$-axial-spin rotation symmetry. With $\mathbb{Z}_2^T$ alone, there are only 2 root states: $eCmC$ and e_fm_f. These remain distinct in the presence of microscopic electrons.

Since all such "bosonized" electron SPTs can be generated from any two representative root states. For subsequent discussions, it will be convenient to choose the "neutralized" root states: $eTmT$ and e_fm_f. This choice also allows us to remain agnostic about whether we imagine forming bosons from spin- or Cooper- pair degrees of freedom (this choice evidently does not effect the resulting classification).

6.2 Classification of Interacting Electronic Topological Insulators

With this understanding of effectively bosonic SPT phases arising from strongly interacting electron systems, we are now ready to address the more general question of

[4]For the $U(1) \ltimes \mathbb{Z}_2^T$, the constant offset could be removed by accompanying $\mathcal{T}$ with aa global shift of ϕ. For the $U(1) \times \mathbb{Z}_2^T$ case, even if this constant is shifted away in $\mathcal{T}$ it reappears in $\mathcal{T}^2$, and cannot be entirely removed.

Physical Fermion-Type	Classification
$\frac{1}{2}$-Integer Spin (Kramers)	$\mathbb{Z}_2^3 = \mathbb{Z}_2 \times \mathbb{Z}_2^2$ (free-fermion)$\times$(neutral boson)^2
Integer Spin (Non-Kramers)	$\mathbb{Z}_2^2 = \mathbb{Z}_2^2$ (chargeless boson only)

Table 6.1: Classification of interacting topological insulators. For both Kramers and non-Kramers fermions, SPT states made out of charge neutral bosons (e.g., spins) made out of the fermions are included, which gives a $\mathbb{Z}_2^2$ structure. The Kramers fermion has an additional non-trivial root phase coming from the free fermion topological insulator.

classifying all possible electron TIs. We focus on time reversal symmetric insulating phases of electrons with a conserved global charge (corresponding to a global $U(1)$ symmetry). These are the symmetries that protect the familiar electronic topological insulator. Non-interacting insulators with this symmetry in $3D$ have a well known $\mathbb{Z}_2$ classification so that there is only one non-trivial state[82].

The two spin-SPT root states described above, and their possible combinations with the $\theta = \pi$ TBI, give a total of 6 new topological insulating states with no band-structure analogs (see Table 6.1). While such spin-SPT phases can clearly exist, one might have also imagined that there could be new intrinsically fermionic TI phases arising from strong interactions. However, we give very general arguments that there are no other time reversal symmetric topological insulators of electrons in $3D$. In particular, the only intrinsically fermionic root state is the original and familiar one.

In total, there are a 8 electron phases. These phases have a natural algebraic group structure, where the group operation two phases can be combined by superimposing them and allowing electrons to tunnel between them. Under this operation, the electron topological insulators have a $\mathbb{Z}_2^3$ group structure, generated by 3 'root' states and taking combinations. These 3 root states are just the ordinary topological band-insulator, and the two root spin-SPT phases described above.

The symmetry class discussed above is for physical electrons which are half-integer spin objects, that transform non-trivially under the two-fold action of time-reversal ($T^2 = -1$ when acting on the electron operator, implying a Kramers doublet structure, even in the absence of spin-conservation). In the free-fermion limit, the Kramers structure is well understood to play a crucial role in allowing the topological band structure. In the interacting problem we first clarify the fundamental connection between the topological magnetoelectric effect and Kramers structure. To better understand the role of Kramers-structure it is interesting to consider topological insulators of artificial integer-spin fermions with $T^2 = 1$ (corresponding to integer spin). For such artificial particles, the classification reduces to $\mathbb{Z}_2^2$, reflecting the loss of an intrisically fermionic topological band insulator. These results are summarized in Table. 6.1, with the three non-trivial root states briefly described in Table. **??**.

Topological Insulator	**Representative surface state**	**$\mathcal{T}$-breaking transport signature**
Free fermion TI	Single Dirac cone	$\sigma_{xy} = \frac{\kappa_{xy}}{\kappa_0} = \pm 1/2$
Topological paramagnet I $(eTmT)$	$\mathbb{Z}_2$ spin liquid with Kramers doublet spinon(e) and vison(m)	None
Topological paramagnet II $(e_f m_f)$	$\mathbb{Z}_2$ spin liquid with Fermionic spinon(e) and vison(m)	$\frac{\kappa_{xy}}{\kappa_0} = \pm 4$

Table 6.2: Brief descriptions of the three fundamental non-trivial topological insulators, with their representative symmetry-preserving surface states, and surface transport signatures when time-reversal is broken on the surface. σ_{xy} is the surface electrical Hall conductivity in units of $\frac{e^2}{h}$. κ_{xy} is the surface thermal Hall conductivity and $\kappa_0 = \frac{\pi^2}{3}\frac{k_B^2}{h}T$ (T is the temperature). A more detailed description of the less familiar topological paramagnets can be found in the main text.

6.2.1 Generalities

For any fully gapped insulator in 3D, the effective Lagrangian for an external electromagnetic field obtained by integrating out all the matter fields will take the form

$$\mathcal{L}_{eff} = \mathcal{L}_{Max} + \mathcal{L}_{\theta} \tag{6.1}$$

The first term is the usual Maxwell term and the second is the 'theta' term:

$$\mathcal{L}_{\theta} = \frac{\theta}{4\pi^2}\mathbf{E}\cdot\mathbf{B} \tag{6.2}$$

where $\mathbf{E}$ and $\mathbf{B}$ are the external electric and magnetic fields respectively.

Under time reversal, $\theta \to -\theta$ and in a fermionic system the physics is periodic under $\theta \to \theta + 2\pi$. Time reversal symmetric insulators thus have $\theta = n\pi$ with n an integer. Trivial time-reversal symmetric insulators have $\theta = 0$ while free fermion topological insulators have $\theta = \pi$[106]. Suppose that for interacting electrons there is a new topological insulator that also has $\theta = \pi$. Then by combining it with the usual one we can produce a TI with $\theta = 0$. Thus without loss of generality we can restrict attention to the possibility of new TIs which have $\theta = 0$.

Let us consider the symmetry properties of monopole sources of the external magnetic field. At a non-zero θ, this elementary monopole carries electric charge $\frac{\theta}{2\pi}$ so that it is chargeless when $\theta = 0$. Under time reversal the monopole becomes an anti-monopole as the magnetic field is odd. Formally if we gauge the global $U(1)$ symmetry to introduce a dynamical monopole field m it must transform under time

reversal as

$$\mathcal{T}^{-1} m \mathcal{T} = e^{i\alpha} m^\dagger \quad (6.3)$$
$$\mathcal{T}^{-1} m^\dagger \mathcal{T} = e^{-i\alpha} m \quad (6.4)$$

However as explained in Ref. [85] by combining with a gauge transformation we can set the phase $\alpha = 0$. In particular the monopoles must be regarded as Kramers singlet. Physically this is because the time reversed partner of a monopole lives in a different topological sector with opposite magnetic charge and hence is not simply a Kramers partner.

Thus the symmetry properties of the bulk monopole are fixed. There are still in principle two distinct choices corresponding to the statistics of the monopole: it may be either bosonic or fermionic. We will consider them in turn below. Bosonic monopoles will be shown to allow for the topological paramagnets mentioned above and nothing else. Fermionic monopoles will be shown to not occur in strictly three dimensional systems built out of charge-1 electrons.

6.2.2 Topological insulators at $\theta = 0$ - bosonic monopoles

Consider the surface of any insulator with $\theta = 0$ and a bosonic monopole. We need to incorporate the consequences of this in an effective field theory of the surface. To that end it is extremely convenient to formulate the effective theory in terms of degrees of freedom natural when the surface is superconducting, *i.e*, it spontaneously breaks the global $U(1)$ but not time reversal symmetry. The suitable degrees of freedom then are $\frac{hc}{2e}$ vortices and (neutralized) Bogoliubov quasiparticles[89] (spinons) which have mutual semion interactions. In general we can also allow for co-existing topological order, i.e. other fractionalized quasi-particles, in the surface superconductor[5]. This gives a dual description of $2D$ electronic systems that is particularly convenient to studying not just the superconducting phase but also some topologically ordered insulating phases.

Now imagine tunneling a monopole from the vacuum to the system bulk. Since the monopole is trivial (chargeless and bosonic) in both regions, the tunneling event - which leaves a 2π-vortex (or $\frac{hc}{e}$ vortex in the usual units) on the surface - also carries no non-trivial quantum number. Hence the surface dual effective field theory has a $\frac{hc}{e}$-vortex that carries no non-trivial quantum number (chargeless and bosonic). We can therefore proliferate (condense) the $\frac{hc}{e}$-vortex on the surface which disorders the superconductor and restore the $U(1)$ symmetry. Since we can always choose a gauge to make $\mathcal{T}^2 = 1$ for vortices (or the corresponding bulk monopoles), the vortex condensate also preserves time-reversal symmetry. Hence we are left with an insulator with the full symmetry $U(1) \ltimes \mathcal{T}$ unbroken. However as is well known from dual vortex descriptions[88, 89] of spin-charge separation in $2D$, the resulting state has intrinsic topological order.

[5]Such a phase with coexistence of topological order and superconductivity was denoted SC* in Ref. [89].

Recent work on bosonic[84, 85, 86, 75] and fermionic[87, 7, 75, 76, 77] SPTs has emphasized the possibility of such intrinsic topological order at the surface of SPT states. The surface topological order of the SPT phases realizes symmetry in a manner not allowed in strictly $2D$ systems, and provides a particularly useful perspective. We will now study the surface topological order of the $\theta = 0$ fermion insulator with a boson monopole source as a route to access new fermion TIs.

Specifically, we prove that any electronic topological insulators with $\theta = 0$, and a bosonic monopole, can be reduced to a bosonic topological paramagnet. It is convenient to start with a symmetry preserving surface termination that has intrinsic topological order. Such a surface state is characterized by a set of anyons $\{1, c, X, \bar{X}, Y_I\}$ where I is a discrete label, and their corresponding braiding and fusion rules. Each anyon will be characterized by a sharply quantized charge q under the global $U(1)$ symmetry. Let us denote this topological information and symmetry assignments as the initial surface anyon theory: $\mathcal{T}_{\text{initial}}$.

A useful theoretical device is to consider creating a monopole source of an external (non-dynamical) magnetic field, and dragging that monopole through the topologically ordered surface at position $\mathbf{R}$. Such a monopole insertion event changes the external magnetic flux, Φ_B, piercing the surface by $\frac{2\pi}{e}$ (in units where $\hbar = c = e = 1$). When the monopole sits close to the under-side of the surface, this extra flux, $\delta\Phi_B$, is concentrated in the vicinity of $\mathbf{R}$. Suppose we take a surface excitation, Y, with fractional charge q_Y, and drag it around a sufficiently large loop that encloses (nearly all) the additional magnetic-flux from the monopole insertion. This process accumulates Berry phase $e^{2\pi i q_Y} \neq 1$ because of Y's fractional charge. However, the total monopole insertion event is a local physical process, and since there are no gapless excitations in the system it cannot have non-trivial action on distant events (clearly if Y is arbitrarily far from the $\mathbf{R}$, it should not be able to discern whether the monopole is infinitesimally above or infinitesimally below the surface). Therefore, if $\mathcal{T}_{\text{initial}}$ contains quasi-particles Y_I with fractional charge, q_I, the monopole insertion event must also create a quasi-particle of type X in the surface theory which has mutual statistics $\theta_{X,Y_I} = e^{-2\pi i q_I}$. This mutual statistics then exactly compensates the non-trivial Berry phase from encircling the additional flux from the monopole insertion, and ensures that the overall monopole insertion event does not have unphysical non-local consequences. Furthermore, since the bulk monopole is chargeless and bosonic, X, is a neutral boson.

We can similarly consider the time-reversed version of this process by inserting an anti-monopole from the vacuum into the bulk. Let us denote by $\bar{X}$ the particle nucleated at the surface. Clearly X and $\bar{X}$ are exchanged by $\mathcal{T}$, indicating that, like X, $\bar{X}$ is a charge-neutral boson. The mutual statistics of an anyon Y with $\bar{X}$ is then $e^{2\pi i q_Y}$. Further as the monopole and antimonopole can annihilate each other to give back the ground state $\bar{X}$ must be the antiparticle of X.

These mutual statistics indicate that driving a phase transition in which $X, \bar{X}$ condense will confine all fractionally charged particles. However, in general it is not guaranteed that the condensation of $X, \bar{X}$ preserves $\mathcal{T}$. To avoid this issue, we take a detour through an intermediate superconducting phase in which descendants of $X, \bar{X}$ can be safely condensed while preserving $\mathcal{T}$. This results in a topologically ordered

state, T_{final}, which has the desired structure of a neutral boson theory.

Our strategy is to first enter a superconducting phase obtained by condensing the physical Cooper pair, $b \equiv c_\uparrow c_\downarrow$, from T_{initial} and then to exit it through a different phase transition to reach the final topological order T_{final}. In the theory, T_{initial}, the Cooper pair is local with respect to all nontrivial anyons. Thus its condensation preserves the topological order T_{initial}. The resulting topologically ordered superconductor is conventionally denoted SC* (see Ref. [89]) to distinguish it from the ordinary non-fractionalized BCS superconductor, SC.

Let us denote the Cooper pair field by $b = \sqrt{\rho_b} e^{i\phi}$. A long-wavelength effective Lagrangian density for the theory can be written:

$$\begin{aligned}\mathcal{L}[b, X, \bar{X}, \cdots] = \frac{\rho_b}{2} (\partial_\mu \phi)^2 + \mathcal{L}_{T_{\text{initial}}}[X, \bar{X}, Y_I, \dots] \\ + \mathcal{L}_{\text{mixed}}[b, Y_I, \dots]\end{aligned} \tag{6.5}$$

where $\mathcal{L}_{T_{\text{initial}}}[X, \bar{X}, Y_I, \dots]$ is the Lagrangian density encoding the topological content of the topologically ordered phase, and $\mathcal{L}_{\text{mixed}} = \sum \lambda_{\{N_I\}} \prod_I \left(e^{iq_I \phi/2} Y_I\right)^{N_I}$ encodes all charge-conserving interaction terms between b and gauge-invariant combinations of operators in the topologically ordered theory. When b condenses to obtain a superconducting phase, apart from the original topological quasiparticles, there will also be quantized vortex excitations where the phase ϕ of b winds by $2n\pi$ with n an integer. Following the terminology of Ref. [89] we will call these vortons (to distinguish from the vortices of conventional superconductors without topological order).

We wish to disorder the superconducting order by condensing a suitable vortex to obtain the desired insulating surface theory T_{final}. This may be done in a dual effective field theory in terms of the vorton degrees of freedom. To formulate such a dual field-theory, it is very convenient to introduce "neutralized" fields: $\tilde{Y}_I = e^{iq_I \phi/2e} Y_I$, obtained by binding a fraction of the Cooper pair to Y_I. In terms of these neutralized variables:

$$\mathcal{L} = \frac{\rho_b}{2} (\partial_\mu \phi)^2 + \tilde{\mathcal{L}}[X, \bar{X}, \tilde{Y}_I] \tag{6.6}$$

The advantage of this choice of variables is now manifest, as the Cooper-pair phase ϕ is no longer directly coupled to the neutralized fields $\tilde{Y}_I$. The $\tilde{Y}_I$ however now acquire a phase $e^{\pi i q_I}$ on encircling an elementary vorton. Following the standard duality transformation, we can re-write the boson current $j_b^\mu = \rho_b \partial_\mu \phi$ as the flux of a gauge-field α_μ: $j_b^\mu = \frac{\varepsilon^{\mu\nu\lambda}}{2\pi} \partial_\nu \alpha_\lambda$. In the dual theory, the vorton field, denoted by v, is a bosonic field that couples minimally to this gauge field, and in addition has statistical interactions with the $\tilde{Y}$ particles:

$$\begin{aligned}\mathcal{L}_{\text{dual}} = &\frac{1}{8\pi^2 \rho_b} \left(\varepsilon^{\mu\nu\lambda} \partial_\nu \alpha_\lambda\right)^2 + \frac{1}{2} \left| \left(\partial_\mu - i\alpha_\mu - i a_\mu^I\right) v \right|^2 \\ &+ V(|v|^2) + \tilde{\mathcal{L}}[X, \bar{X}, \tilde{Y}_I] + \frac{\varepsilon^{\mu\nu\lambda}}{4\pi} a_\mu^I K_{IJ} \partial_\nu a_\lambda^J \\ &+ \ell_J^{(I)} a_\mu^J j_{Y_I}^\mu\end{aligned} \tag{6.7}$$

where the gauge fields, a^I, integer vectors $\ell^{(I)}$, and multi-component Chern-Simons term with K-matrix K_{IJ} capture the mutual statistics between the vortons and the fields Y_I. Here, $j^\mu_{Y_I}$ is the current of the Y_I particles, and $V(|v|^2))$ is a potential for the vorton field.

Now consider the particles $v^2X, \left(v^\dagger\right)^2 \bar{X}$. These carry vorticity ± 2 and are interchanged under time reversal. These are the relics of a monopole tunneling event in this superconducting state discussed in the main text. Due to the coupling of v to the dual gauge field, α_I, we may always choose a gauge such that time reversal is implemented as:

$$\mathcal{T}^{-1} v^2 X \mathcal{T} = \left(v^\dagger\right)^2 \bar{X} \tag{6.8}$$

$$\mathcal{T}^{-1} \left(v^\dagger\right)^2 \bar{X} \mathcal{T} = v^2 X \tag{6.9}$$

We may now condense $v^2X, \left(v^\dagger\right)^2 \bar{X}$ and preserve time reversal symmetry. The condensation also destroys the superconducting order and produces the desired new topological order T_{final}. Note that the neutralized particles $\tilde{Y}_I$ have no non-trivial mutual statistics with v^2X as the phase around the v^2 exactly cancels the phase around X. Hence they survive in T_{final} as quasiparticles. The vortex condensate however quantizes electric charge to be an integer. In particular the charge q bosons obtained by fractionalizing the Cooper pair $b_q = e^{\frac{iq\phi}{2}}$ are confined unless q is an integer. In effect the original electrically charged Y_I particles are confined to the fractional bosons to produce the neutral $\tilde{Y}_I$ particles. The vortons v also survive as particles in final but they are electrically neutral.

The detour through the superconductor essentially implements a 'charge-anyon' separation of the original topological theory T_{initial}. This is completely analogous to the conceptual utility of superconducting degrees of freedom in implementing 'spin-charge' separation in $2d$ insulators[89, 88]. Though we will not elaborate this here an alternately route from T_{initial} to T_{final} is through a parton construction where we fractionalize the charged anyons into a charged boson and a neutral anyon.

This proves that T_{final} only has integer charged quasi-particles. Without loss of generality, we may relabel the quasi-particle content of T_{final} by binding an appropriate number of electrons to each quasi-particle to remove the remaining integer charge. The resulting theory has quasi-particle content $\{1, v, \tilde{Y}_I\} \times \{1, c\}$, that can be decomposed into the direct product of a neutral boson sector $\{1, v, \tilde{Y}_I\}$ trivially accompanied by a gapped electron. This completes the desired proof that the $\theta = 0$ classification reduces to the classification of neutral bosonic phases.

Thus, from the previous section we see that for $\theta = 0$ and a bulk bosonic monopole source we have two root phases which can both be understood as Mott insulators in topological paramagnet phases. Adding to this the usual $\theta = \pi$ TI captured by band theory we have 3 root states corresponding to a $\mathbb{Z}_2^3$ classification. To establish that there are no other states we need to still consider the other possibility left open for the bulk response: a fermionic monopole.

6.2.3 On the (im)-possibility of fermionic monopoles

The possibility that the monopole may be fermionic in a system which also has fermionic charges is interesting and naively consistent with time-reversal symmetry. However we now show that such a state cannot occur in a strictly $3D$ system built out of charge-1 fermions. Crucial to our argument is the requirement of 'edgability' defined in Ref. [85]. Any theory that can occur in strictly d-dimensions (as opposed to the surface of an SPT in $(d+1)$ dimensions) must admit a physical edge to the vacuum. We will show that time reversal symmetric electronic systems with a fermionic monopole are not edgable.

First we construct a bulk state with the desired properties. Consider a Bose-Fermi mixture, with both the boson b and the electron c carrying charge-1. Now put the electron into a trivial band insulator, and the boson into a boson SPT state (labelled by its surface topological order $eCmC$). Then the charge-neutral external monopole source becomes a fermion[85, 75]. We initially consider such a system in a geometry with no boundaries. We then tune the boson charge gap to infinity, so that the charged bosons disappear from the spectrum, and we are left with a purely electronic theory. But since the fermionic monopole does not carry any boson charge, it survives as the only charge-neutral monopole. Now the bulk theory is exactly what we were looking for, but we need to examine its boundary and see if it is consistent with a time-reversal invariant electronic system.

As the electrons are in a trivial insulator they do not contribute anything special on the boundary, so we only have to worry about surface states of the $eCmC$ boson SPT. We first consider a symmetric surface state with topological order. It is known[84] that one of the possible surface states of the $eCmC$ boson SPT is described by a $\mathbb{Z}_2$ gauge theory with both e and m carrying charge-$1/2$ and the ϵ fermion being charge-neutral. By setting the boson charge-gap to infinity, the e and m particles disapppear from the spectrum, but the neutral ϵ fermion survives as a gauge-invariant local object, which is not allowed in a system purely made of charged fermions. Another way to see the inconsistency of the surface is to look at the surface state without topological order in which time-reversal symmetry is broken. The boson topological insulator leads to a surface electrical quantum hall conductance $\sigma_{xy} = \pm 1$ and thermal hall conductance $\kappa_{xy} = 0$.[84] The difference of σ_{xy}, κ_{xy} between the two time-reversal broken states should correspond to an electronic state in two dimensions without topological order. Here we have $\Delta\sigma_{xy} = 2$ and $\Delta\kappa_{xy} = 0$, which cannot be realized from a purely electronic system without topological order. Hence the boundary as a purely electronic theory is not consistent with time-reversal symmetry, and the bulk theory cannot be realized in strict three dimensions, although it may be realizable at the surface of a four dimensional system.

6.2.4 Surface-Transport Characteristics

The arguments above show that there are 8 distinct time reversal symmetric insulators of interacting electrons in 3D which are short range entangled in the bulk. We now discuss their distinct physical characterizations. A powerful conceptual distinction

between these 8 phases is in terms of the structure of the symmetry preserving surface state with intrinsic topological order. For the conventional band electron TI such a gapped symmetry preserving surface state has been discussed recently. However despite its conceptual utility such a surface topological order is currently not practical as an experimental tool in distinguishing these different phases, and it is useful to discuss other characterizations.

Of the 8 insulating phases, four have electromagnetic response $\theta = \pi$ (of which one is the topological band insulator) and four have $\theta = 0$ (of which one is the trivial insulator). Consider breaking time reversal on the surface to obtain an insulating surface state without topological order. The θ term in the response means that such a surface state will have quantized electrical Hall conductivity $\pm\frac{e^2\theta}{2\pi h}$. A further distinction is obtained by considering the thermal Hall effect κ_{xy} in this surface state. In general in a quantum Hall state $\kappa_{xy} = \nu_Q \frac{\pi^2}{3}\frac{k_B^2}{h}T$ where k_B, T are Boltzmann's constant and the temperature respectively. The number ν_Q is a universal property of the quantum Hall state.

Two of the $\theta = \pi$ insulators have $\nu_Q = \pm\frac{1}{2}$ (including the topological band insulator) while the other two have $\nu_Q = \pm\frac{9}{2}$. Similarly two of the $\theta = 0$ insulators (including the trivial one) have $\nu_Q = 0$ while the other two have $\nu_Q = \pm 4$. In all cases the *sign* of κ_{xy} is the same as σ_{xy}. Thus a combined measurement of electrical and thermal Hall transport when $\mathcal{T}$ is broken at the surface can provide a very useful practical (albeit partial) characterization of these distinct topological insulators.

6.2.5 Kramers fermions and $\theta = \pi$ topological insulators

We now discuss the role of the Kramers structure of the electron. For the free fermion topological insulator it is well known that the Kramers structure is what allows the topological insulator in the first place. Here we wish to address the role of the Kramers structure non-perturbatively directly from the electromagnetic response. What precise role, beyond free fermion band theory, does the Kramers structure of the electron play in enabling a $\theta = \pi$ response? On the face of it it appears that $\theta = \pi$ is still an acceptable response in a time reversal invariant insulator of non-Kramers (integer spin) fermions. However we now give a general argument showing that any gapped insulator with a $\theta = \pi$ response and no intrinsic topological order necessarily has charge carriers that are fermionic and are Kramers doublet.

Consider the fate of the state when the global $U(1)$ symmetry is gauged. The θ value of π now implies that the monopoles of the resulting $U(1)$ gauge field are 'dyons' (in the Witten sense) and have electric charge shifted from integer by $\frac{1}{2}$. Let us examine these dyons carefully.

For convenience we label particles by (q_m, q_e), where q_m is the magnetic charge (monopole strength) and q_e is the electric charge. Consider a strength-1 monopole (dyon) which carries charge-1/2 due to $\theta = \pi$, labeled as $(1, 1/2)$, which under time-reversal transforms to the $(-1, 1/2)$ dyon, since electric charge is even while magnetic

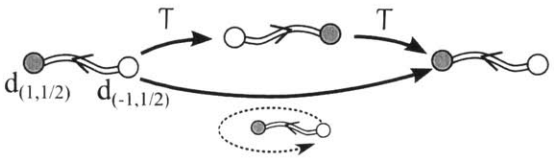

Figure 6-1: For $\theta = \pi$, a monopole and anti-monopole become charge-$\frac{e}{2}$ dyons. Acting twice with $\mathcal{T}$ is equivalent to rotating the pair by 2π, which gives Berry-phase -1 due to the half-angular momentum of the EM field of the dyon-pair.

charge is odd under time-reversal. More precisely, we have

$$\begin{aligned} \mathcal{T}^{-1} d_{(1,1/2)} \mathcal{T} &= e^{i\alpha} d_{(-1,1/2)} \\ \mathcal{T}^{-1} d_{(-1,1/2)} \mathcal{T} &= e^{i\beta} d_{(1.1/2)} \end{aligned} \tag{6.10}$$

where $d_{(q_m,q_e)}$ denotes the corresponding dyon operator. The exact value of the phase factor $e^{i(\alpha-\beta)}$ is not meaningful since it is not gauge-invariant (see Ref. [85] for a discussion).

Now let's consider the bound state of $d_{(1.1/2)}$ and $d_{(-1,1/2)}$, it has $q_m = 0$ and $q_e = 1$, which is nothing but the fundamental charge of the system. The crucial point here is that the two dyons see each other as an effective monopole. A quick way to see this is to view the $(-1, 1/2)$ dyon as the bound state of the electric charge $(0, 1)$ and $(-1, -1/2)$ which is the anti-particle of $(1, 1/2)$, hence the Berry phase seen by the $(-1, 1/2)$ dyon is the same as that seen by a charge from a monopole. Hence their bound state will carry half-integer orbital angular momentum and fermionic statistics. The half-integer angular momentum can also be obtained by calculating the angular momentum of the gauge field[90] which is given by

$$L = \frac{q_{e,1} q_{m,2} - q_{e,2} q_{m,1}}{2} = 1/2. \tag{6.11}$$

Hence we have established that the fundamental charge is a fermion. To determine whether or not the fermion is a Kramers doublet, we need to consider contributions from the internal and orbital degrees of freedom separately. The internal contribution follows readily from Eq. (6.11), which contributes to $\mathcal{T}^2$ by $e^{i(\beta-\alpha)} e^{i(\alpha-\beta)} = 1$. The orbital part contributes to $\mathcal{T}^2$ by -1 due to the half-integer angular momentum. More precisely, since time-reversal exchanges the two dyons, it is generated by a π-rotation along a great circle, hence $\mathcal{T}^2$ is generated by a 2π-rotation along a great circle, which picks up a Berry phase of π due to the mutual-monopole structure of the two dyons. Therefore we conclude that the fundamental charge must be a Kramers fermion, and there's no fermion SPT with $\theta = \pi$ made out of non-Kramers fermions. We emphasize that this argument is non-perturbative, and does not rely on results from free fermion theories.

Let us now briefly consider the question of confined phases obtained by condensing the dyons of the topological Mott insulator phase[107] whose low energy theory is precisely the gauged TI. Since the $(1, 1/2)$ and $(-1, 1/2)$ dyons see each other as

effective monopoles, they cannot condense simultaneously. Condensing one of them should confine the other, just as condensing monopoles will confine electric charges. Since time-reversal relates these two dyons, this implies that the dyons cannot condense (hence confine the gauge theory) without breaking time-reversal symmetry. That the condensation of either of the $(1, \pm 1/2)$ dyons breaks T-reversal was previously pointed[108]. Here we see that it is not possible to simultaneously condense both dyons. Thus the confined phase obtained from the topological Mott insulator necessarily breaks T-reversal and hence is an antiferromagnet.

In the absence of the $\theta = \pi$ TI for non-Kramers fermions ($T^2 = 1$) what are the possible TIs? The arguments advanced earlier go through as before and we again inherit the boson SPTs with symmetry $\mathbb{Z}_2^T$. One difference is that the Cooper pair topological insulator is now smoothly connected to a trivial insulator (rather than to a boson SPT with just $\mathbb{Z}_2^T$ symmetry). The surface topological order of this phase is the eCmC $\mathbb{Z}_2$ gauge theory where both e and m particles carry charge-1. By combining with the physical fermion either of these can be made into a trivial boson which can then condense to give a confined symmetry preserving insulating surface. Thus the classification for interacting non-Kramers fermion TIs with time reversal is $\mathbb{Z}_2^2$.

Before closing we remark that the classification of boson/fermion TIs with $U(1)$ and $\mathbb{Z}_2^T$ symmetries is closely related[85] to the problem of classifying time reversal symmetric $U(1)$ quantum spin liquids in $3D$. Indeed different such spin liquids may be thought of as different gauged SPTs. Our present results may also be readily interpreted as restricting the legal implementation of T-reversal on these $U(1)$ quantum spin liquids.

In summary we described all possible distinct interacting time reversal invariant topological insulators of electrons in $3D$. We showed that apart from the topological band insulator, these are obtained from root states which are Mott insulators whose spins form a bosonic SPT phase, *i.e*, are topological paramagnets. Together these 3 root states generate a group structure $\mathbb{Z}_2^3$ corresponding to 7 non-trivial topological insulators. We also clarified the fundamental connection between the $\theta = \pi$ response of the TI and the Kramers structure of the electron. Identifying these new electronic topological insulators in models/experiments is an important challenge for the future.

Chapter 7

Experimental Signatures: Anomalous Supercurrent

While the the strongly correlated topological paramagnetic phases described in the previous chapter are not sufficiently well understood to propose candidate materials or experimental probes, there are several known experimental systems that realize the more familiar topological band-insulator phase. It is therefore interesting to design experimental probes that are capable of probing the unusual properties of the topological band-insulator surface. A dramatic example is that, when proximitized by a conventional s-wave superconductor, the surface becomes a non-Abelian superconductor with non-Abelian defects carrying Majorana fermion bound-states.

Among the proposed material systems for realizing Majorana states, the superconductor (S)-topological insulator (TI) hybrid structure[34] has several distinctive features. First, as a parent phase for Majorana states, the S-TI interface is topologically nontrivial even at zero magnetic field. Consequently, the induced superconductivity on the topological surface states of a TI is immune to disorder[3]. This provides a robust route to realizing Majorana states at elevated temperatures. Second, by their topological nature, surface states of a TI extend throughout the entire sample boundary. The extended nature of such states has motivated us to propose a TI-based setup for detecting Majorana states.

In this chapter, we study anomalous Josephson current signatures of Majorana states in a superconductor-topological insulator thin film-superconductor junction under an applied magnetic field. Importantly, the superconductors and the TI film are arranged in such a way that induced superconductivity exists on both top and bottom surfaces of the TI. We will consider the device geometry shown in Fig. 7-1a. where the superconductors are deposited only on the top surface, and the superconductivity is transmitted to the bottom surface both through the bulk states (which are present in all experimentally realized TI materials), and around the side surfaces. Supercurrent through such SC-TI-SC junctions has been recently observed[111, 112, 113, 114, 115, 116].

Our main findings and the basic physics behind them can be stated in simple terms. Applying a magnetic field to the S-TI-S junction induces a one-dimensional array of Josephson vortices (one for each flux quantum piercing the junction). Each

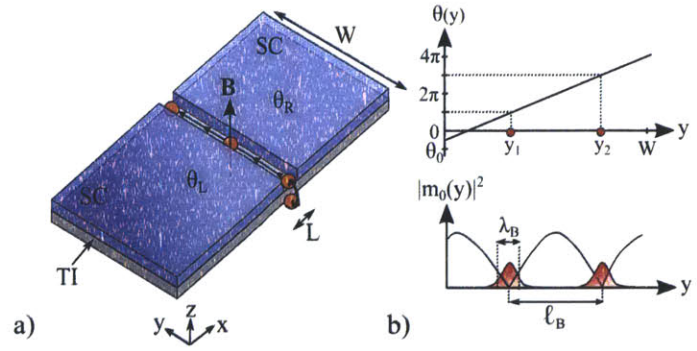

Figure 7-1: Panel a) shows a depiction of the device geometry considered in the text. The top surfac of the topological insulator (grey layer labeled TI) is in contact with the superconductors (blue layers), and the superconductivity is transmitted to the bottom surface through the bulk states. As the global-phase offset between the left and right superconductors ($\theta_0 = \theta_R - \theta_L$) is adjusted, Majorana modes (shown as red-circles) bound to Josephson vortices are created at one end of the junction, move along the junction, and fuse on the opposite side of the junction. Panel b) shows the local phase difference θ_y for along the junction $3\Phi_0 > \Phi_B > 2\Phi_0$ and fixed θ_0, and the corresponding mass term of Eq. 7.2. Wherever $\theta_y = \pi \mod 2\pi$, there is a local gap closing that binds a Majorana state.

vortex traps two localized Majorana states, one each on the the top and bottom surfaces of the TI. The two are aligned vertically (see Fig. 7-1). The global phase offset $\theta_{y=0}$ defined at a reference point $y = 0$ is an independent variable, which can be controlled in a SQUID geometry. For a given magnetic field, increasing θ_0 shifts the positions of the vortices and their bound Majorana states along the junction, towards one edge of the TI sample. As a Josephson vortex approaches the edge, the wave-functions of the Majorana states on the top and bottom surfaces overlap on the *side* surface. The states thereby hybridize, splitting from zero-energy and eventually annihilating each other.

This phase dependent splitting gives rise to a supercurrent carried by the Majorana states. When the magnetic flux through the junction is (close to) an integer multiple of flux quanta, the normal contribution to the supercurrent oscillates with position y along the junction and (nearly) cancels to zero, and the supercurrent carried by the Majorana states can dominate. This leads to a narrow peak in Josephson current as a function of phase difference (see Fig.1d).

7.1 Model and Majorana Bound States -

We now derive the Majorana states and the Josephson current-phase relation for a *short* and *wide* S-TI-S junction, under the condition $L < \xi < W$ where L is the length of the junction, W is the width, and ξ is the coherence length of topological surface states with proximity-induced superconducting gap. Moreover, for simplicity we consider the case that the Josephson current is unable to screen the external magnetic field.

The Hamiltonian for the top surface of the S-TI-S junction is

$$H = \int d^2\mathbf{r}\psi^\dagger(\mathbf{r})\left[v\hat{z}\cdot(\boldsymbol{\pi}\times\mathbf{s}) - \mu(\mathbf{r})\right]\psi(\mathbf{r}) + \left[\Delta(\mathbf{r})\psi_\uparrow^\dagger(\mathbf{r})\psi_\downarrow^\dagger(\mathbf{r}) + \text{h.c.}\right] \tag{7.1}$$

Here, $\pi_j = -i\partial_j - eA_j(\mathbf{r})$ $(j = x, y)$, and $\psi(\mathbf{r}) = (\psi_\uparrow(\mathbf{r}), \psi_\downarrow(\mathbf{r}))$ describes the TI surface states, which have a Dirac dispersion with Fermi velocity v. Due to doping from the superconductors, the chemical potential in the superconducting region $\mu(\mathbf{r}) = \mu'$ at $|x| > L/2$ is different from the junction area $\mu(\mathbf{r}) = \mu$ at $|x| < L/2$. $A_j(\mathbf{r})$ is the vector potential associated with the magnetic field B. It is convenient to chapter in the Landau gauge $A_x = 0$. $A_y(\mathbf{r})$ is then given by $A_y(\mathbf{r}) = -Bx$ for $|x| < L/2$, $-BL/2$ for $x > L/2$ and $BL/2$ for $x < -L/2$. In this gauge, the superconducting gap is: $\Delta(\mathbf{r}) = \Delta e^{i\theta_y/2}$ for $x > L/2$, $\Delta e^{-i\theta_y/2}$ for $x < -L/2$, and 0 for $|x| < L/2$. The phase winding $\theta_y = \pi y/l_B$ ensures zero supercurrent along the y direction in the superconducting region. Here, the magnetic length is defined as: $l_B = W\frac{\Phi_0}{\Phi_B}$, where Φ_B is the magnetic flux through the junction.[1]

Since $\Delta(\mathbf{r})$ varies slowly with the position y, we use semiclassical method to first solve the Hamiltonian without the kinetic energy term $-iv\partial_y s_x$ at an arbitrary y. This one-dimensional problem was previously solved for TI Josephson junction[34] and for a related problem in graphene[119]. When the junction length L is shorter than the coherence length $\xi \equiv v/\Delta$, there is a single pair of subgap Andreev bound states at energy $\pm E(y)$, where $E(y) = \Delta\cos(\theta_y/2)$ depends on the local phase difference and oscillates with the position y (see Fig. 7-1b).

Taking the kinetic energy along the $y-$direction into account gives the following effective Hamiltonian for the junction, written in terms of two branches of counter-propagating Majorana fermions $\gamma_{L,R}$ is then:[34]

$$H_{\text{eff}} = iv_M(\gamma_L\partial_y\gamma_L - \gamma_R\partial_y\gamma_R) + iE(y)\gamma_L\gamma_R, \tag{7.2}$$

The velocity v_M depends on intrinsic properties of the junction. For a ballistic junction, it was found that $v_M \simeq v(\Delta/\mu)^2$ for $\mu = \mu'$ in Ref.[34] and $v_M \simeq v(\Delta/\mu)\sin(\mu L/v)$ for $\mu \ll \mu'$ in Ref.[119].

To analytically examine the Majorana bound-state structure, it is instructive to consider the region near a level crossing point $y = y_1$, where $E(y) \approx \pi\Delta(y - y_1)/l_B$. The bound state energy $E(y)$ corresponds to the hybridization between the two Majorana states, and vanishes linearly at $y = y_1$. The sign reversal of $E(y)$ as a function of y gives rise to a zero-energy Majorana bound state that is spatially localized in the

[1]Flux expulsion from the superconductors can concentrate flux into the junction region. Consequently the magnetic flux through the junction, Φ_B, defines an effective area: $A_{\text{eff}} = \Phi_B/B$ which is in general different than the geometry area $W \times L$.

junction at the position y_0. The corresponding Majorana operator γ_1 is given by:

$$\gamma_1 = \int dy \frac{e^{-(y-y_1)^2/2\lambda_B^2}}{\sqrt{2\pi\lambda_B^2}} \frac{1}{\sqrt{2}} [\gamma_L(y) + \gamma_R(y)] \tag{7.3}$$

where the decay length in the y direction λ_B is: $\lambda_B = \sqrt{v_M l_B/\pi\Delta}$. This Majorana state is confined by the TI band gap in the z direction, the proximity-induced superconducting gap in the x direction, and the magnetic-field-induced linear potential $E(y)$ in the y direction. The decay length in the z direction is given by the penetration depth of topological surface states into the bulk, which is typically a few nanometers. The decay length in the x direction is given by the coherence length ξ (typically a few hundred nanometers).

Since Δ/μ is typically of the order 10^{-3}, the decay length of Majorana states λ_B along the junction is much smaller than their separation, and the overlap of two Majorana states along the junction is negligible, except when a pair of them nears the edge of the TI.

Near each π-crossing the zero-energy Majorana state is accompanied by other non-zero energy Andreev-bound-states (ABS's). Approximating the mass term by a linear potential, $E(y) = \pi\Delta(y-y_1)/\ell_B$, (valid in the vicinity of $\theta(y) \approx \pi$), these ABS's have energies $\pm E_n$, where $E_n \approx \sqrt{2\pi n v_M \Delta/l_B}$, $n = 1, 2, \ldots, n_{\max}$, and $n_{\max} \approx \ell_B\Delta/v_M$.

We also support this analytical picture by numerically computing the spectrum of Andreev bound-states discretizing Eq. 7.2 on a finite lattice of spacing a, with $E(y) \approx \Delta \cos\left(\frac{\pi y}{\ell_B}\right)$. In this simulations, we used realistic parameters of v_F and Δ for an Al/Bi_2Se_3/Al junction, and junction geometry comparable to that in Ref. [114, 115, 116]. While μ for Bi_2Se_3 is typically $\approx$ 0.1eV, for simplicity, we illustrate the case for smaller $\mu \approx$ 10meV which can readily be achieved by gating[116, 111]. The Andreev bound-state spectrum are shown in Fig. 7-2 for half a magnetic flux quantum (left panel) and a single magnetic flux quantum (right), and are well described by the simplified analytical picture developed above.

7.2 Contrast to Conventional Junctions

Low-energy Andreev bound-states can also occur near π phase difference in conventional metallic Josephson junctions under ideal conditions. For a transparent superconductor-normal interface, and in the absence of spin-orbit coupling, a conventional 2D metallic junction can be thought of as two separate copies of Eq. 7.2 one for right moving spin-up electrons and left-moving spin-down holes, and another for the corresponding time-reversed partners. This would lead to low-energy ABS's bound to Josephson vortices similar to those described above, except doubly degenerate.

However, in practice normal scattering at the S-N interface (for example due to the chemical potential mismatch in S and N region) and spin-orbit coupling will push ABS up in energy towards the bulk gap Δ, and even completely remove them in a short Josephson junction. In contrast, the helical nature of the TI surface state gives rise to topologically protected ABS's. Therefore, in the short-junction limit,

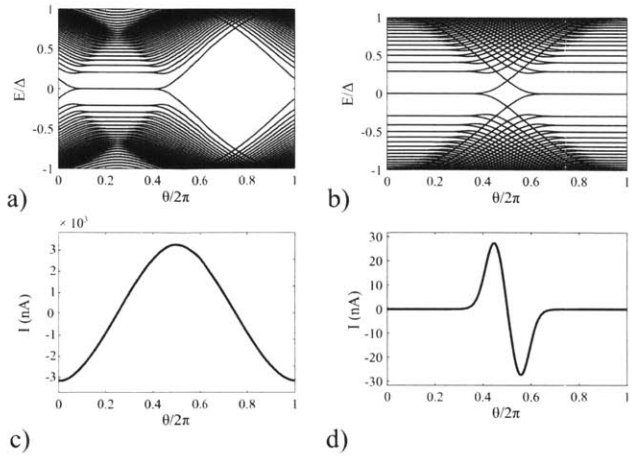

Figure 7-2: Numerical computation of the Andreev bound-state spectrum, and Josephson current for Eq. 7.2 with the parameters $v_F = 4.2 \times 10^5$m/s, $\mu = 10$meV, $\Delta = 151\mu$eV, and $W = 2\mu$m relevant for Al/Bi_2Se_3/Al junctions. Panels a and b show the low-lying Andreev bound-state spectrum as a function of phase difference θ between the superconductors for $\Phi_B = 0.5\Phi_0$ and $\Phi_B = \Phi_0$ respectively. The Josephson current corresponding to a) and b) are shown in panels c) and d) respectively. Panel d) displays the characteristic sharp peak-dip structure from topological Andreev bound-states fusing at the edge of the junction, as discussed in the text.

the Josephson signatures described below are particular to the special properties of the S-TI-S junction.

7.3 Josephson Current

Having discussed the structure of low-energy Andreev bound-states in the junction, we now analyze their effect on Josephson current. When the number of magnetic flux quanta, Φ_B/Φ_0, is not close to a non-zero integer then the Josephson current is carried predominately by conventional states (extended states with $E > \Delta$, and non-zero energy ABS's) and shows a nearly sinusoidal current phase dependence (see Fig. 7-2a). Near integer values of flux quanta, $\Phi_B/\Phi_0 = \pm 1, \pm 2, \text{etc}\ldots$, however, the conventional contribution becomes vanishingly small.

In this regime, the Majorana bound-state contribution to Josephson current dominates. For simplicity, we will first describe the situation for $\Phi_B = \Phi_0$ (see Fig. 7-2b). The case of $\Phi_B = N\Phi_0$ is similar. When $\Phi_B = \Phi_0$, and $\theta_0 \neq \pi$, there is exactly one Josephson vortex piercing the junction, which binds Majorana modes at $y_0 = \frac{W}{2}(1 - \frac{\theta_0}{\pi})$ on both the top and bottom surfaces of the TI. These Majorana modes hybridize by tunneling into each other around the perimeter of the junction. The resulting energy splitting is exponentially suppressed as $e^{-2\min[y_0,(W-y_0)]/\lambda_B}$, and is negligibly small when the position of Majorana modes y_0 is more than a few λ_B away from the edges of the junction. In this regime, the splitting is insensitive to y_0 and θ_0, and the Majorana modes do not contribute to the Josephson current.

In contrast, when $\theta_0 \approx \pi$, $y_0 \approx 0$ and the Majorana states are strongly coupled near the edge and split away from zero-energy. If the junction height $h \lesssim \lambda_B$, then we may ignore then finite thickness of the TI film, and the Majorana states are split by energy $\delta E_M \approx \sqrt{\frac{v_M \Delta}{\ell_B}}$. As θ_0 approaches π from below, the Majorana states move towards the junction edge at $y = 0$ and begin to fuse and split when $\theta_0 \approx \pi\left(1 - \frac{\lambda_B}{W}\right)$. Increasing θ_0 beyond π causes a different set of Majorana states to emerge from near $y = W$, and move to decreasing y, reversing the process that occurred near $y = 0$ for $\theta_0 > \pi$. The hybridization of Majorana states at the two edges gives rise to local supercurrents in *opposite* directions. At $\theta_0 = \pi$, the splitting of Majorana states is large, but supercurrents from two edges cancel. Slight deviation from $\theta_0 = \pi$ tips the balance by increasing the magnitude of supercurrent at one edge and suppressing the other, thereby generating a nonzero total supercurrent. The sensitivity of the Majorana splitting energy to the phase difference implies that the Majorana states contribute a peak in the Josephson current near $\phi_0 \approx \pi\left(1 - \frac{\lambda_B}{W}\right)$ followed by a dip in the Josephson current near $\phi_0 \approx \pi\left(1 + \frac{\lambda_B}{W}\right)$ (see Fig. 7-2d.).

By these considerations, we find that the maximal supercurrent carried by the Majorana state is $I_M \approx \frac{2\pi}{\Phi_0}\frac{\delta E_M}{\delta \theta_0} \approx \Delta/\Phi_0$, which for Al SC layers is $I_M \approx 10\text{nA}$. This result is largely independent of details. In particular it is completely independent of v_M, μ, W, and L (though it can depend slightly on finer details such as the degree of asymmetry between the top and bottom surfaces, or between the two edges). The Majorana current $I_M \approx \Delta/\Phi_0$ roughly corresponds to the maximal amount of Josephson current carried by a single quantum channel[121]. By comparison, for junctions of a few μm in width, such as those measured in Ref. [114], there are roughly $k_F W \approx 10^2 - 10^3$ quantum channels in the entire junction. Consequently, the Majorana contribution to Josephson current, which dominates near an integer flux quanta, is $10^{-2} - 10^{-3}$ smaller than the maximum supercurrent for zero flux quanta. These expectations are born out in detail by numerical simulations of Eq. 7.2 (see Fig. 7-2).

The situation is similar when a larger integer number, N, of magnetic-flux quanta pierce the junction. Here, there are N Josephson vortices, each with a bound Majorana state. For $N \ll \frac{W}{\lambda_B}$, the splitting of these states from tunneling between Majoranas is negligible, except in the vicinity of $\theta_0 \approx \pm\pi$ where Majorana states fuse and annihilate at the edges of the junction. A similar peak-dip current-structure is observed for higher integer number of flux, N, with maximal current $I_M \approx \frac{\Delta}{\Phi_0}$ independent of N, and with the peak (dip) width $\delta\theta \approx \frac{\pi\lambda_B}{N\ell_B}$.

Like the Majorana zero-modes, as $y_1 \to 0, W$, the non-zero energy ABS's on the top and bottom surfaces hybridize and split. However, unlike the Majorana modes, both branches of the hybridized finite-energy ABS's are occupied and tend to give opposite and cancelling contributions to the Josephson current (see Fig. 7-2).

Fig. 7-3 shows the current phase-relation for various values of flux through the junction. The Majorana mode contribution only starts to become visible for flux within $\approx 5\%$ of a single flux quantum (see right panel of Fig. 7-3). This contribution appears initially as a shoulder on the background sine-curve, which strengthens and becomes dominant within 1% of a single flux quantum. Finally, the critical current,

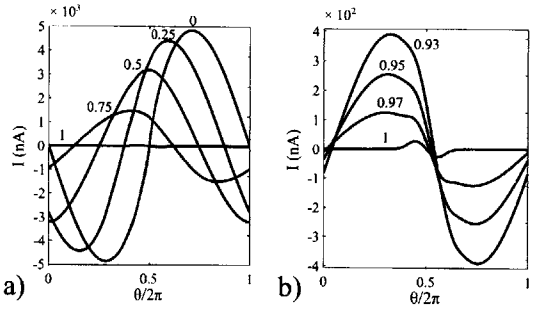

Figure 7-3: Current-phase relationship for the parameters listed in Fig. 7-2 for a wide range of flux, Φ, (left) and for Φ_B within a few percent of Φ_0 (right). Each curve is labeled by value of Φ_B/Φ_0. The Majorana contribution to the Josephson current becomes appear as a shoulder in the curves of the right panel which grows and eventually dominates very close to $\Phi = \Phi_0$.

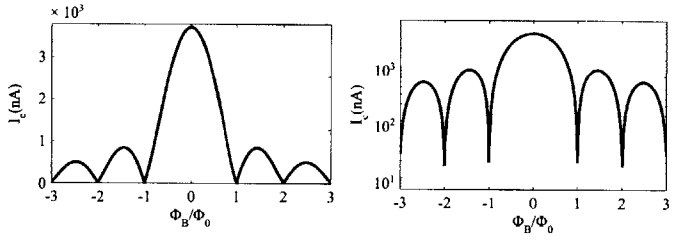

Figure 7-4: Critical current, I_C, as a function of flux, Φ_B in linear (left) and log- scale (right). The curve is quite close to the conventional Frauenhofer pattern, with the exception that I_C does not vanish at integer number of flux quanta due to the extra contribution of the Majorana bound-states (as can be seen in the log-scale plot).

I_C, as a function of flux through the junction. I_C nearly follows the characteristic Frauenhofer pattern, except that I_C does not vanish for integer flux due to the Majorana contributions to the Josephson current. In the experiments of Ref. [114], the avoided zero in the Frauenhofer pattern is substantially larger ($\approx$ 10% of the maximal I_C). As described below (and also in the suppplemental information), this discrepancy can be explained by accounting for the non-negligible thickness of the TI film in these experiments.

7.4 Discussion of Experimental Issues

Up to now we have assumed that the thickness, h, of the TI film is smaller than the size of the Majorana states, λ_B. In practice, λ_B is at most a few tens of nanometers. For thicker films with $h > \lambda_B$, the side of the TI may host additional states compared to $h = 0$ when the phase difference at the edge is close to π. As shown in Fig. 7-5, these states will conduct Josephson current, as their energies are sensitive to the phase difference along the sides of the junction. Like the Majorana contribution described above, the contribution of current from these sides can dominate when there are close to an integer number of magnetic-flux quanta piercing the junction. Unlike the Majorana contribution however, these states exhibit a more conventional sinusoidal

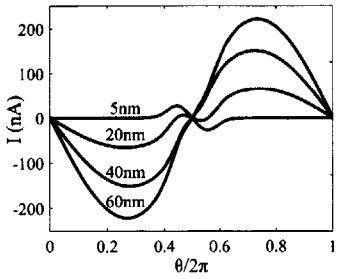

Figure 7-5: Current-phase relationship for a single magnetic flux, and varying TI thickness h = 0nm, 20nm, 40nm, and 60nm. Thicker sides tend to contribute conventional Josephson signatures that mask the topological Andreev-bound-state contributions.

current-phase relationship, rather than a sharp peak-dip structure (see Fig.7-5).

Therefore, for the purpose of observing Josephson-current signatures of Majorana fermions, it is advantageous to make the TI film as thin as possible without strongly hybridizing the top and bottom surfaces. Since the confinement length in the z-direction is only a few nanometers, this last constraint is not too severe. Furthermore, it is advantageous to limit the junction width W (while maintaining $W > \lambda_B$) in order to suppress the contributions from conventional extended states (which scales as $I \sim W$, in contrast to the width independent contribution from the Majorana bound-states).

Lastly, while we have mainly considered the geometry shown in Fig. 7-1, where superconductors are deposited on the top and bottom surfaces. In practice it is easier to fabricate devices where superconductors are deposited only on the top surface. As described above, we expect our analysis to also apply to this simpler to fabricate geometry, so long as the TI thickness is less than a coherence length, and so long as superconductivity is transmitted from top to bottom surfaces via either bulk TI states or boundary states on side surfaces. The main difference from the case discussed in the text is that there will be a non-zero hybridization of the ABS's on the top and bottom surfaces through the bulk. Nonetheless, in this case the energy splitting of the top and bottom ABS's is position independent, which will not qualitatively alter the Josephson signatures discussed above so long as the splitting is much smaller than the bulk gap Δ.

Throughout this chapter we have implicitly assumed that the system is in its ground state. Finite temperature will not qualitatively alter our results, provided $T < \delta E_M$. Deviations from ground-state behavior may also occur due to sources of single electrons, such as localized impurity states near the junction. When the Majorana states are far from the junction edge, their mutual fermion parity can be switched by tunneling to local single-electron sources. After such a parity switching, the Majorana modes will follow the positive energy branch as they approach the junction boundary and fuse, thereby contributing the opposite sign of Josephson current compared to the equilibrium case discussed above. Such parity switching events can thereby lead to hysteretic current-phase behavior, whose observation would provide strong evidence for the Majorana character of the Andreev bound-states in

the junction.

Part III

Gapless Spin-Liquids

The previous two sections concerned themselves only with gapped states. The topological superconductor and SPT phases examined there had non-trivial topological properties, which require some amount of care and thinking to deduce, but from a technical standpoint, these phases are quite simple to describe, as their low energy effective field theories contain only gapped, sharply defined quasi-particle excitations. In this Chapter, we venture out of the safety and comfort of gapped phases with simple quasi-particle excitations to make a foray into the most highly-entangled and complex known phases of matter: gapless non-Fermi liquids.

Despite a long history of theoretical attempts, these phases remain somewhat poorly understood. Known numerical techniques are of little use for non-Fermi liquids. Monte-Carlo methods general suffer from a sign problem. A large degree of entanglement is in some sense the defining feature of a non-Fermi-liquid, and makes such systems poorly suited for DMRG methods valid for short-range entangled states.

Some progress has been made with analytic theories, but these theories are typically quite challenging to analyze. Field theoretic descriptions of non-Fermi liquids typically involve strong coupling between gapless highly-fluctuating bosonic modes (e.g. quantum-critical order parameters or emergent gauge-fields), and a finite density of gapless fermion excitations, and are inherently non-perturbative. Traditional non-perturbative methods such as large-N expansions or dimensional regularization that have proven successful in other strongly-correlated systems, generically fail for non-Fermi liquids[145, 146, 147]. In one case, a controlled calculation scheme was constructed by introducing a large number of fermion flavors and artificially modified boson dynamics[147]. While useful, to describe the real systems in question, these sorts of approximations must inevitably be extrapolated outside their region of valididity, and it is often difficult to extract answers with confidence.

Such difficulties pose an interesting thoeretical challenges, but the issue of constructing theories for non-Fermi liquids is not just a matter of esoteric interest. Important experimental examples exist, most famously the strange-metal phase of high-temperature cuprate superconductors. The experimental existence of exotic gapless phases of matter demands a deeper understanding of these phases. Fortunately, experimental access to material candidates offers an important opportunity to put uncontrolled aspects of theories to the test.

This Part of the thesis will focus on a particular class of recently discovered materials whose ground-states appear to be a particular brand of non-Fermi liquids known as gapless quantum spin-liquids (QSLs). These are ground-states of interaction driven Mott insulators, in which the electron spins have locally antiferromagnetic interactions, but where strong quantum fluctuations prevent long-range magnetic order.

We first discuss weak Mott insulators, in which strong fluctuations come from a combination of both geometrical frustration and charge-fluctuations due to close proximity to a Mott transition. Known experimental materials of this type include two organic charge-transfer salts known as $\kappa-$ET and dMIT, which can be essentially described by a single-orbital triangular lattice Hubbard model[14, 15]. Thermodynamic and transport measurements on these materials reveal the presence of a finite density of mobile gapless excitations that carry spin but not charge[14, 15]. These measurements are broadly consistent with a theoretically proposed spinon Fermi-surface

phase[137, 136] (though finer-details remain to be sorted out). Numerical studies of related models suggest that such a spinon Fermi-surface state is stabilized by strong charge fluctuations[137, 190], which are generated by close proximity to a continuous or nearly-continous metal-insulator transition(MIT). Based on these lessons, we propose looking for a spin-liquid near the vicinity of a different continous MIT known to occur in randomly doped semiconductors. In addition to shedding new light on the random-Anderson/Mott transition, and providing another interesting example of gapless spin-liquid behavior, the discovery of a QSL phase in these materials would provide a powerful, though indirect, test of the lessons thought to have been learned from the organic materials. To this end, we outline a some experimentally testable consquences of such a scenario. Apart from the introductory sections, the work presented in Chapter 8 essentially follows Ref. [10], except that the supplementary material of that paper has been blended into the main text in order to provide a more detailed account.

In the subsequent chapter, we study a second example of a material with a QSL ground-state: Herbertsmithite, which is a spin-1/2 antiferromagnetic system with structurally perfect Kagome lattice layers. Unlike the organic triangular-lattice materials, Herbertsmithite resides deep in the Mott insulating phase and the spin-liquid behavior in this system is thought to arise purely from the highly-frustrated Kagome lattice structure. QSLs arising near a Mott transition are continously connected to a metal with a Fermi-surface, suggesting that the resulting QSL is closely related to the metal, e.g. by having a Fermi-surface of neutral spinon excitations. In contrast, QSLs in strong Mott insulators, like Herbertsmithite, need not be closely connected to a metallic state, and there is less a priori theoretical guidance for choosing a state. Consequently, many different states have been proposed and examined. Of these, the energetically dominate contenders are a gapped $\mathbb{Z}_2$ spin-liquid with intrinsic topological order, and a gapless spin-liquid with Dirac-cone band-structure for spinon excitations. Whereas numerical evidence favors the former, experimental probes see no sign of an excitation gap for Herbertsmithite. Unfortunately, the existing experimental data is complicated by impurity effects and has not yet been able to clearly pin-down the correct theoretical picture. In the second subsequent chapter, we develop optical conductivity as a new possible measurement technique that will be less sensitive to these complications. This work is motivated in large part by recent experiments at MIT, which show substantial low-frequency optical absorption in Herbertsmithite which is likely due to low-energy spin-excitations of the spin-liquid ground-state. The work of Chapter 9 closely follows Ref. [11] with only slight modification and added introductory material.

Chapter 8

Gapless Fractionalized Phases I: Weak Mott Insulators

8.1 Hubbard, Heisenberg, and Ring-exchange

Spin-liquid behavior tends to develop in Mott insulating materials with a single active orbital per site, otherwise orbital degeneracies can be exploited to alleviate frustration in which case symmetry breaking order tends to occur. The essential physics of such single orbital Mott insulators is captured by the deceptively simple fermionic Hubbard model:

$$H_{\text{Hubbard}} = -\sum_{\langle ij\rangle,\sigma}\left(t_{ij}c^{\dagger}_{i,\sigma}c_{j,\sigma} + \text{h.c.}\right) + \frac{U}{2}\sum_{i} n_i(n_i - 1) \tag{8.1}$$

Here, $c_{i,\sigma}$ is the electron operator at site i with spin $\sigma \in \{\uparrow,\downarrow\}$, t_{ij} describes hopping between sites i and j, and U is the energy for doubly occupying a site. The filling is assumed to be such that there is one electron per site on average.

Except in special cases, such as the square lattice, for which the Fermi-surface has a singular density of states, this model realizes a metallic phase in the weakly interacting limit $U \ll t$. By contrast, for $U \gg t$, the ground-state is clearly dominated by configurations with a single particle for each site. For a single electron per site, this phase will then be insulating, as mobile excitations inevitably require continuous double-occupation, which is energetically costly.

Nevertheless, even in this strongly insulating $U \gg t$ limit, a single, degenerate spin-1/2 degree of freedom is left at each site. For $U \gg t$, one can perturbatively integrating out virtual double occupancies to obtain an effective model purely in terms of electronic spins, $\mathbf{S}$:

$$H_{\text{Heisenberg}} = \sum_{\langle ij\rangle} J_{ij}\mathbf{S}_i \cdot \mathbf{S}_j \tag{8.2}$$

where, in the $U \gg t$ limit, the exchange coupling J is given by:

$$J \approx \frac{4t^2}{U} + \mathcal{O}\left(\frac{t}{U}\right)^3 \tag{8.3}$$

8.1.1 Geometric Frustration

On simple bi-partite lattices, like the square lattice, the above Heisenberg model of Eq. 8.2, admits a simple Neel-type antiferromagnetic ground-state with spins up on one sub-lattice and down on the other. On such lattices this simple colinear antiferromagnet (AFM) state is typically the ground-state, as it is the optimal classical configuration that maximally satisfies J on every bond.

In contrast, for lattices with triangular motifs, there is not such simple classical-type Neel arrangement in which neighboring spins are fully anti-aligned. Lattices with this property are called geometrically frustrated. In certain extremely frustrated lattices, like the Kagome lattice system described in the next chapter, geometric frustration and quantum fluctuations of the spin-1/2 moments alone are sufficient to prevent long-range AFM order and produce a QSL state.

8.1.2 Charge-Fluctuations

Though geometrical frustration appears to be a necessary ingredient for producing a QSL, it is generally not sufficient. For example, the triangular lattice is clearly frustrated, however the ground state of the pure Heisenberg model on the triangular lattice has co-planar AFM order where neighboring spins are rotated from eachother by 120-degrees.

However, this statement is strictly true only in the $U \gg t$ limit. If we reduce U within the Mott insulating phase, the higher-order in $\frac{t}{U}$ corrections begin to play an increasing role. Apart from renormalizing J, the first non-trivial contribution in powers of $\frac{t}{U}$ comes from processes in which electrons hop in a circle around a 4-site plaquette[1]. In the spin-model this corresponds to a ring-exchange term:

$$H_{\text{ring-exchange}} = K \sum_{ijkl} P_{ijkl} + \text{h.c.} \tag{8.4}$$

where the operator P_{ijkl} cyclically permutes the spin in the CCW sense around a plaquette with corners $ijkl$, and $K \approx \mathcal{O}\left(\frac{t^4}{U^3}\right)$. Such ring-exchange processes frustrate the tendency towards AFM order, and there is a growing body of evidence that sufficiently large K can produce QSL behavior.

Consequently, except for extreme examples of frustrated lattices, like the Kagome lattice, obtaining a spin-liquid phase requires working in the weak-Mott insulator regime where U is not too much larger than t. In many cases, especially in Mott transitions to magnetically ordered phases, Mott transitions are first-order. However, it is possible for the Mott transition to be a continuous second order transition, or

[1] or, the next smallest plaquette-type for lattices without 4-site plaquettes

at least be a nearly continous weakly first-order phase transition. In the latter case, as the Mott transition is approached by reducing U this, and longer-range, ring-exchange processes become increasingly important, until eventually they quantum-melt the Mott insulator to produce a metal. In these cases, an excellent place to look for QSL phases is the weak Mott insulating phase just on the insulating side of such a continuous metal-insulator transition.

8.1.3 Gapless Spin-Liquids in Organic Materials

The compounds κ-(BEDT-TTF)$_2$Cu$_2$(CN)$_3$, and EtMe3Sb[Pd(dmit)$_2$]$_2$ (henceforth abbreviated κ-ET and dmit respectively) are layered Mott insulator compounds consisting of an array of large organic molecules that can essentially be thought of as a (slightly-anisotropic) triangular lattice, with a single active electronic orbital degree of freedom on each site[14].

These materials are charge-insulators with activated temperature dependence in electrical conductivity, but which have gapless, conducting spin-excitations[14, 15]. The thermodynamic and thermal-transport properties associated with these gapless spin-excitations are peculiar, and lead to thermodynamic properties (spin-susceptibility, NMR relaxation rate, heat-capacity etc...) having the same universal temperature dependence as those in a metal[14].

Moreover, thermal conductivity measurements also show that the spin-excitations are mobile and conduct heat, giving rise to thermal conductivity $\kappa \sim T$ that scales linearly with temperature at low temperatures (see Fig. 8-1c).[2]

Together, these measurements show that these organic spin-liquid candidates behave like a metal, from the point of view of magnetic and thermal excitations, but are insulating from the electrical point of view, indicating a state with a finite density of states for extended, gapless spin excitations. The only other known states with a finite density of extended gapless states are metals with a Fermi-surface. This strongly suggests that the organic QSL materials can be thought of as having fermionic spin-excitations dubbed "spinons", that form a Fermi-surface.

Such a phase is most conveniently described in the slave-boson language[135, 136], reviewed in Appendix A, in which the electron operator is written as $c_{i,\sigma} = e^{i\phi_i} f_{i,\sigma}$. The gapless QSL state with a spinon-Fermi-surface is described by placing f_σ into a band-structure with a full Fermi-surface, and placing $b = e^{i\phi}$ into a Bose-Mott insulating phase with $\langle b \rangle = 0$[136]. The low-energy effective field theory of this state involves a gapless spinon Fermi-surface interacting with a gapless bosonic emergent gauge-field a_μ.[137]

The spinons have a large phase-space for transverse scattering off of gauge excitations[138, 141, 142, 143, 144, 145, 146, 147], that is expected to give rise to singular self-energy corrections for the spinon excitations, which destroy the notion of well-defined spinon quasi-particles. Such singular scattering is also expected to show up in the scaling behavior of thermodynamic and thermal-transport quantities[137].

[2]The linear dependence of thermal conductivity is more cleanly displayed by dmit. κ-ET shows a low-temperature dip in the thermal conductivity that could be associated with some unknown phase transition, or possible could be due to loss of thermal contact with the sample.[14]

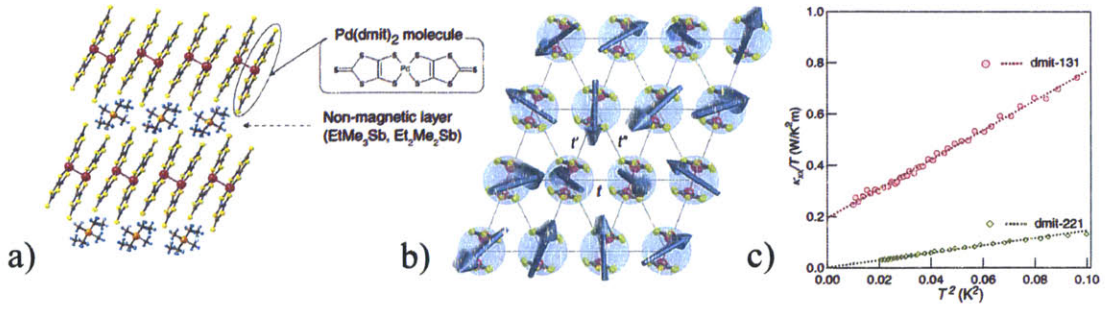

Figure 8-1: Organic gapless spin-liquid candidate dmit (figure adapted from Ref. [15]): Panel a) depicts the underlying molecular structure in which large organic molecules form a triangular lattice (see panel b). Each site of the triangular lattice has only a single electronically active orbital that is singly occupied on average (indicated by the blue arrows in Panel b, which show the residual electron spin-degree of freedom). Despite being a charge insulator, the compound has metallic-like linear-T thermal conductance (Panel C). In contrast to a non-metallic analog (green symbols), which has no such linear-T component to κ, indicating that the thermal conductivity is carried by spin-excitations.

However, so far no singular non-Fermi liquid behavior has been observed in the experimentally realized organic materials. The precise reason for this disagreement is not fully understood in detail. It is conceivably possible that a different theory than the spinon Fermi-surface state is required to describe the experiment. However, the spinon Fermi-surface state emerges so naturally from the Fermi-liquid, as appropriate for a continous Mott transition, and is so successful at producing the most striking qualitative behavior, that it should not be quickly abandoned.

One possibility is that disorder scattering, e.g. by impurities, is known to cut-off the singular behavior and produce metallic like thermodynamic and transport behavior. This could account for the absence of non-Fermi liquid behavior in κ-ET and dmit, though the mean-free paths of these organic materials are thought to be quite long. A second, more likely possibility, is that the non-Fermi liquid effects are suppressed to very low-energy scales. Due to the close proximity to a continuous (or nearly continuous) Mott transition, the charge gap is quite small, which is expected to lead to substantial dielectric screening emergent gauge fluctuations. These screening effects suppress the effects of gauge-fluctuations such that they may not play an important role at experimentally accessible temperatures.

Another unresolved mystery is that κ-ET exhibits a low-temperature anomaly in thermodynamic and transport measurements. It was previously proposed that this anomaly could signal a low-temperature phase transition, for example to a superconducting instability of the spinon Fermi-surface[128]. Another possibility is that this anomaly, especially in thermal transport, is an experimental artifiact due to loss of thermal contact with the sample.

8.2 Gapless Spin-Liquids in the Vicinity of a Metal-Insulator Transition II: Randomly Doped Semiconductors

The organic materials described in the previous section are thought to be gapless spin-liquids due to lattice frustration and close proximity to a continuous (or nearly continuous) metal-insulator transition. These materials are rather clean, and disorder is thought to play only a very weak role in their physics.

This clean metal-insulator transition (MIT) was actually not the first example of a continous MIT. An earlier, and much more widely studied example is the MIT in randomly doped semiconductor materials. Such systems are conceptually much more complicated, since they are highly random, and disorder is thought to play an important role in driving the MIT. However, the initial studies of this transition were done in a time preceding the idea that quantum spin-liquids were possible. In this chapter, we re-examine the MIT in doped semiconductor materials and explore the possibility and consequences of a spin-liquid phase on the weakly-insulating side of the continuous MIT in these systems.

8.2.1 The Metal-Insulator Transition in Doped Semiconductors

Phenomena near the metal-insulator transition (MIT) in doped semiconductors such as Si:P or Si:B have been studied extensively for more than three decades[122, 123, 124, 125]. Nevertheless, several aspects of the physics, for instance the detailed critical behavior[126, 127, 125], remain mysterious. In this paper we explore and develop the consequences of a new possible route to the MIT where a quantum spin liquid insulator appears as an intermediate phase between the metal and the Anderson-Mott insulator. In recent years such a quantum spin liquid Mott insulator has been observed to intervene between the Fermi liquid metal and conventional magnetically ordered Mott insulators in a few different clean materials[14, 15, 129]. Here we study the strongly disordered situation appropriate to doped semiconductors and describe a variety of experimental consequences.

When P is doped into Si, the extra electron of P forms a Hydrogen-like state with an effective Bohr radius of about $a \approx 20$ Å[122]. A simple picture of the doped semiconductor is as a collection of randomly placed "Hydrogen" atoms. The system may then be described as a half-filled Hubbard model on a random lattice supplemented by the inclusion of the long range Coulomb interaction V_{ij} between the electrons:

$$H = -\sum_{ij;\alpha} t_{ij} \left(c^{\dagger}_{i\alpha} c_{j\alpha} + h.c \right) + U \sum_{i} n_{i\uparrow} n_{i\downarrow} + \sum_{i \neq j} V_{ij} n_i n_j \tag{8.5}$$

At low concentrations, the $t_{ij} \approx t_0 e^{-r_{ij}/a}$ are small, the on-site U dominates and a Mott insulator of local moments results. The local-moments are coupled antiferromagnetically, and due to their random placement, preferentially form singlets with

their closest available neighbor. The resulting random-singlet phase has an extremely broad distribution of singlet binding energies, giving rise to a diverging density of states for low-energy spin-excitations, contributing a divergent coefficient of heat capacity, $\gamma = C/T$ and spin-susceptibility χ[132].

As the concentration of dopants, n, is increased, eventually the typical t_{ij} dominates over the U and a diffusive metal is obtained. A continuous phase transition between metal and insulator occurs at some critical intermediate concentration, n_c, where $t_{ij} \approx U$.[3] Because of the random placement of dopants, a fraction of the local moments are very weakly coupled to the conducting electrons and survive unscreened into the metallic phase. The diffusive metal appears to be well described by a "two-fluid" model where the conducting electrons exist essentially decoupled from a random fraction of weakly-coupled local-moments[122, 133]. As in the insulating phase, these local moments continue to dominate the low-temperature thermodynamic and magnetic properties of the metallic phase, but do not appear to strongly modify its transport properties.

It is natural to ask: What is the fate of the conducting fluid across the metal–insulator transition? The conventional answer, implicitly adopted by most existing work[123, 124], is that all electron degrees of freedom are localized by disorder[134], which is perturbatively enhanced by interactions. In this scenario, shown in Fig. 8-2a, decreasing $n < n_c$ gives a localized Anderson-Mott insulator with non-zero average density of states. As n is further decreased, the system crosses over continuously towards a correlation driven Mott-insulator of local moments.

8.2.2 Spin-Liquid Scenario

In this Chapter, we point out a new and conceptually distinct scenario for the metal–insulator transition in doped semiconductors. In this scenario, the charged–conducting fluid is localized into a gapless quantum spin-liquid, but the electron thermal transport remains diffusive into the weakly insulating regime. There is growing theoretical and experimental evidence that such gapless spin-liquids occur in clean Mott insulators, where strong charge fluctuations and frustration prevent magnetic ordering[14, 15, 129]. This experience makes it natural to ask whether or not one should expect a spin-liquid phase to form in (uncompensated) doped semiconductors near the MIT where charge fluctuations are strong, the system is at half-filling, and magnetic order is prevented by the random lattice structure, the competition between antiferromagnetic direct-exchange and random-sign RKKY exchange, and by quantum fluctuations.

The possibility of a spin-liquid phase in doped semiconductors due to multi-particle ring-exchange effects was previously suggested but not explored in [130]. Also, fractionalization of the random singlet phase of local moments was suggested[131] as a possible mechanism for unconventional superconductivity in B doped diamond.

[3] Using a hydrogenic model for P:Si gives $U \approx 30$meV. At the MIT the typical spacing is $\approx 4a$, corresponding to typical hopping strength $t_c \approx 3\text{meV} \approx U/10$, and ratio of Coulomb to kinetic energies of $r_s \approx 2$.

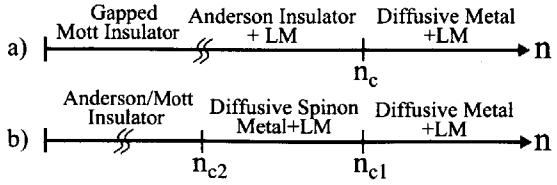

Figure 8-2: Two scenarios for the MIT in doped semiconductors. (a) Conventional picture electron localization transition to Anderson-Mott insulator, which crosses over continuously to a pure Mott insulator (indicated by wiggly lines). (b) In the newly proposed scenario, the transition is to a spin-liquid with gapless fermionic spinon excitations, here the electrical MIT and spin/thermal MIT occur separately at n_{c1} and n_{c2} respectively. "+LM" indicates the fraction of randomly decoupled local spin-moments that inevitably accompany all phases.

The proposed spin-liquid phase is most conveniently described by formally dividing the electron into a bosonic U(1) rotor $e^{i\phi}$ that carries the electron–charge, and a fermionic spinon f_α that carries the electron–spin: $c_i = e^{i\phi_i} f_{i\alpha}$[135, 136]. This description allows extraneous unphysical states that must be removed by constraining $n_{b,i} - \sum_\alpha f^\dagger_{i\alpha} f_{i\alpha} = 1$ on each site, i. Here n_{bi} is the number operator conjugate to ϕ_i. The above decomposition has a U(1) gauge redundancy associated with $\phi_i \to \phi_i + \Lambda_i$ and $f_i \to e^{-i\Lambda_i} f_i$, which manifests itself in the low-energy effective theory as an emergent U(1) gauge field, $\mathbf{a}(\mathbf{r}, t)$ [137]. A similar slave-particle description was previously developed for the weakly disordered 2D case for the triangular lattice organics[150].

Decoupling the hopping term $-t_{ij} c^\dagger_{i,s} c_{j,s} = -t_{ij} e^{i(\phi_i - \phi_j)} f^\dagger_{i,s} f_{j,s}$ in a mean field approximation and including gauge fluctuations gives the following effective action: $S_{\text{eff}} = \int d\tau \, (L_b + L_f)$

$$\begin{aligned} L_b &= \textstyle\sum_i \frac{1}{2} \left(\partial_\tau \phi_i + a^0_i\right) \left(U \delta_{ij} + V_{ij}\right)^{-1} \left(\partial_\tau \phi_j + a^0_j\right) \\ &\quad - t_{ij} \textstyle\sum_{ij} \chi^f_{ij} e^{i(\phi_i - \phi_j + a_{ij})} \\ L_f &= \textstyle\sum_{ij} f^\dagger_i \left[\left(\partial_\tau - a^0_i - \mu\right) \delta_{ij} - t_{ij} \chi^b_{ij} e^{-i a_{ij}}\right] f_{j,s} \end{aligned} \tag{8.6}$$

where $\chi^f_{ij} = \langle f^\dagger_{i,s} f_{j,s} \rangle$ and $\chi^b_{ij} = \langle e^{i(\phi_i - \phi_j)} \rangle$ are determined self-consistently. Note that, due to the random placement of sites, in general $\sum_s \langle f^\dagger_{i,s} f_{i,s} \rangle$ will be spatially varying. Consequently, even at the mean-field level, the bosons will experience a random chemical potential; this changes the universality class of the Bose-Mott transition compared to the clean case (where $\langle n_b \rangle = 1$ for every site on both sides of the Mott transition).

The metallic Fermi-liquid state corresponds to a superfluid–ordered phase of the bosonic rotors with $\langle e^{i(\phi(\mathbf{x}) + \int^{\mathbf{x}} \mathbf{a}(\mathbf{y}) \cdot d\mathbf{y})} \rangle \neq 0$, coexisting with a diffusive Fermi-liquid of spinons. In this phase, the emergent gauge field is gapped by the condensate of charged rotors through the Anderson–Higgs mechanism, and the rotors and spinons are "glued" together into ordinary electrons.

Eq. 8.6 also naturally describes a deconfined state in which the rotors form a Bose-glass/Mott-Insulator, while the spinons remain diffusive. This results in an exotic charge–insulator with finite-density of states for gapless spin-1/2 excitations. We

suggest that this spin-liquid phase may occur near the MIT for doped semiconductors. In this scenario, shown in Fig. 8-2b, the magnetic properties of the system change only gradually across the MIT at n_{c1}, and are qualitatively identical in both the metal and insulator. In particular, we expect that one would still find a decoupled fraction of local-moments. As these local moments dominate the low-temperature thermodynamics and magnetic properties, the clearest signature of the spin-liquid is metallic thermal conductivity, $\kappa \sim T$ at low T[15]. While there has been extensive experimental analysis of the conductivity of doped semiconductors near the MIT, very little is known about thermal–transport.

In the slave-rotor language, the formation of local moments comes from rare strong fluctuations in disorder that locally bind the rotor and fermion back into a correlation–localized electron. We assume that the principal effect of correlated disorder among the rotor, spinon, and gauge-field sectors is to produce such local moments, and that the physics of the remaining non-local moment bulk can be well described by treating disorder separately in each sector.

In principle, a full treatment of disorder would need to account for correlations in the effects of local disorder fluctuations among the boson, fermion and the gauge field sectors. We assume that the principal effect of such correlations is to produce local patches where the rotor and fermion are locally confined, i.e. to produce the dilute fraction of local-moments that are observed in each phase, but appear to decouple from the remainder of the system. We expect that the formation of local-moments accounts for the effects of the rare-long tails of the disorder distribution, and that the remaining connected component of the system is reasonably characterized by treating disorder separately in each sector.

In the boson-sector, the superfluid-insulator transition will occur in the presence of a random potential, and the resulting insulating phase will be a mixture of glassy puddles of superfluid which do not percolate, coexisting with a Mott-localized bulk. In the spin-liquid scenario, the thermally conducting fluid of spinons (not including local moments) form a diffusive metal. As shown below, the phase transition in the boson sector is not affected by the presence of gapless fermions or gauge fluctuations, and is identical to that of the ordinary dirty Bose-Hubbard model with random chemical potential and long-range Coulomb interactions[139].

8.2.3 Gauge Fluctuations

In the spin-liquid phase, the emergent gauge field is deconfined, and in clean systems its fluctuations lead to singular self-energies for the spinons resulting in non-Fermi-liquid behavior (2D)[138, 141, 142, 143, 144, 145, 146, 147] or marginal Fermi-liquid behavior (3D)[151, 148, 149]. For the strongly disordered doped semiconductors, the inelastic scattering rate for the spinons from gauge fluctuations scales as $\tau_g^{-1} \sim T$ and is dominated by the elastic impurity scattering for low T. Consequently, the low-energy properties of the disordered spinon Fermi-liquid will be largely unaltered by the emergent gauge field. Furthermore, the gauge field propagation is strongly damped by the diffusive spinons, leading to an $\omega \sim q^2$ scaling of gauge-excitations. This scaling implies that the gauge-field contribution to thermodynamic quantities

is sub-dominant compared to the spinon contribution. For example the gauge-field specific heat scales as $C_a \sim T^{3/2} \ll C_{\text{spinon}} \sim T$.

In 2D, a deconfined phase for the gauge-field requires the presence of extended, gapless fermionic excitations to suppress instanton configurations [152, 153]. In 3D, however, a compact U(1) gauge–field may remain deconfined even without extended, gapless matter [152]. Therefore, in addition to the gapless, thermally–conducting spinon Fermi-surface state described above, it is also possible to form an insulating state where the charge degrees of freedom are Mott localized and the spinons are Anderson-localized by disorder. Such a spinon Anderson insulator is distinguished (in principle) from the conventional Anderson-Mott insulator by the presence of a gapless emergent U(1) gauge-field (though experimentally detecting the emergent gauge-field would be challenging).

Including gauge fluctuations generically gives rise to a spinon-rotor density-density coupling of the form $\lambda_0 \delta n_f n_b$, where δn_f is the deviation of n_f from its average value. Here we give a simple scaling argument that such a coupling does not alter the critical behavior of the boson–sector near the Mott transition. Consider integrating out the spinons. The leading order term in the effective action for the bosons will be of the form: $\lambda \sum_{\omega,\mathbf{q}} \langle \delta n_f(\omega,\mathbf{q}) \delta n_f(-\omega,-\mathbf{q}) \rangle |n_b(\omega,\mathbf{q})|^2$. In the transition to the spin-liquid, the spinon density-density correlator is diffusive and evolves smoothly across the transition: $\langle \delta n_f(\omega,\mathbf{q}) \delta n_f(-\omega,-\mathbf{q}) \rangle \sim \frac{Dq^2}{|\omega|+Dq^2}$.

After a momentum-shell renormalization–group (RG) step, integrating out modes with $q \in [\Lambda/s, \Lambda]$, with $s \gtrsim 1$, one rescales $q \to sq$ and $\omega \to s^z \omega$ to compare the new effective action to the original. Due to the random chemical potential provided by the spinon sector, the Boson Mott transition is in the same universality class whether one tunes through the transition either by changing chemical potential or hopping strength (this would not be true without the presence of a random chemical potential, where the Bose–Mott transition takes place at fixed density per site, with the random potential however, the density per site is only fixed on average). For the chemical potential driven transition, under an RG step, the scaling part of the boson density rescales as $n_b(r,t) \to s^{d+z-1/\nu} n_b(r,t)$ where ν is the correlation length exponent. Equivalently, the fourier component rescales as $n_b(q,\omega) \to s^{-1/\nu} n_b(q,\omega)$.

For $z < 2$, the denominator of the diffusive fermion correlator is dominated by the $|\omega|$ term, and the density–coupling term scales as: $\lambda g \int d^d q d\omega q^{d-z} |n_b(q,\omega)|^2 \to \lambda' s^{2(d-1/\nu)} \int d^d q d\omega q^{d-z} |n_b(q,\omega)|^2$, indicating that the coupling constant λ rescales as $\lambda \to s^{2(1/\nu-d)} \lambda$. Since $\nu d \geq 2$, λ is irrelevant. Similarly if $z \geq 2$, the diffusive fermion correlator scales like a constant under RG, and the coupling constant $\lambda \to s^{2\nu-d-z} \lambda$ is again irrelevant.

Coupling to Gauge Fluctuations –

The rotor–gauge field coupling generically takes the form $\int d^d r d\tau a_\mu j_b^\mu$, where j_b is the boson current. Integrating out the gauge-field at the RPA level generates a term of the form $g \int d^d q d\omega G_a |j_b(\omega,\mathbf{q})|^2$, where $G_a = \langle |\mathbf{a}(\omega,q)|^2 \rangle$. Current–continuity requires that $j_b(\omega,q) \sim \frac{\omega}{q} n_b(\omega,q)$, where n_b is the *total* boson density which scales like $n_b \sim 1/L^d$, indicating that $j_b(\omega,q) \to s^{-1} j_b(\omega,q)$ in each RG step. As shown

below, the gauge-field propagator scales like $G_a \sim (\omega + q^2)^{-1}$.

For $z \leq 2$, under RG the gauge-fluctuation term rescales as $g \int \bar{d}^d q \bar{d}\omega G_a |j_b(\omega, \mathbf{q})|^2 \to g' \int s^{d+z} \bar{d}^d q \bar{d}\omega s^{-z} G_a s^{-2} |j_b(\omega, \mathbf{q})|^2$. Consequently $g \to g s^{2-d}$ flows to zero under RG and is irrelevant. Similarly, for $z \geq 2$, the term rescales as $g \int \bar{d}^d q \bar{d}\omega G_a |j_b(\omega, \mathbf{q})|^2 \to g' \int s^{d+z} \bar{d}^d q \bar{d}\omega s^{-2} G_a s^{-2} |j_b(\omega, \mathbf{q})|^2$, indicating $g \to s^{4-(d+z)} g$, and the term is again irrelevant.

RPA Effective Action for the Emergent Gauge Field in the Diffusive Spinon Metal

Since the spinons and bosons have opposite charge under the emergent gauge field a, the gauge field couples to the currents as $S_{a-j} = \int d\tau d^3 r \left(j_\mu^b - j_\mu^f\right) a^\mu$ (here and throughout, we work in imaginary time). Therefore integrating out the spinon and boson fields within the RPA approximation, gives the following disorder-averaged effective action for the gauge field:

$$S_{\text{eff}}^{(\text{RPA})} = \sum_{\omega, q} a_\mu(\omega, q) \left[K_b^{\mu\nu}(\omega, q) + K_f^{\mu\nu}(\omega, q)\right] a_\nu(\omega, q) \tag{8.7}$$

where $K_{f/b}^{\mu\nu}$ are the disorder–averaged current–current correlators (equivalently linear-response kernels) for the fermions and bosons respectively.

The temporal fluctuations of the gauge field are screened by the compressible fermions and become massive. At the critical point and in the insulating phase the Boson conductivity vanishes, and consequently the gauge field dynamics are determined by the fermion response. The disorder-averaged density-density part of the fermion electric response kernel is diffusive:

$$K_{00}^f = \frac{2N(0)Dq^2}{|\omega| + Dq^2} \tag{8.8}$$

where, we have expanded the diffusion "constant" $D(\omega, q)$ (which generally has some ω and q dependence, but does not vanish for $q, \omega \to 0$ outside of the disorder–localized phase) near $\omega = 0 = q$, and dropped the irrelevant higher order terms. The other components of electric field response-function are related to K_{00}^f by gauge invariance and charge conservation: $K_{0i}^f = K_{i0}^f = \frac{-\omega q_i}{q^2} K_{00}^f$, and $K_{ij}^f = \delta_{ij} \frac{-\omega^2}{q^2} K_{00}^f$. Furthermore, we can identify $2N(0)D$ as the static uniform spinon–conductivity σ_f. In addition, there is the usual diamagnetic response to fluctuating magnetic fields for $\omega \ll q$: $\chi_d q^2$, where χ_d is the Landau diamagnetic susceptibility of the spinons (whose average value is not altered by disorder).

Combining these considerations, and working in the Coulomb gauge ($\nabla \cdot \mathbf{a} = 0$ so that only the transverse gauge field $\mathbf{a}_\perp$ remains) gives the following RPA action for the gauge-field $\mathbf{a}$:

$$S_a^{(\text{RPA})} = \sum_{\omega, q, \mu} \left[\chi_d q^2 + \frac{\sigma_f \omega^2}{|\omega| + Dq^2}\right] |\mathbf{a}_\perp(\omega, q)|^2 \tag{8.9}$$

where $D = \frac{v_F^2 \tau}{d}$ is the diffusion constant (τ is the disorder scattering time), and σ_f is the spinon-conductivity.

Inelastic Scattering of Spinons from Gauge Fluctuations

Using the RPA expression for the gauge field propagator, one can find the leading (one-loop) self-energy for low-energy spinons near the Fermi-energy:

$$\begin{aligned}
\Sigma(i\omega, k) &= \int đ\omega đ^2 q_\perp đ q_\parallel D_a(i\Omega, q) \left(v_F \frac{q_\perp}{q}\right)^2 G_f\left(i(\omega - \Omega), k + q\right) \\
G_f(i\omega, \mathbf{k}) &= \frac{1}{i\omega - \xi_{\mathbf{k}} + \frac{i}{2\tau}\mathrm{sgn}\omega} \\
D_a(\Omega, q) &= \frac{1}{\chi_D q^2 + \frac{\sigma_f \Omega^2}{|\Omega| + Dq^2}}
\end{aligned} \tag{8.10}$$

In the fermion Green's function $\xi_{k+q} \sim v_F q_\parallel + \mathcal{O}(q^2)$, indicating that $q_\parallel \sim \Omega$. Consequently one may approximate $q_\parallel^2 \ll q_\perp^2$ in the gauge field propagator, making D_a a function of $q_\perp$ only. Furthermore, in this approximation, the current vertex $\left(v_F \frac{q_\perp}{q}\right)^2 \approx v_F^2$.

Performing the $q_\parallel$ integral then gives $N(0)\mathrm{sgn}(\omega - \Omega)$ independent of the disorder scattering time τ. Considering the case of $\omega > 0$ for definiteness, this limits the range of Ω integration from 0 to ω. Since the dominant contributions come from $\Omega \sim q_\perp^2$, one finds that the spinon self-energy due to diffusively–screened gauge fluctuations scales like: $\Sigma(i\omega) \sim \omega \log(1/\omega)$ Continuing to real-time one finds the inelastic gauge field scattering rate scales like $\mathrm{Im}\left[\Sigma^R(\omega)\right] \sim \omega$, or equivalently $\tau_{\mathrm{inelastic}}^{-1} \sim T$. At low-temperature, this inelastic scattering is clearly sub-dominant compared to the elastic impurity scattering.

8.2.4 Generalized Phase Diagram

The MIT achieved by changing n, though experimentally relevant, is conceptually complicated since disorder and interactions are simultaneously affected. It is conceptually simpler to consider a generalized phase-diagram where disorder strength W and interaction strength U can be separately adjusted, as in Fig. 8-3. Here we restrict our attention to 3D, half-filling, and non-nested Fermi-surfaces (which are not inherently unstable to magnetic ordering). Furthermore, we remain agnostic about the particular realization of disorder, with the expectation that such details will not alter the qualitative discussion that follows.

We begin by considering various limiting cases. The $(U = 0, W \neq 0)$ limit is completely understood[134]: here a diffusive Fermi-liquid occurs up until a critical disorder strength beyond which all states near the Fermi-energy become localized leading to an Anderson insulator (AI). Each of these phases is known to be stable to infinitesimal interactions, and therefore extends at least to small U. The limit of $(U \neq 0, W \to \infty)$ is also straightforward. Here the Anderson localized insulator at

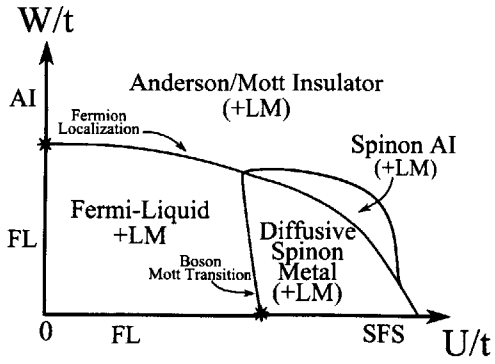

Figure 8-3: Schematic generalized phase–diagram as a function of disorder strength W and interaction strengths U measured with respect to the typical hopping t.

weak interactions crosses over continously to the Mott insulator of local-moments at strong-interactions. At $T = 0$, the local moments are magnetically ordered in either a random–singlet or spin-glass phase.

Finally, the line $(U \neq 0, W = 0)$ is also reasonably well understood[136], albeit with slightly less confidence. The clean Fermi-liquid survives up until some critical interaction strength, beyond which it becomes a weak Mott-insulator with a spinon Fermi surface (SFS). For large U, the emergent gauge field undergoes a confinement transition and anti-ferromagnetic order develops. Here again, each of the clean interacting phases is stable to infinitesimally small amounts of disorder and extends to finite W. The only distinction being that, for any $(U \neq 0, W \neq 0)$, disorder creates a non-zero density of decoupled local moments (indicated in Fig. 8-3 by "+LM").

These considerations greatly constrain the structure of the generalized phase–diagram. Each of the phases at the boundary are known to extend to finite values of W and U. Given the understanding of the boundaries of the phase diagram, the main issue here is not whether a strongly disordered fermionic spin-liquid could exist, but rather which particular path through the generic W and U phase–diagram is appropriate to tuning n in doped semiconductors. Fig. 8-3 depicts an extension of the well-understood outer boundary of the phase diagram to the interior. While one can conceive of many intermediate insulating phases at intermediate U and W, in the slave-rotor language, the only other natural candidate is the deconfined spinon Anderson insulator described above.

8.3 Transport Signatures

8.3.1 Thermal Conductivity

– In the spin-liquid scenario, the electrical MIT and thermal MIT occur separately: whereas electrical conductivity vanishes in the insulating phase, thermal conductivity remains metallic, scaling as $\kappa_{sp} \sim T$ at low temperatures. Since the ever-present concentration of local-moments dominates the low-temperature thermodynamical properties of the system (but contributes only weakly to transport), linear-T metallic conductivity is the clearest experimental signature of the spin-liquid.

While $\kappa_{sp} \sim T$ at the lowest temperatures there will be Altshuler-Aronov–type corrections to κ from interactions and disorder: $\kappa_{AA} \sim T^{3/2}$ [154, 155, 156]. Also, one expects a large contribution, κ_{ph} from phonons: $\kappa_{ph} \sim T^3$.[4] Therefore, to observe the metallic spinon-contribution, it may be necessary to work at very low temperature, and carefully subtract sub-dominant contributions.

8.3.2 Quantum Critical (QC) Scaling

Despite extensive experimental and theoretical effort, the quantum-critical (QC) behavior of electrical conductivity remains contentious and poorly understood. The existence of a spin-liquid phase would have important implications for how QC scaling should be extracted and interpreted. For $T = 0$ and $n > n_c$, the system is a Fermi-liquid obeying the Wiedemann-Franz law: $\kappa/\text{Ł}T = \sigma$ (where the Lorenz number Łis a constant). Since σ vanishes at the transition while $\kappa/text\text{Ł}T$ remains non-zero there must be a discontinuous jump in the $T = 0$ electrical conductivity at the MIT. In the slave-rotor description, this jump arises from the Ioffe and Larkin rule[176] that the electrical resistivity ρ equals the sum $\rho = \rho_b + \rho_f$ of the resistivities of the bosonic rotors ρ_b and spinons ρ_f respectively. Crossing the MIT at $T = 0$, the bosons transition from a superfluid with $\rho_b = 0$ to an insulator with $\rho_b = \infty$. In contrast, the fermionic contribution, ρ_f evolves smoothly through the transition, implying a non-universal jump in the zero-temperature conductivity. Though superficially similar to Mott's early proposal[157], this jump in conductivity is unrelated to the idea of a "minimum metallic conductivity".

Evidence against a discontinuous jump in conductivity in Si:P comes mainly from pressure tuning studies[126] that show conductivity droping sharply but apparently continously to zero at the MIT. However, determining whether one is truly accessing the asymptotic behavior near the QC point is very challenging, and the proper interpretation of the conductivity scaling remains controversial and poorly understood [127]. For example, the pressure tuned experiments extract a conductivity scaling exponent $\nu = 1/2$ that is incompatible with general exponent inequalities for a metal-insulator transition[158], but could be explained as a thermally rounded version of the true $T = 0$ conductivity jump. In the spin-liquid scenario, as we will argue below, issues with extrapolating to $T \to 0$ and $n \to n_c$ are further exacerbated.

Near the quantum critical point (QCP) (i.e. $T \approx 0$, and $\delta n = n - n_c \ll n_c$), $\rho_b(T, \delta)$ obeys the quantum critical (QC) scaling for the disordered Bose-Hubbard model Mott transition as shown in Fig. 8-4a. In the high-temperature critical regime where T is the dominant perturbation away from criticality, $\rho_b(T) \sim T^{-1/z}$. At lower temperatures $T < T^* \sim (\delta n)^{z/\nu}$, where δn is the dominant perturbation from criticality $\rho_b(T)$ crosses over from the $T^{-1/z}$ to 0 as superfluidity develops. Here z is the dynamical exponent for the disordered Bose-Mott transition with Coulomb interactions[5].

[4]The thermal-conductivity of a random-singlet phase of local moments is found to follow $\kappa_{LM} \sim T^{p'}$ with $p' \approx 4$ in 3D, and is also subdominant at low T. See Appendix C for details.

[5] In 3D z need not be 1, but $z \approx 1$ is appropriate when the energetics are dominated by the long-range Coulomb interaction, which is plausible in the vicinity of the charge insulator. Here we

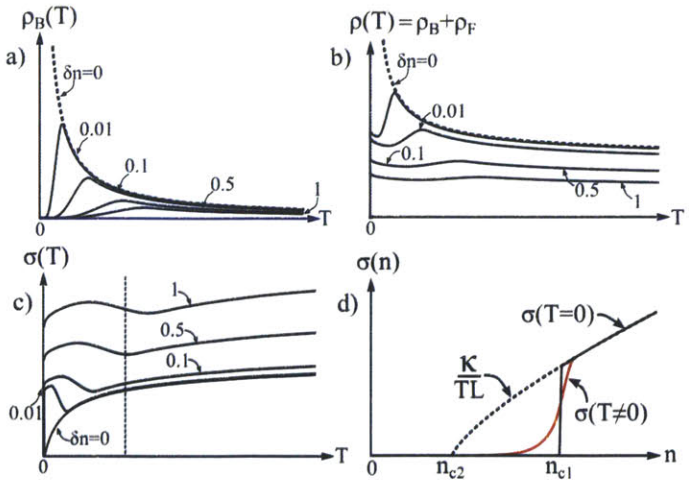

Figure 8-4: Quantum critical scaling (with $z = 1$) of electrical conductivity σ and linear–T coefficient of thermal conductivity κ/TL (L is the Lorenz number) near the MIT as a function of concentration and temperature.

The spinon contribution to the resistance tends to a constant at zero temperature, due to the elastic scattering from disorder. At finite temperature, there will also be non-constant contributions to ρ_f: $\rho_{\rm AA} \sim \sqrt{T}$,[159] and $\rho_{\rm ph} \sim T^{\sim 3-5}$, from interactions and phonons respectively. The resulting electrical resistance, $\rho = \rho_b + \rho_f$, is depicted in Fig. 8-4b. for various δn near the MIT. The main feature here, is the resistance upturn due to the nearly–critical fluctuating bosons, which quickly disappears below $T < T^*$ as ρ saturates to a non-universal constant set by ρ_f. The corresponding T dependence of $\sigma = 1/\rho$ is shown in Fig. 8-4c. Notice the discontinous jump in the very-low temperature conductivity between $\delta n \to 0^+$ and $\delta n = 0$. As shown in Fig. 8-4d, this jump will be rounded at non-zero temperature, and could escape notice (consider, for example, if the lowest achievable temperature were indicated by the vertical dotted line in Fig. 8-4c).

The spin-liquid scenario outlined here suggests a very different scheme for extracting the QC behavior of conductivity, than that for a conventional localization transition. Here, one should include only data for which the resistance saturates to a nearly constant value set by the spinon contribution. In practice there is a minimum achievable value of temperature, $T_{\rm min}$. Consequently, this saturation region will disappear as the MIT is approached when $\delta n \lesssim T_{\rm min}^{\nu/z}$. Beyond this point, extrapolations based on the curvature of σ would fail to capture the true $T \to 0$ behavior.

The spin-liquid scenario will also complicate efforts to extract the critical scaling of $\sigma(n)$ near the MIT. This difficulty is illustrated in Fig. 8-4d, which shows $\sigma(T = 0, n)$. As the concentration is decreased in the metal, the conductivity curves slowly towards an eventual localization transition at n_{c2} (which may or may not occur). However, in the present scenario, the Mott transition of the rotors intervenes at $n_{c1} > n_{c2}$ before the spinons localize. In this case, extrapolations of QC scaling based on a conventional Anderson transition from the metallic side would be misleading.

---

illustrate $z = 1$ for definiteness, but stress that a different value will not qualitatively affect our results.

8.3.3 Discussion

In summary, we propose an alternative scenario to the Mott transition in doped semiconductors where the weakly insulating state is a spin-liquid with fermionic excitations. While such a transition has definite consequences for the quantum critical scaling of conductivity near the MIT, such quantum critical behavior is notoriously difficult to determine.

Other possible signatures of spin-liquid behavior include sub-gap optical conductivity[160] in the insulator from gauge fluctuations and vanishing quasi-particle residue approaching the MIT (measurable by tunneling on the metallic side). However, the former coexists with sub-gap conductivity from exciting weakly bound local moments, and the latter behavior will also be produced by a soft Coulomb gap (which will develop at the MIT)[161]. Consequently, such probes are indirect, and would require a detailed quantitative comparison.

Therefore, we suggest that the clearest test for spin-liquid behavior in doped semiconductors would come from a careful study of thermal transport near the MIT. A spinon Fermi-liquid would lead to $\kappa \sim T$ for low T, which, if observed, would strongly indicate the presence of gapless fermionic excitations.

Chapter 9

Gapless Fractionalized Phases II: Strong Mott Insulators

The previous chapter concerned itself with spin-liquid phases in weakly insulating phases near a metal-insulator transition. Spin-liquids can also arise in strongly insulating compounds purely out from geometrical frustration. The best known example is the spin-1/2 antiferromagnetic Heisenberg model on the Kagome lattice. This model is thought to have a spin-liquid ground-state due to the interplay of geometric frustration and large quantum fluctuations of spin-1/2 moments[162, 163, 164, 165, 166, 167]. To a reasonably good approximation this model is realized in the material Herbertsmithite ($ZnCu_3(OH)_6Cl_2$), which consists of layers of Cu^{2+} ions with antiferromagnetically interacting spin-1/2 magnetic moments arranged in a structurally perfect Kagome lattice[16].

There is compelling evidence that Herbertsmithite has a spin-liquid ground-state. It shows no signs of magnetic order down to the lowest accessible temperatures $\approx$ 30mK, well below the magnetic exchange scale $J \approx 190$K. Instead, at low-temperatures, it exhibits power law temperature dependence of spin-susceptibility χ_s and heat capacity C_v[168], as well as a Knight shift that tends to a constant at low T.[169, 170] These features are suggestive of gapless (or at least nearly gapless) spinon excitations. Moreover, recent neutron measurements show a broad spectrum of spin-excitations consistent with a low-energy spinon continuum[171].

While Herbertsmithite is a promising spin-liquid candidate, the detailed nature of its putative spin-liquid ground-state remains mysterious. Evidence for gapless spinon excitations led to early suggestions that the material might realize a U(1) Dirac spin-liquid (DSL) with fermionic spinons whose low-energy dispersion consists of two Dirac cones[172, 174]. Projected wave-function studies showed that spin-wave-functions obtained from the DSL mean-field ansatz have very good energy with no variational parameters[172] (even lower energies can be achieved by applying a few Lanczos steps to the DSL wave-function[173]). However, recent advances in density-matrix renormalization group (DMRG) techniques have enabled simulation of wide 1D strips, which suggest that the ground state of the Kagome Heisenberg model is instead a Z_2 spin-liquid with a sizcable spin-gap[167]. The issue is complicated by the observation that the Z_2 spin-liquid found in DMRG for is very sensitive to small

perturbations away from the pure Heisenberg model[175]. In light of this observation, it is quite plausible that additional ingredients such as disorder or spin-orbit coupling play an important role in determining the ground-state properties of Herbertsmithite.

These theoretical difficulties highlight the need for new experimental probes that can more directly measure the properties of emergent spinon excitations. For example, it was recently proposed that spin-orbit coupling could enable neutron scattering measurements to detect the gapless emergent gauge fluctuations present in the U(1) Dirac spin-liquid theory[177].

AC electrical conductivity measurements offer another route for measuring the structure of low-energy spin excitations. Despite the host material being a strong Mott insulator, it was previously pointed out for a U(1) spin-liquid that virtual charge-fluctuations can enable power-law absorption deep within the Mott gap[176, 160]. Indeed, in-gap optical absorption has been observed in organic spin-liquid candidates[178], but the data does not go to very low frequencies. These suggestions have led to recent measurements of the electromagnetic properties of single-crystal samples of Herbertsmithite, at terahertz frequencies[179]. This work finds a low-power-law frequency dependence to AC conductivity inside the Mott gap, whose magnitude increases as temperature is lowered.

Inspired by this work, we revisit the issue of sub-gap AC electrical conductivity of candidate spin-liquid states for Herbertsmithite. We consider two scenarios in which Herbertsmithte forms either 1) a U(1) Dirac spin-liquid with fermionic spinons and an emergent U(1) gauge field or 2) a nearly gapless Z_2 spin-liquid in the vicinity of a quantum phase transition to non-collinear antiferromagnetic (AFM) order. Within these scenarios, we find three distinct mechanisms for power-law optical absorption. All of these mechanisms produce conductivity with frequency dependence: $\sigma \sim \omega^2$, but are expected to have different magnitudes.

The first two mechanisms are specific to a U(1) spin-liquid and rely on linear coupling between the applied AC electrical field and the emergent gauge electric field. First, in a U(1) spin-liquid, an external electric field creates virtual charge fluctuations that produce emergent electric fields. This mechanism is a strong-coupling generalization of the Ioffe-Larkin mechanism for optical absorption previously discussed in Refs. [176, 160]. Here, we adapt strong-coupling expansion results by Bulaevskii et al.[180], which shows that certain spin configurations exhibit a net dipole moment. This fact is surprising in a Mott insulator, which is typically viewed as an electrically dead state where a single charge is frozen to each lattice site. While such a picture provides a useful cartoon of the Mott insulator, in reality, the electron density is only fixed to one-electron per site *on average*. Quantum fluctuations of the local charge density inevitably occur as electrons virtually hop to neighboring sites creating double occupancies and vancies with a net dipole moment. Such hopping requires anti-parallel spin allignment on neighboring sites, due to Pauli exclusion, and hence the fluctuation induced dipole moments are closely tied to local spin-correlations[180]. This approach allows us to establish a clear microscopic origin for AC optical absorption in the U(1) Dirac spin-liquid, and enables semi-quantitative estimates of its magnitude.

Second, an external electric field can create a lattice distortion that is non-uniform

within the unit cell, but uniform across different unit-cells. Such lattice distortions perturb the spin-system with the same symmetry as the virtual polarization mechanism[180]. The magnitude of conductivity from the first mechanism is expected to be parametrically smaller than that of the second, since virtual charge excitations are suppressed by a factor of $\left(\frac{t}{U}\right)^3$ in a strong Mott insulator (where t is the hopping and U is the on-site repulsion). However, it turns out that the charge-fluctuation mechanism is enhanced by a large numerical prefactor, and may actually be of the same order as the second magneto-elastic mechanism. Both of these effects give roughly the same order of magnitude as observed in Terahertz measurements by Pilon et al.[179].

In addition, we have identified a third mechanism for absorption based on magneto-elastic and spin-orbit couplings. Here, an applied electric field induces lattice distortions, perturbing the magnetic system. Due to the special pattern of Dzyaloshinskii-Moriya interactions for the Kagome lattice, these spin-perturbations induce uniform spin-currents. Absorption from this mechanism follows $\sigma \sim \omega^2 \sigma_s$, where σ_s is the spin-conductivity of the magnetic system, thereby allowing an all electrical probe of spin-transport. Moreover, this mechanism is quite generic; it is not particular to U(1) spin-liquids, but will also produce $\sigma \sim \omega^2$ absorption in a nearly gapless Z_2 spin-liquid, or even in a thermal paramagnetic with diffusive spin-transport. Absorption through this spin-orbit based mechanism is suppressed by a factor of $\left(\frac{D}{J}\right)^2 \sim 10^{-2}$ compared to the second mechanism described above, where D is the magnitude of the Dzyaloshinskii-Moriya interactions, and J is the magnetic exchange coupling.

Before describing possible sub-gap absorption mechanisms, we briefly review the slave-particle effective theory approaches for describing U(1) and Z_2 spin-liquids. The ground-state properties of strong ($U \gg t$) Mott insulators at half-filling are well described by eliminating doubly occupied sites in a t/U expansion to obtain an effective spin model $H_{\text{Heisenberg}} = J \sum_{\langle ij \rangle} \mathbf{S}_i \cdot \mathbf{S}_j$, where i and j label sites of the Kagome lattice. To describe quantum disordered spin-liquid states of this strongly coupled spin-theory, it is convenient to re-write the spin-degrees of freedom in terms of auxiliary Schwinger fermions or bosons: $\mathbf{S}_i = \frac{1}{2} f^\dagger_{i,a} \boldsymbol{\sigma}_{ab} f_{i,b}$ or $\mathbf{S}_i = \frac{1}{2} b^\dagger_{i,a} \boldsymbol{\sigma}_{ab} b_{i,b}$ respectively, subject to the constraint that $n_f = 1$ ($n_b = 1$). Such descriptions have a U(1) gauge redundancy associated with the local U(1) transformation $f_i, b_i \to e^{i\theta_i}(f_i, b_i)$, and naturally lead to low-energy effective theories with emergent U(1) gauge fields.

9.1 U(1) Dirac Spin Liquid

9.1.1 Mean-Field Ansatz and Effective Field Theory

Fermionic spin-liquid states of spin-models can be described by re-writing spins as Schwinger fermions: $\mathbf{S}_i = \frac{1}{2} f^\dagger_{i,a} \boldsymbol{\sigma}_{ab} f_{i,b}$, subject to the constraint that the number of fermions, $n_f = 1$. A spin-wavefunction can be obtained by first decomposing

$H_{\text{Heisenberg}}$ into a mean-field Hamiltonian:

$$H_{\text{MF}} = J \sum_{\langle ij \rangle} \left[\chi_{ij} f^\dagger_{i,\sigma} f_{j,\sigma} + \sum_{\langle ij \rangle} \Delta_{ij} \left(f^\dagger_{i\uparrow} f^\dagger_{j,\downarrow} + h.c. \right) \right] - \mu \sum_i f^\dagger_{i,\sigma} f_{i,\sigma} \tag{9.1}$$

which respects the constraint $n_f = 1$ only on average. A physical spin-wave function can be obtained from the mean-field Hamiltonian by projecting out the unphysical doubly occupied sites: $|\Psi_{\text{spin}}\rangle = \mathcal{P}_G |\Psi_{H_{MF}}\rangle$, where $\mathcal{P}_G$ denotes a projection that removes double occupancies. This spin-wave function can then be used as a variational ansatz.

At the mean-field level, $\chi^{\text{MF}}_{ij} = \langle f^\dagger_{i,\sigma} f_{j,\sigma} \rangle$, and $\Delta^{\text{MF}}_{ij} = \langle f_{j,\downarrow} f_{i,\uparrow} \rangle$. For the Kagome lattice Heisenberg model, the procedure outlined above favors a state with $\Delta_{ij} = 0$ and with a sign structure of χ_{ij} such that each hexagon has an odd number of negative bonds, and each triangle has an even number[172]. One can go beyond a mean-field treatment by incorporating fluctuations in the phase of χ_{ij}: $\chi_{ij} \to \chi^{\text{MF}}_{ij} e^{i a_{ij}}$, and in the magnitude of μ: $\mu \to \mu - a^0_i$, where a^0_i and a_{ij} are the space- and time- components of the vector potential for the emergent U(1) gauge field.

Linearizing the low-energy spinon dispersion near the Fermi-energy, the resulting low-energy effective theory consists of four-flavors of two-component Dirac fermions (one for each combination of valley and spin), coupled to an emergent U(1) gauge field[172, 174]. In imaginary time the effective Lagrangian density for the DSL is:

$$\mathcal{L} = \bar{f}_{\mathbf{k},\omega} \left[-i\omega + v_D \boldsymbol{\tau} \cdot \mathbf{k} \right] f_{\mathbf{k},\omega} + \left(j_{\mathbf{q},\Omega} \right)_\mu a^\mu_{\mathbf{q},\Omega} \tag{9.2}$$

Where we have introduced the 8-component field, f_α, where α is a super-index labeling spin, valley, and Dirac-components, Here, τ are Pauli-matrices in the Dirac component basis[174], $v_D \approx J|\chi^{\text{MF}}_{ij}|$ is the Dirac velocity, $j = \begin{pmatrix} j^0 \\ \mathbf{j} \end{pmatrix}$ is the spinon-number-current with $j^0_{\mathbf{q},\Omega} = \sum_{\mathbf{k},\omega} \bar{f}_{\mathbf{k}-\mathbf{q},\omega-\Omega} f_{\mathbf{k},\omega}$ and $\mathbf{j}_{\mathbf{q},\Omega} = v_D \sum_{\mathbf{k},\omega} \bar{f}_{\mathbf{k}-\mathbf{q},\omega-\Omega} \boldsymbol{\tau} f_{\mathbf{k},\omega}$, and $a^\mu = \begin{pmatrix} a^0 \\ \mathbf{a} \end{pmatrix}$, where a^0 and $\mathbf{a}$ are continuum versions of the long-wavelength components of the lattice-vector potentials a^0_i and a_{ij}.

The emergent gauge degrees of freedom arising in the slave-rotor effective theory are sometimes described as "fictitious", as they arise out of a redundancy of the slave-rotor formalism. However, while the emergent vector potential, a^μ, has no direct physical meaning, gauge invariant quantities derived from a^μ have observable physical meaning in terms of spin.

The functional form of the expression of the emergent electric and magnetic fields may be deduced on symmetry grounds and for a strong Mott insulator. Furthermore, their parametric dependence on the parameters of the Hamiltonian can be fixed by dimensional analysis, at least for a strong Mott insulator where there is only one length scale, a, and one energy scale, J. It is nevertheless gratifying to produce an

explicit derivation of the microscopic meaning of the gauge flux through an elementary plaquette and electric field along a lattice link. One should keep in mind, however, that these microscopic operators will be renormalized in going to a low-energy effective description and will receive contributions from all other low-energy operators with the same symmetries.

By considering spatial Wilson loops of a^μ within the slave-particle effective theory, Refs. [188, 189] demonstrated that the emergent magnetic flux through a triangular plaquette corresponds to scalar spin-chirality of the triangle:

$$b_{ijk} \sim \mathbf{S}_i \cdot (\mathbf{S}_j \times \mathbf{S}_k) \tag{9.3}$$

where sites i, j, k form corners of the triangle (traversing cyclically in the clock-wise direction). As shown in Refs. [190, 180], in a strong Mott insulator, the vector spin-chirality is just the electrical current circulating around the triangle in the clock-wise sense:

$$b_{ijk} \sim j^{\text{circ}}_{ijk} \approx -e\left(\frac{24t^3 a}{U^2}\right)\mathbf{S}_i \cdot (\mathbf{S}_j \times \mathbf{S}_k) + \mathcal{O}\left(\frac{t^5}{U^4}\right) \tag{9.4}$$

We follow a similar route to establish the physical meaning of the emergent electrical field $\mathbf{e}$. We will show that, in terms of the physical spin-degrees of freedom, the electric field corresponds to the gradient of bond-energy, which in turn corresponds to the electrical polarization arising from virtual charge fluctuations (as described in Ref. [180]).

9.1.2 Physical Meaning of the Emergent Magnetic Field

We begin by reviewing the arguments of Ref. [188] to identify b as the scalar spin-chirality. In the Schwinger-fermion approach one rewrites spins as auxiliary fermions: $\mathbf{S}_i = f^\dagger_{i,a}\frac{\boldsymbol{\sigma}_{ab}}{2}f_{i,b}$, subject to the constraint $\sum_\sigma f^\dagger_{i,\sigma}f_{i,\sigma} = 1$. Converting the resulting Heisenberg Hamiltonian into a functional integral with fields $\bar{f}, f$ (corresponding to $f^\dagger, f$) and introducing Hubbard-Stratonovich fields χ_{ij} to decouple the resulting four-fermion hopping term yields the following term in the effective action:

$$\begin{aligned}\mathcal{L}_{\text{J}} =& J\bar{f}_{i,a}(\tau)f_{j,a}(\tau)\bar{f}_{j,b}(\tau)f_{i,b}(\tau) \\ &\longrightarrow J\chi_{ij}\bar{f}_{i,a}f_{j,a} + J\bar{\chi}_{ij}\bar{f}_{j,a}f_{i,a} + \frac{J}{2}\bar{\chi}_{ij}\chi_{ij}\end{aligned} \tag{9.5}$$

In the resulting low-energy theory, fluctuations of the magnitude of χ_{ij}, around their saddle-point (mean-field) value are massive, and the phase fluctuations about the saddle point value are simply $e^{ia_{ij}}$. The Wilson loop around a spatial loop Γ is:

$$W_\Gamma = \prod_{\langle ij\rangle\in\Gamma} e^{ia_{ij}} \approx \prod_{\langle ij\rangle\in\Gamma}\chi_{ij} \tag{9.6}$$

where a_{ij} is the vector-potential on the bond $\langle ij\rangle$.

This Wilson loop can be generated by introducing an infinitesimal source term

$$\delta\mathcal{L} = \bar{\eta}_{ij}\chi_{ij} + \eta_{ij}\bar{\chi}_{ij} \tag{9.7}$$

By making the change of variables:

$$\chi_{ij} \to \chi_{ij} - \eta_{ij} \quad \bar{\chi}_{ij} \to \bar{\chi}_{ij} - \bar{\eta}_{ij} \tag{9.8}$$

one shifts the source for χ_{ij} to a source for $f^\dagger_{i,a}f_{j,a}$, indicating that the Wilson loop is equivalently expressed in terms of a string of fermion fields:

$$W_\Gamma = \prod_{\circlearrowleft\Gamma} e^{ia_{ij}} \approx \prod_{\circlearrowleft\Gamma} \bar{f}_{i,a}f_{j,a} \tag{9.9}$$

For example, the flux through a triangular plaquette is $W^k_{i\triangle_j}\bar{f}_{i,a}f_{j,a}\bar{f}_{j,b}f_{k,b}\bar{f}_{k,c}f_{i,c}$.

One can then restore the Grassman expression to operator form[1]: $W^k_{i\triangle_j} \to f^\dagger_{i,a}f_{j,a}f^\dagger_{j,b}f_{k,b}f^\dagger_{k,c}f_{i,c}$ which can be expressed purely in terms of physical variables of through the identities:

$$\begin{aligned} f^\dagger_{i,a}f_{i,b} &= \frac{\delta_{ab}}{2}n_{f,i} + \mathbf{S}_i\cdot\boldsymbol{\sigma}_{ab} \approx \frac{\delta_{ab}}{2} + \mathbf{S}_i\cdot\boldsymbol{\sigma}_{ab} \\ f_{i,a}f^\dagger_{i,b} &= \frac{\delta_{ab}}{2}(2-n_{f,i}) - \mathbf{S}_i\cdot\boldsymbol{\sigma}_{ab} \approx \frac{\delta_{ab}}{2} - \mathbf{S}_i\cdot\boldsymbol{\sigma}_{ab} \end{aligned} \tag{9.10}$$

where $n_{f,i}$ is the spinon occupation number of cite i, which can be regarded as approximately constant: $n_f \approx 1$, and σ are the spin-1/2 Pauli matrices.

The magnetic flux through a triangle ijk is then $b_{ijk} = \frac{1}{2i}\left(W_{ijk} - W_{kji}\right) = \Im m\left(W_{ijk}\right) \approx \mathbf{S}_i\cdot(\mathbf{S}_j\times\mathbf{S}_k)$. The same procedure identifies the magnetic flux through a square plaquette with vertices $ijkl$ as:

$$b_{ijkl} = \frac{1}{2}\left(b_{ijk} + b_{jkl} + b_{kli} + b_{lij}\right) \tag{9.11}$$

9.1.3 Physical Meaning of the Emergent Electric Field

Proceeding by analogy to the previous section, the electric field on a link $\langle ij\rangle$ is given by the space-time Wilson loop:

$$\begin{aligned} e_{ij} &= \lim_{\delta t\to 0}\frac{1}{\delta t}\left[e^{i\left(a_{ij}(t)+a^0_j(t)-a_{ij}(t+\delta t)-a^0_i(t)\right)}\right] \\ &\to \frac{1}{2}\left[\mathbf{S}_i\cdot\left(\mathbf{S}_j\times\dot{\mathbf{S}}_j\right) - \mathbf{S}_j\cdot\left(\mathbf{S}_i\times\dot{\mathbf{S}}_i\right) + h.c.\right] \end{aligned} \tag{9.12}$$

[1]To restore this equal-time product of Grassman fields to operator form, in principle, one needs to resolve an operator ordering ambiguity. However, for determining the flux through a triangular loop the choice of orderings turns out to be unimportant. For larger loops however, the ordering convention makes some difference. In particular, the choice of Refs. [188, 189] leads to an expression for the U(1) Wilson loop that depends explicitly on the choice of base-point. This undesireable feature can be avoided by averaging over choice of base-points.

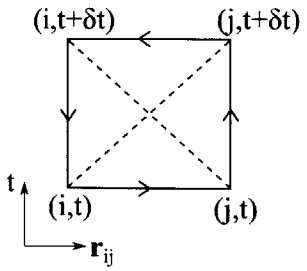

Figure 9-1: Space-Time Wilson loop corresponding to the emergent electric field e_{ij} on lattice-bond $\langle ij \rangle$.

where we have explicitly forced e_{ij} to be Hermitian in order to avoid operator ordering ambiguities in restoring the path-integral expression to operator form. The time-evolution of $\mathbf{S}_i$ follows from evolving under the Heisenberg Hamiltonian $H = J \sum_{\langle ij \rangle} \mathbf{S}_i \cdot \mathbf{S}_j$:

$$\dot{\mathbf{S}}_i = -i[H, \mathbf{S}] = J \sum_{\mathbf{d}} \mathbf{S}_{i+\mathbf{d}} \times \mathbf{S}_i \tag{9.13}$$

where $\mathbf{d}$ are the vectors connecting site i to its nearest neighbors. Combining Eqs. 9.13 and 9.12 gives:

$$e_{ij} = \frac{J}{2} \left[\sum_{d_j} \mathbf{S}_i \cdot \mathbf{S}_{j+d_j} - \sum_{d_i} \mathbf{S}_j \cdot \mathbf{S}_{i+d_i} \right] \tag{9.14}$$

where d_i, d_j are the nearest neighbor vectors of sites i and j respectively.

For a 3-site triangle, Eq. 9.14 reduces to a discrete gradient of bond-energy (on the lattice of bonds), which was shown by Bulaevskii et al. to be proportional to the polarization arising from virtual charge fluctuations.

9.2 Z_2 Spin-Liquids

While the Dirac Spin-Liquid wave-function gives a good energy for the spin-1/2 Kagome Heisenberg model without any variational parameters, DMRG studies indicate that a Z_2 spin-liquid with a sizeable ($\approx 0.15J$) gap to spin excitations has even lower variational energy. For Herbertsmithite, a large-gap Z_2 spin-liquid is inconsistent with observations of gapless behavior[168, 169, 170] down to energy scales well below $0.15J$. However, additional ingredients such as disorder and spin-orbit coupling, not present in the pure Heisenberg model, could suppress the Z_2 gap, leading to a nearly gapless state consistent with experiments. For example, slave particle mean-field studies of large N analogs of the spin-1/2 Kagome Heisenberg model suggest that the spin-1/2 model is naturally close to such an $O(4)$ quantum critical point between a Z_2 spin-liquid and $\sqrt{3} \times \sqrt{3}$ magnetic order[181].

Therefore, while the main focus of this paper will be on the U(1) Dirac spin-liquid, we will also explore optical conductivity mechanisms for a nearly gapless Z_2

spin-liquid. In this section, we give a brief review of the slave-particle formulation of Z_2 spin-liquids, and their possible phase transitions to magnetically ordered states.

Z_2 spin-liquids may be described in the Schwinger fermion effective field theory approach by introducing non-vanishing pairing terms Δ_{ij} into the spinon-mean-field ansatz. An alternative description can be obtained by using bosonic rather than fermionic spinons: $\mathbf{S}_i = b^\dagger_{i,a}\frac{\sigma_{ab}}{2}b_{i,b}$ subject to the constraint that $n_b = 1$. This description also has a local U(1) redundancy leading to emergent, compact U(1) gauge degrees of freedom. In the Schwinger boson formulation, the Z_2 spin-liquid state is a superfluid of pairs of bosons with $\langle b_{ia}\rangle = 0$ but $\langle b_{ia}b_{ja}\rangle \neq 0$. The pair condensate breaks the $U(1)$ gauge degree of freedom down to a residual Z_2 degree of freedom associated with $b_i \to -b_i$. When treated exactly, the fermionic and bosonic formulations of the Z_2 spin-liquids are of course equivalent; and in certain cases one can explicitly construct a duality between the two descriptions, where the boson b is just a vortex in the fermionic paired superfluid[183].

Unlike the fermionic decomposition, the bosonic formulation allows a simple description of magnetically ordered states as superfluid states with $\langle b_{i,a}\rangle \neq 0$. Since the frustrated Kagome geometry precludes collinear antiferromagnetic (AFM) order, it is natural to consider non-collinear (but co-planar) AFM order with $\langle \mathbf{S}(\mathbf{r})\rangle = \mathbf{n}_1 \cos \mathbf{Q}\cdot\mathbf{r} + \mathbf{n}_2 \sin \mathbf{Q}\cdot\mathbf{r}$, where $\mathbf{n_1}\cdot\mathbf{n_2} = 0$, and $\mathbf{Q}$ is a lattice-scale wave-vector whose precise form depends on the particular type of non-collinear AFM order[182]. This formulation also naturally describes a continuous phase transition between Z_2 spin-liquid and non-collinear AFM, in which the spinon pairing order parameter-amplitude vanishes continuously without proliferating topological defects of the superfluid order. The critical theory of such a transition contains gapless, deconfined spinons, and the critical properties are those of a relativistic O(4)* quantum critical point[182]. Here * denotes the fractionalized critical point in which the fractionalized objects obey the ordinary O(4) critical scaling, but in which the physical degrees of freedom are composite operators of these fractionalized fields. Interestingly, the quantum critical properties are largely independent of the particular details of the type of Z_2 spin-liquid or non-collinear AFM order.

9.3 Optical Absorption - Some General Symmetry Considerations

On symmetry grounds, a uniform external electric field, $\mathbf{E}$, will couple to any time-reversal even and spatially uniform operator that transforms like a vector representation of the Kagome symmetry group. In the absence of spin-orbit coupling, the electric field couples only to spin-singlet operators. In the U(1) Dirac theory, the operators with lowest scaling dimension are the 15 fermion-bilinear mass terms[174]: $\mathbf{N}^i_A = \bar{f}\tau^3\mu^i\boldsymbol{\sigma}f$, $\mathbf{N}_B = \bar{f}\tau^3\boldsymbol{\sigma}f$, and $N^i_C = \bar{f}\tau^3\mu^i f$, where μ^i are Pauli matrices in the valley basis. Since N_A and N_C break translational invariance they cannot couple to a uniform $\mathbf{E}$, and since N_B is a scalar, only its spatial derivative can couple to $\mathbf{E}$ (which would not contribute in the optical conductivity regime: $q \approx 0$, $\omega \neq 0$).

The next lowest dimensional operators are: the emergent gauge fields $\mathbf{e}$ and b, and conserved spinon-number current $\mathbf{j}_f$ and spinon spin-current j^i_{Sk} (here i refers to the direction of the current of the k component of spin). In the absence of spin-orbit coupling, only $\mathbf{e}$ has the right symmetries to couple to $\mathbf{E}$. In the presence of spin-orbit coupling, $\mathbf{j}_S$ may also couple to $\mathbf{E}$. Therefore, we expect the electric field along the i-direction to couple to the operator $\mathcal{O}^i_{\mathrm{U}(1)} = \lambda_1 e^i + \lambda_2^{ikl} j^k_{Sl} + \ldots$ where λ_1 and λ_2 are, for the moment, unknown coefficients and $\ldots$ represents operators with higher numbers of time-derivatives that make negligible contributions to AC conductivity at low frequency. As explained in more detail below, the scaling dimensions of $\mathbf{e}$ and $\mathbf{j}_S$ are fixed by conservation laws, indicating that the conductivity from coupling to these operators scales like $\sigma \sim \omega^2$.

Similar symmetry arguments can be applied to identify the low-energy operators of the critical Z_2 spin-liquid theory that may couple to an external electrical field. While there is no gapless emergent electric field in this scenario, in the presence of spin-orbit coupling, the conserved spin-current may couple to $\mathbf{E}$ again giving $\sigma \sim \omega^2$. The emergent $O(4)$ symmetry of the Z_2-AFM quantum critical point gives rise to 9 low-dimensional operators with the small scaling dimensions[182]. If coupling to these operators were allowed, it would contribute very low power-law frequency dependence $\sigma \sim \omega^{0.5}$ based on their known scaling dimensions. However, only higher time-derivatives of these operators can couple to $\mathbf{E}$, giving higher power conductivity $\sigma \sim \omega^{2.5}$. Therefore, the operator that couples to $\mathbf{E}$ in the Z_2-AFM critical point is: $\mathcal{O}_{Z_2} = \lambda_3 \mathbf{j}_S + \ldots$, where λ_3 is an unknown coefficient and $\ldots$ represent less relevant operators.

These general considerations greatly constrain the operator form of the physical current operator, and predict conductivity scaling like $\sigma \sim \omega^2$. In the following sections, we explore microscopic origins of these symmetry allowed couplings, in order to estimate the size of the coefficients $\lambda_{1,2,3}$.

9.4 Purely Electronic Mechanism for Sub-Gap Absorption in U(1) Spin-Liquids

In states with emergent U(1) gauge fields, linear coupling between external electromagnetic fields and the emergent electromagnetic fields are generally allowed by symmetry. Dissipation by coupling to gapless emergent degrees of freedom was originally discussed by Ioffe and Larkin[176] within the slave-boson approach, who argued that the physical conductivity σ was equal to the inverse sum of the boson and spinon conductivities, σ_b and σ_f:

$$\sigma = \frac{\sigma_b \sigma_f}{\sigma_b + \sigma_f} \tag{9.15}$$

This result was later adapted specifically to the spinon-Fermi surface state and the Dirac spin-liquid by Ng and Lee[160].

Here we will revisit this absorption mechanism for the case of a Dirac spin-liquid in

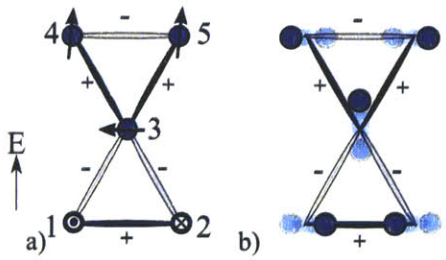

Figure 9-2: Panels a) and b) show the spin- and magneto-elastic mechanisms that couple the emergent gauge electric field $\mathbf{e}$ to an applied external field $\mathbf{E}$ shown here along the vertical (y) direction. Panel a) depicts a spin configuration that has a net polarization along the electric field due to virtual charge fluctuations. Dark shaded bonds labeled + and light shaded bonds labeled − respectively indicate strong and weak spin-singlet correlations. The arrows schematically indicate spin-orientation; since the individual spin operators $\mathbf{S_i}$ do not commute with the polarization operator the true quantum states associated with definite polarization will be in some entangled superposition of similar spin-configurations. Panel b) shows a distortion of the Cu^{2+} ions induced by the electric field. This distortion alters the bond distance, which increases the exchange coupling J_{ij} for dark bonds labeled + and decreases it for light bonds labeled −. Both mechanisms have the same symmetry.

a strong Mott insulator. We adapt the strong-coupling expansion results of Ref. [180] to reveal the microscopic origin to the Ioffe-Larkin absorption mechanism, enabling us to make semi-quantitative estimates of the magnitude of this effect for Herbertsmithite. While our results in this section are qualitatively similar to the previous study of Ref. [160], we find some differences. In particular, we find a different t/U dependence of the optical absorption than obtained from a slave-rotor mean-field description. Moreover Ref. [160] found that the Ioffe-Larkin mechanism produced conductivity scaling like $\sigma_{\rm IL} \sim \omega^{2-\beta}$ where β was an unknown anomalous dimension. Here, we argue that the emergent gauge invarianes exactly fixes $\beta = 0$.

While real charge transitions are forbidden in the Mott insulating phase, virtual charge transitions can mediate a coupling between an externally applied physical electromagnetic field, A^μ and the emergent gapless gauge and spinon degrees of freedom of the spin-liquid, thereby generating dissipation. In p.3 of Ref. [180], Bulaevskii et al. derived an expression for the electron polarization and current operators for a 3-site Hubbard model triangle: ${}_1\overset{3}{\triangle}_2$, in the large U limit. The resulting operators are expressed purely in terms of spin-variables, using a strong coupling expansion in $t/U \ll 1$, to eliminate configurations with double occupancies. The leading order contribution to the polarization for a triangle of spins was found to be:

$$\begin{aligned}\mathbf{P} &= 12ea\left(\frac{t}{U}\right)^3 \begin{pmatrix} \mathbf{S}_3 \cdot (\mathbf{S}_2 - \mathbf{S}_1) \\ \frac{1}{\sqrt{3}}\left[\mathbf{S}_3 \cdot (\mathbf{S}_1 + \mathbf{S}_2) - 2\mathbf{S}_1 \cdot \mathbf{S}_2\right] \end{pmatrix} \\ &\equiv 12ea\left(\frac{t}{U}\right)^3 \boldsymbol{\nabla}\left(\mathbf{S}_i \cdot \mathbf{S}_j\right) \end{aligned} \tag{9.16}$$

where e is the charge of an electron (which should not be confused with $\mathbf{e}$, the emergent

electric field), a is the lattice spacing (which should not be confused with the emergent vector potential $\mathbf{a}$). Here, $\boldsymbol{\nabla}$ is the discrete lattice derivative defined on the lattice of bond-centers with bonds labeled by their endpoints i and j. The x and y components of this discrete gradient are written out explicitly in the first line.

This polarization will couple the spins of each triangle linearly to an external electric field $\mathbf{E}$, giving a perturbation to the spin-Hamiltonian:

$$\delta H_{\mathbf{E}}(t) = -\int d^2 r \mathbf{P}(\mathbf{r},t)\cdot\mathbf{E}(\mathbf{r},t) \tag{9.17}$$

A small magnitude applied AC electric field $\mathbf{E} = \mathbf{E}_0 e^{-i\omega t}$ produces an induced polarization: $\langle P\rangle_E = \langle \mathbf{P}_\omega \mathbf{P}_{-\omega}\rangle E(\omega)$, delivering energy through $\delta H\mathbf{E}$ at a rate of $\Re e\left[\langle \mathbf{P}_\omega \mathbf{P}_{-\omega}\rangle\right] E_0^2$, or, equivalently, giving conductivity $\sigma = i\omega\langle \mathbf{P}_\omega \mathbf{P}_{-\omega}\rangle n_\triangle$ where $n_\triangle = \frac{1}{\sqrt{3}a^2}$ is the density of triangles in the kagome lattice with lattice spacing a.

Expressing the polarization operator P as a sum of the polarizations on each triangle, re-written in terms of spin-operators through Eq. 9.16, we find that the spin-electric field coupling produces the conductivity:

$$\sigma_{\text{IL}}(\omega) \approx \frac{1}{\sqrt{3}} i\omega\,(12e)^2 \left(\frac{t}{U}\right)^6 \langle |\boldsymbol{\nabla}(\mathbf{S}_i\cdot\mathbf{S}_j)(\omega)|^2\rangle \tag{9.18}$$

In the large U limit, the bond energy gradient was previously shown to be directly related to the emergent electric field :

$$\mathbf{e} \approx \frac{J}{2}\boldsymbol{\nabla}(\mathbf{S}_i\cdot\mathbf{S}_j) \tag{9.19}$$

where $J \approx \frac{4t^2}{U}$ is the magnetic exchange coupling. From this expression, we see that there is a linear coupling between the physical electrical field and the emergent electromagnetic field. Such a linear-coupling was previously identified by Ioffe and Larkin based on a slave-boson effective field theory description of the Hubbard model.

The result presented here is simply a strong-coupling generalization of the Ioffe-Larkin result valid for $t \ll U$. Though the functional form of the $\mathbf{E}\cdot\mathbf{e}$ coupling is identical to the slave-rotor treatment, the strong-coupling expansion predicts a different t/U dependence compared to a mean-field slave-rotor treatment of the Hubbard model. For example, comparing to Eq. 9.18, and using $\sigma = \frac{1}{i\omega}\langle j_{\text{ph}} j_{\text{ph}}\rangle$, we identify the physical electromagnetic current (in the optical conductivity limit, $\mathbf{q} = 0$, $\omega \neq 0$) as:

$$\mathbf{j}_{\text{ph}} \approx 6ean_\triangle \frac{t}{U^2}\partial_t \mathbf{e} \tag{9.20}$$

This result disagrees with the slave-rotor mean-field theory in the large U limit, which would have predicted $\mathbf{j}_{\text{ph slave-rotor}} \sim \frac{t^2}{U^3}\partial_t \mathbf{e}$. We believe that this discrepancy is due to the mean-field treatment of the slave-rotor theory, which does not properly account for the gauge constraint in determining the properties of virtual charge excitations. A simple illustration of the shortcoming of the slave-rotor mean-field, is that it predicts

that gapped charge excitations propagate with velocity $ta \sim v_F$ rather than Ja as would be appropriate for the strong-Mott limit. In contrast, the strong-coupling t/U expansion maintains the physical electron Hilbert space, and in our view, provides a more reliable determination of the coupling between spins and external electromagnetic fields. The results of the t/U expansion can then be taken as a starting point for the slave-particle effective field theory, which we can better expect to correctly capture the low-energy physics of the spin-system.

These considerations show that the contribution to AC conductivity from coupling to the emergent gauge field is:

$$\sigma_{\mathrm{IL}} \approx \frac{72\pi}{\sqrt{3}} \frac{e^2}{h} i\omega \frac{t^2}{U^4} \langle e_\omega e_{-\omega} \rangle \tag{9.21}$$

In the absence of magnetic instantons the emergent gauge field components form a conserved current:

$$\begin{aligned} j^\mu_{\mathrm{em}} &= \begin{pmatrix} b \\ \mathbf{e} \times \hat{z} \end{pmatrix} \\ \partial_\mu j^\mu_{\mathrm{em}} &= \partial_t b + \hat{z} \cdot \nabla \times \mathbf{e} = 0 \end{aligned} \tag{9.22}$$

where the second line is Faraday's law of induction for the emergent gauge field, which becomes asymptotically exact at low energies due to the emergent gauge symmetry. In a deconfined U(1) spin-liquid state with emergent scale invariance, such as the Dirac spin-liquid, the electric field cannot acquire any anomalous dimension due to this emergent conservation law. These considerations exactly fix the scaling of $\sigma_{\mathrm{IL}} \sim \omega^2$ for the Dirac spin-liquid.

To estimate the magnitude of the prefactor, we need to rely on an approximate treatment of the low-energy effective field theory. In a random-phase approximation (RPA) treatment of the low-energy effective action, the gauge field propagator is set by the spinon electromagnetic response kernel. Starting with the low-energy effective Dirac theory, Eq. 9.2, choosing a gauge such that $a^0 = 0$, and adding a source term, $\mathbf{J}^e$, for $\mathbf{e}_{\mathbf{k},\omega} = -\omega \mathbf{a}_{\mathbf{k},\omega}$:

$$\begin{aligned} \mathcal{L} =& \bar{f}_{\mathbf{k},\omega} \left[-i\omega + v_D \boldsymbol{\tau} \cdot \mathbf{k} \right] f_{\mathbf{k},\omega} + \mathbf{j}_{\mathbf{q},\Omega} \cdot \mathbf{a}_{\mathbf{q},\Omega} \\ & - \mathbf{J}^e_{-\mathbf{k},-\omega} \cdot \omega \mathbf{a}_{\mathbf{k}\omega} \end{aligned} \tag{9.23}$$

Integrating out the spinons within the RPA yields the following effective action for $\mathbf{a}$:

$$\mathcal{L}_a = \frac{1}{2} a^i_{\mathbf{k},\omega} K^{ij}_f(\mathbf{k},\omega) a^j_{-\mathbf{k},-\omega} - \mathbf{J}^e_{-\mathbf{k},-\omega} \cdot \omega \mathbf{a}_{\mathbf{k}\omega} \tag{9.24}$$

Where $K^{ij}_f = \langle j^i j^j \rangle$ is the spinon electromagnetic response kernel. Integrating out

the emergent gauge field gives the effective action for the source $\mathbf{J}_e$:

$$\begin{aligned}\mathcal{L}_{J^e} &= -\frac{1}{2}\omega^2 \left(J^e_{\mathbf{k},\omega}\right)^i \left(K_f^{ij}(\mathbf{k},\omega)\right)^{-1} \left(J^e_{-\mathbf{k},-\omega}\right)^j \\ &= \frac{\omega}{2\sigma_D}|J^e_{\mathbf{k},\omega}|^2 \end{aligned} \tag{9.25}$$

where σ_D is the conductivity for massless Dirac fermions (with the effective charge set to 1), which is a universal constant at low-frequency. Analytically continuing back to real time, these manipulations show that, in the RPA, the real-time $\langle ee \rangle$ correlator takes the form:

$$\langle e^i_\omega e^j_{-\omega} \rangle_{\text{RPA}} = -\frac{i\omega}{2\sigma_D}\delta_{ij} \tag{9.26}$$

The precise value of this universal constant can depend on whether one has free, interaction dominated, or disorder-dominated fermions. Neglecting the effects of gauge-fluctuations, one has: $\sigma_D = \frac{N_f}{16} = \frac{1}{8}$.[184]

Combining this result with Eq. 9.18 yields:

$$\sigma_{\text{IL}}(\omega) \approx 48\sqrt{3}\pi \left(\frac{t^2\omega^2}{U^4}\right)\frac{e^2}{h} \tag{9.27}$$

Here the large numerical prefactor is primarily due to the factor of 12 in the relation between spin and electric polarization, Eq. 9.16.

The experiments by Pilon et al. [179], examine optical conductivity at terahertz frequencies corresponding to $\hbar\omega \approx 4\text{meV} \approx 50\text{K}$. At $\omega = 1\text{THz}$, they measure three-dimensional conductivity of order $\sigma_{3\text{D}}(1\text{THz}) \approx 0.1\Omega^{-1}\text{cm}^{-1}$. For interlayer spacing $\sim 10\mathring{A}$, this corresponds to two-dimensional conductivity $\sigma(1\text{THz}) \approx 10^{-4}\frac{e^2}{h}$. Comparatively, we have $U \sim 1eV$ and $t \sim U/10$. These numbers give an estimated magnitude for the conductivity produced by coupling to the emergent electric field: $\sigma_{\text{IL}}(1\text{THz}) \sim 10^{-5}\frac{e^2}{h}$, which is slightly smaller than, but roughly the same order as that observed. We will see in the next section, that a coupling with the same symmetry also arises from magneto-elastic coupling, which is expected to contribute additively to this purely electronic contribution.

9.5 Magneto-Elastic Mechanisms for Absorption

In the previous section, we discussed sub-gap optical absorption in a U(1) spin-liquid through the Ioffe-Larkin coupling of the applied and emergent electric fields. Beyond the pure spin-model, there will be additional pathways for optical conduction from magneto-elastic coupling between spin and lattice distortions and from the interplay of magneto-elastic and spin-orbit couplings. In practice, we will argue that these mechanisms may be more important than the purely electronic contributions described above. Furthermore, in the presence of spin-orbit coupling, these additional absorption mechanisms will also be relevant for nearly gapless Z_2 spin-liquids without

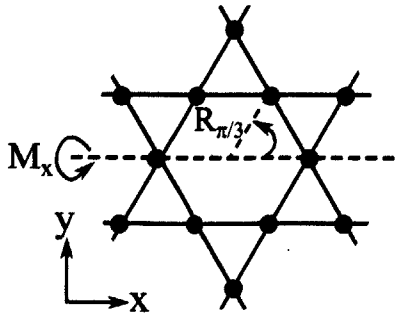

Figure 9-3: The Kagome point group is generated by mirror reflections, M_x, about the x-axis passing through the center of the vertical hour-glasses, and $\pi/3$ rotations, $R_{\pi/3}$ about the center of the hexagons.

an emergent U(1) gauge field.

9.5.1 Magnetoelastic Coupling to Emergent Electric Field

Since the Cu ions have a net charge, an external electric field can give rise to a relative displacement of Cu ions within the unit cell. As shown in Fig. 9-2b, this distortion will increase the hopping strength along some bonds and decrease it along others, yielding a perturbation:

$$\delta H_{\mathrm{ME}} = \sum_{\langle ij \rangle} \delta J_{ij} \mathbf{S}_i \cdot \mathbf{S}_j \tag{9.28}$$

While deriving the precise distortion resulting from an electric field would require knowledge of complicated details of various lattice-elasticity parameters, it is sufficient for our purposes to simply determine what spin-operators can couple to this distortion on symmetry grounds. The pattern of modified exchange couplings, δJ_{ij}, induced by the lattice-distortion shown in Fig. 9-2b can be expressed as linear combinations of the basis elements:

$$\begin{aligned} &\equiv \mathbf{S}_4 \cdot \mathbf{S}_5 - \mathbf{S}_1 \cdot \mathbf{S}_2 \\ &\equiv \mathbf{S}_4 \cdot \mathbf{S}_3 - \mathbf{S}_3 \cdot \mathbf{S}_2 \\ &\equiv \mathbf{S}_5 \cdot \mathbf{S}_3 - \mathbf{S}_3 \cdot \mathbf{S}_1 \end{aligned} \tag{9.29}$$

Here, we represent the resulting pattern of δJ_{ij}'s pictorially for a single unit cell consisting of one upward and one downward facing triangles. Black (white) circled-bond representing $\delta J_{ij} > 0$ ($\delta J_{ij} < 0$) respectively, and it is implicit that the pattern shown should be repeated uniformly throughout the Kagome lattice.

As illustrated in Fig. 9-3, the Kagome point-group is generated by 1) clock-wise $\frac{\pi}{3}$ rotations about the center of a Hexagon, denoted $R_{\pi/3}$, and 2) mirror reflections through the horizontal axis (x-axis) passing through the points of triangles, denoted

M_x. The transformation properties of the basis elements in Eq. 9.29 are:

(9.30)

This three dimensional representation of the Kagome point-group reduces into a one-dimensional pseudoscalar, B_2, irreducible representation (irrep) spanned by:

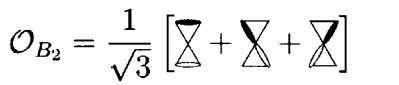

(9.31)

and a two-dimensional vector, E_1, irrep spanned by:

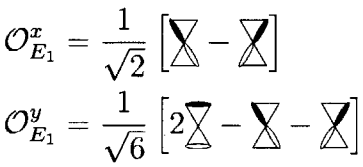

(9.32)

The external electric field $\mathbf{E}$ is a vector, transforming like the E_1 irrep of the Kagome point-group, and hence only couples to the E_1 components: $\delta H_{\mathrm{ME}} \approx \mathbf{E} \cdot \boldsymbol{\mathcal{O}}_{E_1}$. Comparing the symmetry of $\boldsymbol{\mathcal{O}}_{E_1}$, we see that this operator is just the discrete bond-energy gradient corresponding to the polarization operator generated described in the Eq. 9.16 of the previous section. Therefore, as previously pointed out in Ref. [180], the magneto-elastic coupling due to the electric field induced displacement of Cu ions will generate a coupling of the same form as in Eqs. 9.16,9.18, but with a coupling constant $\frac{\partial J_{ij}}{\partial u_{ij}} \frac{\partial u_{ij}}{\partial E} \approx \frac{eJ}{K_{\mathrm{Cu}} a^2}$ in place of the $\left(\frac{t}{U}\right)^3$ appearing in Eq. 9.16, where u_{ij} is the ionic displacement induced by the electric field, and K_{Cu} is the effective spring constant for the Cu displacement shown in Fig. 9-2b.

For the Dirac spin-liquid, the perturbation Eq. 9.28 produces a linear coupling between the external and emergent electric fields, just as with the Ioffe-Larkin mechanism discussed in Sec. 9.4. In this case, following the derivation of Eq. 9.27 in Sec. 9.4, we see that this magneto-elastic coupling leads to optical conductivity:

$$\sigma_{\mathrm{ME}}(\omega) \approx \left(\frac{\omega}{K_{\mathrm{Cu}} a^2}\right)^2 \frac{e^2}{h} \tag{9.33}$$

In contrast, since this magneto-elastic mechanism relies on the presence of an emergent U(1) gauge field, it is not expected to produce low-power-law frequency dependence of optical absorption for the nearly critical Z_2 spin-liquid scenario. The energy scale $K_{\mathrm{Cu}} a^2$ is expected to be of order $\sim$ 1eV, which is comparable to U. Consequently, for the Dirac spin-liquid, this absorption mechanism may dominate over the Ioffe-Larkin contribution of Eq. 9.27, which is smaller by a factor of $\left(\frac{t}{U}\right)^2$.

9.5.2 Spin-Orbit Coupling

The mechanisms described in the previous section relied on the existence of an emergent electric field, a low-dimensional operator with the right symmetries to couple to the external electric field (i.e. a time-reversal invariant, spatially uniform, spin-singlet operator transforming under the E_1 representation of the Kagome point group).

These mechanisms are special to the U(1) spin-liquid, since, in the alternate scenario where the ground state is a nearly critical Z_2 spin-liquid, there are no spin-singlet operators with the right symmetry properties. However, as we will show in this section, the presence of spin-orbit coupling enables the external electric field to couple not only to spin-singlet operators, but also time-reversal invariant spin-pseudovectors. In particular, the combination of spin-orbit and magneto-elastic couplings will generically enable the electric field to couple to spin-current, enabling purely electrical probes of spin-transport. This coupling to spin-current provides alternative mechanisms for optical absorption which lead to AC electrical conductivity scaling like $\sigma \sim \omega^2$ in any gapless relativistic state. In particular this mechanism is also relevant in a nearly gapless state, at finite frequency above the spin-gap, for example in the vicinity of an O(4) quantum critical point between a Z_2 spin-liquid and non-collinear antiferromagnet.

Dzyaloshinskii-Moriya (DM) Terms

We begin with a brief overview of spin-orbit coupling in Herbertsmithite and related Cu spin-1/2 Kagome antiferromagnets. Due to the atomic spin orbit coupling in the Cu d-orbitals, λ_{so}, and because spin-exchange occurs along a bent Cu-O-Cu superexchange pathways, Herbertsmithite has substantial Dzyaloshinskii-Moriya (DM) interactions: $\sum_{\langle ij \rangle} \mathbf{D}_{ij} \cdot (\mathbf{S}_i \times \mathbf{S}_j)$, where the DM vector $D \approx \frac{\lambda_{so} t}{U} \sin \alpha$ where α is the angle of the Cu-O-Cu oxygen bond (defined such that $\alpha = 0$ for a linear superexchange pathway). For Herbertsmithite, the DM interactions are expected to be roughly 10% of the exchange energy: $D \approx 0.1J$.

The dominant effects of the DM interactions come from the z-component of the DM vectors, $\hat{z} \cdot \mathbf{D}_{ij}$, where the $\hat{z}$ denotes the c-axis perpendicular to the Kagome planes. As we will see below, the DM terms generate coupling between external electric fields and spin-current. Since the in-plane components sum to zero within the unit cell, these components can only create a response to spatially inhomogeneous electric fields that vary in sign over short distances of order a single lattice spacing. Such sharp spatial variations are not relevant for AC conductivity measurements that probe the response to long wave-length fields, and therefore the in-plane DM components may be neglected for what follows.

In a Schwinger-fermion mean-field description of the Heisenberg model, the DM terms simply become spin-orbit hopping terms for the spinons:

$$\mathbf{D}_{ij} \cdot (\mathbf{S}_i \times \mathbf{S}_j) \to i \frac{\chi^f_{ij}}{J} \mathbf{D}_{ij} \cdot \left(f^\dagger_{i,a} \boldsymbol{\sigma}_{ab} f_{j,b} \right) \tag{9.34}$$

where $\chi^f = \langle f^\dagger_{i\sigma} f_{j\sigma} \rangle$. For the Dirac spin-liquid state, this pattern of DM interactions

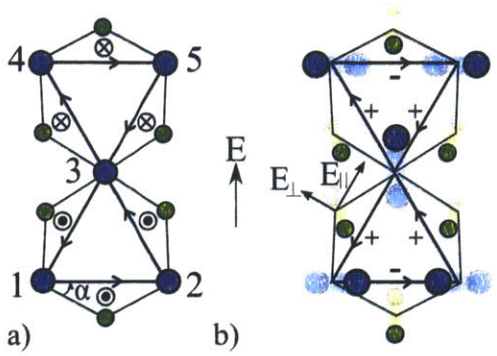

Figure 9-4: Blue and green dots are Cu and O ions respectively. a) DM arises from the bent Cu-O-Cu bonds. The pattern of **D** vectors is shown by $\otimes$ and $\odot$ indicating **D** into and out of the plane respectively for the bond-orientation shown with arrows. b) In an electric field, the oppositely charged Cu^{2+} and O^{2-} ions undergo relative displacements. The O ion displacement changes the bond-angle, and the Cu displacement changes the bond exchange strength as described in Fig. 9-2. As explained in the text, this alters the DM pattern as indicated by the + and − labels, which couples the electric field to the spin-current.

translates into a quantum spin-Hall mass for the Dirac spinons. Such a term is expected to gap out the Dirac spinons, enabling gauge-instantons to proliferate. Due to the quantum spin-Hall response, such instanton flux-insertion events are bound to spin-flips, and their proliferation leads to magnetic order[174]. Similarly, Schwinger-boson mean-field treatments of the Kagome-Heisenberg model indicate that the Z_2 spin-liquid state for the bare Heisenberg model is destabilized by finite DM interactions, which are predicted to drive the model to non-collinear antiferromagnetic order[181]. Experimentally, Herbertsmithite appears to avoid magnetic order to the lowest achievable temperatures, and is either gapless or has a very small gap.

DM Modulation

The lattice distortion discussed above in Sec. 9.5.1 alters the Cu to Cu bond lengths following the pattern shown in Eq. 9.32, thereby changing the hopping strengths along these bonds in the same manner. Since the DM vector on bond ij is related to the Cu-Cu hopping strength by: $D_{ij} \sim \frac{t_{ij}\lambda_{\rm SO}}{U}$, this distortion also changes the magnitude of the DM vectors in the same manner, introducing the perturbation:

$$\delta H_{\rm DM}^{\text{Cu Distortion}} = \sum_{\langle ij \rangle} \alpha_{ij} \hat{z} \cdot (\mathbf{S}_i \times \mathbf{S}_j) \tag{9.35}$$

For definiteness, we consider E along the vertical (y-) direction as shown in Fig. 9-4b. In this case, the magnitudes, $|\alpha_{ij}|$, are twice as large on the horizontal bonds ($\overline{12}$ and $\overline{45}$) as on the angled bonds ($\overline{23}$, $\overline{31}$, $\overline{34}$ and $\overline{53}$). The sign structure of α_{ij} can be

represented pictorially by:

$$\delta H_{\rm DM} \sim 2$$ 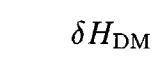 (9.36)

where we have expanded the coupling as a linear combination of the basis operators:

$$\begin{aligned}
&\equiv \hat{z}\cdot(\mathbf{S}_1\times\mathbf{S}_2)+\hat{z}\cdot(\mathbf{S}_4\times\mathbf{S}_5)\\
&\equiv \hat{z}\cdot(\mathbf{S}_3\times\mathbf{S}_2)+\hat{z}\cdot(\mathbf{S}_4\times\mathbf{S}_3)\\
&\equiv \hat{z}\cdot(\mathbf{S}_5\times\mathbf{S}_3)+\hat{z}\cdot(\mathbf{S}_3\times\mathbf{S}_1)
\end{aligned} \qquad (9.37)$$

which form a closed set under the action of the Kagome point group.

Since the oxygen and Cu ions are oppositely charged, they will generally they will undergo a relative displacement in a uniform electric field, E. In particular, the oxygen bond angles will be changed thereby changing the DM terms as indicated in Fig. 9-4b. To linear order the DM change is affected only by the bond-angle change, which depends only to the component oxygen displacement perpendicular to the local bond direction within the kagome plane. For definiteness, we consider E along the vertical direction in Fig. 9-4 resolving the applied field in to directions along and perpendicular to the local bonds: $E_{ij,\parallel}$ and $E_{ij,\perp}$, as shown in Fig. 9-4b. It can be readily seen that this contributes a term of the same form as Eq. 9.36.

This perturbation, $\delta H_{\rm DM}^{\rm O^{2-}}$, can couple to any spin-operator with the same symmetries. Therefore, it is instructive to determine its transformation properties of under the Kagome lattice point-group by considering irreducible representations constructed from the basis of Eq. 9.37. In the presence of spin-orbit coupling terms, the Kagome point-group remains unchanged but the spatial point-group transformations must also be accompanied by spin-rotations[174]. Since, as explained above, we may neglect the in-plane components of the DM vectors the only modification is that mirror reflections about the x-axis must be accompanied by π spin-rotations around the x-axis.

Under the action of $R_{\pi/3}$ and M_x, the vector chirality combinations of Eq. 9.37 transform like:

$$\begin{aligned}
\{\,,\,,\,\} &\xrightarrow{R_{\pi/3}} -\{\,,\,,\,\}\\
\{\,,\,,\,\} &\xrightarrow{M_x} -\{\,,\,,\,\}
\end{aligned} \qquad (9.38)$$

where the minus sign in the first line arises because rotations invert our chosen bond-orientation, swapping $\mathbf{S}_i\times\mathbf{S}_j\to\mathbf{S}_j\times\mathbf{S}_i=-\mathbf{S}_i\times\mathbf{S}_j$. Similarly the minus sign in the second comes from the extra spin-rotation that accompanies the mirror reflection M_x. Furthermore, since all of these combinations arise from linear combinations of vector spin-chirality, each of the basis vectors are invariant under time-reversal symmetry.

The three dimensional representation of the Kagome point-group spanned by the basis shown in Eq. 9.37 is reducible, and decomposes into one-dimensional pseudo-

scalar, A2, irreducible representation (irrep) spanned by (see Appendix C of Ref. [174] for more details about the representation theory for the Kagome point-group):

$$O_{\mathrm{DM},A_2} = \frac{1}{\sqrt{3}} \left[\quad + \quad + \quad \right] \tag{9.39}$$

and a two-dimensional vector, E_1, irrep spanned by:

$$O^{y}_{\mathrm{DM},E_1} = \frac{1}{\sqrt{6}} \left[2 \quad - \quad - \quad \right]$$
$$O^{x}_{\mathrm{DM},E_1} = \frac{1}{\sqrt{2}} \left[\quad - \quad \right] \tag{9.40}$$

The Cu bond-, and oxygen bond angle- distortions couple only to the E_1 vector piece: $\delta H_{\mathrm{DM}} \sim \mathbf{E} \cdot \mathbf{O}_v$. To summarize, $\sum_{\langle ij \rangle} \alpha_{ij} \hat{z} \cdot (\mathbf{S}_i \times \mathbf{S}_j)$ is time-reversal invariant, transforms as the z-component of a vector under spin-rotations, and transforms like a E_1 vector representation of the Kagome point-group. These transformation properties are exactly the same as the z-component of the spin-current, $\mathbf{j}_{S^z}$. Therefore, there one should generically expect a linear coupling between the electric field and the spin-current, mediated by the oxygen bond distortion shown in Fig. 9-4b. Interestingly, this coupling implies that one can directly probe spin-conductivity of Kagome materials with the DM pattern shown in Fig. 9-4a, purely through electrical measurements.

This expectation can be explicitly verified. Noting that the spin-current operator obeys the continuity equation $\frac{\partial S^a}{\partial t} = -i[H, S^a] = -\nabla \cdot \mathbf{J}_{S^a}$, and using the Heisenberg Hamiltonian to compute the time-evolution, one finds that the a-component of spin-current along the $\overrightarrow{ij}$ bond is just $(\mathbf{S}_j \times \mathbf{S}_i)^a$. Alternatively, for the spin-liquid scenarios, one can perform a mean-field decomposition of the perturbation term within the Schwinger fermion (or boson) framework using Eq. 9.34. In either case, one finds that the perturbation, $\delta H_{\mathrm{DM}} \sim \mathbf{E} \cdot \mathbf{O}_v$, induces a uniform spin current, $\mathbf{j}_{S^z}$, perpendicular to the applied $\mathbf{E}$ field in the $\hat{z} \times \mathbf{E}$ direction. Hence, the optical conductivity resulting from this mechanism will be proportional to ω^2 times the spin-conductivity.

Modeling the Cu and Oxygen bond-angle distortions as springs with effective spring-constant K_{Cu} and K_{O} respectively, one can estimate the magnitude of the induced coupling:

$$\delta H_{\mathrm{DM}} \approx \frac{2eD\chi^f}{JK_{\mathrm{eff}}a} \mathbf{E} \cdot (\hat{z} \times \mathbf{j}_{S^z}) \tag{9.41}$$

where $K_{\mathrm{eff}} = \left(\frac{1}{K_{\mathrm{O}} \cos\alpha} - \frac{1}{K_{\mathrm{Cu}}} \right)^{-1}$ is the effective spring constant accounting for the fact that the Cu^{2+} and O^{2-} ions have opposite charge, and α is the Cu-O bond-angle.

For the Dirac spin-liquid, Eq. 9.41 indicates that an external electric field induces a spin-current j_{S^z}:

$$\mathbf{j}_{S^z} \approx \frac{D}{J} \frac{1}{K_{\mathrm{eff}}a} (i\omega\sigma_D) (\hat{z} \times \mathbf{E}) \tag{9.42}$$

where σ_D is the spinon-conductivity. Similar results will hold for the $\mathbb{Z}_2$ case.

Since $\mathbf{j}_{S^z}$ is a conserved quantity, its scaling dimension is fixed in any scale invariant theory, like the Dirac spin-liquid or in the vicinity of a quantum-critical point, resulting in $\sigma(\omega) \sim \omega^2$.

$$\sigma_{\text{DM}} \approx \frac{e^2}{h}\left(\frac{D}{J}\right)^2\left(\frac{\omega}{K_{\text{eff}}a^2}\right)^2\sigma_s \tag{9.43}$$

where $\sigma_s = \frac{1}{i\omega}\langle j_{s^z} j_{s^z}\rangle$ is the spin-conductivity.

For the Dirac spin-liquid: $\sigma_s \approx \sigma_D$ is constant. Comparing to the contribution from the spin-symmetric magneto-elastic coupling of Eq. 9.33, we see that the magnitude of the Ioffe-Larkin mechanism may dominate due to the factor of $\left(\frac{D}{J}\right)^2 \approx 10^{-2}$. However, for the scenario of a nearly gapless Z_2 spin-liquid, the spin-conductivity coupling may be the dominant absorption mechanism.

Spin-Orbit Mechanism in a Thermal Paramagnet

While we have illustrated this result explicitly for the U(1) Dirac spin-liquid, the DM mediated coupling between electric field and spin-current is generically allowed by symmetry, and will be present in any theory of Kagome spin systems with DM interactions. Furthermore, for any scale invariant theory, the resulting conductivity from coupling to this phonon mode will scale as $\sim \omega^2$, including a Dirac spin-liquid or any nearly gapless Z_2 spin-liquid in the quantum critical regime near a continuous phase transition, for example to non-collinear antiferromagnetic order.

Furthermore, the coupling of an electric field to spin-current may be the most important mechanism for thermal paramagnetic states at intermediate to high temperature ranges, well above the low-energy scale Δ_S. For example, the low energy scale Δ_S would be the spin-gap of a Z_2 spin-liquid, the magnetic ordering scale of the frustrated antiferromagnet, or the spinon bandwidth in a $U(1)$ spin-liquid (note that this scale is well-separated from J in a frustrated lattice like the Kagome). Regardless of the nature of the spin ground-state at $T \ll \Delta_S$, for $T > \Delta_S$ one can expect diffusive spin-transport with non-vanishing spin-diffusion coefficient D_s, which tends to $D_s \approx Ja^2$ at high temperature[185]. D_s is related to spin-conductivity, σ_s, by the Einstein relation $\sigma_s \approx D_s\chi_s$ where χ_s is the spin-susceptibility. At intermediate to high temperature one expects Curie-Weiss-like spin-susceptibility: $\chi_s(\omega, T) \approx \frac{1}{T+\theta_{\text{CW}}}$ with $\theta_{\text{CW}} \approx J > 0$. In Herbertsmithite, for example, χ_s is a slowly increasing function of T down to $T \approx 50$K[168], giving rise to a constant spin-conductivity, and power-law electrical conductivity $\sigma \sim \omega^2$. We note that this effect may be difficult to observe in practice, even at higher temperatures, due to the suppression of this conductivity-pathway by a factor of $\left(\frac{D}{J}\right)^2$.

9.6 Discussion of Optical Conductivity and Related Electromagnetic Probes

To summarize, we have identified three important pathways for sub-gap optical absorption mechanisms in a spin-liquid Mott insulator on the Kagome lattice: 1) a purely electronic coupling of virtual polarization and the electric field, 2) a magneto-elastic coupling with the same symmetry as 1), and 3) a magneto-elastic coupling of spin-current to a magnetic field. For a U(1) spin-liquid, absorption will occur primarily through mechanism 2), which produces $\sigma \sim \omega^2$.

The 3rd mechanism arises from the interplay of spin-orbit and magneto-elastic couplings creates a direct coupling of an electric field to the spin-current of the Kagome system. Therefore, optical conductivity measurements are also probing spin-conductivity. This mechanism is quite generic, and will produce $\sigma \sim \omega^2$ electrical conductivity in any gapless relativistic phase or critical point, including the Dirac spin-liquid and the vicinity of the O(4) deconfined critical point between a Z_2 spin-liquid and a non-collinear magnetically ordered state.

In contrast, mechanism 3) will not lead to substantial power-law conductivity deep inside a magnetically ordered state. A magnetically ordered state can be regarded as a spin-superfluid, with spin-waves corresponding to the superfluid density mode. In this state, the spin-current is given by the spatial gradient of the superfluid phase, and due to the huge mismatch in the velocity of light, c, and the spin-wave velocity, Ja, an electromagnetic field can only couple to multi-spin-wave emission processes giving a negligible contribution.

Therefore, at asymptotically low frequency and temperature, power-law optical conductivity can likely be taken as a sign of gapless (or nearly gapless) spinon excitations. At intermediate to high temperatures where the spin-system is a thermal paramagnet, the coupling to spin-current will produce $\sigma \sim \omega^2$ due to spin-diffusion, regardless of the nature of the low-temperature spin-phase (its magnitude may be small due to the factor of $\left(\frac{D}{J}\right)^2$ in Eq. 9.43). However, at temperatures below $\sim 50K$ the spin-susceptibility χ_s dips sharply with decreasing T,[170] indicating the onset of correlations and a departure from the trivial thermal paramagnet.

Within the two spin-liquid scenarios, the temperature dependence of the coefficient of the $\sim \omega^2$ optical absorption is more subtle. Within the scaling regime for both theories, the optical conductivity will act like ω^2 times a universal function of $\frac{\omega}{T}$. For the nearly critical Z_2 spin-liquid, the dominant mechanism is proportional to the spin-conductivity. For the O(4)* critical point, in the high-frequency ($\omega \gg T$) regime relevant to the experiments of Pilon et al.[179], the conductivity is expected to gradually increase, saturating to a constant value as $\frac{\omega}{T} \to \infty$ (see e.g. Ref. [186]). This temperature dependence is in agreement with that observed in Ref. [179].

As described above, in the Dirac spin-liquid case, the Ioffe-Larkin type mechanisms dominate. The resulting conductivity is proportional to the spinon-resistivity $\rho_D(\frac{\omega}{T}) = \left(\sigma_D(\frac{\omega}{T})\right)^{-1}$. Here the finite temperature and frequency scaling is known only in the limit of large-number of Dirac flavors, N_f. For $N_f \to \infty$, one recovers the case of free Dirac fermions for which ρ_D decreases with decreasing temperature

in the $\omega \gg T$ limit. This $N_f = \infty$ prediction shows the opposite temperature dependence of that observed in Pilon et al.'s experiment[179]. However we caution that it is unclear to what extent this prediction applies to the physical case of $N_f = 2$, given the absence of a controlled theory in this limit. For example, in other strongly coupled field theories based on holographic duality the temperature dependence at high frequency can be of arbitrary sign depending on details[187].

Throughout the above discussion, we have focused exclusively on absorption due to the coupling between spin excitations and the electric component of the applied optical field. In addition, there will also generally be a Zeeman coupling to the magnetic component. For conducting systems, the magnetic effects are typically strongly suppressed and subdominant to electric absorption, however in the strong Mott insulator described here the two may be more competitive. Absorption from the magnetic part of the optical field essentially probes the dissipative part of the AC spin-susceptibility. This can be distinguished from the electrical contribution by the polarization dependence, as the spin-susceptibility is more or less directionally uniform within 10% or so. In contrast, electric dipole absoprtion will have a strong polarization dependence, since electrically driven spin excitations can only be driven by the in-plane component of the electric field.

9.6.1 Emergent Gauge Field in the Presence of DM Interactions, and Field Induced Ordered States

In the presence of DM interactions, the above derivation of the physical meaning of b and $\mathbf{e}$ is altered. As described previously, since the in-plane DM vectors vanish within the unit cell, the uniform $z-$component of the DM interactions is expected to be the most important. On general symmetry grounds, the DM terms allow $b_{ijk} \rightarrow \mathbf{S}_i \cdot (\mathbf{S}_j \times \mathbf{S}_k) + \alpha \left(S_i^z + S_j^z + S_k^z\right)$, where α is of order: $\alpha \approx \mathcal{O}\left(\frac{D}{J}\right)$. The precise form of α may be derived from the Wilson loop derivation outlined above but incorporating the DM interactions at the slave-fermion mean-field level as a spin-orbit coupling term for the spinons.

The appearance of this new term shows directly that any perturbation that couples to the z-magnetization will tend to induce an emergent-gauge-magnetic flux. For example, as discussed in further detail in Ref. [188], these considerations demonstrate that neutron scattering experiments can in principle be used to detect gapless fluctuations in b.

9.6.2 Field Induced Ordering

Furthermore, spin-orbit coupling has implications for the behavior of Herbertsmithite in an applied magnetic field. For example, the Zeeman term $\frac{g\mu_B}{2} H^z$ from an external field H^z along z will induce a magnetization $M^z = \chi_s H^z$, which will produce a corresponding gauge magnetic flux $b_{\text{ind}} \sim \alpha \chi_S H^z$. In perfectly clean Dirac spin-liquid, the density of states vanishes at the Dirac point, and the spin susceptibility grows linearly with H: $\chi_S^{\text{Dirac}} \sim \frac{H^z}{J^2}$. Empirically, however, Herbertsmithite appears to have spin-susceptibility that tends to a constant of order a fraction of $\chi_S \sim \frac{1}{J}$

at low temperature[168, 169, 170]. Within the U(1) spin-liquid scenario, one could possibly interpret this finite susceptibility as a finite density of states induced, for example, by impurity scattering.

In this case, the induced magnetization per spin from an external field H^z would be: $M^z \sim \frac{H^z}{J}$, producing an emergent gauge flux through each triangle of order $\Phi_b = ba^2 \sim \frac{DH^z}{J^2} \sim 10^{-3} H^z T^{-1}$. This emergent gauge flux has a magnetic length $\ell_b \sim 30a\sqrt{\frac{H^z}{1\text{ Tesla}}} \sim 10^2 \mathring{A}\sqrt{\frac{H^z}{1\text{ Tesla}}}$, which corresponds roughly to the ordinary orbital magnetic length an electron gas in the field H^z. Therefore we expect that in a U(1) spin-liquid, the spinons will see this induce b flux as an orbital field, with an effective b-flux density that is comparable the physical flux density of H^z. This is effect is surprisingly large, since charge motion is largely frozen deep in the Mott insulating phase, and purely electronic mechanisms give effective flux for spinons that is smaller factor of $\left(\frac{t}{U}\right)^3 \sim 10^{-3}$ compared to the physical flux[190].

This large orbital b field, would then induce Landau levels into the Dirac spectrum. Neglecting Zeeman splitting, and in the absence of interactions would have a four-fold degenerate zeroth Landau level, with an approximate SU(4) symmetry as in single-layer graphene[191, 192]. However, the infinite density of states will generically cause interactions to remove this degeneracy and split the zeroth Landau level, gapping out the spinons and allowing instantons to proliferate. The nature of the resulting broken symmetry state will depend on the manner in which the Landau-level symmetry is broken, as different breakings of the SU(4) symmetry result in different quantum Hall responses (e.g. quantum- spin, valley, etc... hall effects). Within the Dirac spin-liquid scenario, such effects could possibly account for the field induced spin-freezing past a critical external field strength of a couple Tesla, which has been observed in Herbertsmithite through NMR measurements[193]. Moreover, this scenario could also be relevant in a weakly gapped Z_2 spin-liquid scenario, where the Z_2 state arises out of the Dirac spin-liquid state by BCS pairing. In such a scenario, the minimal field required to induce spin-ordering could possibly be interpreted as H_c for the spinon superconductor (one would naively expect spinon superconductors formed by adding pairing to a $U(1)$ spin-liquid to be strongly Type-1 due to the large effective gauge-charge for the emergent gauge field).

At strong-magnetic fields where the Zeeman-energy determines splitting of the lowest Dirac Landau-level, there will be a quantum spin-Hall response[194], tying a spin-flip to each instanton insertion leading to a field-induced magnetically ordered state. At lower fields, alternative scenarios might occur[192]. For example, if the zeroth Landau-level splits by valley polarization, there will be a resulting quantum valley-Hall effect. This would endow instantons with sub-lattice symmetry breaking quantum numbers; and proliferating such instantons would result in a valence-bond crystal (VBC) state. This raises the possibility of a various sequences of continuous phase transitions as a function of field, for instance from Dirac-spin-liquid to low-field VBC state, to a high-field magnetically ordered state.

The emergent gauge electric field will also be altered by the presence of DM interactions. On symmetry grounds, $\mathbf{e}$ can receive contributions of order α from operators like $(\mathbf{S}_i \times \mathbf{S}_\mathbf{j})$, which correspond to spin-current in the spinon theory. However, un-

like the magnetic field case described above, it is difficult to externally couple to spin currents, so it is unclear whether these extra terms enable useful new probes.

Chapter 10

Loose Ends and Future Directions

The work of this thesis leaves many open questions, and I will devote this last chapter to a discussion of loose ends and unanswered questions that are left to future work.

10.1 Universal Topological Quantum Computing

Part I of this thesis focused on developing ways to combine ordinary materials to produce novel types of superconductors whose topological defects (vortices in 2D and boundaries in 1D) host a single zero-energy Majorana fermion. Majorana bound-states of this type are the simplest example of non-Abelian particles. Because of its potentially significant implications for both fundamental physics and quantum computing technology, the prospect of creating Majorana bound-states in solid-state systems has generated a tremendous amount of excitement in the physics community and has spurred an extensive experimental effort. The theoretical understanding of how to engineer Majorana fermions is by now rather complete, and while substantial experimental challenges remain, it seems only a matter of time before these non-Abelian particles are routinely produced.

This dramatic progress constitutes only the first step towards the long-term goal of a noise-proof quantum computer using non-Abelian particles. Majorana fermions are only the simplest type of non-Abelian particles, and only a simple and small set of quantum operations can be implemented by braiding these particles. Consequently, Majoranas are inadequate for building a general purpose ("universal") quantum computer. Therefore, an important outstanding question is whether one can construct a realistic route to more complex types of non-Abelian particles that are capable of universal quantum computing.

Here, it may be fruitful to draw inspiration from the strategies that proved successful in producing Majorana fermions, such as combining relatively well understood materials to produce more complicated phases of matter. Theoretical progress along these lines has been made by considering interfacing fractional quantum Hall edges with superconductors[202, 203], or similarly by considering tunneling-junctions to create "wormholes" between layers of a multi-layer FQH states[204]. In these system, non-Abelian defects can be created from underlying Abelian systems. These

non-Abelian defects are fractional analogs of Majoranas, and have richer non-Abelian statistics. Moreover, like the Majorana wire-networks, these non-Abelian particles are realized in effectively 1D systems (in this case the edge of a larger 2D system). Unlike vortices in a 2D system, it is at least conceptually straightforward to imagine realistic schemes to braid such 1D defects. Unfortunately, even these novel types of non-Abelions are still insufficient for universal quantum computing, and more work is required.

10.2 Strongly Correlated Electron TIs

In Part II of this thesis, time-reversal symmetric electron TI phases were classified, including the presence of interactions. New strongly correlated TI phases with no free particle band-insulator analogs were identified. These could be thought of as topological paramagnets, or alternatively as Cooper pair insulators.

An obvious question is whether there are realistic systems that realize such phases in experiment. It is so far not even clear what types of interactions favor such phases, and an important intermediate step may be to try to simple candidate models with realistic interactions. For solid-state applications, the magnetic route is likely to be more realistic. However, strong attractive interactions between fermions can be realized in cold-atoms systems, where recent advances have enabled synthetic spin-orbit coupling. This provides a potentially promising tool-set for engineering a topological Cooper-pair insulator.

Constructing models of these phases will likely open up further questions. For example, we know that the surface of a topological paramagnet can support a symmetry-preserving surface quantum spin-liquid of a type that cannot be realized in strictly 2D. What happens when we dope such a spin-liquid? Presumably the resulting state is a metal or superconductor; does this metal or superconductor have interesting residual properties stemming from the non-trivial 3D bulk?

A related, and equally important task is to design experimental probes to detect the existence of strongly correlated TI phases. For phases associated with $e_f m_f$ surface-topological order, if TR is broken at the surface, there can be a non-vanishing surface thermal quantum Hall response, with no accompanying electrical quantum Hall response. However, thermal transport is potentially challenging, and it would be interesting to deduce alternative measurement schemes. Furthermore, it is so far unknown, even in principle, how to detect other phases stemming from the beyond-cohomology state labeled by the STO $eTmT$.

10.3 Spin-Liquids

We saw that developing a detailed understanding of spin-liquid materials, especially those with gapless excitations, is extremely challenging because it requires treating strong interactions between electrons and quantum fluctuations on equal footing. These theoretical difficulties have been exacerbated by a lack of experimental guidance

due to a limited number of known materials that cleanly exhibit signs of fractionalization. An exception to this trend comes from the recent discovery of a few quantum spin-liquid materials, in which magnetic degrees of freedom remain gapless and mobile as in a metal, despite the material being a charge-insulator, offering strong hints of spin-charge fractionalization.

For the organic compounds κ-ET and dMIT, the best theoretical understanding is based on a spinon Fermi-surface state with a deconfined emergent $U(1)$ gauge field. While experiments show behavior that is broadly consistent with such a picture, direct evidence the emergent gauge field is missing. Additionally, many more detailed aspects of the physics of these materials remain poorly understood. For instance, a few spin-liquid materials show thermodynamic signatures of low-temperature phase transitions whose nature is completely mysterious. It is necessary to scrutinize whether these phase transitions can be understood within the spin-metal picture, and if so, to find experimentally testable signatures to support such a scenario.

For the Kagome-lattice compound, Herbertsmithite, the experimental situation is much less clear. Chapter 9 developed optical conductivity as a probe of spin-liquid behavior. We saw that, in principle optical conductivity can give some clues regarding the nature of the ground-state of this material. However, we also saw that these signatures could not cleanly distinguish between different scenarios. For example a Dirac spin-liquid and the quantum critical region of a $\mathbb{Z}_2$ QSL/AFM phase-transition have the same frequency scaling for absorption (there are other critical points, e.g. a $\mathbb{Z}_2$ QSL to valence-bond solid phase transition, where the scaling properties are predicted to be very different[205]). Therefore, it is still highly desireable to identify additional, complementary probes to reveal the nature of QSL phases.

The more general hope of such a program of research is that developing a more detailed understanding of experimental materials will lead to new paradigms for understanding not only spin-liquids, but other complicated quantum phases of matter such as high-temperature superconductors or heavy-fermion systems.

10.4 Conclusion

It should be clear from this section that there are many open questions of both conceptual and scientific interest, and also potentially of technological importance. Those described above are just a few of the many possible directions in the pursuit to understand, construct, and probe highly-entangled quantum phases of matter.

Appendix A

"Slave-Boson" Parton Construction

Low-energy effective field theory descriptions of fractionalized phases of matter are most conveniently accessed by re-writing the electron field/operator as a product of auxiliary fields, called partons or "slave-particles", that carry the fractionalized quantum numbers of the desired state. This inevitably introduces unphysical degrees of freedom that must be removed from the theory to describe the original electron system. However, if we ignore that difficulty, we can describe various "mean-field" states by separately placing different partons in different phases. It must then be checked that the resulting phase of matter is consistent, in the sense that it survives once all unphysical degrees of freedom are removed.

In this appendix, we give an overview of the main principles of developing a low-energy effective theory from a parton construction. The focus will be primarily on a particular parton-construction, known as "slave-boson" or "slave-rotor" theories.

The most commonly useful example is the slave-boson, or slave-rotor construction (see e.g. [135]), in which the electron operator with z-spin component σ is rewritten as the product of a spinless charged boson ("chargeon"), $b = e^{i\phi}$, and a spinful neutral fermion ("spinon") f_σ:

$$c_\sigma = e^{i\phi} f_\sigma \tag{A.1}$$

At the operator level, this corresponds to enlarging the Hilbert space of each site of the system, from the original electron Hilbert space, to the new Hilbert space that can be labeled by direct products of states with definite boson occupation number $|n_b\rangle$ ($n_b \in \mathbb{Z}$), and spinon occupation number $\{|0\rangle, f_\uparrow^\dagger|0\rangle, f_\downarrow^\dagger|0\rangle, f_\uparrow^\dagger f_\downarrow^\dagger|0\rangle\}$. Clearly, the infinite number of slave-particle states do not all correspond to physically meaningful states.

Therefore, in order to make the parton description exactly faithful, we must constrain our Hilbert space such that only physical electronic states are present. Physical states are described by those with equal spinon and boson number: $n_b = n_f$. Since b and f have a microscopically conserved number, corresponding to a conserved $U(1)$ current, we can implement the constraint exactly, by introducing a local $U(1)$ gauge

field a, under which b and f have opposite "charges". Then the gauge-invariance of the resulting partition function automatically enforces the physical constraint.

Gauge transformations are generated by rotating $e^{i\phi_j} \to e^{i(\phi_j+\Lambda_j)}$, $f_{j,\sigma} \to e^{-i\Lambda_j} f_{j,\sigma}$, and $a_{ij} \to a_{ij} + \Lambda_i - \Lambda_j$. Clearly, the electron operator $c_{j,\sigma}$ is invariant undert these transformations. Since these transformations are periodic under $\Lambda_i \to \Lambda_j + 2\pi n_j$, for arbitrary $n_j \in \mathbb{Z}$, the emergent gauge field is compact. In 2D systems, this compactness enables instanton tunneling events, in which 2π flux of the emergent gauge-magnetic field is nucleated and then spreads from an elementary plaquette of the lattice. Such instanton events look like monopole configurations of the gauge-field in space-time, and are often referred to as "monopoles" or "monopole tunneling events.

A.1 Confined ("Non-Fractionalized") Phases

Unless somehow prohibited, in 2D, these instanton tunneling events cost a finite amount of action and will occur with finite space-time density, thereby confining gauge-charged matter[152]. Confined phases describe ordinary unfractionalized phases in which the chargeon and spinon are tightly bound together such that they cannot be separated. The excitations of such a theory can be described as local composites of electron operators.

Confined phases of gauge theories tend to be quite difficult to describe, and the slave-boson ansatz are not typically effective in this regime. A notable exception is the ordinary phase described by condensing b to form a superfluid: $\langle b \rangle \neq 0$ [1] A field with the fundamental gauge charge is condensed, which will gap out smooth gauge fluctuations due to the Anderson-Higgs mechanism.

In the absence of symmetry, the Higgs-phase of the gauge theory is adiabatically conected to a confined phase of the gauge theory, in the sense that the two are not separated by a phase transition[206]. The pure Higgs phase exhibits a Meissner effect for vortices: 2π-vortices of the phase are gapped quasi-particle like excitations. The wordlines of these excitations have finite space-time line-tension. However, the vortices are bound to 2π flux of the emergent gauge field $\mathbf{b} = \nabla \times \mathbf{a}$, and the wordlines can therefore start and end on instanton tunneling events. Therefore, wordline-segments of vortices terminating on instantons have finite action cost and therefore occur in the partition function with finite density. The characteristic length of these segments depends on the relative size of the vortex line-tension and instanton action cost. The Higgs-phase can be regarded as the limit where the instanton cost is much larger than the line-tension so that vortex number is approximately conserved at some length-scale. The confined phase can be regarded as the other limit where the instantons are cheaper to produce than vortex word-lines. Clearly these are two sides of the same coin, and are continuously connected without phase transition.

Since these are really the same phase, we can work in the Higgs limit where we can effectively regard b as a classical c-number. Then, f_σ is then essentially the electron

[1] Actually, since b has gauge charge, what we really mean is that the non-local object $\langle e^{i(\phi_i - \int^i d\ell \cdot \mathbf{a})} \rangle \neq 0$ is condensed.

operator (up to a c-number phase), then this phase is an ordinary electron phase where the electrons and f's are in the same band-structure.

A.2 Deconfined ("Fractionalized") Phases

The advantage of parton constructions is really in describing fractionalized phases of matter, where the instantons of the emergent gauge field are eliminated from the low-energy theory. This can be accomplished through three main routes:

1. Charge-N Higgs Field ($N \neq 1$) - above we described that the condensing the charge-1 boson $\langle b \rangle \neq 0$ is the same as confining the gauge theory. However, condensing a higher-charge N object ($N \neq 1$) spontaneously breaks down the $U(1)$ gauge freedom to a residual discrete $\mathbb{Z}_N$ gauge freedom. For example, putting $\langle b \rangle = 0$ and condensing spinon-pairs, $\langle ff \rangle \neq 0$, results in a state with residual $\mathbb{Z}_2$ gauge freedom. The $\mathbb{Z}_2$ gauge field can be in either a confined or deconfined phase depending on the details of interactions.

2. Gapped Matter with a Topological Gauge-Response - Another possibility for suppressing instantons is to place the gauge-charged matter (in this case b and/or f) into gapped, phases with non-trivial topological electromagnetic response. Since the matter fields are gapped, they can be perturbatively integrated out of the low-energy theory. This generates dynamics for the emergent gauge field a, and in particular, can generate a Chern-Simons (CS) term: $\frac{k}{4\pi}\varepsilon^{\mu\nu\lambda}a_\mu\partial_\nu a_\lambda$, with k some non-zero coefficient. Such a CS term gaps out the gauge-fluctuations, and gives infinite action cost to instantons.

3. Gapless Gauge-Charged Fermionic Matter - In the presence of gapless gauge-charged matter instanton events can develop infinite action cost, and be removed from the low-energy theory[153]. In particular, if $\langle b \rangle = 0$, but f_σ form a state with N_f-Dirac cones, then it is known that for sufficiently large N_f, the monopole tunneling events become irrelevant at low energies[153]. A Fermi-surface state of f in some sense corresponds to an infinite number of Dirac cones (N_f" = "∞), and is also thought to be sufficient to suppress instanton events[176].

In the first two cases above, the resulting theories have well-defined quasi-particles excitations that can be simply described in terms of the parton fields b or f (or related vortices). In the last example, even though singular instanton events of the gauge field are prohibited, smooth fluctuations of a coexist with a large number of gapless fermionic excitations. The resulting low-energy effective theory contains a Fermi-surface strongly coupled to a gapless gauge field. The strong transverse scattering of Fermions by the gauge field washes out their quasi-particle nature[138, 141, 142, 143, 144, 145, 146, 147].

Appendix B

Vortex Condensation

A powerful tool for constructing new phases is to start with a superfluid or superconducting phase with vortex excitations, and proliferate or vortices. In this Appendix, we begin by reviewing how vortex proliferation can be described in a field theory language as condensing a non-local vortex field. This perspective is then used to discuss continous phase transitions between an ordinary 2D superconductor and a band-insulator or topologically ordered phase. These constructions are quite useful in Chapters 5 and 6 to describe SPT phases of matter.

B.1 Particle-Vortex Duality

In this section, we review the standard dual transformation between bosonic degrees of freedom with conserved $U(1)$ charge, and vortex degrees of freedom.

Consider a 2+1D space-time lattice system of $U(1)$ rotor degrees of freedom, $e^{i\phi_j}$ where j labels lattice sites. The simplest action that preserves the $U(1)$ shift invariance of ϕ is:

$$S_{\cos} = -\sum_{x,\mu} K_\mu \cos(\phi_{x+\mu} - \phi_x) \tag{B.1}$$

where x is a point in space-time and μ labels different directions of lattice links connecting x to its neighbors. For simplicity, we will drop the μ label on K in what follows, though it would be straightforward to keep.

It is desireable to recast this highly non-linear action into something more tractable. However, the simplest replacementby a quadratic term: $-K\cos(\phi_{x+\mu}-\phi_x) \to \frac{\rho}{2}(\phi_{x+\mu}-\phi_x)^2$ loses the periodic property the action. An alternative that manifestly preserves the shift invariance in ϕ is to expand the cosine term quadratically around a minimum, but then sum the partition function over all possible minima:

$$Z = e^{-S_{\cos}} \approx \sum_{v_{x,\mu}} \int D\phi e^{-\frac{\rho}{2}(\phi_{x+\mu}-\phi_x-2\pi v_{x,\mu})^2} \tag{B.2}$$

Here, $v_{x,\mu}$ are integers defined on lattice links. The resulting action is not precisely

equal to the initial, but it shares the same symmetries, and therefore should be able to correctly capture universal long-wavelength aspects of the original theory.

The action can further be simplified, by decoupling the quadratic term with a Hubbard-Stratonovich field $j_{x,\mu}$:

$$Z \approx \sum_{v_{x,\mu}} \int D\phi e^{-\sum_{x,\mu}\left[\frac{1}{2\rho} j_{x,\mu}^2 + i j_{x,\mu}(\phi_{x+\mu} - \phi_x - 2\pi v_{x,\mu})\right]} \tag{B.3}$$

The field $j_{x,\mu}$ corresponds to the boson current on the link (x, μ).

At this point, we may integrate over ϕ, which now serves as a Lagrange mutliplier constraining the lattice-divergence of j to vanish: $(\Delta \cdot j)_x \equiv \sum_\mu j_{x,\mu} = 0$. This constraint just reflects the fact that the boson current is conserved, and can be enforced by replacing $j_{x,\mu}$ by the dual field $j_{x,\mu} = \frac{1}{2\pi}\Delta \times \alpha$, where α is a lattice-vector field defined on links of the dual lattice, and $\Delta\times$ is the lattice-version of curl (i.e. circulation around an elementary plaquette):

$$Z \approx \sum_{v_{x,\mu}} \int D\alpha e^{-\sum_{x,\mu}\left[\frac{1}{8\pi^2\rho}(\nabla\times\alpha)^2 + iv\cdot\nabla\times\alpha\right]} \tag{B.4}$$

The dual field α is a gauge field, in the sense that its longitudinal part does not enter in the action. The magnetic flux of this gauge field (normalized by 2π) is the particle number of the original bosons.

Next, we can perform the discrete sum over the integer vector field v. This constrains α to be an integer. This integer constraint is somewhat inconvenient, and may be implemented "softly" by introducing an energetic term $g\cos 2\pi\alpha$, which attempts to pin α to an integer value.

At this point, we can take the continuum limit and forget about the underlying lattice structure. It is convenient to divide the vector field $\boldsymbol{\alpha}$ into transverse and longitudinal parts: $\boldsymbol{\alpha} = \boldsymbol{\alpha}_\perp + \nabla\theta_v$. Then, θ_v can be written as the phase of a bosonic field $\Psi_v = \rho_v e^{i\theta_v}$. In this language, the effective dual action reads:

$$\mathcal{L}_{\text{dual}} = \frac{1}{8\pi^2\rho}(\nabla \times \boldsymbol{\alpha})^2 + |(-i\partial_\mu + \alpha_\mu)\Psi_v|^2 + V(|\Psi_v|^2) \tag{B.5}$$

where V is some effective potential for the amplitude of the field Ψ_v.

The object Ψ_v can be interpreted as a vortex field. It is coupled minimal to the vector field α. Moreover, this action has a local gauge redundancy generated by $\theta_v \to \theta_v + \Lambda$ and $\boldsymbol{\alpha} \to \boldsymbol{\alpha} - \nabla\Lambda$. The vortex field therefore couples minimally to the dual boson gauge-field α. In particular, a boson current is seen by the vortex as an orbital magnetic field, indicating that a vortex moving through the boson current will be deflected perpendicular to the current flow and the vortex flow (this is nothing but the usual Magnus force).

We have succeeded in constructing a field theory in terms of a local vortex field Ψ_v. The price for using a local field language to describe a non-local vortex object, is the emergence of a gauge-degree of freedom α. However, we can now use the

familiar results of gauge-field-theories to describe possible phases of the dual theory. In particular, if there is an integer average number of bosons per site in the original theory, then the average flux of α is zero. Then, we can easily imagine a vortex-proliferated phase in which the vortex field is "condensed": $\langle \Psi_v \rangle \neq 0$ (in the usual sense for a superconductor or other condensate coupled to a gauge field), where no other symmetries are broken. In this phase, the dual matter gauge-field $\boldsymbol{\alpha}$ is gapped by the Anderson-Higgs mechanism, and the vortex condensed phase describes a gapped insulator of the original boson degrees of freedom. This phase is nothing but the Bose-Mott Insulator, whose effective low-energy action is just $\mathcal{L} = \frac{m}{2}|\boldsymbol{\alpha}|^2$.

This duality language will be extremeley useful in describing vortex excitation so the phase of a boson or Cooper-pair super-fluid (e.g. arising from a slave-particle description).

B.2 Vortex Condensation in a Conventional Superconductor

As a warm-up for the more-complicated non-Abelian case described in Chapter 5, we begin by reviewing how insulating states can be produced by quantum disordering a conventional 2D s-wave superconductor through vortex proliferation. The following sections will frequently make use of the duality concepts described above.

A superconducting state has a charge $2e$ order parameter $\Delta = |\Delta| e^{2i\phi_s}$ that breaks $U(1)$ charge conservation symmetry. Starting from a conventional s-wave superconductor, one can restore $U(1)_C$ symmetry by proliferating vortices in the phase of the order-parameter, ϕ_s. Since the pairing amplitude $|\Delta|$ remains finite (except inside the vortex cores), the resulting state is clearly gapped. Different gapped phases can be obtained by proliferating different types of vortices. For example, proliferating π-vortices in ϕ_s (i.e. superconducting $\frac{hc}{2e}$ vortices) produces a simple band-insulator[88], whereas proliferating 2π vortices produces a gapped phase with $\mathbb{Z}_2$ topological order[88, 89]. These constructions are well known[88, 89], but are useful to review in order to fix notation and to set the stage for the more complicated non-Abelian superconductors that are the subject of this paper.

All three phases are conveniently described by a parton construction in which the electron annihilation operator with spin-σ, c_σ, is rewritten as $c_\sigma = b f_\sigma$ with b a spinless charge-1 boson (chargon) , and f_σ is a neutral spinful fermion (spinon). This parton description (often referred to as "slave-boson"), has a $U(1)$ redundancy associated with changing the phase of b and f in opposite ways. Consequently, any field theory description will contain an emergent, compact $U(1)$ gauge-field, whose vector potential we will denote by a^μ.

B.2.1 Superconductor

In the parton description, the s-wave superconductor phase is described by condensing the charged boson, $\langle b \rangle \neq 0$, and introducing an s-wave pairing amplitude for f:

$\langle f_\uparrow f_\downarrow \rangle \neq 0$. In this phase, the emergent gauge field is gapped by the Higgs mechanism (or, equivalently confined) due to the charge-1 boson condensate.

The gapped, unpaired f-quasiparticles are neutral fermion excitations. These are ordinary Bogoliubov quasi-particles of the superconductor, that arise from electron states whose charge is screened completely (at long lengthscales) by the pair-condensate.

In addition, there are also π vortices of the f-pair condensate phase. Since f carries internal gauge charge, these vortices carry π "magnetic"-flux of a. The bosons, having internal gauge charge, are also affected by this π flux of a. Writing $b = \sqrt{\rho_b} e^{i\phi_b}$, we see that ϕ_b must wind by π in the vicinity of this vortex in order to avoid an extensive energy penalty. Since b carries the physical electromagnetic charge, this means that a π-vortex in the f-pair-condensate is necessarily accompanied by a physical supercurrent flow in the b-condensate; this object is simply the familiar $\frac{hc}{2e}$ superconducting vortex.

B.2.2 Band-Insulator

In an s-wave SC, $\frac{hc}{2e}$ vortices carry only gapped quasi-particle states in their core. Moreover, the pairing amplitude, Δ, is non-vanishing outside of vortex cores. Consequently, a state with an arbitrary density of non-overlapping vortices has no gapless excitations. Therefore, one can consider starting with a superconductor and creating a quantum superposition of states with various numbers and placements of (well-separated) $\frac{hc}{2e}$ vortices. This state will clearly be gapped.

Moreover, since the spinon excitations of the superconductor see the $\frac{hc}{2e}$ superconducting vortices as π-gauge-magnetic-flux, the spinon and vortex have mutual semionic statistics. This immediately implies that the spinons will be confined in the vortex-proliferated state. The bosonic particles, b, also see the vortices as π-fluxes. Therefore, the physical electron $c = bf$ has trivial mutual statistics with the vortex, remains gapped but deconfined. Therefore, there is no spin-charge separation and the resulting state describes a conventional electron phase.

This phase can be thought of as a Bose-Mott insulator of Cooper pairs. If the electron density is commensurate such that there are an even number of electrons per unit cell, then the Cooper pairs have integer filling and can form a Mott insulating state without further breaking any spatial symmetry. Commensurate Cooper-pair filling is a necessary requirement for forming a band-insulator, and furthermore, the $\frac{hc}{2e}$-vortex-proliferated state has all the properties of an ordinary electronic band-insulator.

Therefore, we see that $\frac{hc}{2e}$ vortex proliferation in a superconductor produces a conventional band-insulator. This description of a band-insulator is clearly more complicated than the usual non-interacting band-structure description. However, this construction provides a complementary "dual" perspective capable of capturing correlated band-insulators, and can be a useful conceptual starting point for constructing more complicated strongly interacting phases.

B.2.3 $\mathbb{Z}_2$ Topological Order

Instead of proliferating $\frac{hc}{2e}$-vortices in the superconductor, one could alternatively proliferate doubled ($\frac{hc}{e}$) vortices. If the electrons are at commensurate filling with the lattice, this proliferation destroys the boson superfluidity ($\langle b \rangle = 0$) without further breaking any other symmetry. Single b-particle excitations are now gapped and the resulting phase is a charge insulator. In this phase a is not confined; rather, the emergent $U(1)$ gauge invariance is broken down to a local $\mathbb{Z}_2$ gauge invariance by the f-pair-condensate. Moreover, since the spinons-f develop a trivial (multiple of 2π) Berry phase upon encircling an $\frac{hc}{e}$ defect, they remain deconfined.

The excitations of the theory are then b, f, and objects with π-flux of a (visons). The visons are their own antiparticles (since two visons make up the condensed $\frac{hc}{e}$ vortex), having mutual π-statistics with b and f, and the resulting state is fractionalized with $\mathbb{Z}_2$ topological order.

It is worthwhile to pause to reflect on the strategy underlying the vortex condensation route to describing insulators proximate to superconducting phases in two space dimensions. In general a useful effective field theory description of such a system is formulated in terms of degrees of freedom natural in the superconductor - namely the $\frac{hc}{2e}$ vortices and the neutralized Bogoliubov quasiparticles (the f field). The $\frac{hc}{2e}$ vortex field is a mutual semion with the f particle and furthermore is coupled to a non-compact $U(1)$ gauge field. The vortex field of this dual Landau-Ginzburg theory is, in the examples reviewed above, bosonic. Vortex fields with strength $\frac{nhc}{2e}$ can therefore be formally condensed to produce various kinds of insulating states.

Appendix C

Thermal Conductivity of the Random Singlet Phase

In Chapter 8, we examined the possibility of a spin-liquid phase emerging in a randomly doped semiconductor system. The most straightforwardly measurable signature of this phase is metallic thermal conductivity: $\kappa \sim T$. An implicit assumption is that such metallic scaling for κ is not likely produced by other means than a gapless spinon metal. For example, strongly random anti-ferromagnetic spin systems can realize a random-singlet (RS) phase consisting of singlet bonds formed between random spin pairs[196, 132]. The distribution of bond-strengths in this random singlet (RS) phase is extremely broad, and features a divergent low-energy density of states.

This unusually large number of low energy triplet excitations has dramatic consequences including: impurity spin-susceptibility that diverges more rapidly than the usual Curie law, divergent specific heat, unusual NMR relaxation behavior, and critical entanglement entropy that exceeds boundary law scaling[132, 197, 198]. While the thermodynamic properties of the RS phase have been extensively explored [132, 198], the transport properties are comparatively less well understood. Here we study the thermal conductivity of the random-singlet phase. In this spin-system thermal conductivity occurs through the hopping of thermally activated triplet excitations. We argue that, due to disorder, these triplet excitations are localized and require inelastic interactions with a thermal bath of phonons to propagate. However, in marked contrast to the case of variable-range hopping in a localized electronic insulator for which conductivity is exponentially suppressed at low temperature, the RS phase is only weakly insulating and its conductivity obeys a power-law in temperature: $\kappa_{\rm sp} \sim T^p$ with $p \approx 4$ in $D = 3$ dimensions and $p \approx 5.5$ in $D = 2$. While this indicates that the spin conductivity will be dominated by the phonon contribution, $\kappa_{\rm ph} \sim T^D$, in the presence of a magnetic field, $\kappa_{\rm sp}$ exhibits a pronounced peak that scales as $\kappa_{\rm ph}(B_{\rm max}) \sim T^{p-1}$ allowing one to isolate the spin-contribution to thermal transport.

Originally introduced to describe the behavior of magnetic impurities in Si on the insulating side of the metal-insulator transition[132], the random singlet phase describes the behavior of spinful impurities a variety of systems. For example, there is also recent evidence that spinful impurities in the spin-1/2 Kagome lattice material, Herbertsmithite, form a random singlet state[168]. These too may possibly realize

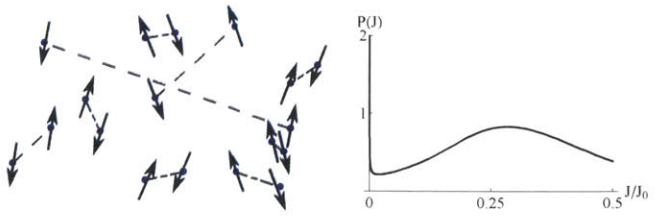

Figure C-1: (Color online) (Left) Illustration of typical random singlet configuration resulting from the strong disorder pairing approach in two dimensions. Blue dots with arrows represent spin impurities, and dashed lines indicate that two spins form a singlet in the ground state. (Right) Probability distribution of singlet bond strength J for the random singlet phase in two dimensions, note the diverging density of states at low energy.

strong randomness.

C.1 Random Singlet Phase

As a simple model we consider randomly distributed spinful impurities in a bulk electronic insulator, for which exchange is isotropic and falls off exponentially with distance:

$$H_{\rm sp} = \frac{1}{2}\sum_{i\neq j} J(r_{ij})\mathbf{S}_i \cdot \mathbf{S}_j \qquad J(r) = J_0 e^{-r/\xi} \tag{C.1}$$

where ξ is the lengthscale associated with the electronic gap. For convenience we subsequently choose units of energy and length such that $J_0 = 1$ and $\xi = 1$. Because of the exponential sensitivity of J to r, if a pair of spins is randomly closer to each other than to other spins, in the ground state configuration, this pair will closely resemble a singlet. Motivated by this observation, one can construct a good approximation to the spin ground state by the following renormalization group (RG) process[196]: 1) find the strongest coupled pair of spins, and lock them into a singlet, 2) renormalize the couplings between other spins due to virtual excitations of the locked pair and 3) iterate this procedure on the remaining spins until all spins are paired. The resulting "random-singlet phase" consists of singlet bonds formed between pairs of spins that are a random distance away[196] (Fig. C-1 illustrates a typical configuration). The most striking feature of this random-singlet phase is that the distribution of singlet bond strengths is extremely broad, leading to a divergent density of states for spin excitations at zero energy (see Fig. C-1).

One can obtain an analytic expression for the probability distribution on bond-lengths by ignoring the weak renormalization of exchange couplings in the RG process[197]. Let the density of spin impurities be $n_s = 1/V_0$, and let $P(V)$ be the probability density for a spin finding its nearest neighbor at a distance $r(V) = V^{1/D}$ away (where D is the number of spatial dimensions). Consider surrounding a given spin by a spherical volume V. The mean number of other spins in this volume is $N(V) = V/V_0 - \left(1 - e^{-V/V_0}\right)$. In order for the spin at the origin to remain unpaired up to V,

these spins must be bonded to other spins (either within V or outside it). Therefore, we must have $(V/V_0)\int_0^V P(v)dv = N(V)$. Solving for $P(V)$ gives:

$$P(V) = \frac{V_0}{V^2}\left[1 + \left(1 + \frac{V}{V_0}\right)e^{-V/V_0}\right] \tag{C.2}$$

We now turn to the issue of thermal transport in the RS phase. In the strong-disorder RG picture, the spins are pair-wise dimerized with each spin having a natural partner. Energy is transported by transferring a thermally activated triplet from one dimer to another. For low temperatures, $T \ll J_0$, only spin pairs with $J < J_T \equiv T/\log(1/\Lambda)$ contribute to transport, where $\Lambda \ll 1$ is a cutoff whose precise value is unimportant to our analysis. We approximate that spins with couplings $J > J_T$ are effectively locked into singlets, or equivalently, ignore spins separated by a distance less than $r_T = V_T^{1/D} \equiv -\log J_T$.

Since heat transport occurs via the hopping of triplet excitations, one may ask whether triplet excitations can hop coherently through the sample, or if they are localized by disorder. In electronic systems, localization occurs when the variation of on-site energies becomes comparable to the hopping strength. Here the analogs of on-site energy and inter-site hopping are the the intra– and inter–dimer exchange couplings for nearby dimers. A crude criterion for determining whether triplet excitations are extended or localized is whether or not there exists a subset of dimers, $\mathcal{S}$, with strengths $J \in [J_T - \Delta J, J_T]$, such that the mean coupling, $\bar{J}$, between dimers in $\mathcal{S}$ satisfies $\bar{J}/\Delta J > 1$. Using Eq. C.2, one finds $\bar{J} \approx \exp[-(1/2V_T - 1/2V_{\Delta J})^{-1/D}]$ where $\Delta J \equiv \exp[-V_{\Delta J}^{1/D}]$. For T less than some critical $T_{\rm loc}$ the condition $\bar{J}/\Delta J > 1$ becomes impossible to satisfy, suggesting that triplet excitations are localized at sufficiently low T.

Continuing to push the analogy to electronic systems[134, 199], in the localized regime, $T < T_{\rm loc}$, we expect that thermal conductance can only occur with the help of an inelastic thermal bath of phonons[200, 201]. For electronic systems, phonon assisted variable-range hopping (VRH) is exponentially suppresed at low temperatures due to the localized nature of the electron wave-functions[200, 201, 161]. In contrast, we will see that, in the RS phase, localization is partially mitigated by the large density of states at low energy, resulting in a much weaker power-law suppression of conductivity at low temperature.

C.2 Spin-Phonon Coupling

In order to analyze conductivity in the localized regime, we develop a simple model for spin-phonon coupling. The spin-coupling J_{ij} between spins i and j arises from the virtual exchange of electrons through the underlying bulk insulator. Phonons are dynamic lattice distortions that alter the distance between the spins, thereby changing the strength of exchange. Since lattice degrees of freedom change on a much slower time-scale than electron excitations, to a good approximation, the exchange adiabatically adjusts to the instantaneous configuration of the lattice: $J_{ij}(t) = e^{-R_{ij}(t)}$. We

decompose $\hat{\mathbf{R}}_{ij}(t) = \vec{R}_{ij} + \hat{\mathbf{u}}_{ij}(t)$, where $\hat{\mathbf{u}}_{ij}(t)$ is the dynamical lattice displacement due to the phonon field, model the phonons by a featureless jellium, and expand J_{ij} to leading order in u_{ij} to find the following expression for the spin-phonon coupling:

$$H_{\text{sp-ph}} = -i\frac{J_{ij}R_{ij}}{\xi}\sum_{\mathbf{q}} q\cos^2(\theta_{\mathbf{q}})\,\hat{\varphi}_{\mathbf{q}}\hat{\mathbf{S}}_i\cdot\hat{\mathbf{S}}_j \tag{C.3}$$

where $\varphi_{\mathbf{q}} = \frac{1}{\sqrt{2\omega_q}}\left(a_{\mathbf{q}} + a^{\dagger}_{-\mathbf{q}}\right)$ is the phonon field, $a^{\dagger}_{\mathbf{q}}$ creates a phonon at momentum $\mathbf{q}$ and energy $\omega_q = c_s q$, and $\theta_{\mathbf{q}}$ is the angle between $\mathbf{q}$ and $\mathbf{R}_{ij}$.

Consider two spin dimers labeled i and j made up of spins (i_1, i_2) and (j_1, j_2) respectively. If dimer i is initially in a thermally activated triplet configuration with z-spin compononent $m = \pm 1, 0$, and dimer j is initially in a singlet, then the matrix element for the triplet to hop from i to j is proportional to: $\langle 0_S; 1, m'|S_{i_{1,2}}\cdot S_{j_{1,2}}|1, m; 0_S\rangle = \delta_{m,m'}\left(\delta_{m,0} + \frac{1}{4}\delta_{m,+} + \frac{1}{4}\delta_{m,-}\right)$. If the difference between the intra-dimer couplings, $\Delta J = J_i - J_j$, is non-zero, then in order to conserve energy a triplet can hop from i to j only by absorbing or emitting a phonon. Let J' be the average coupling between spins in i and spins in j. Typically, we have $J' \ll J_{i,j}$, and the triplet hopping rate is well captured by the perturbative expression:

$$\gamma_{ij} = A\left(J'R'\right)^2(\Delta J)^2\,|n_B(\Delta J)|p_{t,i}p_{s,j} \tag{C.4}$$

where $A \equiv \left(\frac{32}{3}\pi M c_s^4\right)^{-1}$, $R' = -\log J'$, $n_B(\varepsilon) = \left(e^{-\varepsilon/T} - 1\right)$ is the probability of having a thermally activated phonon of energy ε, and $p_{t,i} \approx \left(e^{J_i/T} + 3\right)^{-1}$ and $p_{s,i} = 1 - 3p_{t,j}$ are the probability that bond i is in the triplet or singlet state respectively.

C.3 Low T Thermal Conductivity

The thermal conductivity between two spin dimers labelled i and j is given by the difference between triplet hopping rate from i to j and the reverse rate from j to i times the amount of energy transferred in a hopping event, and divided by the temperature difference between i and j (where we assume that temperature varies sufficiently slowly to permit the definition of a well-defined local temperature for any given spin dimer):

$$\kappa_{ij} = \frac{(J_i + J_j)}{2}\left(\frac{\gamma_{ij}(T_i) - \gamma_{ji}(T_j)}{R'\nabla T_{ij}}\right) = \frac{|J_i^2 - J_j^2|}{2}\frac{\gamma_{ij}}{T^2} \tag{C.5}$$

By definition temperature is comparable to or larger than the typical couplings for thermally activated spins. We can therefore neglect coherence among different triplet hopping paths and treat links between spin dimers as classical resistors that add ohmically. Therefore the thermal conductivity in the RS phase can be recast as that of a random resistor network, made of conductive links consisting of two spin-dimers as in Eq.C.5.

Since this distribution is quite broad, the resistance of a network of conductors

is better described by a percolation based argument rather than by the average conductance[201]. Specifically, let $D(g)$ be the distribution on link-conductances g. In order for the sub-network of resistors whose with conductance $\in [g, \infty]$ to carry current, we need $\int_g^\infty D(g)dg \geq p_c$, where p_c is the critical probability for percolation. The network conductance is then roughly given by g_c defined by: $\int_{g_c}^\infty D(g)dg = p_c$, because links with conductance $\sim g_c$ will be the main bottleneck for current to traverse the full network.

In the present case, it is difficult to construct $D(g)$ exactly, as the conductance of each link depends in a complicated way on each of the Heisenberg couplings in a given four-spin conductance link. To circumvent this difficulty, we consider a restricted variational subset $\mathcal{S}(V, \alpha, V')$ of the resistors satisfying: $v_1 \in [V_T, V]$, $v_2 \in [\alpha v_1, \infty]$, and $V' \in [V_T, V']$ (and also the equivalent subset with $v_1 \leftrightarrow v_2$). Here we have parameterized intra-dimer couplings by $J_{1,2} \equiv \exp\left(-v_{1,2}^{1/D}\right)$ respectively, and the mean inter-dimer coupling by $J' \equiv \exp\left(-v'^{1/D}\right)$. Furthermore, $V, V' > V_T$ and $\alpha > 1$ are variational parameters. After ensuring that the subnetwork $\mathcal{S}$ percolates, we optimize $\{V, \alpha, V'\}$ to maximize the percolation conductivity. Since we consider only a restricted class of subnetworks, the answer resulting from this procedure is a lower-bound on the general percolation-conductivity. The hope (validated by numerical simulations) is that $\mathcal{S}(V, \alpha, V')$ are sufficiently general to provide a good approximation to the true optimally percolating subnetwork.

In the low temperature limit, only the power law tails of Eq. C.2 matter, and we find the following probability distributions on $v_{1,2}$: $P(v_{1,2}) = V_T/v_{1,2}^2$. To obtain the distribution on v', we will assume that the conductivity occurs predominately through neighboring dimers, and ignore complications arising from geometric information about the mutual orientation of the two dimers making up the conductive link. The mean distance between neighboring dimers is $(2V_T)^{1/D}$, and the probability distribution on v' is the same as the probability that the nearest neighboring bond occurs at distance v': $P(v') = (v'/4V_T^2\mathcal{N})\, e^{-v'/2V_T}$ where $\mathcal{N} \approx 0.9$ ensures normalization. The condition that conductors in $\mathcal{S}$ percolate, $2\int_{\{v_{1,2},v'\}\in\mathcal{S}} P(v_1)P(v_2)P(v') = p_c$, gives one relation among V, α and V'. Maximizing the percolation conductivity with respect to the remaining two parameters, we find that V' is a few times V, validating the perturbative approximation $J' \ll J_{1,2}$. Furthermore, the optimal α decreases asymptotically to 1 as $T \to 0$ such that the difference between α and 1 provides only subleading logarithmic prefactor corrections to the conductivity. Inserting these results with Eq. C.5, we find that the low-temperature thermal conductivity follows a power-law behavior at low temperature:

$$\kappa(T) \sim T^p \tag{C.6}$$

where the precise value of p depends on dimensionality and the percolation threshold p_c.

Here we run into the following problem: while p_c is sharply defined for a lattice model, in the continuum the concept of a sharp percolation threshold is approximate[201]. To better determine p, we have performed numerical simulations of random placed

spins. In the simulations, spins are first paired in the strong-disorder RG sense described above. The spin-network is then mapped to a linear random resistor network using Eq. C.5, and the conductivity of the network is computed directly (without falling back on percolation based approximations). We find that $\kappa_{3D} \sim T^4$ and $\kappa_{2D} \sim T^{5.5}$ in $D = 3$ and $D = 2$ respectively. The corresponding percolation thresholds are $p_c^{3D} = 0.1$ and $p_c^{2D} = 0.3$. We see that the spin-contribution will be dominated by the phonon contribution, which scales as $\kappa_{\rm ph} \sim T^D$. However, in the next section we will show that the distinctive magnetic field dependence of $\kappa_{\rm sp}(B)$ will allow one to extract the spin-contribution.

C.4 Conductivity in a Magnetic Field

Because the spin system is sensitive to magnetic field whereas phonons are not, the magnetic field allows one to disentangle the contribution of spin system from the background. An applied field effects the spin-thermal-conductivity by altering the probability for thermally exciting a triplet $p_{t,m}$, which now depends on the z-projection, $m = \pm 1, 0$ of the triplet spin:

$$p_{t,m} = \frac{e^{-m\beta B}}{e^{-\beta J}\left(1 + 2\cosh \beta B\right) + 1} \tag{C.7}$$

Taking B along the z-direction without loss of generality, the field increases the population of $m = 1$ compared to $m = 0, -1$ and singlets. The field liberates $m = 1$ triplet excitations on bonds that previously had $J > J_T$, and were locked in a singlet. For $B \ll T$, this effectively increases J_T for $m = 1$ excitations, while reducing it for $m = -1$. These two effects cancel to leading order, and the low-field conductivity increases quadratically in B/T:

$$\kappa_{B \ll T} \sim T^p \left(1 + \frac{1}{6}\left(\frac{B}{T \log[1/\Lambda]}\right)^2\right) \tag{C.8}$$

where $\beta = T^{-1}$. For $B \gg T$, only bonds with strength $|J - B| \lesssim T$ are thermally active, as stronger bonds are locked into singlets and weaker bonds are polarized along the magnetic field. The fraction of such thermally activated bonds shrinks as $\sim 2T/Br_B^3$ where $r_B = -\log(1/B)$, indicating that the thermally activated bonds become increasingly spearated. Consequently the typical inter-dimer coupling drops exponentially as B is increased resulting in a exponential suppression of thermal conductivity:

$$\kappa_{B \gg T} \sim T^2 \frac{Br_B^3}{2T} \exp\left[-2\left(\frac{Br_B^3}{2T}\right)^{1/D}\right] \tag{C.9}$$

Since conductivity intially increases with applied field and later decreases for stronger field, it must exhibit a maximum at intermediate temperature. Interpolating between the low-field and high-field behavior, we find that $\kappa_{B \ll T} = \kappa_{B \gg T}$ at $B_{\rm max} \sim T$. This

gives the following approximate value for the maximal peak height:

$$\kappa\left(B_{\max}\right) \sim T^{p-1} \sim \frac{\kappa(B=0)}{T} \tag{C.10}$$

Bibliography

[1] Andrew C. Potter and Patrick A. Lee, *Multichannel Generalization of Kitaevs Majorana End States and a Practical Route to Realize Them in Thin Films.* Phys. Rev. Lett. **105**, 227003 (2010).

[2] Andrew C. Potter and Patrick A. Lee, *Majorana end states in multiband microstructures with Rashba spin-orbit coupling.* Phys. Rev. B **83**, 094525 (2011).

[3] Andrew C. Potter and Patrick A. Lee, *Engineering a p+ip superconductor: Comparison of topological insulator and Rashba spin-orbit-coupled materials.* Phys. Rev. B **83**, 184520 (2011)

[4] Andrew C. Potter and Patrick A. Lee, *Erratum: Engineering a p+ip superconductor: Comparison of topological insulator and Rashba spin-orbit-coupled materials [Phys. Rev. B 83, 184520 (2011)].* Phys. Rev. B **84**, 059906 (2011).

[5] Andrew C. Potter and Patrick A. Lee, *Topological superconductivity and Majorana fermions in metallic surface states.* Phys. Rev. B **85**, 094516 (2012).

[6] Jie Liu, Andrew C. Potter, K. T. Law, and Patrick A. Lee, *Zero-Bias Peaks in the Tunneling Conductance of Spin-Orbit-Coupled Superconducting Wires with and without Majorana End-States.* Phys. Rev. Lett. **109**, 267002 (2012).

[7] Chong Wang, Andrew C. Potter, and T. Senthil, *Gapped Symmetry Preserving Surface-State for the Electron Topological Insulator.* arXiv:1306.3223 (2013).

[8] Chong Wang, Andrew C. Potter, and T. Senthil, *Classification of interacting electronic topological insulators in three dimensions.* arXiv:1306.3228 (2013).

[9] Andrew C. Potter and Liang Fu, *Anomalous Supercurrent from Majorana States in Topological Insulator Josephson Junctions.* arXiv:1303.1524 (2013).

[10] Andrew C. Potter, M. Barkeshli, J. McGreevy, and T. Senthil, *Quantum Spin Liquids and the Metal-Insulator Transition in Doped Semiconductors.* Phys. Rev. Lett. **109**, 077205 (2012).

[11] Andrew C. Potter, T. Senthil, and Patrick A. Lee, *Mechanisms for sub-gap optical conductivity in Herbertsmithite.* Phys. Rev. B **87**, 245106 (2013).

[12] C.-Z. Chang et. al *Experimental Observation of the Quantum Anomalous Hall Effect in a Magnetic Topological Insulator.* Science **340**, 6129 (2013).

[13] P.A. Lee, N. Nagaosa, and X.-G. Wen, *Doping a Mott insulator: Physics of high-temperature superconductivity.* Rev. Mod. Phys. **78**, 17 (2006).

[14] Y. Shimizu, K. Miyagawa, K. Kanoda, M. Maesato, and G. Saito, Phys. Rev. Lett. **91**, 107001 (2003); T. Itou, A. Oyamada, S. Maegawa, M. Tamura, and R. Kato, Phys. Rev. B 77, 104413 (2008).

[15] M. Yamashita et al., *Highly mobile gapless excitations in a two-dimensional candidate quantum spin liquid.* Science **328**, 1246 (2010)

[16] M.P. Shores, E.A. Nytko, B.M. Barlett, and D.G. Nocera, *A structurally perfect S= 1/2 kagome antiferromagnet.* J. Am. Chem. Soc. 127, 13462 (2005).

[17] S. Fujimoto, *Topological order and non-Abelian statistics in noncentrosymmetric s-wave superconductors.* Phys. Rev. B **77**, 220501 (2008).

[18] J.D. Sau, R.M. Lutchyn, S. Tewari and S. Das Sarma, *Generic New Platform for Topological Quantum Computation Using Semiconductor Heterostructures.* Phys. Rev. Lett. **104**, 040502 (2010).

[19] R. M. Lutchyn, J. D. Sau, and S. Das Sarma, *Majorana Fermions and a Topological Phase Transition in Semiconductor-Superconductor Heterostructures.* Phys. Rev. Lett. 105, 077001 (2010);

Y. Oreg, G. Refael, and F. von Oppen, *Helical Liquids and Majorana Bound States in Quantum Wires.* Phys. Rev. Lett. 105, 177002 (2010).

[20] A.Y. Kitaev *Unpaired Majorana fermions in quantum wires.* Phys.-Usp. **44**, 131 (2001).

[21] K.T. Law, P.A. Lee, and T.K. Ng, *Majorana Fermion Induced Resonant Andreev Reflection.* Phys. Rev. Lett. **103**, 237001 (2009).

[22] V. Mourik, K. Zuo, S.M. Frolov, S.R. Plissard, E.P.A.M. Bakkers, and L.P. Kouwenhoven, *Signatures of Majorana Fermions in Hybrid Superconductor-Semiconductor Nanowire Devices.* Science **336**, 1003 (2012).

[23] A. Das, Y. Ronen, Y. Most, Y. Oreg, M. Heiblum, H. Shtrikman, *Zero-bias peaks and splitting in an Al-InAs nanowire topological superconductor as a signature of Majorana fermions.* Nat. Phys. **8**, 887 (2012).

[24] M. T. Deng, C.L. Yu, G.Y. Huang, M. Larsson, P. Caro, H.Q. Xu, *Observation of Majorana Fermions in a Nb-InSb Nanowire-Nb Hybrid Quantum Device.* arXiv:1204.4130 (2012).

[25] L. P. Rokhinson, X. Liu and J. K. Furdyna, *The fractional ac Josephson effect in a semiconductor-superconductor nanowire as a signature of Majorana particles.* Nat. Phys. **8**, 795 (2012).

[26] H. O. H. Churchill, V. Fatemi, K. Grove-Rasmussen, M. T. Deng, P. Caroff, H. Q. Xu, and C. M. Marcus, *Superconductor-Nanowire Devices from Tunneling to the Multichannel Regime: Zero-Bias Oscillations and Magnetoconductance Crossover.* Phys. Rev. B **87**, 241401(R) (2013).

[27] N. Read and D. Green, *Paired states of fermions in two dimensions with breaking of parity and time-reversal symmetries and the fractional quantum Hall effect.* Phys. Rev. B **61**, 10267 (2000).

[28] D.A. Ivanov *Non-Abelian Statistics of Half-Quantum Vortices in p-Wave Superconductors.* Phys. Rev. Lett. 86, 268-271 (2001).

[29] C. Nayak, S.H. Simon, A. Stern, M. Freedman, and S. Das Sarma, *Non-Abelian anyons and topological quantum computation.* Rev. Mod. Phys. **80**, 1083 (2008).

[30] D.M. Lee, *The extraordinary phases of liquid ^3He* Rev. Mod. Phys. 69, 645665 (1997).

[31] G. M. Luke et al., *Time-reversal symmetry-breaking superconductivity in Sr2RuO4.* Nature **394**, 558-561 (1998);

K. Ishida et al., *Spin-triplet superconductivity in Sr2RuO4 identified by 17O Knight shift.* Nature **396**, 658-660 (1998)

[32] G. Moore and N. Read, *Nonabelions in the fractional quantum hall effect.* Nucl. Phys. B **360**, 362 (1991).

[33] P.A. Lee, *Proposal for Creating a Spin-polarized $p_x + ip_y$ State and Majorana Fermions.* arXiv:0907.2681 (2009).

[34] L. Fu and C.L. Kane, *Superconducting Proximity Effect and Majorana Fermions at the Surface of a Topological Insulator.* Phys. Rev. Lett **100**, 096407 (2008).

[35] M. Duckheim and P.W. Brouwer, *Andreev reflection from noncentrosymmetric superconductors and Majorana bound-state generation in half-metallic ferromagnets.* Phys. Rev. B **83**, 054513 (2011);

S. B. Chung, H.-J. Zhang, X.-L. Qi, and S.-C. Zhang, *Topological superconductivity and Majorana fermions in half-metal / superconductor heterostructure.* Phys. Rev. B **84**, 060510 (2011).

[36] J.D. Sau, R.M Lutchyn, S. Tewari, and S. Das Sarma, *Robustness of Majorana fermions in proximity-induced superconductors.* Phys. Rev. B 82, 094522 (2010).

[37] C. R. Ast et al., *Local detection of spin-orbit splitting by scanning tunneling spectroscopy.* Phys. Rev. B 75, 201401(R) (2007).

[38] M. Nagano, A. Kodama, T. Shishidou, and T. Oguchi, *A first-principles study on the Rashba effect in surface systems.* J. Phys.: Condensed Matter **21**, 064239 (2009)

[39] K. Wurde, A. Mazur, and J. Pollmann, *Surface electronic structure of Pb(001), Pb(110), and Pb(111).* Phys. Rev. B **49**, 7679 (1994)

[40] A.R. Akhmerov, *Topological quantum computation away from the ground state using Majorana fermions.* Phys. Rev. B 82, 020509(R) (2010)

[41] Y.S. Hor, A. J. Williams, J.G. Checkelsky, P. Roushan, J. Seo, Q. Xu, H.W. Zandbergen, A. Yazdani, N.P. Ong, and R. J. Cava, *Superconductivity in CuxBi2Se3 and its Implications for Pairing in the Undoped Topological Insulator.* Phys. Rev. Lett. 104, 057001 (2010);

Y. S. Hor, J. G. Checkelsky, D. Qu, N. P. Ong, R. J. Cava, *Superconductivity and non-metallicity induced by doping the topological insulators Bi2Se3 and Bi2Te3.* Journal of Physics and Chemistry of Solids **72**, 572 (2011);

Y. Chen, Z. Liu, J. G. Analytis, J.H. Chu, H. Zhang, S.K. Mo, R.G. Moore, D. Lu, I. Fisher, S.C. Zhang, Z. Hussain, and Z.X. Shen, *Observation of Single Dirac Cone Topological Surface State in Compounds TlBiTe2 and TlBiSe2 from a New Topological Insulator Family.* Phys. Rev. Lett. **105**, 266401 (2010)

[42] D.L. Bergman and G. Refael, *Bulk metals with helical surface states.* Phys. Rev. B **82**, 195417 (2010)

[43] P. W. Anderson, *Theory of dirty superconductors.* J. Phys. Chem. Solids **11**, 26 (1959)

[44] P. W. Brouwer, M. Duckheim, A. Romito, and F. von Oppen, *Topological superconducting phases in disordered quantum wires with strong spin-orbit coupling.* Phys. Rev. B **84**, 144526 (2011)

[45] J. Alicea, *Majorana fermions in a tunable semiconductor device.* Phys. Rev. B **81**, 125318 (2010).

[46] M. Wimmer, A.R. Akhmerov, M.V. Medvedyeva, J. Tworzydlo, and C.W.J. Beenakker, *Majorana Bound States without Vortices in Topological Superconductors with Electrostatic Defects.* Phys. Rev. Lett. **105**, 046803 (2010)

[47] J. Alicea, Y. Oreg, C. Refael, F. von Oppen, and M.P.A. Fisher, *Non-Abelian statistics and topological quantum information processing in 1D wire networks.* Nat. Phys. **7**, 412 (2011).

[48] F. Meier, H. Dil, J. Lobo-Checa, L. Patthey, and J. Osterwalder, *Quantitative vectorial spin analysis in angle-resolved photoemission: Bi/Ag(111) and Pb/Ag(111).* Phys. Rev. B. **77**, 165431 (2008).

[49] T.S. Santos et al., *Determining Exchange Splitting in a Magnetic Semiconductor by Spin-Filter Tunneling.* PRL **101**, 147201 (2008)

[50] C. R. Ast et al., *Local detection of spin-orbit splitting by scanning tunneling spectroscopy.* Phys. Rev. B **75**, 201401(R) (2007)

[51] M. Gibertini, F. Taddei, M. Polini, and R. Fazio, *Local density of states in metal - topological superconductor hybrid systems.* Phys. Rev. B **85**, 144525 (2012).

[52] A. Cook and M. Franz, *Majorana fermions in a topological-insulator nanowire proximity-coupled to an s-wave superconductor.* Phys. Rev. B **84**, 201105(R) (2011)

[53] S. LaShell, B. A. McDougall, and E. Jensen, *Spin Splitting of an Au(111) Surface State Band Observed with Angle Resolved Photoelectron Spectroscopy.* Phys. Rev. Lett. **77**, 3419 (1996).

[54] C.R. Ast et al. *Spin-orbit split two-dimensional electron gas with tunable Rashba and Fermi energy.* Phys. Rev. B **77**, 081407(R) (2008);

C.R. Ast et al. *Giant Spin Splitting through Surface Alloying.* Phys. Rev. Lett. **98**, 186807 (2007).

[55] G. Kells, D. Meidan, and P. W. Brouwer, *Low-energy subgap states in multichannel p-wave superconducting wires.* Phys. Rev. B **85**, 060507(R) (2012).

[56] A.R. Akhmerov, J.P. Dahlhaus, F. Hassler, M. Wimmer, C.W.J. Beenakker, *Quantized Conductance at the Majorana Phase Transition in a Disordered Superconducting Wire.* Phys. Rev. Lett. **106**, 057001 (2011)

[57] K. Sengupta, Igor Zutic, Hyok-Jon Kwon, Victor M. Yakovenko, and S. Das Sarma, *Midgap edge states and pairing symmetry of quasi-one-dimensional organic superconductors.* Phys. Rev. B **63**, 144531 (2001)

[58] R.M. Lutchyn, T.D. Stanescu, and S. Das Sarma *Search for Majorana Fermions in Multiband Semiconducting Nanowires.* Phys. Rev. Lett. **106**, 127001 (2011).

[59] P.W. Brouwer, M. Duckheim, A. Romito, and F. von Oppen, *Probability distribution of Majorana end-state energies in disordered wires.* Phys. Rev. Lett. **107**, 196804 (2011);

P.W. Brouwer, M. Duckheim, A. Romito, and F. von Oppen, *Topological superconducting phases in disordered quantum wires with strong spin-orbit coupling.* Phys. Rev. B **84**, 144526 (2011)

[60] T.D. Stanescu, R.M. Lutchyn, and S. Das Sarma, *Majorana fermions in semiconductor nanowires.* Phys. Rev. B **84**, 144522 (2011).

[61] C.-H. Lin, J.D. Sau, S. Das Sarma, *Zero bias conductance peak in Majorana wires made of semiconductor-superconductor hybrid structures.* Phys. Rev. B **86**, 224511 (2012).

[62] T.D. Stanescu, S. Tewari, J.D. Sau, and S. Das Sarma, *To close or not to close: the fate of the superconducting gap across the topological quantum phase transition in Majorana-carrying semiconductor nanowires.* Phys. Rev. Lett. **109**, 266402 (2012).

[63] F. Pientka, G. Kells, A. Romito, P.W. Brouwer, and F. von Oppen, *Enhanced zero-bias Majorana peak in disordered multi-subband quantum wires.* Phys. Rev. Lett. **109** 227006 (2012).

[64] E. Prada, P. San-Jose, and R. Aguado, *Transport spectroscopy of NS nanowire junctions with Majorana fermions.* Phys. Rev. B **86**, 180503(R) (2012).

[65] S. Nadj-Perge, V.S. Pribiag, J.W.G. van den Berg, K. Zuo, S.R. Plissard, E.P.A.M. Bakkers, S.M. Frolov, and L.P. Kouwenhoven, *Spectroscopy of Spin-Orbit Quantum Bits in Indium Antimonide Nanowires.* Phys. Rev. Lett. **108**, 166801 (2012)

[66] S. R. Plissard et al., *From InSb nanowires to nanocubes: Looking for the sweet spot.* Nano Lett. **12**, 1794 (2012).

[67] E.F.C. Driessen, P.C.J.J. Coumou, R.R. Tromp, P.J. de Visser, and T.M. Klapwijk, *Strongly disordered TiN and NbTiN s-wave superconductors probed by microwave electrodynamics.* Phys. Rev. Lett. **109**, 107003 (2012).

[68] P.A. Lee and D.S. Fisher, *Anderson Localization in Two Dimensions.* Phys. Rev. Lett. **47**, 882 (1981);

D.S. Fisher and P.A. Lee, *Relation between conductivity and transmission matrix.* Phys. Rev. B **23**, 6851 (1981).

[69] K.T. Law and P.A. Lee, *Robustness of Majorana fermion induced fractional Josephson effect in multichannel superconducting wires.* Phys. Rev. B **84**, 081304 (2011).

[70] H. Shiba, *Classical spins in superconductors.* Prog. Theor. Phys. 40, 435 (1968).

[71] J.D. Sau and. E.A. Demler, *Shiba impurity bound states as a probe of topological superconductivity and Fermion parity changing quantum phase transitions.* arXiv:1204.2537 (2012).

[72] D. Bagrets and A. Altland, *Class D spectral peak in Majorana quantum wires.* Phys. Rev. Lett. **109**, 227005 (2012)

[73] T. D. Stanescu and Sumanta Tewari, *Disentangling Majorana fermions from conventional zero energy states in semiconductor quantum wires.* Phys. Rev. B **87**, 140504(R) (2013)

[74] M.-T. Rieder, G. Kells, M. Duckheim, D. Meidan, and P. W. Brouwer, *Endstates in multichannel spinless p-wave superconducting wires.* Phys. Rev. B **86**, 125423 (2012).

[75] Max A. Metlitski, C. L. Kane, and Matthew P. A. Fisher, *A symmetry-respecting topologically-ordered surface phase of 3d electron topological insulators.* arXiv:1306.3286 (2013).

[76] X. Chen, L. Fidkowski, and A. Vishwanath, *Symmetry Enforced Non-Abelian Topological Order at the Surface of a Topological Insulator.* arXiv:1306.3250.

[77] Parsa Bonderson, Chetan Nayak, and Xiao-Liang Qi, arXiv:1306.3230.

[78] M.Z. Hasan and C.L. Kane, *Colloquium: Topological Insulators.* Rev. Mod. Phys. **82**, 3045 (2010);

M. Zahid Hasan, Joel E. Moore *Three-Dimensional Topological Insulators* Ann. Review.Condensed Matter Physics **2**, 55 (2011);

X.-L. Qi and S.-C. Zhang *Topological Insulators and Superconductors.* Rev. Mod. Phys. **83**, 1057 (2011).

[79] Xie Chen, Zheng-Cheng Gu, Zheng-Xin Liu and Xiao-Gang Wen, *Symmetry protected topological orders and the group cohomology of their symmetry group.* Phys. Rev. B 87, 155114 (2013).

[80] F.D.M. Haldane, *Nonlinear Field Theory of Large-Spin Heisenberg Antiferromagnets: Semiclassically Quantized Solitons of the One-Dimensional Easy-Axis Neel State.* Phys. Rev. Lett. **50**, 1153 (1983).

[81] X. G. Wen, *Quantum Field Theory Of Many-body Systems: From The Origin Of Sound To An Origin Of Light And Electrons.* Oxford University Press (2004).

[82] Liang Fu, C. L. Kane, and E. J. Mele, *Topological Insulators in Three Dimensions.* Phys. Rev. Lett. **98**, 106803 (2007)

[83] A.Y. Kitaev *Anyons in an Exactly Solved Model and Beyond.* Ann. Phys. **321**, 2 (2006).

[84] A. Vishwanath and T. Senthil, *Physics of Three-Dimensional Bosonic Topological Insulators: Surface-Deconfined Criticality and Quantized Magnetoelectric Effect.* Phys. Rev. X **3**, 011016 (2013).

[85] C. Wang and T. Senthil, *Boson topological insulators: A window into highly entangled quantum phases.* arxiv:1302.6234 (2013).

[86] F. J. Burnell, Xie Chen, Lukasz Fidkowski and Ashvin Vishwanath, *Exactly Soluble Model of a 3D Symmetry Protected Topological Phase of Bosons with Surface Topological Order.* arXiv:1302.7072 (2013).

[87] Lukasz Fidkowski, Xie Chen and Ashvin Vishwanath *Non-Abelian Topological Order on the Surface of a 3D Topological Supercoductor from an Exactly Solved Model.* arXiv:1305.5851 (2013).

[88] L. Balents, M.P.A. Fisher, and C. Nayak, *Dual order parameter for the nodal liquid.* Phys. Rev. B **60**, 1654 (1999).

[89] T. Senthil and M.P.A. Fisher, $\mathbb{Z}_2$ *gauge theory of electron fractionalization in strongly correlated systems.* Phys. Rev. B **62**, 7850 (2000).

[90] E. Witten, *Dyons of Charge* $e\theta/2\pi$. Phys. Lett. B **86**, 283 (1979).

[91] M. Metlitski, C.L. Kane, and Matthew P.A. Fisher, *Bosonic topological insulator in three dimensions and the statistical Witten effect*, arXiv:1302.6535.

[92] J. Preskill. *Lecture Notes for Physics 219: Quantum Computation* Chapter 9. http://www.theory.caltech.edu/people/preskill/ph229/

[93] Y.-M. Lu and A. Vishwanath, *Theory and classification of interacting 'integer' topological phases in two dimensions: A Chern-Simons approach.* Phys. Rev. B **86**, 125119 (2012)

[94] M. Levin and A. Stern, *Classification and analysis of two dimensional abelian fractional topological insulators.* Phys. Rev. B **86**, 115131 (2012)

[95] M. Z. Hasan and C. L. Kane, *Colloquium: Topological insulators.* Rev. Mod. Phys. 82, 3045 (2010);

X.-L. Qi and S.-C. Zhang, *Topological insulators and superconductors.* Rev. Mod. Phys. 83, 1057 (2011);

M. Z. Hasan and J. E. Moore, *Three-dimensional topological insulators.* Annu. Rev. Condens. Matter Phys. 2, 55 (2011).

[96] Alexei Kitaev, *Periodic table for topological insulators and superconductors.* arXiv:0901.2686 (2009);

S. Ryu, A.P. Schnyder, A. Furusaki and A.W.W. Ludwig, *Topological insulators and superconductors: tenfold way and dimensional hierarchy.* New J. Phys. 12 065010 (2010).

[97] L. Fidkowski and A. Kitaev, *Topological phases of fermions in one dimension.* Phys. Rev. B **83**, 075103 (2011);

A. M. Turner, F. Pollmann, and E. Berg, *Topological phases of one-dimensional fermions: An entanglement point of view.* Phys. Rev. B **83**, 075102 (2011);

X. Chen, Z.-C. Gu, and X.-G. Wen, *Classification of gapped symmetric phases in one-dimensional spin systems.* Phys. Rev. B **83**, 035107 (2011);

N. Schuch, D. Pérez-Garcia, and I. Cirac, *Classifying quantum phases using matrix product states and projected entangled pair states.* Phys. Rev. B **84**, 165139, (2011).

[98] M. Levin and Z.-C. Gu, *Braiding statistics approach to symmetry-protected topological phases.* Phys. Rev. B 86, 115109 (2012).

[99] Y.-M. Lu and A. Vishwanath, *Theory and classification of interacting integer topological phases in two dimensions: A Chern-Simons approach.* Phys. Rev. B **86**, 125119 (2012).

[100] T. Senthil, M. Levin, *Integer Quantum Hall Effect for Bosons.* Phys. Rev. Lett. 110, 046801 (2013).

[101] Z.-X. Liu and X.-G. Wen, *Symmetry-Protected Quantum Spin Hall Phases in Two Dimensions.* Phys. Rev. Lett. **110**, 067205 (2013).

[102] C. Xu and T. Senthil, *Wave functions of bosonic symmetry protected topological phases.* Phys. Rev. B 87, 174412 (2013).

[103] X. Chen, Y.-M. Lu, and A. Vishwanath, *Symmetry protected topological phases from decorated domain walls.* arXiv:1303.4301 (2013).

[104] S. Ryu and S.-C. Zhang, *Interacting topological phases and modular invariance.* Phys. Rev. B **85**, 245132 (2012);

X.-L. Qi, *A new class of* $(2+1)$*-d topological superconductor with* $\mathbb{Z}_8$ *topological classification.* New J. Phys. **15**, 065002 (2013).

H. Yao and S. Ryu, *Interaction effect on topological classification of superconductors in two dimensions.* arXiv:1202.5805 (2012);

Z.-C. Gu, M. Levin, *The effect of interactions on 2D fermionic symmetry-protected topological phases with Z2 symmetry.* arXiv:1304.4569 (2013).

[105] Z.-C. Gu and X.-G. Wen, *Symmetry-protected topological orders for interacting fermions – fermionic topological non-linear sigma-models and a group supercohomology theory.* arXiv:1201.2648 (2012).

[106] X.-L. Qi, T.L. Hughes, and S.-C. Zhang, *Topological field theory of time-reversal invariant insulators.* Phys. Rev. B 78, 195424 (2008).

[107] D. A. Pesin and L. Balents, *Mott physics and band topology in materials with strong spinorbit interaction.* Nat. Phys. 6, 376 (2010).

[108] G.Y. Cho, C. Xu, J.E. Moore and Y.B. Kim, *Dyon condensation in topological Mott insulators.* New J. of Phys. **14**, 115030 (2012)

[109] L. Fu, *Electron Teleportation via Majorana Bound States in a Mesoscopic Superconductor.* Phys. Rev. Lett. **104**, 056402 (2010).

[110] C. Beenakker, *Search for Majorana fermions in superconductors* arXiv:1112.1950, (2011)

[111] B. Sacepe, J.B. Oostinga, J. Li, A. Ubaldini, N.J.G. Couto, E. Giannini, and A.F. Morpurgo, *Gate-tuned normal and superconducting transport at the surface of a topological insulator.* Nat. Comm **2**, 575 (2011).

[112] D. Zhang, J. Wang, A. M. DaSilva, J. S. Lee, H. R. Gutierrez, M. H. W. Chan, J. Jain and N. Samarth, *Superconducting proximity effect and possible evidence for Pearl vortices in a candidate topological insulator.* Phys. Rev.B. **84**, 165120 (2011).

[113] M. Veldhorst, M. Snelder, M. Hoek, T. Gang, V. K. Guduru, X. L.Wang, U. Zeitler, W. G. van der Wiel, A. A. Golubov, H. Hilgenkamp and A. Brinkman, *Josephson supercurrent through a topological insulator surface state.* Nature Mat. **11**, 417 (2012).

[114] J.R. Williams, A. Bestwick, P. Gallagher, S. Hong, Y. Cui, A. Bleich, J. Analytis, I. Fisher, and D. Goldhaber-Gordon, *Unconventional Josephson Effect in Hybrid Superconductor-Topological Insulator Devices.* Phys. Rev. Lett. **109**, 056803 (2012).

[115] F. Qu, F. Yang, J. Shen, Y. Ding, J. Chen, Z. Ji, G. Liu, J. Fan, X. Jing, C. Yang and L. Lu, *Strong Superconducting Proximity Effect in Pb-Bi2Te3 Hybrid Structures.* Sci. Rep. **2**, 339 (2012)

[116] S. Cho, B. Dellabetta, A. Yang, J. Schneeloch, Z. Xu, T. Valla, G. Gu, M.J. Gilbert, and N. Mason *Symmetry Protected Josephson Supercurrents in Three-Dimensional Topological Insulators.* arXiv:1209.5830 (2012).

[117] E. Grosfeld and A. Stern, *Observing Majorana bound states of Josephson vortices in topological superconductors.* PNAS **108**, 11810 (2011).

[118] P. Zareapour, A. Hayat, S. Yang, F. Zhao, M. Kreshchuk, A. Jain, D. C. Kwok, N. Lee, S. W. Cheong, Z. Xu, A. Yang, G. D. Gu, S. Jia, R. J. Cava, K. S. Burch, *Proximity-induced high-temperature superconductivity in the topological insulators Bi_2Se_3 and Bi_2Te_3.* Nat. Commun. **3**, 1056 (2012).

[119] M. Titov and C.W.J. Beenakker, *Josephson effect in ballistic graphene.* Phys. Rev. B **74**, 041401(R) (2006).

[120] L. Fu and C. L. Kane, *Josephson current and noise at a superconductor/quantum-spin-Hall-insulator/superconductor junction.* Phys. Rev. B **79**, 161408(R) (2009).

[121] C. W. J. Beenakker and H. van Houten, *Josephson current through a superconducting quantum point contact shorter than the coherence length.* Phys. Rev. Lett. **66**, 3056 (1991)

[122] R. N. Bhatt, *Magnetic Properties of Doped Semiconductors.* Phys. Scr. **T14**, 7 (1986);

R.N. Bhatt, M.A. Paalanen, and S. Sachdev, J. Phys. 49, C8 1179 (1988).

[123] D. Belitz and T.R. Kirkpatrick, *The Anderson-Mott transition.* Rev. Mod. Phys. **66**, 261 (1994)

[124] P.A. Lee and T.V. Ramakrishnan, *Disordered electronic systems.* Rev. Mod. Phys. **57**, 287 (1985) and references therein.

[125] H. v. Löhneysen, *Electron-electron interactions and the metal-insulator transition in heavily doped silicon.* Ann. Phys. **523** 599 (2011).

[126] M.A. Paalanen, T.F. Rosenbaum, G.A. Thomas, and R.N. Bhatt, *Stress Tuning of the Metal-Insulator Transition at Millikelvin Temperatures.* Phys. Rev. Lett. **48** 1284, (1982);

[127] H. Stupp, M. Hornung, M. Lakner, O. Madel, and H. v. Löhneysen, *Possible solution of the conductivity exponent puzzle for the metal-insulator transition in heavily doped uncompensated semiconductors.* Phys. Rev. Lett. **71** 2634 (1993);

[128] T. Grover, N. Trivedi, T. Senthil, and P.A. Lee, *Weak Mott insulators on the triangular lattice: Possibility of a gapless nematic quantum spin liquid.* Phys. Rev. B **81**, 245121 (2010)

[129] Y. Okamoto, M. Nohara, H. Aruga-Katori, and H. Takagi, *Spin-Liquid State in the S=1/2 Hyperkagome Antiferromagnet Na4Ir3O8.* Phys. Rev. Lett. 99, 137207 (2007).

[130] K. Voelker and S. Chakravarty, *Multiparticle ring exchange in the Wigner glass and its possible relevance to strongly interacting two-dimensional electron systems in the presence of disorder.* Phys. Rev. B **64**, 235125 (2001).

[131] G. Baskaran, J. Supercond. Novel Magnetism **21**, 45 (2008)

[132] R. N. Bhatt and P. A. Lee, *Scaling Studies of Highly Disordered Spin- Antiferromagnetic Systems.* Phys. Rev. Lett. **48**, 344 (1982).

[133] R.N. Bhatt and D.S. Fisher, *Absence of spin diffusion in most random lattices.* Phys. Rev. Lett. 68, 3072 (1992);

M. Milovanovic, S. Sachdev, and R.N. Bhatt, *Effective-field theory of local-moment formation in disordered metals.* Phys. Rev. Lett. **63**, 82 (1989).

[134] E. Abrahams, P.W. Anderson, P.A. Lee, and T.V. Ramakrishnan, *Quasiparticle lifetime in disordered two-dimensional metals.* Phys. Rev. B **24**, 6783 (1982).

[135] S. Florens and A. Georges, *Slave-rotor mean-field theories of strongly correlated systems and the Mott transitionin finite dimensions.* Phys. Rev. B **70**, 035114 (2004)

[136] T. Senthil *Theory of a continuous Mott transition in two dimensions.* Phys. Rev. B **78**, 045109 (2008)

[137] S.-S. Lee and P. A. Lee, *(1) Gauge Theory of the Hubbard Model: Spin Liquid States and Possible Application to ?-(BEDT-TTF)2Cu2(CN)3.* Phys. Rev. Lett. **95**, 036403 (2005).

[138] P.A. Lee, Phys. Rev. Lett. **63**, 680 (1989); P.A. Lee and N. Nagaosa, Phys. Rev. B **46**, 5621 (1992).

[139] M. P. A. Fisher, P. B. Weichman, G. Grinstein and D. S. Fisher,

[140] Phys. Rev. B **40**, 546 (1989).

[141] J. Polchinski, *Low-energy dynamics of the spinon gauge system.* Nucl. Phys. B **422**, 617 (1994) arXiv:cond-mat/9303037.

[142] C. Nayak and F. Wilczek, *NonFermi liquid fixed point in (2+1)-dimensions.* Nucl. Phys. B **417**, 359 (1994) arXiv:cond-mat/9312086, *Renormalization group approach to low temperature properties of a non-Fermi liquid metal.* Nucl. Phys. B **430**, 534 (1994) arXiv:cond-mat/9408016.

[143] B.I. Halperin, P.A. Lee, and N. Read *Theory of the half-filled Landau level.* Phys. Rev. B **47**, 7312 (1993)

[144] B. L. Altshuler, L. B. Ioffe and A. J. Millis, *Low-energy properties of fermions with singular interactions.* Phys. Rev. B **50**, 14048 (1994).

[145] S.-S. Lee, *Low-energy effective theory of Fermi surface coupled with U(1) gauge field in 2+1 dimensions.* Phys. Rev. B **80**, 165102 (2009)

[146] M. Metlitski and S. Sachdev, *Quantum phase transitions of metals in two spatial dimensions. I. Ising-nematic order.* Phys. Rev. B **82**, 075127 (2010)

[147] D. F. Mross, J. McGreevy, H. Liu, and T. Senthil, *Controlled expansion for certain non-Fermi-liquid metals.* Phys. Rev. B **82**, 045121 (2010)

[148] T. Holstein, R. E. Norton, and P. Pincus, *de Haas-van Alphen Effect and the Specific Heat of an Electron Gas.* Phys. Rev. B **8**, 2649 (1973).

[149] M. Y. Reizer, *Relativistic effects in the electron density of states, specific heat, and the electron spectrum of normal metals.* Phys. Rev. B **40**, 11571 (1989).

[150] K.-S. Kim, *Role of disorder in the Mott-Hubbard transition.* Phys. Rev. B **73**, 235115 (2006).

[151] D. Podolsky, A. Paramekanti, Y. B. Kim, and T. Senthil, *Mott Transition between a Spin-Liquid Insulator and a Metal in Three Dimensions.* Phys. Rev. Lett. **102**, 186401 (2009).

[152] A. M. Polyakov, Gauge Fields and Strings (Harwood, Chur, 1987).

[153] M. Hermele, T. Senthil, M. P. A. Fisher, P. A. Lee, N. Nagaosa, and X.-G. Wen, *Stability of U(1) spin liquids in two dimensions.* Phys. Rev. B **70**, 214437 (2004).

[154] G. Catelani and I. L. Aleiner, Zh. Eksp. Teor. Fiz. **127**, 372 (2005) [Sov. Phys. JETP **100**, 331 (2005)].

[155] D.R. Niven and R.A. Smith, *Electron-electron interaction corrections to the thermal conductivity in disordered conductors.* Phys. Rev. B **71**, 035106 (2005).

[156] D.V. Livanov, M.Y. Reizer, and A.V. Sergeev, Zh. Eksp. Teor. Fiz. **99**, 1230 (1991) [Sov. Phys. JETP **72**, 760 (1991)].

[157] N. F. Mott, *Conduction in non-crystalline systems IX. the minimum metallic conductivity.* Philos. Mag. 26, 1015 (1972)

[158] J. T. Chayes, L. Chayes, D. S. Fisher and T. Spencer, *Finite-Size Scaling and Correlation Lengths for Disordered Systems.* Phys. Rev. Lett. **57**, 2999 (1986)

[159] B. L. Altshuler and A. G. Aronov, Solid State Commun. 36, 115 (1979); [Zh. Eksp. Teor. Fiz. 77, 2028 (1979)]

[160] TK Ng and P.A. Lee, Phys. Rev. Lett. *Power-Law Conductivity inside the Mott Gap: Application to κ-(BEDT-TTF)2Cu2(CN)3* **99**, 156402 (2007)

[161] A.L. Efros and B.I. Shklovskii, *Coulomb gap and low temperature conductivity of disordered systems.* J. Phys. C, **8** L49 (1975).

[162] C. Zeng and V. Elser, *Numerical studies of antiferromagnetism on a Kagome net.* Phys. Rev. B **42**, 8436 (1990).

[163] J.B. Marston and C. Zeng, *Spin-Peierls and spin-liquid phases of Kagome quantum antiferromagnets.* J. Appl. Phys. **69**, 5962 (B) (1991).

[164] S. Sachdev, *Kagome- and triangular-lattice Heisenberg antiferromagnets: Ordering from quantum fluctuations and quantum-disordered ground states with unconfined bosonic spinons* Phys. Rev. B **45**, 12377 (1992).

[165] P.W. Leung and V. Elser, *Numerical studies of a 36-site kagome antiferromagnet.* Phys. Rev. B **47**, 5459 (1993)

[166] P. Lecheminant, B. Bernu, C. Lhuillier, L. Pierre, and P. Sindzingre, *Order versus disorder in the quantum Heisenberg antiferromagnet on the kagome lattice using exact spectra analysis.* Phys. Rev. B **56**, 2521 (1997).

[167] S. Yan, D. A. Huse, and S. R. White, *Spin-Liquid Ground State of the S = 1/2 Kagome Heisenberg Antiferromagnet.* Science **332**, 1173 (2011).

[168] J.S. Helton, et al. *Spin Dynamics of the Spin-1/2 Kagome Lattice Antiferromagnet $ZnCu_3(OH)_6Cl_2$.* Phys. Rev. Lett. **98**, 107204 (2007).

[169] T. Imai, E. A. Nytko, B.M. Bartlett, M.P. Shores, and D. G. Nocera *^{63}Cu, ^{35}Cl, and ^{1}H NMR in the S=1/2 Kagome Lattice $ZnCu_3(OH)_6Cl_2$.* Phys. Rev. Lett. **100**, 077203 (2008).

[170] A. Olariu, P. Mendels, F. Bert, F. Duc, J.C. Trombe, M.A. de Vries, and A. Harrison, ^{17}O *NMR Study of the Intrinsic Magnetic Susceptibility and Spin Dynamics of the Quantum Kagome Antiferromagnet* $ZnCu_3(OH)_6Cl_2$. Phys. Rev. Lett. **100**, 087202 (2008).

[171] Tianheng Han et al., to be published.

[172] Y. Ran, M. Hermele, P. A. Lee, and X.-G.Wen, *Projected-Wave-Function Study of the Spin-1/2 Heisenberg Model on the Kagome Lattice.* Phys. Rev. Lett. **98**, 117205 (2007).

[173] Y. Iqbal, F. Becca, S. Sorella, and D. Poilblanc, *Gapless spin-liquid phase in the kagome spin-1/2 Heisenberg antiferromagnet.* arXiv:1209.1858 (2012).

[174] M. Hermele et al. *Properties of an Algebraic spin-liquid on the Kagome lattice* Phys. Rev. B **77**, 224413 (2008)

[175] White, S. R. *The spin liquid ground state of the S=1/2 Heisenberg model on the kagome lattice.* Bull. Am. Phys. Soc. 57 MAR.L19.1 (2012); available at http://meetings.aps.org/link/BAPS.2012.MAR.L19.1.

[176] L.B. Ioffe, A.I. Larkin *Gapless Fermions and Gauge Fields in Dielectrics.* Phys. Rev. B (1989)

[177] P.A. Lee, N. Nagaosa *A Proposal to Use Neutron Scattering to Measure Scalar Spin Chirality Fluctuations in Kagome Lattices.* arXiv:1210.3051 (2012)

[178] S. Elsasser, D. Wu, M. Dressel, J.A. Schlueter, *Power-law dependence of the optical conductivity observed in the quantum spin-liquid compound* κ*-(BEDT-TTF)*$_2$*Cu*$_2$*(CN)*$_3$. Phys. Rev. B **86**, 155150 (2012).

[179] D.V. Pilon, C.H. Lui, T. Han, D.B. Shrekenhamer, A.J. Frenzel, W.J. Padilla, Y.S. Lee, and N. Gedik *Spin Induced Optical Conductivity in the Spin Liquid Candidate Herbertsmithite* arXiv:1301.3501 (2013)

[180] L.N. Bulaevskii, C.D. Batista, M.V. Mostovoy, and D.I. Khomskii *Electronic orbital currents and polarization in Mott insulators* Phys. Rev. B (2008)

[181] Y. Huh, L. Fritz, and S. Sachdev *Quantum criticality of the kagome antiferromagnet with Dzyaloshinskii-Moriya interactions* Phys. Rev. B **81**, 144432 (2010)

[182] A. Chubukov, S. Sachdev, and T. Senthil, *Quantum phase transitions in frustrated quantum antiferromagnets* Nucl. Phys. B **426**, 601 (1994).

[183] Y.-M. Lu and Y. Ran Z_2 *spin liquid and chiral antiferromagnetic phase in the Hubbard model on a honeycomb lattice* Phys. Rev. B, **84**, 024420 (2011)

[184] A.W.W. Ludwig, M.P.A. Fisher, R. Shankar, and G. Grinstein *Integer quantum Hall transition: An alternative approach and exact results.* Phys. Rev. B, **50**, 7526 (1994)

[185] see e.g. N. A. Luric, D. L. Huber, and M. Blume, *Computer studies of spin and energy transport in one-dimensional Heisenberg magnets.* Phys. Rev. B **9**, 2171 (1974) and references therein

[186] S. Sachdev, *Quantum Phase Transitions* (Cambridge University Press, Cambridge, 1999).

[187] R. C. Myers, S. Sachdev, and A. Singh, *Holographic Quantum Critical Transport without Self-Duality* Phys. Rev. D **83**, 066017 (2011)

[188] P.A. Lee and N. Nagaosa *Gauge theory of the normal state of high-T_c superconductors* Phys. Rev. B, **46**, 5621 (1992)

[189] X.G. Wen, F. Wilczek, and A. Zee *Chiral spin states and superconductivity* Phys. Rev. B, **39**, 11413 (1989)

[190] O. Motrunich *Orbital magnetic field effects in spin liquid with spinon Fermi sea: Possible application to $\kappa - (ET)_2Cu_2(CN)_3$.* Phys. Rev. B **73**, 155115 (2006)

[191] K. Nomura and A.H. MacDonald *Quantum Hall Ferromagnetism in Graphene* Phys. Rev. Lett. **96**, 256602 (2006).

[192] J. Alicea and M.P.A. Fisher, *Graphene integer quantum Hall effect in the ferromagnetic and paramagnetic regimes.* Phys. Rev. B **74**, 075422 (2006)

[193] M. Jeong, F. Bert, P. Mendels, F. Duc, J. C. Trombe, M. A. de Vries, and A. Harrison, *Field-Induced Freezing of a Quantum Spin Liquid on the Kagome Lattice.* Phys. Rev. Lett. **107**, 237201 (2011)

[194] D.A. Abanin, P.A. Lee, and L.S. Levitov, *Spin-Filtered Edge States and Quantum Hall Effect in Graphene.* Phys. Rev. Lett. **96**, 176803 (2006)

[195] C.L. Kane, P.A. Lee, and N. Read *Motion of a single hole in a quantum antiferromagnet* Phys. Rev. B. **39** 6880 (1989)

[196] D. S. Fisher *Random antiferromagnetic quantum spin chains.* Phys. Rev. B **50**, 37993821 (1994)

[197] Z. Z. Gan and P. A. Lee, *Nuclear-spin relaxation near the metal-insulator transition.* Phys. Rev. B **33**, 3595 (1986)

[198] G. Refael and J. E. Moore, *Entanglement Entropy of Random Quantum Critical Points in One Dimension.* Phys. Rev. Lett. 93, 260602 (2004)

[199] D.M. Basko, I.L. Aleiner, and B.L. Altshuler, *Metalinsulator transition in a weakly interacting many-electron system with localized single-particle states.* Ann. Phys. 321, 5 (2006).

[200] N. F. Mott, *Conduction in non-crystalline materials: III. Localized states in a pseudogap and near extremities of conduction and valence bands.* Phil. Mag. 19, 835 (1969).

[201] V. Ambegaokar, B.I. Halperin, and J.S. Langer, *Hopping Conductivity in Disordered Systems.* Phys. Rev. B **4**, 2612 (1971).

[202] J. Motruk, A.M. Turner, E. Berg, and F. Pollmann, *Topological Phases in Gapped Edges of Fractionalized Systems.* arXiv:1303.2194 (2013).

[203] D.J. Clarke, J. Alicea, K. Shtengel, *Exotic non-Abelian anyons from conventional fractional quantum Hall states.* Nature Commun. **4**, 1348 (2013).

[204] M. Barkeshli, C.-M. Jian, and X.-L. Qi, *Genons, twist defects, and projective non-Abelian braiding statistics.* Phys. Rev. B **87**, 045130 (2013);

M. Barkeshli and X.-L. Qi, *Synthetic Topological Qubits in Conventional Bilayer Quantum Hall Systems.* arXiv:1302.2673 (2013);

M. Barkeshli, C.-M. Jian, and X.-L. Qi, *Theory of defects in Abelian topological states.* arXiv:1305.7203 (2013).

[205] Y. Huh, M. Punk, and S. Sachdev, *Optical conductivity of visons in Z2 spin liquids close to a VBS transition on the kagome lattice.* arXiv:1303.7235 (2013).

[206] E. Fradkin and S.H. Shenker, *Phase diagrams of lattice gauge theories with Higgs fields.* Phys. Rev. D **19**, 3682 (1979).